Design, Preparation and Characterisation of Polyurethane Nanocomposites Membranes for Apparel Applications

Rebecca Chadwick

A thesis submitted in partial fulfilment of the requirements of Sheffield Hallam University

for the degree of Doctor of Philosophy

In collaboration with PIL Membranes LTD

February 2024

Candidate Declaration

I hereby declare that:

1. I have not been enrolled for another award of the University, or other academic or professional organisation, whilst undertaking my research degree.

2. None of the material contained in the thesis has been used in any other submission for an academic award.

3. I am aware of and understand the University's policy on plagiarism and certify that this thesis is my own work. The use of all published or other sources of material consulted have been properly and fully acknowledged.

4. The work undertaken towards the thesis has been conducted in accordance with the SHU Principles of Integrity in Research and the SHU Research Ethics Policy.

5. The word count of the thesis is 51824

Name	Rebecca Chadwick
Award	PhD
Date of Submission	February 2024
Research Institute	MERI
Director(s) of Studies	Dr. Francis Clegg

Acknowledgments

I would like to thank the following people, without whom I would not have been able to complete this research, nor would I have made it through my PhD.

Thank you to the Vice Chancellors Scholarship and PIL Membranes LTD for providing funding for this project. A special thank you to the team at PIL Membranes LTD, especially Dr. James Woods for excellent knowledge and straight forward attitude.

Fellow MERI PhD candidates; Ronak, Jacob, Alex, Olly, Hadi and Jorge at Sheffield Hallam University for their continued support, encouragement, and kindness. Special mentions go to James Durham for tolerating my constant teasing. Dr. Hassan Judah for being like a big brother and providing me with the best banana bread. Mirjam Skoff for technical and emotional support plus lovely handmade gifts and chocolates from abroad. Shruti Mandhani, who I met on the first day of our PhD's and have since bonded over the continued torture of completing a PhD. We have been joined at the hip from day one, even jointly winning the MERI symposium poster and presentation award. We survived this rollercoaster together and formed a lasting friendship.

Thank you to my PhD supervisor Dr. Francis Clegg, who has the patience of a saint. Whose insight and knowledge into the subject matter steered me through this research. His detailed feedback was often a blessing and a curse, I'm relieved to no longer see pages scrawled with red ink. Thank you for providing unwavering support and encouragement.

And my biggest thanks to my family, Mum, Dad, and Auntie Sue for all the support you have shown me through this research. With special mention to my Mum whose ears are sore from my constant gripes and moans about this PhD. Her words of encouragement and support have been unmeasurable. A huge thanks for her final no nonsense pep talk which whipped me into shape and motivated me to finish writing the thesis this century.

To Dr. Jack Slater, meeting you during this PhD is one of the few positives to come from it. Your carefree unburdened nature is just what my overstressing self needs. To more adventures with you and a future were we never talk about PhD's again. All my love.

Abstract

Breathable waterproof membranes protect the wearer from the climate and potential hazards. The membrane must be waterproof yet breathable to maintain comfort to the wearer. Previously the inclusion of layered silicates and graphene oxide (GO) have been shown to improve mechanical properties of polyurethane (PU) however, limited studies have been conducted on montmorillonite (MMT) and GO's impact on breathability, waterproofness and microporosity of PU membranes. This research project in conjunction with a sponsoring company, PIL Membranes LTD, aims to fill that void in knowledge. The effects of MMT and GO on both monolithic and microporous PU membranes for applications in outdoor wear will be investigated. Specific interest, due to the nature of the membrane's application, will focus on the nanofillers effect on mechanical properties (storage modulus & Young's modulus), surface roughness, wettability, breathability, and waterproofness. The MMT nanofiller C20 dispersed well in both monolithic and microporous PU membranes, often providing modest improvements to a range of properties including, breathability, surface roughness and static dissipative.

Table of Contents

Abbreviations

4,4'-MDI	4,4'-diphenylmethane diisocyanate
AFM	Atomic Force Microscopy
ATR-FTIR	Attenuated Total Reflection - Fourier-Transform Infrared Spectroscopy
AW-GO	Acid Wet Graphene Oxide
BW-GO	Basic Wet Graphene Oxide
C10A	Cloisite® 10A Previously Known as Claytone-APA
C15A	Cloisite® 15A Previously Known as Cloisite® 15
C20	Cloisite® 20 Previously Known as Cloisite® 30B
CEC	Cation Exchange Capacity
CNa^+	Cloisite® Na^+
CNF	Cellulose Nanofibres
CNTs	Carbon Nanotubes
CVD	Chemical Vapour Desposition
DABCO	1,4-diazabicyclo-[2.2.2]-octane
DBTDL	Tin Dibutyltindilaurate
DMA	Dynamic Mechanical Analysis
DMF	Dimethylformamide
DSC	Differential Scanning Calorimetry
EDS	Energy Dispersive Spectroscopy
EDX	Energy Dispersive X-ray
FVM	Focus-variation Microscopy
G'	Storage Modulus
G''	Loss Modulus
GDP	Gross Domestic Product
GNPs	Graphene Nanoplatelets
GO	Graphene Oxide
HCl	Hydrochloric Acid
HMDI	Hexamethylene Di-isocyanate
HS	Hard Segments
Lc	Lambda C
IFM	Infinite-focus Microscopy
IR	Infrared
MDI	Diphenylmethane 4,4'-di-isocyanate
Micro_PU	Microporous Polyurethane Membrane
MIM	Compare Metal Injection Moulds
MMT	Montmorillonite
Mono_PU	Monolithic Polyurethane Membranes
Mono_PU_Con	Control Sample Monolithic Polyurethane with Additional DMF
OMMT	Organo-modified MMT
PPF	Poly(propylene fumarate)
PTMEG	Poly(tetramethylene ether glycol)
PTFE	Poly-tetrafluoroethylene
PU	Polyurethane
PVA	Poly(vinyl alcohol)

Ra	Profile Roughness Measurement
rGO	Reduced Graphene Oxide
R_{rms}	Surface Root-mean-square Roughness
Sa	Arithmetical Mean Height of Selected Area
SEM	Scanning Electron Microscope
Sku	Provides Information on the Sharpness of the Surface Height Distribution
SPEs	Solid Polymer Electrolytes
Sq	Surface Texture Measurement (Root-mean-square Height of Selected Area)
SS	Soft Segments
Ssk	A Measure of Asymmetry of a Surface About a Mean Plane
Tan δ	Damping Coefficient
T_c	Re-crystallisation Temperatures
TDI	Tolyene Di-isocyanate
TEM	Transmission Electron Microscopy
T_g	Glass Transition
T_m	Melting Point
T_{max}	Maximum Degradation Rate
VFM	Variant-focus Microscopy
W	Wettability
WPU	Waterborne Polyurethanes
WVTR	Water Vapour Transmission Rates
WW-GO	Water Wet Graphene Oxide
XRD	X-ray Powder Diffraction
γ_{LV}	Liquid – Vapour Phase
γ_{SL}	Solid – Liquid Phase
γ_{SV}	Solid – Vapour Phase

Chapter 1

1.1 Introduction

Breathable waterproof membranes are important in protecting the human body from extreme climatic environments. They must provide shielding from heat, wind, rain, and harmful agents while allowing the wearer to be comfortable; the latter is achieved by the transmission of water vapour, produced via perspiration, through the membrane from the inside to the outside atmosphere (Fig. 1).

PIL Membranes LTD, part of KL Technologies Group, develop and manufacture polymers and membranes for use in garments, technical applications, gloves, and footwear. They produce their protective membranes from PU; a polymer which is commonly utilised in high-tech membranes as it can maintain good barrier properties while providing high breathability as well as maintain flexibility, particularly at low temperatures.[1] Furthermore, PU has high abrasion resistance, tear strength and elasticity.[2,3] PU is only one of several components in a waterproof garment and Porelle® is a brand name for PIL Membranes LTD most established version of a PU membrane (Fig. 1). Although PU is a well-established membrane for use in a range of apparel, further advancements can be made. This project mainly involves the exploration of two types of nanofillers, layered silicates specifically MMT and organo-modified MMT (OMMT) and GO and graphene nanoplatelets (GNPs) within both monolithic and microporous PU membranes to aid in the improvement of PU membrane barrier and mechanical properties. Due to the industrial collaboration nanofillers and processing methods have been selected with transferability and industrial scale up in mind.

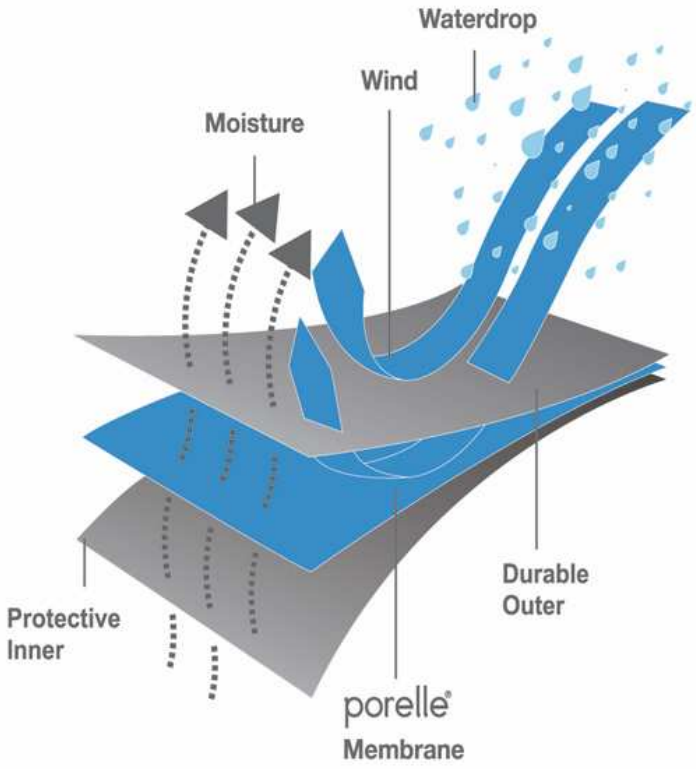

Figure 1. Diagram of how PIL Membranes branded film Porelle® provides wind and waterproofness while allowing for the transmission of water vapour.[4]

1.2 Aims and Objectives

Overall aim

Provide improvements to PU membranes, monolithic and microporous through the addition of nanofillers with a potential variety of applications in mind.

Objectives

1) To explore and obtain optimum nanofiller dispersion as this often leads to the best performance while minimising changes to the current industrial processing methods for each membrane. Readily available nanofillers which can be mass produced at a relatively affordable cost were chosen.
2) Thoroughly characterise membranes using a wide range of techniques focusing on three key areas: dispersion and surface morphology, barrier properties and mechanical and thermal properties. In order to understand how nanofillers improve and/or negatively affect properties. Often the improvement of one property comes at the expense of another. It is easy to focus on the positives

rather take the whole picture in to account hence the in-depth study into a wide range of properties.

3) A specific interest was to assess surface roughness, a novel application for assessing this was utilised. Variant-focus microscopy (VFM) has been used in analysing the surface roughness of 3D structures such as drill bits, however this investigation studied its application on relatively flat membranes. Surface roughness is linked to breathability, permeability, wettability properties and adhesion to other fabrics in multi-layered garments.

Chapter 2

Literature Review

2.1 Polyurethane

Polyurethane (PU) is a block copolymer and one of the most widely used polymers in the world, it can be found in everyday items such as cars, shoes, clothing, furnishings, elastomers, coatings, and wall and roofing insulation. It is no surprise that PU is the sixth most commonly produced polymer globally in 2016, with an estimated production of 18 million tons and a global value of 53 billion euros.[5] With increasing demands it is expected that PU production would rise to 22.5 million tons in 2024 new.[6]

2.1.1 History of Polyurethane

Otto Bayer and co-workers developed PUs in the 1930s as a way to circumnavigate patents on polyamide fibres (nylon) to produce materials with similar properties.[5] Bayer and co-workers built upon the work of Wûrtz, who in 1849 discovered urethane groups through the reaction of aliphatic monofunctional isocyanates and alcohols.[7] During World War II PU was developed to replace rubber, which was expensive and hard to obtain at the time. PU was used largely as a chemical and corrosion-resistant coating to protect metal and wood.[8] By the mid-1950s PUs were used in many applications due to their extreme versatility, from coatings to foams and adhesives to elastomers. In the following years the development of polyesters or polyether polyols made PUs more economical to produce.[5,8]

2.1.2 The Urethane Bond Synthesis

PU is an alternative copolymer produced during the reaction between an isocyanate group and a hydroxyl-group forming a urethane linkage, a schematic is provided in Figure 2 showing how the urethane bond is formed. The most basic synthesis of a urethane linkage involves the catalyst 1,4-diazabicyclo-[2.2.2]-octane (DABCO), a Lewis-base which facilitates polymerisation *via* a non-radical hydrogen abstraction process

between isocyanate groups and hydroxyl groups. The proposed reaction mechanism commences with the deprotonation of alcohol 1 by the DABCO catalyst 2 to produce the catalytic intermediate 3 and an alkoxide 4. Isocyanate 5 then undergoes nucleophilic attack at the electron deficient carbon centre by the alkoxide 4 to generate intermediate 6. The newly formed anionic nitrogen group is capable of abstracting the acidic hydrogen of catalytic intermediate 3 thus forming the desired urethane dimer 7 which can repeatedly undergo this process to form PU.[9]

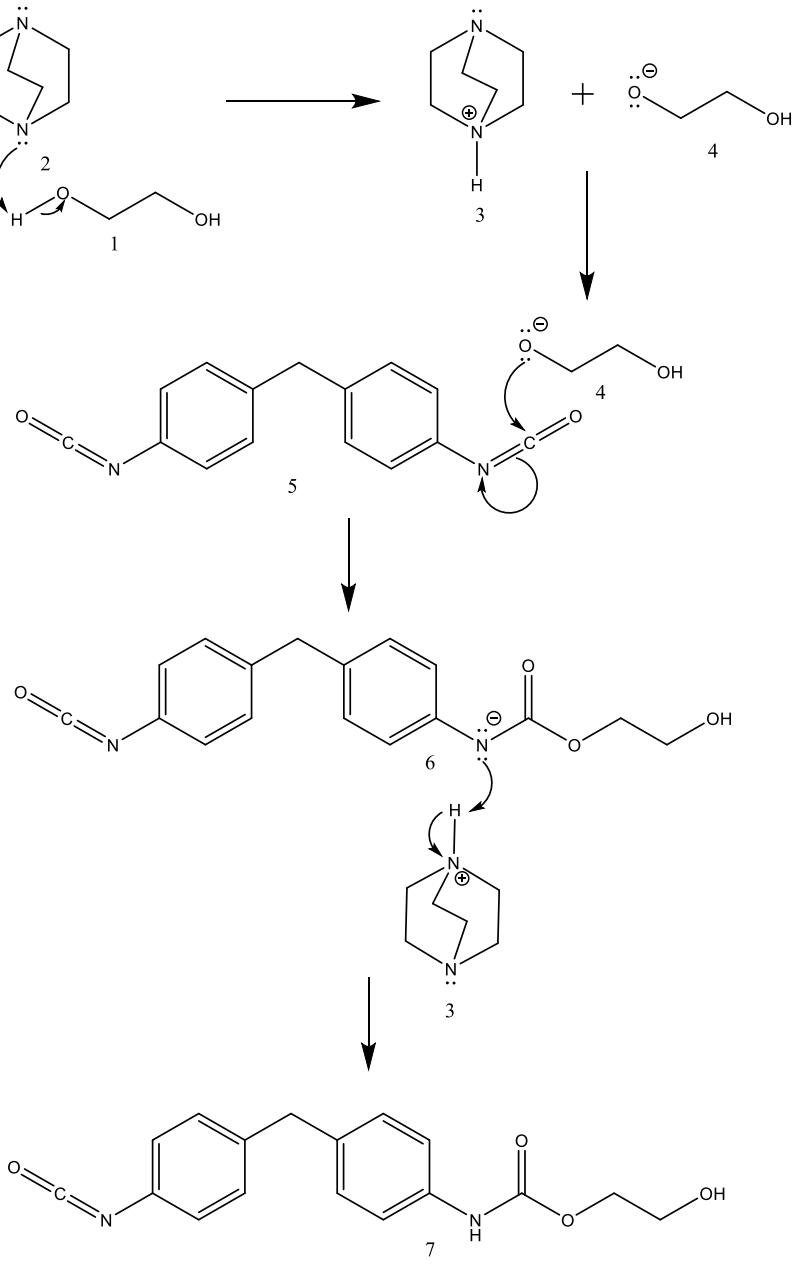

Figure 2. Schematic reaction diagram of urethane bond synthesis.

2.1.3 Polyurethane Synthesis

Often in more complex PU synthesis there is a diverse range of isocyanates, polyol chain extenders and catalysts to choose. This allows the synthesis of a wide variety of PU structures.[2,9,10] Commercially three different types of isocyanates are typically used, tolyene di-isocyanate (TDI), hexamethylene di-isocyanate (HMDI) and diphenylmethane 4,4'-di-isocyanate (MDI).[11] Moreover, the hydroxyl group compounds are often polymers themselves, known as oligomers, comprised of only a few monomer units such as polyesters and polyethers.[11] PU reactions can occur in one-step or two-step reaction, however most PU is synthesised via a two-step reaction.[9,10] A two-step reaction involves the formation of a di-isocyanate prepolymer through the poly-addition process between diisocyanate and bi-functional or even multi-functional polyols with hydroxyl terminal groups (Fig. 3a).[9]

The pre-polymer formed from this reaction can be extended through the second step reaction with a low-molecular weight compound with active hydrogen atoms (e.g., 1, 4-butanediol) (Fig. 3b). A one-step reaction involves these two steps, formation of a diisocyanate prepolymer and chain extension occurring at the same time. A one-step reaction gives less autonomy over the chain structure and therefore careful selection of relative ratios of all monomers and chain extenders is crucial.[9]

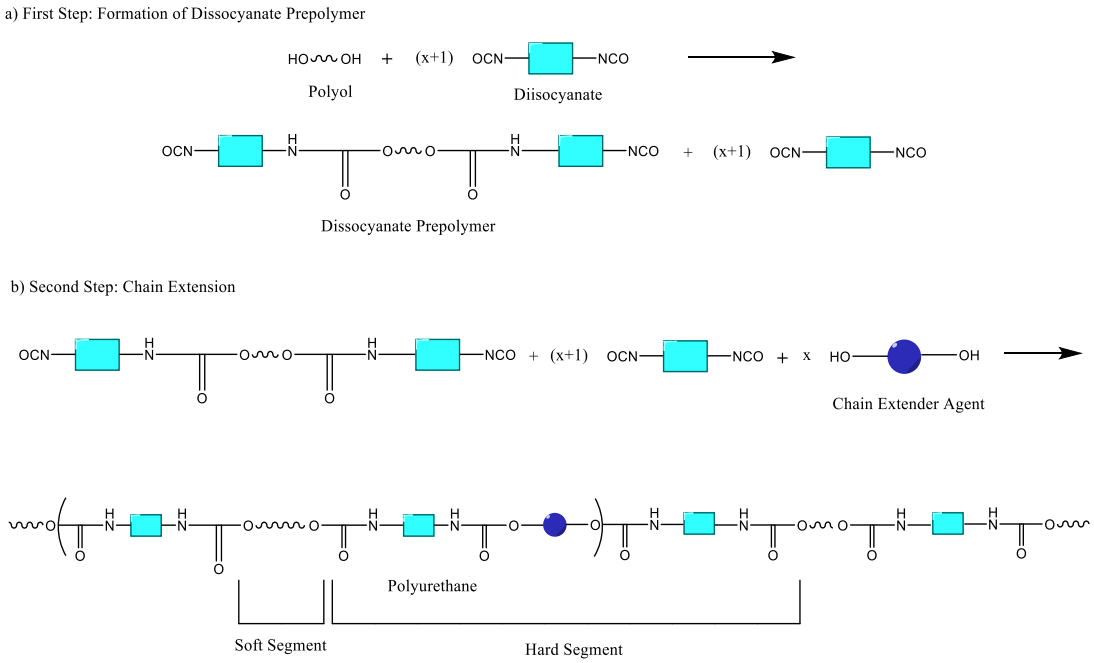

Figure 3. a) Schematic diagram of the formation of diisocyanate prepolymer. b) Schematic diagram of chain extension of diisocyanate prepolymer forming PU with hard and soft segments.

Multifunctional polyols can lead to three-dimensional crosslinking. The size and terminal end groups of the prepolymer can be selected through using an excess amount of one component e.g., a higher proportion of diisocyanate (A) in relation to polyol (B) (Figure 4).[9,10]

$$2A + B \rightarrow ABA$$

$$3A + 2B \rightarrow ABABA$$

$$etc.$$

Figure 4. Schematic to demonstrate the polymerisation of PU alternating copolymer.

2.1.4 Morphology of Polyurethane

PU is composed of blocks known as hard segments (HS) and soft segments (SS), which are thermally immiscible and thus phase separate.[5,12,13] The HS is a combination of isocyanates and triol or diol chain extenders whereas the SS is comprised of long flexible polyester or polyether units (Fig. 3b).[12,14] The HS form microdomains through mutual attraction involving hydrogen bonding within the HS and is thought to be the reason why phase separation occurs.[15] The SS are in an amorphous state and provide elastomeric properties to the polymer. On the other hand, the HS can be either in an amorphous glassy state or in a crystalline state depending on the presence of hydrogen bonds. PU properties can be altered through the relative quantities of SS and HS, an increase in SS may increase the polymer elongation, flexibility, and resilience at low temperature. Whereas an increase in HS may increase the melting point, the Young's Modulus, wear resistance and hardness.[12–14]

Furthermore, the properties of PU can be altered through the type of isocyanate, polyol, chain extender and catalyst employed.[13,14] The elasticity and Young's Modulus have been found to increase when an aliphatic diisocyanate is used in place of an aromatic diisocyanate.[14] Different catalyst such as an amine 1,4-diazabicyclo-[2.2.2]-octane (DABCO) or tin dibutyltindilaurate (DBTDL) allow for very specific catalytic systems, offering high selectivity of polyol components with different molecular weights and with primary, secondary or tertiary hydroxyl groups.[9]

2.2 Membrane Types, Formation, and their *Modus Operandi*

This study focuses on two types of PU membranes: monolithic or microporous. Monolithic membranes are a solid sheet of polymer while microporous membranes have an interconnected porous structure. Scanning electron microscope (SEM) cross sections of these two membrane types gives a clear visual indication of the difference (Fig. 5).

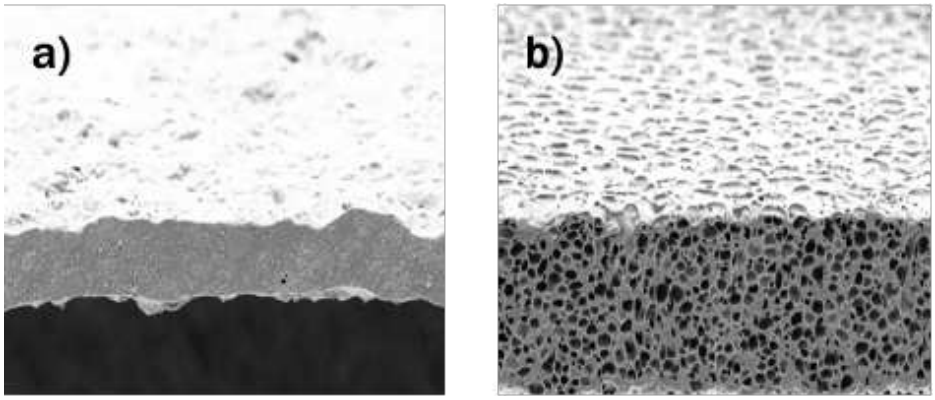

Figure 5. SEM images of a) PIL Membrane's monolithic membrane.[4] b) PIL Membrane's microporous membrane.[4]

2.2.1 Monolithic Membranes

Monolithic membranes are thin and often hydrophilic, they are utilised in sports and leisure apparel. PU polymers can be modified with up to 40 % by weight poly(ethylene oxide) which forms hydrophilic amorphous regions within the PU system and has an affinity for water vapour.[16] The balance between hydrophobic and hydrophilic components must be tightly controlled and optimised to produce a breathable, waterproof, flexible and durable membrane. Furthermore, it must not be soluble in water or dry-cleaning solvents.[16]

The diffusion of water vapour through a monolithic membrane occurs via an adsorption-diffusion-desorption process. When there is a build-up of water vapour produced by the wearer a concentration gradient is formed, this causes water vapour to be adsorbed onto the surface of the membrane on the side closest to the body where the water vapour concentration is greatest.[17,18] The adsorbed water vapour molecules interact with hydrophilic groups within the polymer chains, which act as 'inter-molecular pores'

within the PU matrix.[19] These interactions are weak and can easily be displaced by newly adsorbed water vapour molecules; this forces the molecules through the membrane *via* diffusion.[18,19] When the water vapour molecules reach the outer surface, the side of lower concentration, the water vapour is desorbed.

PIL Membranes monolithic PU membrane is extremely waterproof due to its solid (non-porous) structure, physically stopping the passing of water droplet, as well as being lightweight and thin (12-40 microns) this makes the membrane ideal for use in smaller accessories, garments and footwear often exposed to snow, wind, and rain.[4] It is often used in sports and leisure wear however when wet it can produce a clammy feeling reducing insulation leaving the wearer feeling cold.[19]

2.2.2 Microporous Membranes

Common polymers employed to form microporous films include PU, poly-tetrafluoroethylene (PTFE), polyamides and polyesters however PU and PTFE are the most popular due to their toughness, flexibility and processability. Microporous PU membranes are generally hydrophobic with an interconnected porous structure which allows for air and water vapour permeation. The membrane is often laminated to a textile fabric producing a clothing layer which is windproof, waterproof, and breathable.[18,19] The hydrophobic nature of the polymer combined with the extremely small pore diameters of 0.1 - 50 µm requires a very high pressure for water to penetrate the membrane.[19] Waterproofness is achieved because of the large size difference between individual water molecules, a water molecule is 2.75 Å in diameter (0.000275 µm) while a water droplet is >100 µm. The membrane remains breathable due to being thin and porous thus offering little resistance to the diffusion of water vapour.

PIL Membranes LTD uses a coagulation bath to produce microporous membranes. The resulting microporous membrane is hydrophobic and consists of interconnecting porous structure with pores less than one micron in diameter.[4] It is waterproof and breathable while being lightweight. It is often used in accessories, footwear, and garments, such as sports and leisure wear as it remains dry while exercising.[4]

2.3 Nanofillers

Nanofillers have at least one dimension in the nanometre range; many exist such as carbon nanotubes and fibres, metal oxides, nanodiamonds and nanocellulose. [20,21] This work focuses on clay, graphene oxide (GO) and graphene nanoplatelets (GNP). The potential properties imparted by the nanofillers to the polymer are dependent on several factors; the nanofillers properties and shape, the effective dispersion within the polymer matrix, and the polymer-filler interactions.[21]

2.3.1 Layered Silicates

Clay can be both natural and synthetic clay minerals, which consist of different sheets bonded to each other by shared oxygen atoms.[20] The clay employed in nanocomposites commonly belong to the structural family; 2:1 phyllosilicates and is composed of an octahedral sheet of aluminium atoms bonded to eight oxygen atoms sandwiched between two tetrahedral silicate layers of silicon atoms bonded to four oxygen atoms (Fig. 6).[20,21] The stacking of these three sheets forms a platelet and the space between the clay layers is known as the interlayer space, here exchangeable cations are present (e.g., sodium ions).

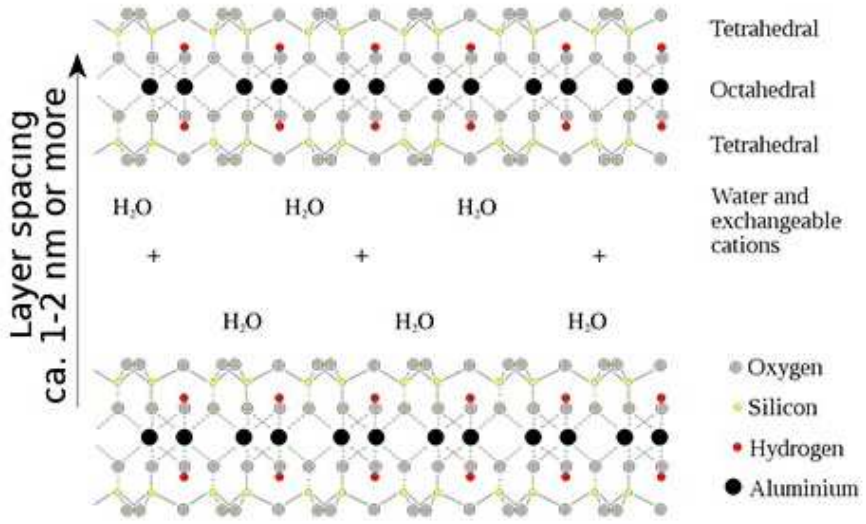

Figure 6. Molecular structure of montmorillonite, a 2:1 phyllosilicate.[22]

Phyllosilicates are hydrophilic and to render them more organophilic and aid dispersion in hydrophobic polymer matrices the cations within the interlayer space can undergo cationic exchange with surfactants such as primary, secondary, tertiary, and quaternary

alkylammonium or alkylphosphonium cations (Fig. 7).[21] This cationic exchange lowers the clay's surface energy and increases the d-spacing. These surfactants aid the dispersion of the nanoclay into a polymer matrix by expanding the interlayer space, reducing the surface energy, and increasing the hydrophilic nanoclay's miscibility with a hydrophobic polymer which has allowed for applications in industry.[20,23] The cation exchange capacity (CEC) of a clay measures the ability to exchange its interlayer cations. It is quantified by the amount of interlayer cations that can be exchanged to balance the electrical charge per 100g of calcined clay.[23] The CEC for each clay used in this study is detailed in Figure 8.

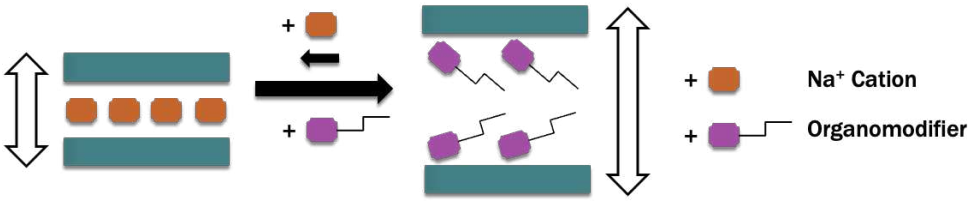

Figure 7. The cation exchange mechanism of clay. Arrows indicate the increasing d-space after cationic exchange.

The clay used in this research project are Cloisite® clays known as CNa+, C20, C10A and C15A. CNa+ has sodium ions present within the interlayer space (Fig. 8a) while in C20, C15A and C10A these sodium ions have undergone cationic exchange with three different organomodifiers forming three different organomodified Cloisite® clays; the organomodifier used in each organomodified Cloisite® clays is shown in Figure 8 b to d.

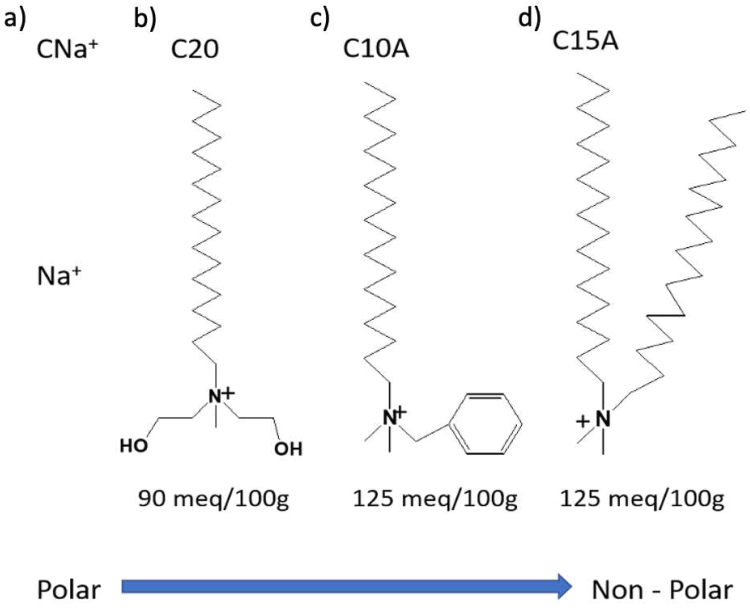

Figure 8. Organomodifier chemical structure for each of the four clay nanofillers a) sodium cation b) C20 organomodifier c) C10A organomodifier d) C15A organomodifier. The arrow indicates the decreasing polarity of the clays.

2.3.2 Graphene Nanofillers

Geim and Novolosev of the University of Manchester first isolated and characterised pristine graphene from graphite (stacked graphene sheets held together by strong Van der Waal's forces) in 2004.[24] Their method, though rudimental and simplistic, using scotch tape to remove a single atom thick layer of pristine graphene was a novel breakthrough worthy of a Nobel prize in Physics in 2010.[25] Graphene is a one-atom thick two-dimensional monolayer of carbon atoms arranged in a honeycomb lattice.[24] Graphene is essentially the building block for all graphitic carbon materials; fullerene, carbon nanotubes and graphite (Fig. 9).[26,27] While graphene is extraordinarily strong it is also very light weight at 0.77 mg per square metre, highly elastic, and has interesting electrical and optical properties.[28,29] There are many ways to synthesize graphene such as; mechanical exfoliation, thermal chemical vapour desposition (CVD), un-zipping of carbon nanotubes (CNTs) and thermal decomposition.[30] However chemical oxidation and reduction has been a traditional technique for producing GO and rGO for many years . There are several methods pertaining to this such as Staudenmaier, Brodie, Hummers.[30,31] Hummer's method is the most popular due to a short reaction time, exfoliation is easier, and the toxic by-products were eliminated by replacing the oxidation agent $KClO_3$ with $KMnO_4$.[31] Treatment with H_2O_2 eliminates permanganate ions and additional water washing can be utilised.[30] GO can then undergo a reduction process to produce reduced graphene oxide (rGO), there are several ways to reduce GO such as thermal reduction, chemical reduction or photocatalyst reduction each producing slightly different rGO thus affecting the particular properties of each rGO (Fig. 10).[27,32]

Although graphene is hailed as a breakthrough modern material that will revolutionise various industries across the globe it has one major stumbling block; it is extremely difficult to produce on a large scale and to date one atom thick graphene layers have not been produced on a large scale.[26] However recent advancements in the past decade have seen graphene being produced in large quantities composed of a few layers of imperfect graphene. This product, although still having many desirable properties lacks some of the exciting and extremely unique attributes first reported by Geim and Novolosev such as a remarkably high charge-carrier mobility of 2000–5000 $cm^2/V\ s$.[24,26]

Despite the struggle to produce large volumes of graphene, academia and industry are already investigating the potential affects graphene may have on polymers.

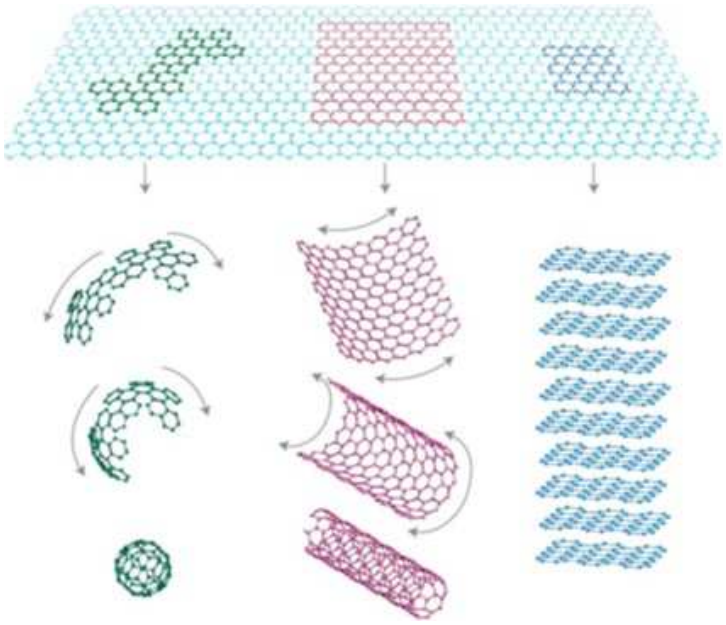

Figure 9. Diagram to illustrate how graphene (top) is the building block for all graphitic carbon materials: fullerene (bottom left); carbon nanotubes (bottom centre); and graphite (bottom right).[26]

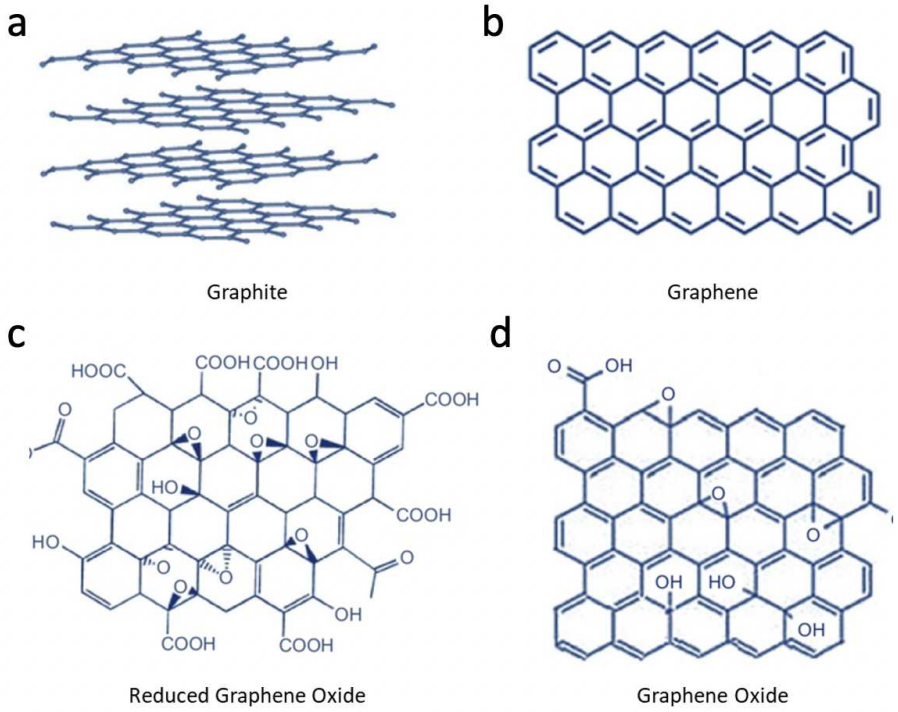

Figure 10. Structure of different versions of graphene, a) graphite b) graphene c) reduced graphene oxide (rGO) d) graphene oxide (GO).[33]

2.4 Polymer Nanocomposites

Polymers typically require reinforcement via fillers to improve a variety of properties however typical composites have phase mixing on a microcomposite scale and require large amounts of filler in order to give desired property enhancement. The large amounts of filler often result in opaque bulky polymers.[34] Despite improving some of the polymer's properties, there are downsides to using microcomposites such as high costs incurred through high filler loading, poor filler dispersion which can result in negatively affecting the mechanical properties of a polymer. Moreover, the opaqueness reduces the capability for aesthetic customisation in industry.

2.4.1 Introduction to Polymer Nanocomposites and Properties

Polymer nanocomposites were reported as early as 1961 however it wasn't until 1985 that Toyota Central Research Laboratory coined the term "nanocomposite" when they successfully produced a nylon-montmorillonite nanocomposite for timing-belt covers.[23,35] From then on research on nanocomposites, including layered silicates, boomed in the 1990s and still remains a sizeable active research field to date.[34,36] Since then, numerous nanofillers have been investigated in a variety of polymers. Graphene, upon its discovery in 2004, became one of the latest nanofillers of interest due to its highly coveted properties; strong, light weight, highly elastic, and has interesting electrical and optical properties.[24,28,29]

Nanofillers, as long as they are well dispersed, have negated these issues outlined above. They can more readily achieve better dispersion within polymer matrices than fillers, often forming a nanocomposite that falls between intercalated and exfoliated systems. Nanofillers can also achieve desired property improvements at far lower loading than that of conventional composites. This results in a reduction in the amount of raw materials required leading to a reduction in cost. Extensive research has been conducted globally on polymer nanocomposites, resulting in remarkable enhancements.

Polymer nanocomposites have remained a sizeable research area owing to their wide range of applications from smart catalysts to packaging materials and energy storage to

barrier membranes to name only a few.[37] The nanofiller, depending on structure, morphology, chemistry, and crystallinity, has potential to improve a polymer's electrical, optical, mechanical, thermal and barrier properties.[38]

Most notably the earliest development of industrial polymer nanocomposites was timing belt covers by Toyota; they successfully produced the first practical example of polymer nanocomposites for automotive applications. They created a nylon 6 clay nanocomposite, using montmorillonite modified with amino acids. The resulting nanocomposite exhibited excellent mechanical properties compared to nylon 6, the tensile modulus almost doubled from 1.1 GPa to 2.1 GPa at only 1.6 vol.% clay.[39]

A study investigated the design, development, and mechanical properties of novel biodegradable polymer nanocomposites implants for bone tissue applications. They used poly(propylene fumarate) (PPF) and a selection of GOs at concentrations between 0.01 and 0.2 weight %. They found all the PPF/GO nanocomposites significantly increased the mechanical properties (compressive yield strength and modulus, and flexural modulus and yield strength) compared to PPF.[40]

Polymer nanocomposites can be utilised in energy-related functional materials. There have been recent advancements using rGO to improve durability of energy storage devices such as electrochemical capacitors. A crosslinked rGO aerogel was combined with poly(vinyl alcohol) (PVA). Crosslinked rGO has a lower density and higher porosity than pristine RGO, these key properties make crosslinked rGO more desirable for use in high-capacity materials.[41,42] Furthermore, the crosslinked rGO dispersed better than pristine rGO. Other researchers have utilised RGO in solid polymer electrolytes (SPEs) used in lithium-ion batteries. They found RGO improved the tensile strength by 300% and the lithium-ion conductivity of SPEs.[41,43]

Despite the vast potential of polymer nanocomposites, the research and development of novel polymer nanocomposites with high performance functionality for industrial applications is challenging.[37]

2.4.2 Polymer-Nanofiller Preparation Methods

In addition to the physical and chemical modifications to clay and graphene nanofiller there are generally three methods for the preparation of polymer-nanofiller nanocomposites: solution-blending, melt-blending, and *in situ* polymerisation. The solution blending method involves the polymer and nanofiller dispersed in the same solvent separately before being combined together and subsequently cast onto a flat support to evaporate the solvent. Melt-blending requires the polymer-nanofiller mixture to be at temperatures usually higher than the polymer melting point. This results in the nanofillers directly reinforcing the polymer matrix. *In situ* polymerisation involves dispersing nanofillers in a monomer or monomer solution which is then polymerised.[23,44]

Chemical modification of the nanofillers along with either melt-blending and *in situ* polymerisation would allow for the best dispersion and possible nanofiller-polymer interactions. However due to processing techniques at PIL Membranes LTD it was required that the nanofillers be easily integrated into their current system with as little disruption as possible. As such, physical clay modification via organomodifiers and the oxidisation of graphene in combination with solution-blending method for nanofiller dispersion in the PU matrix was utilised as it allows for the easiest and cheapest industrial scale up despite the potentially poorer dispersion and polymer-nanofiller interactions than other methods.

Solution mixing requires agitation in the form of either magnetic stirring, shear mixing or sonication to mix polymer-nanofiller nanocomposites.[23,44] In this project shear mixing was used to mix clay or GO/GNP and PU via the solution blending method (Fig. 11). In the case of GO and GNP, sonification was used to aid dispersion of GO and GNP into Dimethylformamide (DMF) prior to shear mixing. Shear mixing was selected as it assured adequate mixing of PU despite its high viscosity, this method also mimics the industrial set up at PIL Membranes. Furthermore, a study investigated the structure and properties of natural rubber and MMT via two methods; solution mixing and melt compounding. While both methods produced nanocomposites of similar structures the solution mixing methods improved the dynamic mechanical properties.[45]

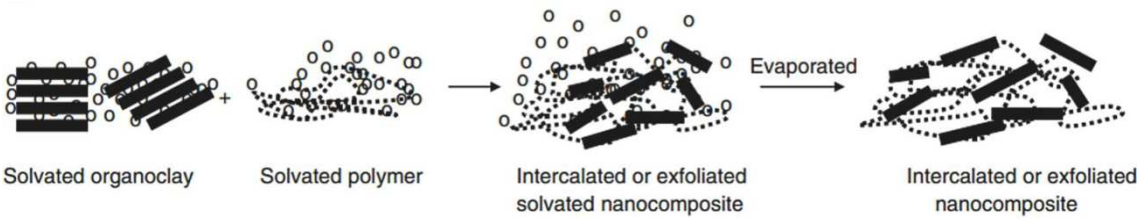

Figure 11. Schematic of nanocomposite preparation via solution mixing method.[23]

2.4.3 Dispersion of Nanofillers Within Polymer Matrices

It is important that nanofillers are well dispersed within a polymer matrix to allow for even distribution and reinforcement of potential property improvements. One way to increase exfoliation within a polymer is to modify a nanofiller; clays can undergo cationic exchange while graphene can be oxidised producing GO.

Several studies have shown organomodification of various MMTs has improved dispersion within a polymer matrix. One study found that dispersion of MMT within a PU matrix was improved when the MMT was organomodified with one tallow group rather than two.[12] Another study supported this claim, while also suggesting better dispersion can be achieved if the surfactant has a longer tallow chain and hydroxyl ethyl groups on the ammonium ion rather than methyl groups.[46] They found C20 with two hydroxyl groups and one tallow chain dispersed the best out of the four MMT/OMMT examined.[46]

It is not yet possible to isolate pure single sheets of graphene on a large industrial scale, as such GO, rGO or other functionalised graphene membranes are often utilised.[30] The oxidation of graphite to form GO disrupts the sp^2 hybridized structure and increases the interlayer spacing from 3.35 Å of pristine graphite powder to 6.8 Å for GO powder which aids in exfoliation of the graphene layers.[47] In addition, the oxygen-containing molecular groups, which can vary in type and extent depending on supplier, also offers a variance in polarity and thus a potential range against which to assess compatibility with the PU. The increased d-spacing and oxidation increases the chance of good dispersion within a PU matrix and thus an increase in desired properties.

X-ray Powder Diffraction (XRD) is a technique used to examine the dispersion of nanofillers within a polymer matrix, a homogeneous dispersion is often essential to

improving the properties.[48] Figure 12 provides idealised XRD patterns and structural confirmation of the three categories involving the dispersion of nanofillers in a polymer matrix; microcomposite, intercalated (organised and disorganised) and exfoliated.

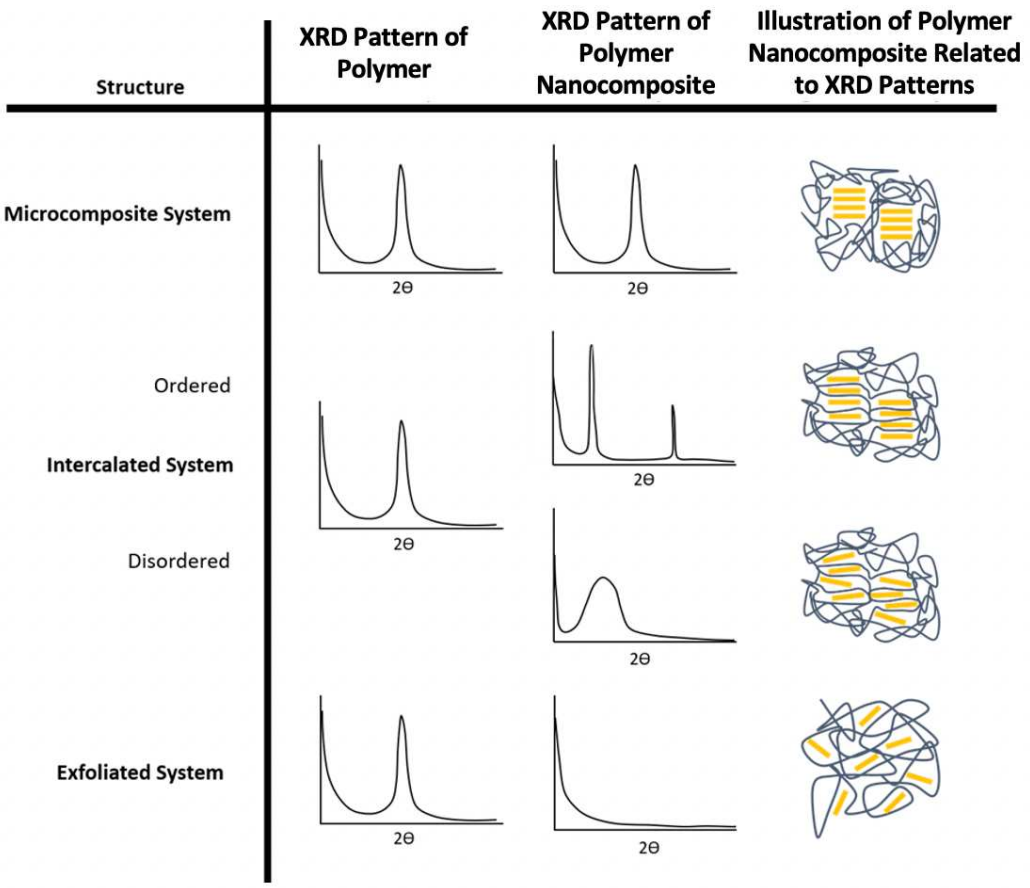

Figure 12. Schematic of idealised powder XRD traces which indicate the possible clay/polymer nanocomposite structures; microcomposite, intercalated (ordered and disordered) and exfoliated.

During intercalation of the polymer chains by the nanofiller, the interlayer spacing is increased and the diffraction shifts towards a lower angle value. D-spacing can be calculated using Bragg's Law which relates interlayer spacing to reflection angle.[49] Equation 1 demonstrates how the d-spacing is calculated using the wavelength of X-rays (Cu K-alpha lambda, 1.5406 Å) and 2θ from XRD patterns.

Equation 1. Bragg's Equation

$$d=n\lambda/2\sin\theta$$

2.4.4 Barrier Properties of Polymer Clay Nanocomposites

The addition of clay reduced the gas permeability of methane by at least half and helium was reduced by at least two thirds with all clay types when the minimum loading tested, when 5 wt.% was added to PU matrix.[12] This is due to the tortuous path, where the inclusion of impenetrable particles or platelets blocks the diffusion pathway for molecules therefore extending the time taken for said molecule to navigate through the polymer.[50] This reduction is ideal for barrier materials, packaging, and protective coatings.

Although there are numerous papers on the layered silicates within monolithic PU, very few of these studies have examined the effect of clay on the waterproof properties and breathability of the PU membranes. A study published in 2008 found the addition of clay to a PU film reduced the water absorption, additionally they discovered 1 wt.% to be the optimum clay concentration reducing water absorption from 90% to 50% after 60 hours.[51]

2.4.5 Barrier Properties of Polymer GO Nanocomposites

Although rGO and GO can provide increased mechanical properties to PU it has also been shown that rGO decreases water vapour transmission rates by 76% with the addition of 3 wt.% rGO.[52] Although this is counterintuitive to the research project aims as clays and GO have been shown to reduce breathability within monolithic films, however there is limited research on the effects of clay and GO on microporous PU films, the effects of these nanofillers on porosity and microporous structure is relativity unknown.

A study published in 2013 investigated the effects of rGO on cellulose nanofibres (CNF) paper, the results showed increased mechanical strength but more relevant to this project found the contact angle was increased from 47° to 75° and 90° at the inclusion of GO and rGO respectively.[53] The surface root-mean-square roughness (R_{rms}) of the CNF paper was consistent with the cellulose nanofiber diameter of 3.5–4.2 nm. Whereas the

addition of rGO increased the R_{rms} to 5.1–6.0 nm, an explanation given for these results was the van der Waals or restoration π–π stacking between adjacent RGO layers.

2.4.6 Mechanical Properties of Polymer Clay Nanocomposites

It has been well established that the inclusion of MMT/OMMT can cause significant improvements in a polymer's mechanical properties. A study has shown the inclusion of C20, C10A and C15A all increased the glass transition temperature of PU.[12] The study also found the addition of MMT/OMMT, even at low loading, caused an increase in the Young's modulus in all nanocomposites. As OMMT concentrations increased, C20 produced the largest increase and C15A the smallest.[46] The inclusion of MMT into waterborne polyurethanes (WPU) increased both tensile strength and elongation at break by 70% with the inclusion of 3 wt.% MMT.[54] Another paper found the addition of organically modified OMMT to PU increased both the Young's modulus and tensile strength 2-fold and the elongation at break by 42% at 3.5 wt.% OMMT.[55] Above 3.5 wt.% OMMT the elongation at break was reduced due to aggregation of OMMT.[55]

2.4.7 Mechanical Properties of Polymer GO Nanocomposites

Functionalised GO has been successfully dispersed in PU matrices with promising results in regard to membrane applications. The inclusion of GO into PU has been shown to increase hardness and elastic modulus by 327% and 182%, respectively.[56] Another study also found the inclusion of rGO to increase hardness by 300% and tensile modulus was increased 21-fold.[52] Most studies found properties stopped increasing and sometimes reduced after the addition of 5 wt.% GO.[52,56,57] Peak property improvements based on the wt.% of GO vary in several studies.[52,56,57] Unfortunately, these improvements were at the expense of reduced ductility and elongation at break when rGO content is increased above 1 wt.% a reduction of over 90% can be observed.[52] The observed reduction in elongation at break is attributed to weak interactive forces between graphene and polyurethane. However, this can be overcome through chemical grafting which will improve bonding between the nanofiller and graphene, providing a more reasonable reduction in elasticity.[57]

2.5 Microporous Polyurethane

One study, conducted in 2016, investigated modifying microporous PU with 0.25% - 1.25% rGO *via in situ* polymerization.[58] The presence of rGO increased the thermal stability and mechanical properties of the microporous PU. The maximum degradation rate (T_{max}) for nanocomposites with 1 wt.% or 1.25 wt.% rGO was 51% greater than unmodified microporous PU. Increased rGO concentrations were found to produce larger pores and greater numbers of irregular shaped pores. Larger pore size has a direct correlation with water absorption resulting in an 18% increase with the addition of 1.25% rGO compared to pure microporous PU indicating the addition of rGO may have increased the pore size and thus the breathability. Higher tensile strength and elongation at break were observed but only within 0.5 wt.% rGO, any larger concentrations had a negative impact on the mechanical properties.

However, the most relevant study found pertaining to this research project is a patent from 1996 Toray Industries Inc. claims to have produced a microporous PU film coated to a fabric that has a water pressure resistance of at least 5000 mm and a moisture permeability of at least 8000 g/m^2/24hr. This is achieved by dispersing 0.5-20 wt.% of organomodified phillosilicate into a PU/DMF mix then coating onto a fabric before immersion within a coagulation bath, washing with water and drying.[59] To the best of the author's knowledge this is the only published evidence of the effects of layered silicates on microporous PU films for applications in protective clothing.

2.6 Surface Topography Imaging and Measurements

There are many different types of instrumentation used to image and analyse surface topography these include variant-focus microscopy (VFM), atomic force microscopy (AFM), transmission electron microscopy (TEM) and scanning electron microscopy (SEM). VFM and SEM were used in this study and are discussed in more detail below.

2.6.1 Scanning Electron Microscope (SEM)

Since the development of SEM in the early 1950s it has become a robust and common method to study samples ranging from biological specimens to material science. SEM

uses a focused beam of electrons to scan a sample in a series of continuous lines. Upon hitting a sample's surface electrons are either reflected back (backscatter electrons) or generated through interaction of primary electrons with the sample (secondary electrons).[60] This produces a high-resolution magnified image of the sample. SEM provides many advantages over traditional microscopes including a large depth of field and high resolution. Typically the human eye cannot distinguish objects smaller than 200 μm (0.2mm), a optical microscope can magnify images up to 1000x to resolve details at 0.2 μm while an SEM can reach magnifications of 400,000x with a resolution of ~1 nm.[60,61] SEM can only image surface topography on a smaller scale than either stylus or optical instruments but can be used over a much larger area than AFM. SEM provides a high-resolution image of a sample surface, but it has limitations, it only produces a 2D image and analysis in the 3-dimensial plane is subjective to shading; it is difficult to ascertain if an image contains peaks or valleys.[60] In addition, samples must be placed under vacuum and artefacts are possible during gold or carbon coating.

However, SEM can be coupled with energy dispersive X-ray (EDX) spectroscopy, also referred to as energy dispersive spectroscopy (EDS), to provide elemental composition of a sample. During SEM the collision of the electron beam with the sample produces characteristic X-rays, due to the principle that elements have their own X-ray emission spectrum, and the X-rays can be sorted and measured to ascertain an element type and concentration within a sample.[62] EDX can detect elements with an atomic number higher than boron at a concentration of at least 0.1%.[62] Furthermore, EDX can be used for contamination identification, quality control screening and assessing the dispersion of nanofillers within a polymer sample.

2.6.2 Surface Texture Measurements and Variant Focus Microscopy

VFM is one form of instrumentation used to image a surface and obtain a surface texture measurement. The history as well as modern application of surface texture measurements and VFM is described below.

2.6.2.1 Historical Background of Surface Texture Measurements and Instrumentation

In mechanical engineering, surface texture analysis is critical in the functionality of a component or material. It is estimated that surface defects alone cause approximately 10 % of all manufactured parts to fail, this can have a significant impact on a nation's gross domestic product (GDP).[63] Prior to the twentieth century, surface texture analysis was rudimental, often carried out using our senses of sight and touch. During the early 1900s the use of these senses underwent a technological upgrade. One of the first stylus methods for analysing a surface texture used a sapphire needle attached to a pick-up arm that was dragged across a surface. It relayed a vibration to a speaker much like a Gramophone and the differences in electrical current were read on a voltmeter.[64] One of the first optical instrument designs for measuring surface texture was developed by Gustav Schmaltz of Germany in 1929. This method also involved a stylus but with the addition of a mirror which was attached to the stylus. As the stylus traced the samples surface a beam of light reflected by the mirror traced a graph on a moving photographic chart. Providing an outline of a surface profile although slightly distorted.[65]

Throughout the first half of the 1900s the field of surface texture metrology exploded. Numerous advancements were made, often fuelled by the requirement for accurate surface measurements of machine parts critical to war time needs, such as finely finished bearing surfaces of aircraft engines. Many individuals were critical to the advancement of this field but none more so than two brothers, Thomas Smithies Taylor and William Taylor, and their associate William S. Hobson, who established a company called Taylor, Taylor and Hobson known as TTH. By the 1940s there was pressure for surface texture measurements to produce a single number, that could define a surface and allow for easier comparisons to be made. TTH bought to the market the Talysurf, an instrument which provided a graph and the average surface roughness value read directly from a meter (Fig. 13).[65]

Figure 13. The original Talysurf instrument which provided average surface roughness measuremnets.[66]

2.6.2.2 Surface Profile Measurements and Areal Surface Texture Measurement

Before exploring different instrumentation for surface texture measurements, it is vital to understand the two key types of measurements: surface profile measurement and Areal surface texture measurement. A surface profile measurement (2D) is the measurement of a line across a sample surface. It can be represented mathematically as a height function with lateral displacement z(x).[63] A profile measurement is carried out traversing a sample surface in a line using a stylus. Whereas a 3D measurement otherwise known as an areal surface texture measurement is the measurement of an area on the surface that can be represented mathematically as a height function with displacement across a plane z(x, y).[63] Areal measurements have several advantages over a surface profile measurement. Areal measurements provide a more realistic representation of a sample surface, the 3D map provides information on a sample peaks and valleys. This cannot be achieved with a surface profile measurement alone which may indicate a change in surface height across the Z-axis but it cannot infer whether that change is a peak or a valley.[65] In addition, areal measurements have more statistical significance with less chance of missing significant features compared to a profile measurement.[65]

2.6.2.3 Modern Surface Texture Understanding and Instruments

As mentioned, there is a wide range of instrumentation available that can provide information about a sample's surface texture, these techniques range from stylus and optical instruments to scanning probe and electron microscopes. These are discussed briefly in the following sections.

2.6.2.3.1 Stylus Instruments

A stylus instrument usually involves a conisphere diamond tipped stylus which makes physical contact with a sample surface. The stylus transverses the surface at a constant speed where a transducer converts the vertical movement into an electrical signal. Modern instruments often obtain measurements within the sub-nanometre range and achieving a profile measurement only takes a few minutes. However, the instrument can have limitations, during contact with the sample's surface the stylus may damage the sample. While areal scanning with a stylus involves taking 1000s of data points and can take up to several hours.

2.6.2.3.2 Optical Instruments

Optical instruments can measure both the surface texture and surface form of a sample using optical light, these instruments do not require contact with the sample unlike stylus instruments. Some types of optical instruments include scattering instruments, confocal microscopes, and VFM.

2.6.2.4 Variant Focus Microscopy

VFM provides a topographical image and surface roughness measurement of a sample surface by combining the small depth of focus of an optical system with vertical scanning. A semi-transparent mirror is inserted into the white light source pathway allowing the light to be focused upon the sample via the objective. The light is reflected in several directions dependent upon the sample's topography. The reflected light is gathered by a light sensitive sensor, behind the mirror, and algorithms convert this data into a 3D true colour image with a full depth of field. This is achieved by analysing the sample through the variation of focus along the vertical axis. Since the technique relies upon analysing the variation of focus along the vertical axis it is only applicable to

surfaces which vary sufficiently during the vertical scanning process. Transparent samples and relatively smooth samples, such as those examined in this thesis, are difficult to measure. Herein lies the novelty and challenge of applying VFM to polymer nanocomposite membranes.

2.6.2.4.1 History of Variant Focus Microscopy

Although this principle was developed in the mid-1920s by H. von Helmholtz, research and surface roughness profiles producing a numerical parameter, Ra, was only utilised in the early 1930s to provide surface manufacturing process control.[67] The development on the focus-variation instrument did not take place until the 1990s. Commercially available focus-variation instruments appeared in the 21st century making this a relatively new analytical technique.[68,69] Over the decades research increased the detail by which a single numerical value can describe the surface of a material. There are several parameters which relate to a different profile; P-parameter is calculated from the primary profile, R-parameter from the roughness profile and W-parameter from the waviness profile.[70]

2.6.2.4.2 Application of Variant Focus Microscopy

When exploring the applications of VFM it is important to note this technique is referred to by other names these are; focus-variation microscopy (FVM) and infinite-focus microscopy (IFM). VFM is commonly used to study metal components within engineering, including quality insurances of metal parts used in the aerospace sector.[71–73] VFM has been used to compare metal injection moulds (MIM) to the respective metal produced from the mould, surface roughness was assessed by VFM in the form of *Sq.*[74] Another study exploring MIM found areal surface texture measurements provided more reliable and repeatable information about surface topography than surface profile measurements.[75] In recent years the application of VFM has widened. A study investigated the novel use of VFM analysis of micro finishing films and other coated abrasive tools. These results from VFM were compared to other analytical techniques such as a confocal microscope and SEM. The study found VFM to be a promising measurement technique for coated abrasive tools with future applications in other

fields. They found VFM to be a modern and advanced measurement technique with the following advantages: high measurement efficiency, high repeatability, and easy and intuitive operation with a dedicated software with a range of useful functions.[69] Further studies explored the novel application of VFM in biomedical alloys used in hip replacement to assess wear and tear, VFM was validated against AFM. VFM was found to be able to accurately measure wear and tear scars on the alloys at the nanoscale.[76]

With regards to VFM applications on polymers there is limited research. A book detailing various types of polymer microscopy instruments describes several techniques including SEM and AFM however VFM is not included.[77] This is reflected in the literature search, surface topography of polymers is often carried out by SEM, AFM and TEM with some examples of optical light microscopy. An international study comparing AFM measurements to surface texture measurements on polymer surfaces using three different VFM instruments from different manufacturers concluded VFM was not suitable for accessing the nanometre range of polymer surfaces. Although it should be noted this study does not detail the type of polymer investigated. It also does not provide detailed results of VFM analysis on the polymer, and it does not state the specific VFM manufactures investigated.[78] However, VFM is beginning to be used in the pharmaceutical industry to aid in understanding punch surfaces for producing tablets and for surface compacts for intrinsic dissolution measurements.[79,80] This has led to an explorative study investigating three different hydrophilic polymers used in a wide range of extended release pharmaceutical formulations via VFM.[81] The study introduces VFM analysis of polymer compacts and attempts to attribute surface topography differences to dissolution behaviour. The three polymers displayed significant differences in surface topography despite the same compacting process. With VFM providing a more in-depth analysis into the influence of particle morphology on surface roughness.

With regards to textiles, VFM has begun to be utilised in a range of applications, this includes the surface characterisation of tissues and historical textiles. A study investigated the novel use of VFM as an analytical technique to provide quantitative measurements of tissue surfaces rather than rely solely on hand feel described properties.[82] They found the use of VFM to have potential in providing a more thorough understanding of tissue surface topography and human skin interactions. Another study

applied the use of VFM to image an historic textile fragment dated 1625 AD with the aim to provide a 3D visual image and potentially a 3D printed prototype for wider accessibility for the general public without risking the fragile textile.[83] VFM was able to capture the textile weave structure in a 3D image however further investigations are required to fully utilise the technique and couple it with computer modelling software such as MATLAB and ANSYS to produce an adequate 3D image of 3D printed model.

2.7 Summary

It is evident that monolithic and microporous PU/clay nanocomposites membranes have not been fully investigated with waterproof and breathability properties in mind. Furthermore, rGO is a popular type of GO nanofiller within the literature and as outlined above there are several studies on rGO, in both monolithic and microporous PU membranes. However, there are few studies on the effects of GO on PU membranes and even fewer that have studied GNPs. Due to the lack of research of clay, GO and GNPs within PU monolithic and microporous membranes and their potential impacts on the membrane barrier properties this research project will contribute to global polymer/nanocomposite knowledge. It is common to analyse and image the surface topography of polymer membranes with SEM and AFM however the use of VFM in a range of applications outside of metal components within the field of engineering is gaining traction. This study will provide insight into VFM's potential application in imaging and analysing relatively flat polymer membranes used in the apparel industry.

Chapter 3

Experimental

3.1 Introduction

To understand the effect of nanofillers (clay, graphene nanoplatelets (GNP) and graphene oxide (GO) on the chemical, physical and barrier properties of monolithic and microporous polyurethane membranes a series of experiments were designed and conducted as follows.

3.2 Raw materials

3.2.1 Pre-polymerised PU

In this research two types of pre-polymerised polyurethane were used, one suitable for monolithic membranes (Mono_PU) and one for microporous membrane (Micro_PU). Both contain 4,4'-diphenylmethane diisocyanate (4,4'-MDI), 1,4-butanediol and poly(tetramethylene ether glycol) (PTMEG) (Fig. 14).

Pre-polymerised Mono_PU was supplied in two separate batches, Mono_PU batch 1 from the production line used exclusively for the study described in Chapter 4 investigating Mono_PU/Clay. Mono_PU batch 2 in PIL Membranes LTD R&D laboratory used solely for investigations described in Chapter 5 into Mono_PU/GNP & GO. It should be noted that the chemical components of these two batches are identical however slight variation in production method, resulted in minor differences between these two batches. It is thought these differences has mainly manifested themselves as changes in molecular weight distribution which can easily be affected by stirrer torque and N^2 flow of the reaction vessel which is likely to be more consistent with a laboratory setting than on a production line.

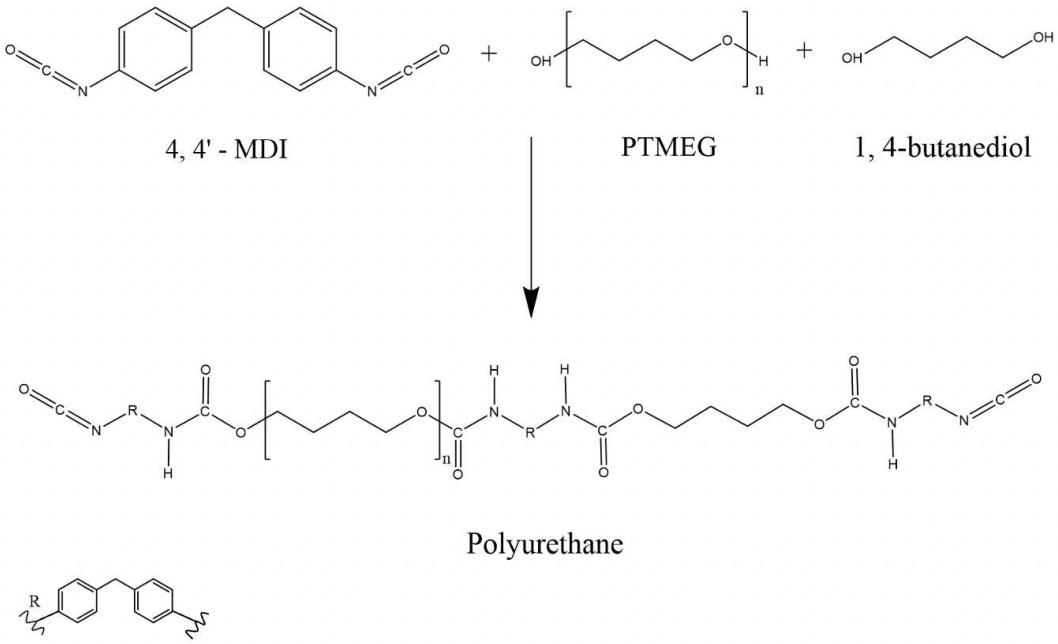

Figure 14. Structure of 4,4'-diphenylmethane diisocyanate (4,4'-MDI), 1,4-butanediol, poly(tetramethylene ether glycol) (PTMEG), polyurethane and R group.

3.2.2 Layered silicates

Clay nanofillers were used in this research due to their commercial availability and low cost. Four Cloisite®, a brand of bentonite, clays were chosen because of their plate-like morphology with high aspect ratio and their capability for cation exchange. Cloisite® Na^+ (CNa^+) was chosen along with 3 organomodified clays; Cloisite® 20 (C20), formally known as Cloisite® 30B, Cloisite® 15A (C15A) now known as Cloisite® 15, and Cloisite® 10A (C10A) now known as Claytone-APA. The molecular structure of these organomodifiers can be found in Section 2.3.1 Figure 8. Their characteristics are detailed in Table 1.

Table 1. The technical details of the four Cloisite® clays used in this research.

Commercial Name	Cloisite® Na^+	Cloisite® 20	Cloisite® 15A	Cloisite® 10A
Organic Modifier	N/A	MT2EtOH	2M2HT	2MBHT
Modifier Concentration	N/A	90 meq/100 g	125 meq/100 g	125 meq/100 g
Moisture	4-9%	<2 wt.%	<2 wt.%	<2 wt.%
Density	2.86 g/cc	1.98 g/cc	1.66 g/cc	1.90 g/cc
Colour	Off white	Off white	Off white	Off white
X-ray Data	d_{001} = 11.7 Å	d_{001} = 18.5 Å	d_{001} = 31.5 Å	d_{001} = 19.2 Å

3.2.3 Graphene Nanoplatelets and Graphene Oxide

Graphene oxide (GO) is a novel nanofiller, first isolated in 2004 at The University of Manchester by Professor Andre Geim and Professor Kostya Novoselov. Now large-scale production of GO is being developed and optimised. On account of the novel nature of GO there are many different suppliers and variations on the market, including Sigma-Aldrich's graphene nanoplatelets (GNP). Due to this, several types of GO and GNP were chosen from three different suppliers: Graphitene, Abalonyx and Sigma-Aldrich. The details of each GO and GNP are in Table 2.

Table 2. The technical details of the four GO and two GNP used in this research.

Supplier	Graphitene	Abalonyx			Sigma-Aldrich	
Name	GO	Water Wet – GO (WW-GO)	Acid Wet -GO (AW-GO)	Basic Wet -GO (BW-GO)	GNP - A120	GNP - A500
Ratios	6mg/ml of GO in 85% DMF and 15% water	10 % GO and 90% water	25% GO, 74 % water and 1-1.5 % HCl	5 % GO and 95 % water	Powder with surface area 120 – 150 m^2/g	Powder with surface area of 500 m^2/g.

The acid-wet GO from Abalonyx comes straight from production and is unaltered, it has a C/O atomic ratio of 2.5-2.6. The water-washed GO from Abalonyx was prepared by washing it extensively with de-ionised water to reduce acidity. The product was dispersed in de-ionised water using an ultra-sound bath for 30 minutes. However, it cannot be re-dispersed if dried. The C/O atomic ratio is 3.1-3.2 and when diluted to 0.1 weight % the suspension has a pH about 4. The basic-washed GO from Abalonyx was prepared by washing it extensively with de-ionised water to reduce acidity. Ammonia was added to adjust the pH to ~ pH 9. The product was dispersed in de-ionised water using an ultra-sound bath for 30 minutes. It can be redispersed if dried.

According to the manufacturer GNP - A120 from Sigma-Aldrich are powders of 5 µm particle size, surface area 120 – 150 m^2/g and containing <0.5 wt. % residual acid. The oxygen content is <1% and it has an average thickness of 6-8 nm. GNP – A500 has a particle size of <2 µm, a thickness of a few nm and a surface area of 500 m^2/g.

3.3 Dispersion of Nanofiller in Polyurethane

Several parameters were investigated in order to optimise the dispersion of nanofillers within Mono_PU and Micro_PU. This involved trialling a magnetic stirrer and overhead stirrer, optimising the amount of additional DMF required which was dependent on nanofiller type, as well as determining the length of mixing time. Optimised parameters are discussed below.

3.3.1 Dispersion of Nanofillers

1, 3 and 5 wt. % of clay nanofillers were weighed, pre-dispersed and stirred in 40 ml of DMF for 2 hours at room temperature. GO and GNP nanofillers were added at a concentration of 0.1, 0.3 and 0.5 wt.%, pre-dispersed in 30 ml of DMF and sonicated for 1 hour in a water bath held at 37°C. The nanofiller/DMF mix was added to the pre-polymerised monolithic and microporous polyurethane and mixed using a Dispermat® overhead stirrer with a saw tooth mixer for 20 minutes at 5000 rpm. The samples were left to rest overnight to reduce air bubbles before the formation of membranes.

Control membranes were established for the Mono_PU samples studied, this involved casting the pre-polymerised PU without alteration (Mono_PU batch 1, Chapter 4 and Mono_PU batch 2, Chapter 5). In addition, a second control spiked with additional DMF solvent was established for Mono_PU samples; 40ml of DMF was added to pre-polymerised PU (Mono_PU_Con batch 1, Chapter 4). While 30ml of DMF was added to pre-polymerised PU (Mono_PU_Con batch 2, Chapter 5).

A control membrane of pre-polymerised microporous PU was cast (Micro_PU, chapter 6). Attempts to cast DMF-spiked control samples of Micro_PU rendered no viable membranes.

3.3.2 Triple Roll Mill

Triple roll mill was also investigated as a potential way to improve dispersion of GO and GNP within PU. WW-GO at 0.5 wt. % and GNP_500 at 0.5 wt. % were added to Mono_PU

and Micro_PU separately via the process described in Section 3.3.1 before being processed using an Exact 80E Plus triple roll mill. Each sample passed though the machine seven times. Table 3 presents both gap widths and speeds for each pass through the triple roll mill.

Table 3. Processing settings used for triple roll mill of samples, includes gap width for each roll mill and the speed for each pass.

Pass	Gap 1 (µm)	Gap 2 (µm)	Speed (rpm)
1	20	10	100
2	5	5	200
3	5	7.5	150
4	5	8.5	150
5	5	10	150
6	5	10	170
7	5	11	170

3.4 Preparation of Polyurethane Nanofiller Nanocomposites Membranes

After dispersion of the nanofiller within PU, different casting methods were trialled before selecting the following procedures for monolithic and microporous membranes.

3.4.1 Monolithic

Mono_PU/nanofiller was spread onto polyester casting paper using an RK 60 µm K-bar coater at 2 m/min before being dried at 120°C for 10 minutes. Samples were left overnight before being removed from the casting paper to ensure they were dry and to reduce static.

3.4.2 Microporous

Micro_PU/nanofiller was spread 100 µm thick using an adjustable micrometre film applicator onto polyester casting paper before entering a coagulation bath and then dried at 120°C for 10 minutes.

3.5 Characterisation of Polyurethane Nanocomposite Membranes

3.5.1 Morphology and Structure

Several analytical techniques were used to help understand and describe the morphology, topography, structure, and dispersion of nanofiller within the PU/nanofiller membranes; these are described in the following sections.

3.5.1.1 X-ray Powder Diffraction

X-ray Powder Diffraction (XRD) can determine the crystalline and amorphous natures of a sample since the X-ray wavelengths (0.2 to 10 nm) are equivalent to the interatomic spacing of a crystalline solid.[84] The technique depends on the spacings between the atoms and the wavelength of the incident radiation, which is related to Bragg's Law (Fig. 15 and Equation 2). The law states that when an X-ray is incident on a crystal surface, the angle of incidence, θ, it will reflect back with the same scattering angle, θ. This angle depends on the interplane spacing, d, which is directly related to unit cell size of the crystal structure. When d, is equal to a whole number, n, of wavelength, λ, a constructive interference will occur and be detected. The size of the unit cell can be determined using Bragg's equation and position of the reflection. XRD was used to assess the dispersion of the nanofillers within the PU matrix.

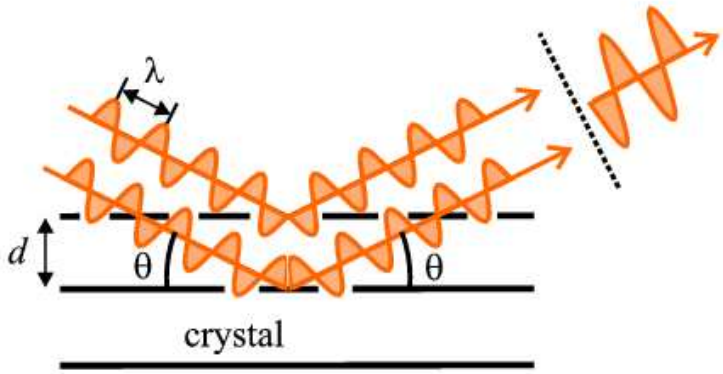

$$n\lambda = 2dsin\theta$$

Figure 15. Principle of XRD. The diffraction of an X-ray on a crystalline solid, showing the angle of incident, θ, and the scattering angle, θ. This angle relates to the d-spacing which in turn relates to Bragg's Law (Equation 2)

XRD was used to assess the dispersion of the nanofillers within the PU matrix by evaluating the spacing between nanofiller layers. The d-spacing of the nanofillers were determined by rearranging Bragg's Law (Equation 2).

$$d = \frac{n\lambda}{2sin\theta}$$

Equation 2

Equation 2. Rearranged Bragg's Law to determine d-spacing of nanofillers.

Experiments were performed on a Malvern Panalytical X'pert XRD, using Cu K-alpha (λ = 1.5406 Å) radiation. Samples were either powders or membranes mounted on a glass slide. Mono_PU/clay and Micro_PU/clay and GO samples were scanned from 2° to 30° at a rate of 0.02° per minute. Mono_PU/GO and GNP samples were scanned from 5° to 40° at a rate of 0.02° per minute.

3.5.1.2 Scanning Electron Microscope

The scanning electron microscope (SEM) produces images by scanning the sample surface using a high-energy beam of electrons. The electron beam penetrates the surface of the sample to a depth of a few microns, depending on the accelerating voltage and the density of the sample (Fig. 16). This interaction between electron beam and sample produces a variety of signals, such as secondary electrons (electrons from the sample itself), back-scattered electrons (beams of electrons that bounce of the nuclei of the atoms in the sample), and characteristic X-rays. These signals are collected via detectors and stitched together to form an image of the sample surface. This technique is used to examine the topography of a specimen's surface.

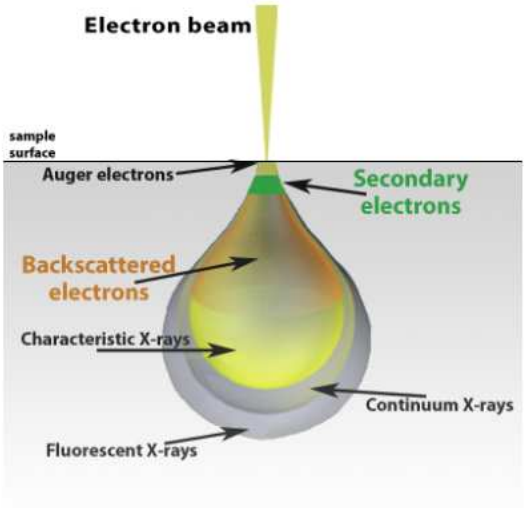

Figure 16. SEM electron beam penetrates the sample surface this produces a variety of signals. The three main signals are secondary electrons, back-scattered electrons, and characteristic X-rays.[85]

Mono_PU/nanofiller samples were attached to aluminium stubs using carbon tabs and splutter coated with 15 nm of gold to provide an electrically conductive layer which suppressed charging effects and minimised damage to samples from the electron beam. Micro_PU/nanofiller samples were prepared in the same way but coated with 15 nm of carbon instead.

Fractured samples used for imaging the cross-section were prepared by submerging the sample in liquid nitrogen then fracturing using tweezers. Samples were mounted to aluminium stubs and coated with gold or carbon depending on the sample. Samples were imaged utilising secondary electrons with a FEI NOVA 200 NanoSEM. Analysis of the sample surface and cross section (e.g., porosity) was conducted using ImageJ.

3.5.1.3 Scanning Electron Microscope/Energy-Dispersive X-ray

Energy-dispersive X-ray (EDX), otherwise known as Energy-dispersive X-ray spectroscopy (EDS) is an analytical technique used to determine the elemental composition of a sample using SEM. EDX can detect elements with a greater atomic number than boron and at a concentration greater than 0.1 wt. %.[62] An incident beam of high energy excites an electron from the inner shell, ejecting it, causing an electron

hole which is filled by an electron from an outer, higher-energy shell. The difference in energy between the higher-energy shell and the lower-energy shell is released as an X-ray and is measured by an energy-dispersive spectrometer. Each element has a unique atomic structure of which the energy of the X-ray released acts as a fingerprint which allows for elemental identification and composition of a specimen to be measured.[86]

Carbon coating was employed for all specimens to allow for easy identification of the elements, oxygen, silicon, and aluminium. Due to charging effects which affected EDX imaging samples in addition to the steps detailed in Section 3.5.1.2, to overcome this charging effect samples were sandwiched between two carbon tabs and in some cases silver paint was added to the edges to aid conduction. Samples were imaged with FEI NOVA 200 NanoSEM and EDX data was analysed using Aztec software.

3.5.1.4 Attenuated Total Reflection - Fourier-Transform Infrared Spectroscopy

Attenuated Total Reflection - Fourier-Transform Infrared Spectroscopy (ATR-FTIR) is an important technique for material analysis and is based on the vibrations of atoms in a molecule. An infrared (IR) spectrum is collected by reflecting IR radiation off a sample and determining what fraction of the incident radiation is absorbed at a particular energy level.[87,88] Radiation is emitted from the infrared light source and split in two by the beam splitter within the interferometer. Fixed and moving mirrors reflect each beam back to the beam splitter where they are recombined to produce interference light, which is transmitted through the sample and detected as an interferogram (Fig. 17). A mathematical process called Fourier transformation converts the interferogram into an infrared spectrum. ATR-FTIR is an excellent analytical technique for polymer characterisation as it provides information on composition, structure, and intermolecular interactions. Alterations in the characteristic absorption band patterns indicate a change in material composition; this is useful for understanding the polymer-nanofiller interactions.

Spectra were obtained in triplicate for both the upper and lower surfaces of each sample to establish if there is a homogenous structure and distribution of nanofiller, as well as explore if polymer-nanofiller interactions are occurring and if these interactions are

preferential to either the upper or lower surfaces. Samples were measured using a Nicolet Nexus FTIR, each measurement was the combination of 64 scans at a spectral resolution of 4 cm^{-1}.

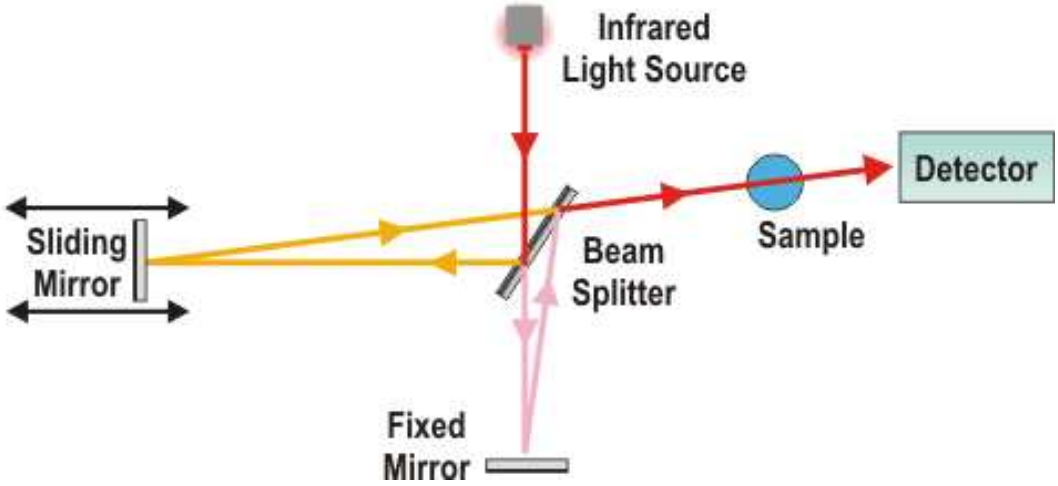

Figure 17. The principle of FTIR spectroscopy, an infrared light source is split by a beam splitter then reflected off mirrors before hitting a sample, any unabsorbed photons, or wavelengths of light pass through to a detector producing a spectrum.[89,90]

3.5.1.5 Variant-Focus Microscopy

Variant-focus microscopy (VFM) provides a topographical image and surface roughness measurement of a sample surface by combining the small depth of focus of an optical system with vertical scanning. A semi-transparent mirror is inserted into the white light source pathway allowing the light to be focused upon the sample via the objective. The light is reflected in several directions dependent upon the sample's topography. The reflected light is gathered by a light sensitive sensor, behind the mirror, and algorithms convert this data into a 3D true colour image with a full depth of field. This is achieved by analysing the sample through the variation of focus along the vertical axis (Fig. 18).

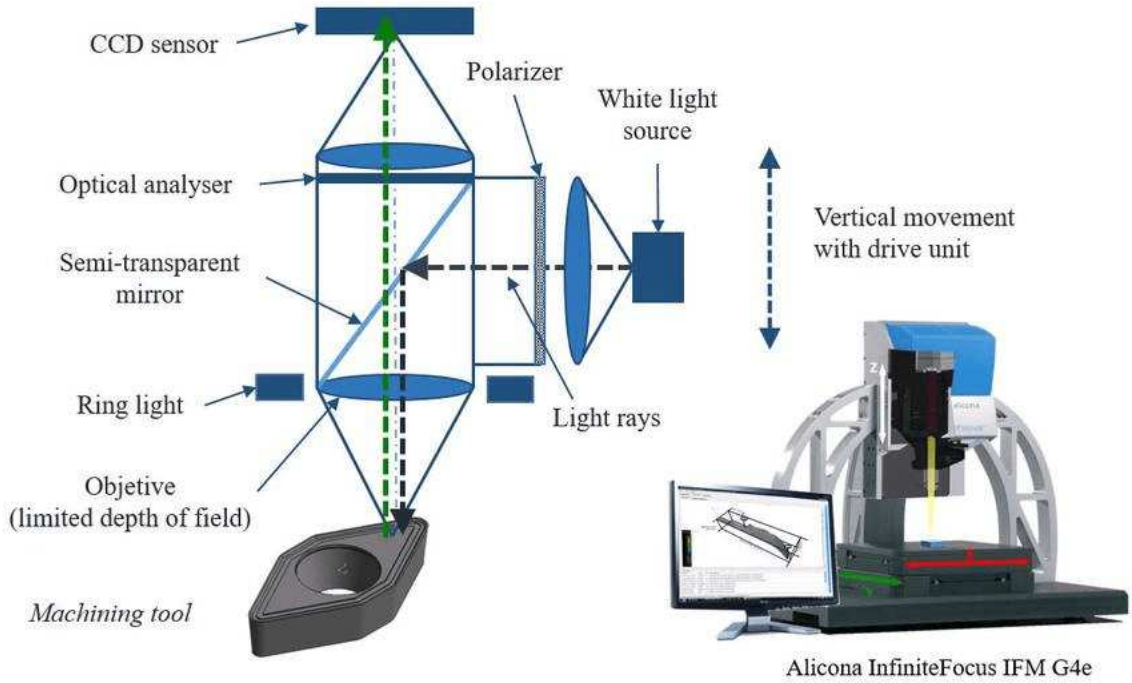

Figure 18. Principles of VFM, white light is focused onto a samples surface using a semi-transparent mirror. The light is reflected in several directions' dependant on the sample's topography, this reflected light is collected by the sensor and an algorithm covert it to a 3D true colour image.[90]

Characterisation of 3D images can be defined using S-parameters, which has sub-parameters to provide extra surface detail. Only the key parameters are detailed herein but it should be noted VFM provides far more extensive information on a sample which is beyond the scope of this thesis (Table 4).[67,91] After careful consideration and analysis S-parameter was selected as it provides information on the whole sample area as opposed to a single line which is used in Ra measurements. As such *Sq*, was used in the analysis of Mono and Micro_PU/nanofiller membranes as it provided a comprehensive value for the surface roughness of a sample. Other measurements such as *Ssk* (a measure of asymmetry of a surface about a mean plane) and *Sku* (provides information on the sharpness of the surface height distribution) were considered. However due to time limitations these measurements were not fully explored.[92]

Sq was chosen over *Sa* as it provides a more accurate representation of the surface by expelling outliers and is more sensitive to peaks and valleys than *Sa*. A difference between *Sq* values will be more likely due to true surface topography than to outliers skewing the data. Typically, *Sq* values are 11-15% higher than *Sa*.

Table 4. The main sub-parameters of VFM S-parameters with accompanying descriptions.[91,92]

S-parameter			
Amplitude parameters (average of ordinates)		Amplitude parameters (peak and valley)	
Sa	Arithmetical mean height of selected area	*Sp*	Maximum peak height of selected area
Sq	Root-mean-square height of selected area	Sv	Maximum valley depth of selected area
Ssk	Skewness of selected area	*Sz*	Maximum height of selected area
Sku	Kurtosis of selected area		
Sdq	Root-mean-square gradient		

Since the technique relies upon analysing the variation of focus along the vertical axis it is only applicable to surfaces which vary sufficiently during the vertical scanning process. Transparent samples and relatively smooth samples are difficult to measure. Samples were thus gold coated via the same method described in 3.5.1.2. Samples were imaged using a Alicona InfiniteFocus Microscope and analysed using the Alicona IF-measuresuite version 5.1. Many different parameters were trailed before an optimised imaging methodology was finalised; details are outlined below.

Key notes to understand the basic principles of VFM image analysis.[90,93]

- **Profile Roughness Measurement (*Ra*):** is determined from a single line across a sample. VFM automatically checks Ra measurements conform to EN ISO 4287/88 (which provides the comparability of the optical results to tactile measurements).
- **Surface texture measurement (*Sq*):** is determined from the whole sample area.
- **Lambda C (Lc):** is dependent on the *Ra* measurement and the length of measurement. Lc is determined in accordance with ISO 21920 and is used to remove waviness from a surface texture measurement.

- **Primary Profile:** A measurement extracted in the profile analysis module without the application of a filter.
- A sample's surface can be characterised by high and low frequency waves or shorter and longer wavelengths respectively.
- **Roughness**: Roughness includes the finest (shortest wavelength or highest frequency) irregularities of a surface. Roughness generally results from a particular production process or material condition.
- **Roughness Profile:** A measurement after the application of a roughness filter to the primary profile.
- **Waviness:** Waviness includes the more widely spaced (longer wavelength or low frequency) deviations of a surface from its nominal shape and needs to be filtered out for our application.
- **Waviness Profile:** A measurement after the application of a waviness filter to the primary profile.
- In order to remove waviness from a surface texture measurement Lambda C (Lc) is required.

Instrument Set Up

1) Set magnification objective at 50X, has a lateral resolution of 0.45 μm and a vertical resolution of 0.045 to 0.455 μm.[94]
2) Set exposure to ~384.
3) Set contrast to ~0.54.
4) Deactivate polarizer, if polariser is activated it can alter the measurement procedure and cause increases in surface roughness. It should only be used if samples are difficult to measure, for example, they are slanted and thus brightness is not uniform and attempts at illuminating effectively have failed.
5) Set auto averaging to off.

Imaging a Sample

1) Place gold coated sample under magnification.
2) Achieve an in-focus image of the sample area (X and Y-axis) and set the instrument control to 0 (Fig. 19).

3) To specify the Z-axis (i.e., the 3D element of the image), move the machine up the Z- axis reaching the Z-axis upper limit, this is when the sample is slightly out of focus. Now set the distance travelled in µm for the Z-axis upper limit. Repeat this step for the Z-axis lower limit by moving the machine down the Z-axis. These values vary depending on the sample morphology and roughness (Fig. 19).
4) A 3D image and pseudo coloured image of the sample is now available.

Figure 19. VFM 3D image of Micro_PU shows the X, Y and Z axis of the 3-dimensional image.

Sample Analysis

1) Perform a profile roughness measurement and filter for roughness to achieve an *Ra* value which conforms to EN ISO 4287/88. *Ra* results also provide the Lc value required later on (Fig. 20).[95]
2) Next perform a surface texture measurement, *Sq* (Fig. 20).
3) Select filter surface for roughness and input the determined Lc value.
4) Select robust gaussian filter for arbitrary surfaces. The robust filter should be used on porous structures, it also performs well with outliers and edges of samples i.e., “holes”.
5) Image analysis is now complete and wide array of images and information on the surface texture is available; this includes the 2D image and pseudo-coloured images plus the *Sq* value.

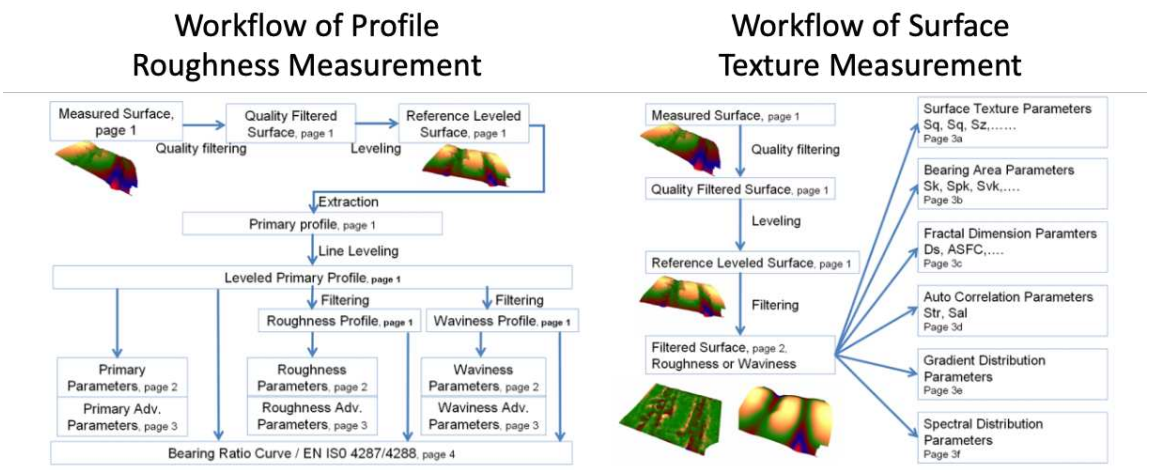

Figure 20. Workflow diagrams of VFM sample analysis for both profile roughness measurements and surface texture measurements.[93]

3.5.2 Wettability and Breathability

3.5.2.1 Contact Angle

To evaluate the resistance of a barrier membrane to water, contact angle provides an inverse measure of wettability. Wetting is the ability of a liquid to maintain contact and spread on a surface. The degree of wettability (W) is expressed as a function of the surface energies (Equation 3).[96]

Equation 3

$$W = \gamma_{SV} - (\gamma_{SL} + \gamma_{LV})$$

Where γ_{SV}, γ_{SL} and γ_{LV} denotes the surface free tension between the solid – vapour phase (γ_{SV}), solid – liquid phase (γ_{SL}), and the liquid – vapour phase (γ_{LV}). Positive wetting values indicate high hydrophilicity whilst negative values are typical of hydrophobic surfaces. The static contact angle is measured by placing a droplet of solvent onto a surface; a tangent is drawn from the contact point along the γ_{LV} interface (Fig. 21).

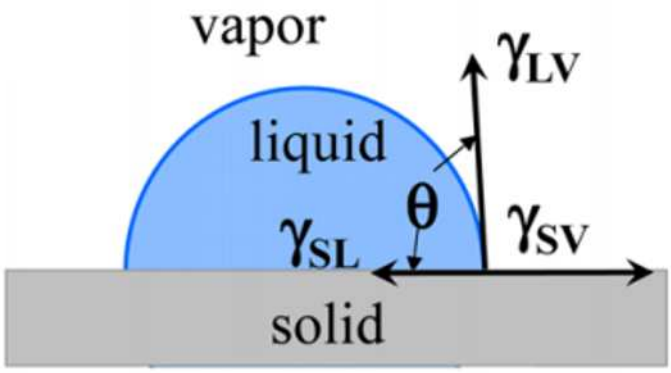

Figure 21. Schematic of contact angle measurements, the angle of contact between the water droplet and the sample can be described using Equation 3.[97]

The contact angle between the tangent and surface is calculated using Young's equation (Equation 4).[96]

Equation 4

$$\cos\theta = \frac{\gamma_{SV} - \gamma_{SL}}{\gamma_{LV}}$$

Typically, a surface with a contact angle < 90° is referred to as hydrophilic with good wettability, while > 90° a surface is hydrophobic and has poor wettability, and a surface with a contact angle above >150° is described as superhydrophobic.[98,99]

Contact angle was measured using a DataPhysics OCA15 instrument. Membranes were mounted to glass slides and 4 µl of deionised water was dispensed onto the surface at a rate of 2 µl/second forming a sessile drop. The contact angle was calculated at time 0 min.

3.5.2.2 Hydrostatic Head

A hydrostatic head test, otherwise known as a hydrostatic pressure test, was performed to measure the waterproofness of a selection of Mono_PU/clay and GO nanocomposite membranes. A column of water under pressure is placed onto the membrane which has been backed to a polyester gauze, water is added to the column until water penetrates

the membrane at which point the test is stopped, the amount of water in the column (mm) at the time of penetration is considered the hydrostatic head value (Fig. 22).[100]

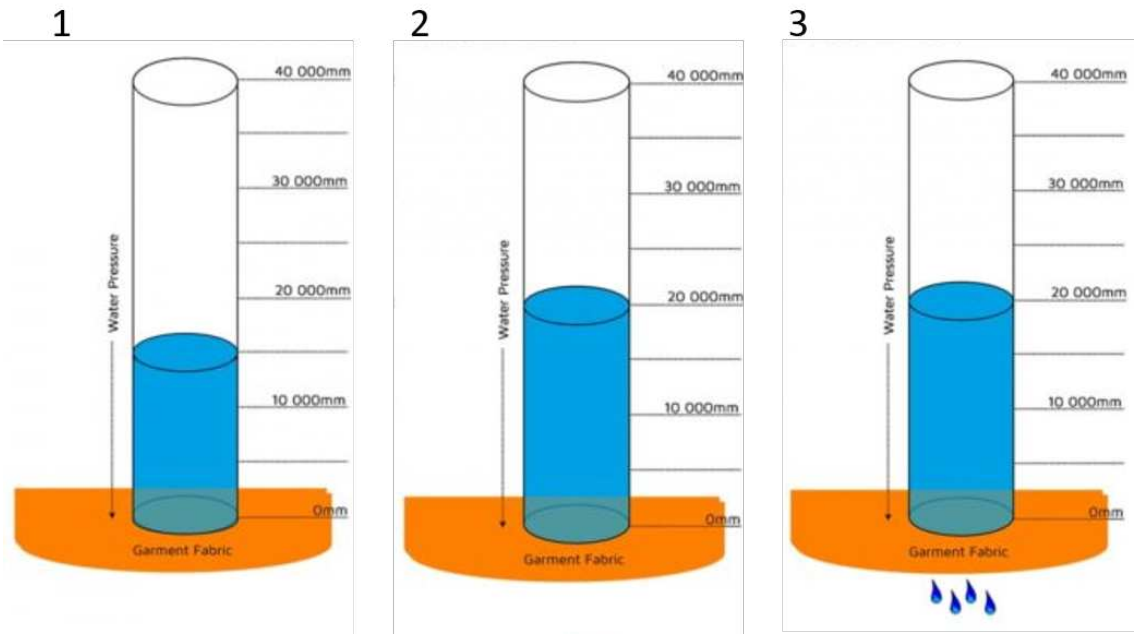

Figure 22. Diagram of how hydrostatic head test is performed, 1) column of water placed on top of fabric under pressure, 2) water is gradually increased, 3) water is added until water penetrates the membrane, at which point the total amount of water in the column indicated the hydrostatic head value (mm).

A hydrostatic head value of 5000 mm is considered rainproof, and 10,000 – 15,000 mm is classed as waterproof. At 15,000 to 30,000 mm, the material is considered a high-quality waterproof membrane suitable for aggressive conditions.[100]

Hydrostatic head test was performed at PIL Membranes LTD in accordance with British standard 20811 – 1992 on the Werner Mathis under standard atmosphere at room temperature.[101] Water pressure was applied from above at a rate of increase of 60 cm/min. A polyester gauze was placed on top of the membrane before testing to prevent the sample stretching and bursting immediately. The test was only performed once due to limited material. Reproducibility of this test varies and as such the results of this experiment must be considered with this in mind.

3.5.2.3 Water Vapour Transmission Rates

The breathability of a material is described by the water vapour transmission rates (WVTR) and is calculate in grams per square meter per 24 hours (Equation 5). Samples were measured by the dish method in accordance with British standard 2782-8: 1996.[102] Membranes were acclimatised in a humidifier overnight at 95 % humidity and 38 °C before being transferred to a cup filled with dried silica beads. The membrane is sandwiched between the cup and an outer ring, weighed, and placed in the humidifier at 95 % humidity and 38 °C for 7 hours (Fig. 23). The samples were measured in triplicate and weighed every 90 minutes.

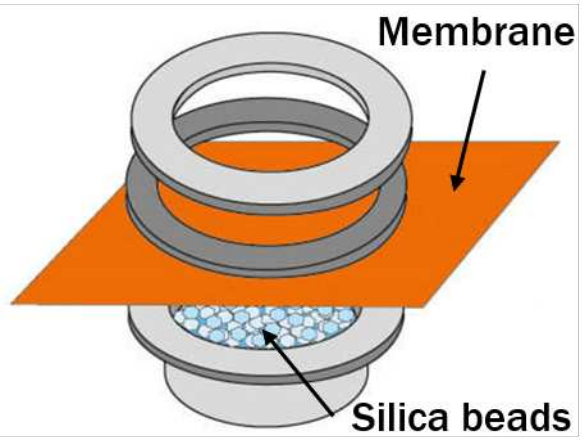

Figure 23. Schematic diagram of WVTR dish method set up, dried silica beads are placed in a cup, the sample is sandwiched between rings attached to the cup creating a seal. Water vapour must pass through the sample to hydrate the silica beads.

The WVTR was calculated using Equation 5.

Equation 5

$$WVTR = \frac{240 \times m_2}{S \times t}$$

Where *S* being the area in square centimetres of the tested piece surface, *t* is the total duration in hours of the last two exposure periods and m_2 is the increase in mass, in milligrams during time *t*. Each sample varies slightly in thickness and as such the WVTR values have been normalised to the thinnest membrane which was 0.02 mm.

3.5.3 Mechanical and Thermal Properties

3.5.3.1 Differential Scanning Calorimetry

Differential scanning calorimetry (DSC) is a thermal analytical technique which measures the difference in the amount of heat required to increase the temperature of a sample of known weight and a reference pan as a function of temperature. This technique allows for the detection of glass transition (T_g), melting point (T_m) and re-crystallisation temperatures (T_c) of polymeric materials (Fig 24).[103]

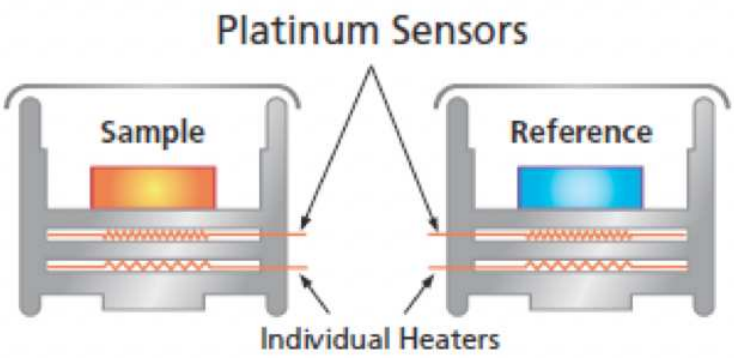

Figure 24. Principles of DSC, both a pan containing the sample and an empty reference pan are heated at the same time. The difference in heat required to heat the two pans provides information on the samples glass transition (T_g), melting point (T_m) and re-crystallisation temperatures (T_c).[104]

Samples of ~10 mg were placed in an aluminium pan, an aluminium lid was placed on top, and the pan and lid were crimped. The lid was pierced to allow volatile gases to escape. Measured using a Perkin Elmer DSC 8000, they were cooled to -80°C, held for 3 minutes before being heated to 230°C, then cooled again to -80°C at a heating rate of 5°C/minute. Pyris software was used to calculate the onset temperature and area for the melting and re-crystallisation peaks present.

3.5.3.2 Dynamic Mechanical Analysis

Dynamic mechanical analysis (DMA) measures the storage modulus (elastic modulus, *G'*), loss modulus (viscous modulus, *G''*) and tan δ (damping coefficient, tan δ) by applying a sinusoidal stress or strain to a sample as a function of temperature or

frequency (Fig. 25).[105,106] Storage modulus is a measure of a sample's elastic behaviour and is directly related to the energy storage capabilities of the material. Although it is conceptually related to Young's modulus, they are not the same.[106] The loss modulus is the dissipation of energy (hysteresis) of a material under damping (cyclic loading). The ratio of loss modulus to storage modulus is tan δ.[107] DMA has been used to provide information on the viscoelastic properties and thermal transitions of Mono_PU and Micro_PU nanocomposite membranes.

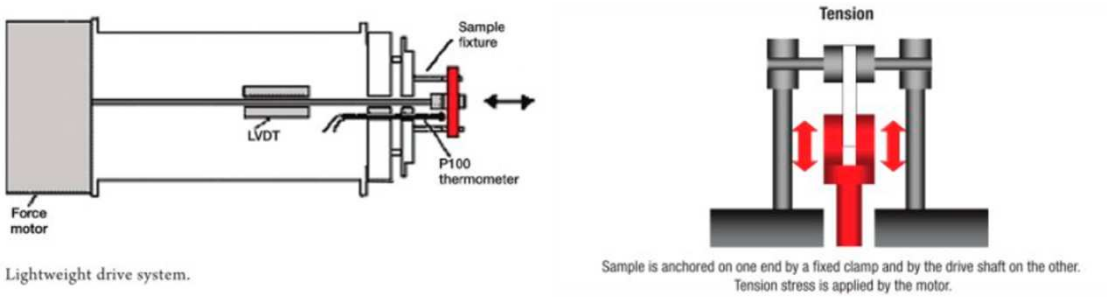

Figure 25. Left) Schematic diagram of DMA 8000 set up and force motor. Right) Diagram of specific tension mode set up used relevant to this study. The sample is secured under light tension between two clamps. A sinusoidal stress or strain is applied to the sample as a function of temperature.[108]

Samples of ~10 mm x 8 mm x 0.03 mm were measured in tension mode at a single frequency (1 Hz), under a displacement distance of 0.02 mm, an initial force of -1.0 N was applied before the sample was measured during heating from -100 °C to 120 °C at a rate of 3°C/minute using a Perkin Elmer DMA 8000.

3.5.3.3 Tensile

Tensile testing is a destructive test that typically uses a dogbone-shaped mould cut from the sample. The sample is loaded into a tensile loading frame and undergoes a user specified force applied unidirectionally until the sample breaks (Fig.26). The load force (F) and the change in length (ΔL) in millimetres (mm) are monitored. ΔL is also known as strain (ε), while stress (σ) can be deduced from force divided by the cross-sectional area of the dogbone mould sample.[109] A tensile test can provide information on sample Young's modulus, yield point, and elongation at break.

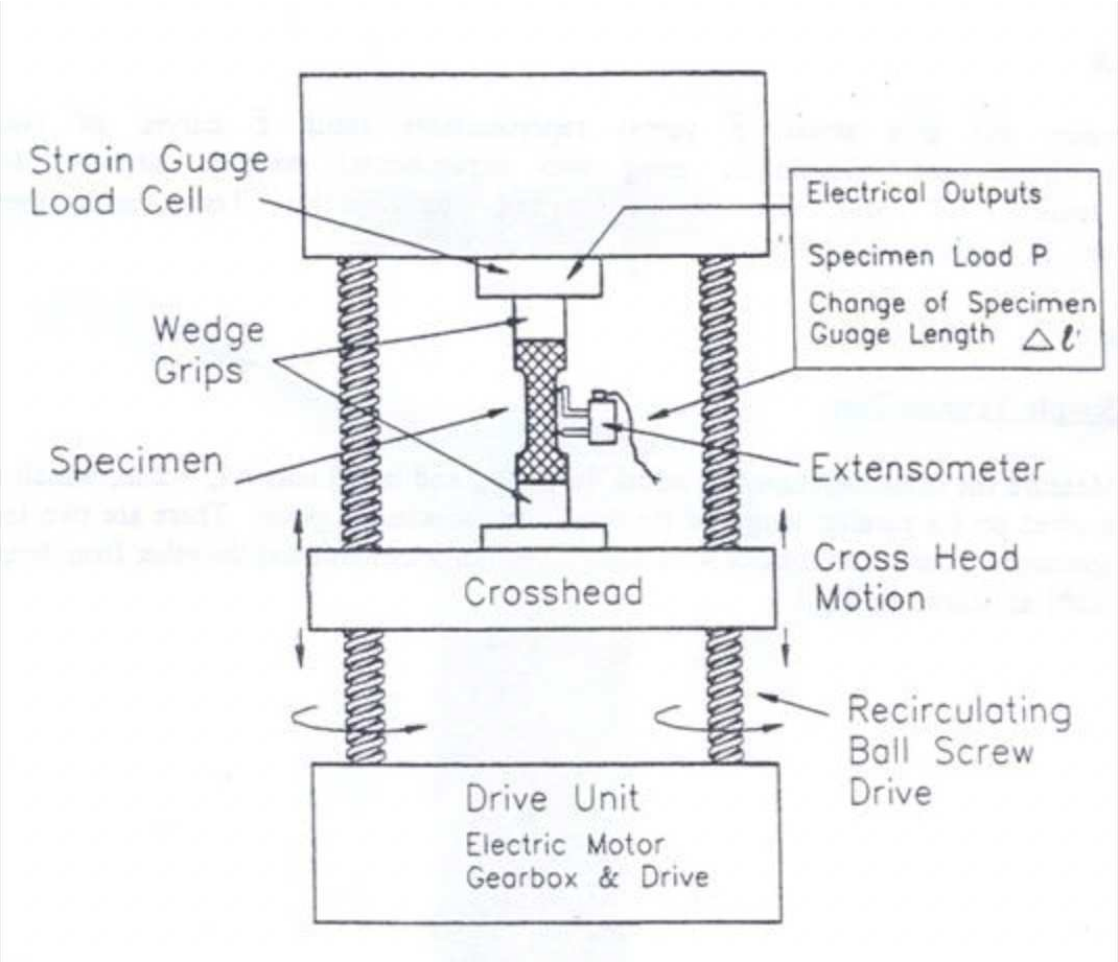

Figure 26. Schematic diagram of a tensile testing machine, a dogbone-shaped sample is clamped under slight tension. A user specified force is applied unidirectionally until the sample breaks. The load force (F) and the change in length (ΔL) in millimetres (mm) are monitored. From this, a samples Young's modulus, yield stress and elongation at break can be determined. [110]

Young's modulus describes the relative stiffness of an elastic material and is measured by the ratio of stress to strain in the linear region of a stress-strain curve. A low Young's modulus typically indicates the material is ductile in nature while a brittle material would have a high Young's modulus.[111] Yield stress, otherwise known as yield point and stress at peak, occurs at the point of non-linear pattern on the stress-strain curve. At the yield point the material has undergone permanent tensile deformation and no longer behaves elastically.[112] Elongation at break is the ratio between changed length and initial length after breakage of the sample. It expresses the capability of a material to resist permanent changes in shape.[113]

The tensile tests were performed on a selection of samples at PIL Membranes LTD following the ASTM D638 standard on a Metrotec Single Column Universal Testing Machine. The sample size was 50 mm by 6 mm by sample thickness (~0.03 mm).

3.5.3.4 Static Test

A large build-up of static electricity can have serious consequences within the oil, gas, and chemical industries.[114] Accidents within the petrochemical industry frequently occur due to build-up of static electricity. Machinery often has an antistatic coating to prevent such disasters.[115] It is also important for protective apparel to dissipate harmful static charge to further reduce the risk of explosion in hazardous environments. There are two types of antistatic materials: intrinsic antistatic or composite antistatic. Intrinsic antistatic materials are typically conductive polymers with a conjugated π bond such as polyacetylene and polystyrene.[114,115] Composite antistatic materials are typically insulative polymers combined with an antistatic agent or conductive filler (carbon nanotubes or metal oxides) via deposition or dispersion methods.[116,117] An issue however is the poor dispersion of fillers with the polymer.

A selection of Mono_PU/clay and GO nanocomposite membranes were investigated for their antistatic properties using an Antistat™ surface resistance meter (Fig. 27). Samples were measured in Ohms per centimetre (Ω/cm). A material is considered insulative if it measures 10^{12} Ω/cm, static dissipative between 10^{11} and 10^{6} Ω-cm and conductive between 10^{5} and 10^{3}.

Figure 27. Antistat™ surface resistance meter for measuring antistatic properties of materials.

Chapter 4

Mono_PU/Clay Nanocomposites

4.1 Introduction

Mono_PU is a monolithic membrane for applications in protective apparel, it is one type of PU developed by PIL Membranes LTD. This chapter explores the level of dispersion and resulting effects the addition of four types of clay nanofillers, CNa^{+}, C20, C15A and C10A, each at three different concentrations has on Mono_PU morphology, structure, and properties. Extensive characterisation of the resulting membranes is separated into three main categories: morphology and structure, barrier properties and mechanical, thermal, and antistatic properties. This includes the novel application of VFM imaging to characterise relatively flat polymer membranes. The results are compared to one another to give a synergist overview of the nanofiller effects on Mono_PU with relation to application in protective apparel.

Despite vast research on clay nanofiller effects on the mechanical properties, and broadly the barrier properties of a polymer there is limited research on water vapour and waterproof barrier properties of monolithic barrier membranes for apparel and thus here lies one of the novelties of this research.

4.2 Characterisation of Polyurethane Nanofiller Nanocomposite Membranes

The characterisation of Mono_PU/clay monolithic nanocomposite membranes are subdivided into three overarching categories: morphology and structure, barrier properties, and mechanical properties. Several characterisation techniques have been employed in each section; they will be discussed separately but also in combination with one another where necessary. The dispersion of clay nanofillers and the effects they have upon the surface morphology of Mono_PU are described within morphology and structure. The effect of the clay type and concentration on the mechanical, thermal, barrier and breathability properties on Mono_PU are described later in this chapter.

4.2.1 Morphology and Structure

Several techniques, such as X-ray powder diffraction (XRD), scanning electron microscopy/energy dispersive X-ray analysis (SEM/EDX) and attenuated total reflection

- Fourier-transform infrared spectroscopy (ATR-FTIR), were utilised to assess the dispersion of clay nanofillers with the Mono_PU matrix. Understanding how well or poorly a specific clay type and concentration is dispersed is useful when comparing how that same clay has affected the mechanical and barrier properties of Mono_PU. The effect of the clay on surface morphology was also investigated through SEM imaging of surface topology and fracture cross-section, as well as variant focus microscopy (VFM) to provide an understanding of surface roughness. Surface morphology is compared later to the barrier properties of the nanocomposites, such as comparing surface roughness to wettability.

4.2.1.1 X-ray Powder Diffraction

X-ray Powder Diffraction (XRD) is a technique used to examine the dispersion of nanofillers within a polymer matrix, a homogeneous dispersion is often essential to improving the properties.[48] Idealised XRD traces and structural confirmation of the three categories involving the dispersion of nanofillers in a polymer matrix; microcomposite, intercalated (organised and disorganised) and exfoliated can be seen in Section 2.4.3 Figure 12.

During intercalation of the polymer chains by the nanofiller, the interlayer spacing is increased and the diffraction shifts towards a lower angle. D-spacing can be calculated using Bragg's Law which relates interlayer spacing to reflection angle. Section 2.4.3 Equation 1 demonstrates how the d-spacing is calculated using the wavelength of X-rays (Cu K-alpha lambda, 1.5406 Å) and 2θ from XRD traces.

XRD traces of Mono_PU/clay nanocomposite membranes at 1, 3 and 5 wt. % concentrations compared against Mono_PU, Mono_PU_Con, clay powders and dried clay powders dispersed in DMF (Fig. 28). The Cloisite® clay powder samples show broad XRD reflections due to relatively low crystallinity and small particle size. Furthermore, they are consistent with XRD traces of the same Cloisite® within the literature characterised by the broad d_{001} reflection.[118,119] d_{001} or "basal plane spacing" is the distance between a plane in two adjacent corresponding unit layers.[120] Table 5 shows the respective d-spacing values of the d_{001} reflections of the clay powders and relevant nanocomposites at 1, 3 and 5 wt. %.

CNa+ powder has a broad d_{001} reflection at 7.3 °2θ (12.2 Å), this reflection remains present when CNa+ is incorporated into Mono_PU. The reflection does shift to a lower angle (~6.9°2θ) which causes a slight increase in basal spacing (Table 5) which indicates an intercalated structure. A similar trend is also observed for Micro_PU/CNa+ in Section 6.2.1.2.

C20 powder has a strong d_{001} reflection at 4.9 °2θ, when incorporated with Mono_PU the d_{001} reflections are weak. As the concentration of C20 increases the intensity of the reflection at 5.1 °2θ increases. In addition, the samples display an increasing baseline towards lower angles (< 5° 2θ); this alongside the weak d_{001} reflection is indicative of a partially exfoliated system.[48] As concentration increases the system becomes slightly less exfoliated and slightly more intercalated.

The XRD trace of C15A powder shows broad reflections with a shoulder at 4.4 ° 2θ, this suggests the organomodifier and clay are not evenly distributed. The XRD trace for C15A/DMF shows two distinguished reflections at 3.3 °2θ and 6.7 °2θ, no shoulder is present. During mixing with DMF, C15A becomes more ordered either by reordering the organomodifier or by removing it from the interlayer spacing. The addition of C15A/DMF to Mono_PU created highly ordered intercalated systems, evidenced by intense relatively narrow reflections that have shifted to lower angles and strong orders of reflection being present (i.e., strong d_{-001}, d_{-002}, d_{-003} reflections at ~ 3° 2θ, 5.7° 2θ and 8.3°2θ, are visible for Mono_PU/C15A at both 3 and 5 wt. %). This suggests the clay undergoes further ordering potentially due to intercalation with polymer chains within the interlayer space of the clay.

C10A powder has a d_{001} reflection at 4.6 °2θ (19.4 Å), when mixed with additional DMF C10A shifts to a slightly lower angle 4.2 °2θ (20.9 Å) indicating DMF has increased the order of C10A and possibly intercalated between clay layers. When incorporated into Mono_PU the reflection shifts to a lower angle ~3.3 °2θ (~27 Å). The basal spacing increased by 7-8 Å indicating the expansion of the C10A galleries and the intercalation of Mono_PU within them, thus resulting in an ordered intercalated system. There is a strong order of reflection similar to Mono_PU/C15A, however it is much weaker.

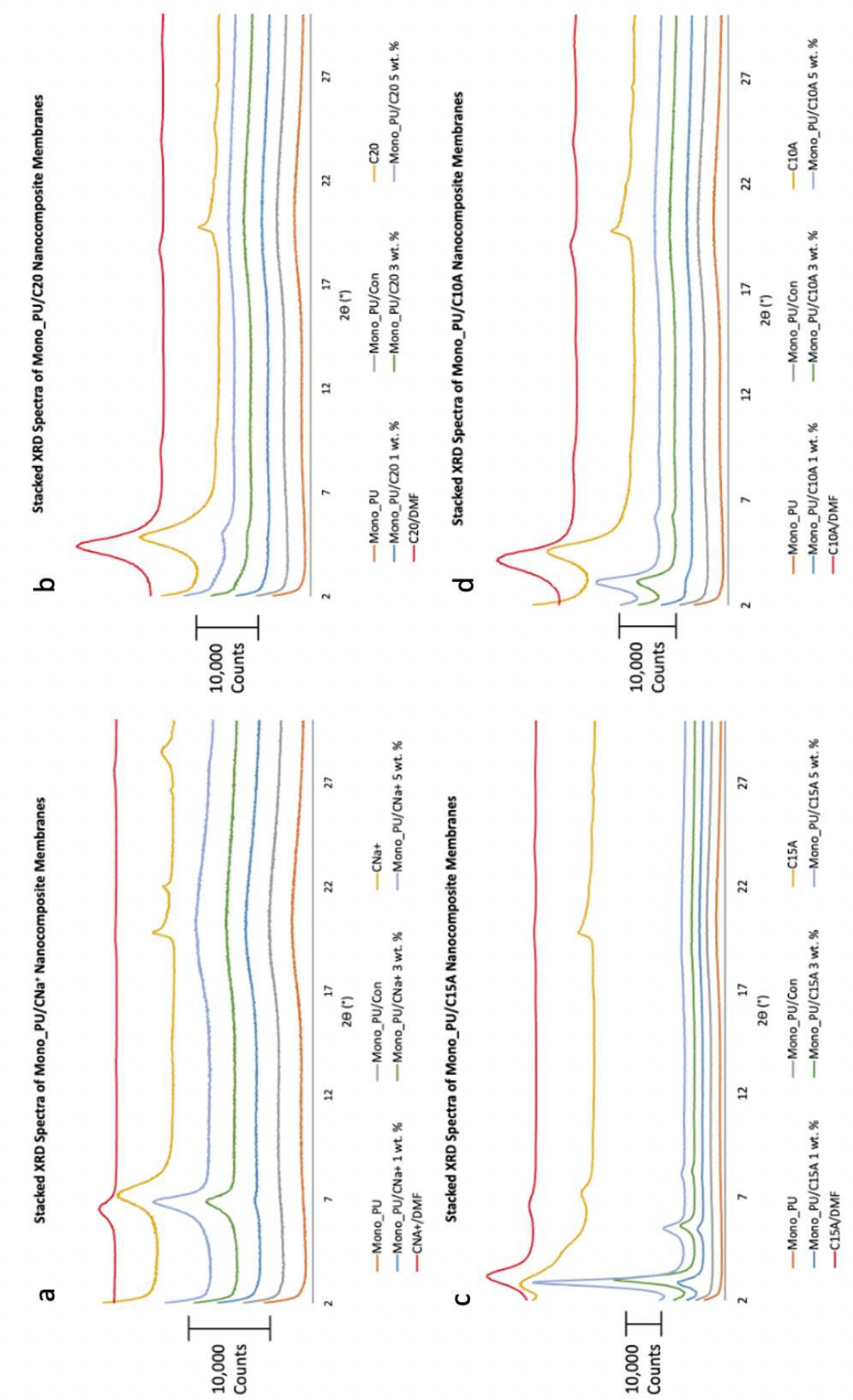

Figure 28. Stacked XRD spectra of Mono_PU/clay nanocomposite membranes each image contains a spectrum for the clay, dried clay/DMF, Mono_PU_Con and Mono_PU/clay membranes at 1,3 and 5 wt.%. a) CNa^+ b) C20 c) C15A d) C10A.

Table 5. d-spacing values in Å of all d_{001} of Mono_PU/clay nanocomposite membranes (Fig. 28).

d_{001} (Å) of Clay Powder (DMF) and Mono_PU/Clay Nanocomposite Membranes					
	Clay Powder	Clay Powder/DMF	1 wt. %	3 wt. %	5 wt. %
CNa+	12.2	13.5	12.8	13.0	12.9
C20	18.2	20.0	18.5	17.7	17.6
C15A	32.1	27.1	30.5	28.9	31.0
C10A	19.4	20.9	26.4	27.7	27.8

4.2.1.2 Attenuated Total Reflection - Fourier-Transform Infrared Spectroscopy

Attenuated Total Reflection - Fourier-Transform Infrared Spectroscopy (ATR-FTIR) has been used to confirm the structure of Mono_PU and explore the intermolecular interactions between polymer and nanofiller. Table 6 provides frequencies of groups commonly found within PU; these specifically correlate to the ATR-FTIR spectra obtained from the upper surface of Mono_PU (Fig. 29). Mono_PU contains aromatic rings derived from 4,4'-MDI, the functionalities are free C=O vibration from the urethane bond at 1732 cm^{-1} and C=O hydrogen bonding with amide groups and ethers at 1703 cm^{-1}. Also present within the urethane link are N-H stretching groups, undergoing hydrogen bonding at 3326 cm^{-1}, N-H bending vibration at 1530 cm^{-1} and C=C stretching vibration of the aromatic rings at 1598 cm^{-1}.[121] PTMEG is responsible for the asymmetrical and symmetrical C-H bonds at 2942 cm^{-1} and 2859 cm^{-1}, respectively, as well as ether bonds at 1310 cm^{-1}.[10,122] The assigning of these common PU peaks confirms the purity and structure of Mono_PU.

Table 6. Common functional frequencies of PU.[10,122,123]

Group	Mode	Frequency (cm^{-1})
N-H	Free	3445-3450
N-H	N-H...N-H	3315-3340
N-H	N-H...0 (Ether)	3260-3290
N-H	N-H...O=C	3250-3450
N-H	Bending	1520-1600
C=O (Urethane)	Free	1730-1740
C=O (Urethane)	C=O...H-N	1703-1710
C-O-C	Stretching	1000-1300
C=C	Stretching	1400-1600
C-H	Asymmetrical	2800-3000
C-H	Symmetrical	2800-3000

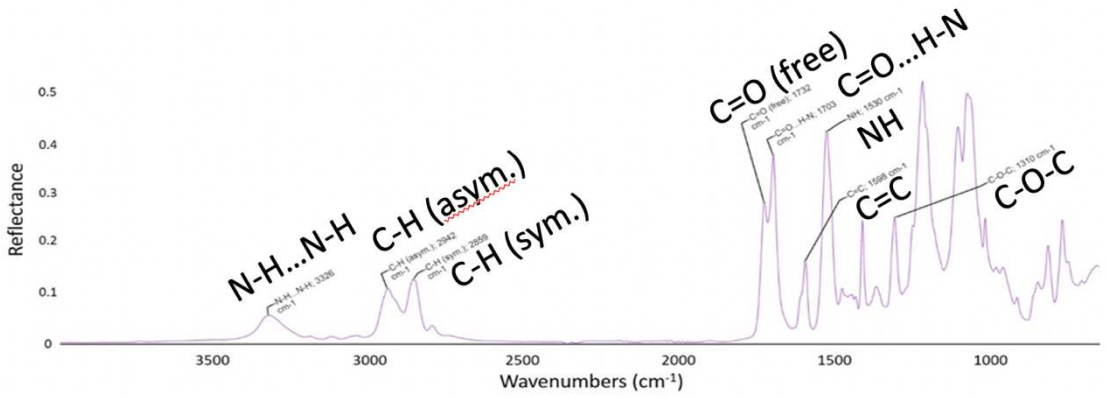

Figure 29. ATR-FTIR of Mono_PU upper surface membrane with annotations of representative bands and the associated chemical bonds.

Similarities within repeats performed in triplicate for both upper and lower surfaces indicate a homogeneous distribution of clay in all samples; spectra in Figure 30 are a single representation of the repeats. Intercalation of the polymer by the clay can be evidenced by changes in the strong bands at 1100 - 1000 cm^{-1} relating to the Si-O stretching vibrational modes within the clay. These involve the basal oxygens of the Si-O tetrahedral designated in-plane and the apical oxygens for example the $Si\text{-}O^-$ bonds directed towards the Na^+ ions at the centre of the clay layer, these are referred to as out-of-plane.[124] Peak fitting of the Si-O band envelope shows four bands: 3 in-plane at ~1115, ~1045 and ~1024 cm^{-1} and one out-of-plane at ~1080 cm^{-1}.[125,126] The position and intensity of these bands change as the clay layers delaminate, the out of plane Si-O bond becomes more intense and appears as a shift of the bands to a higher wavenumber.[127]

Although Mono_PU has strong bands in the 1100 – 1000 cm^{-1} region, addition of clay in some samples (Mono_PU/C20 at 5 wt. % and Mono_PU/C15A at 3 and 5 wt. %) caused increased broadening and intensity of the C-O-C band at 1078 cm^{-1}. The peak apex is rounded as opposed to having two ridges. The broadening and intensity increased as clay concentration increased. This indicates clay is present within the sampled area.

Other samples did not show any subtle changes to the C-O-C band and all samples showed no changes in the Si-O band or N-H band. This indicates that despite clay being present within the samples, there are limited to no intermolecular interactions between Mono_PU and the nanofiller. There is also no difference observed between the upper and lower surfaces of the membranes.

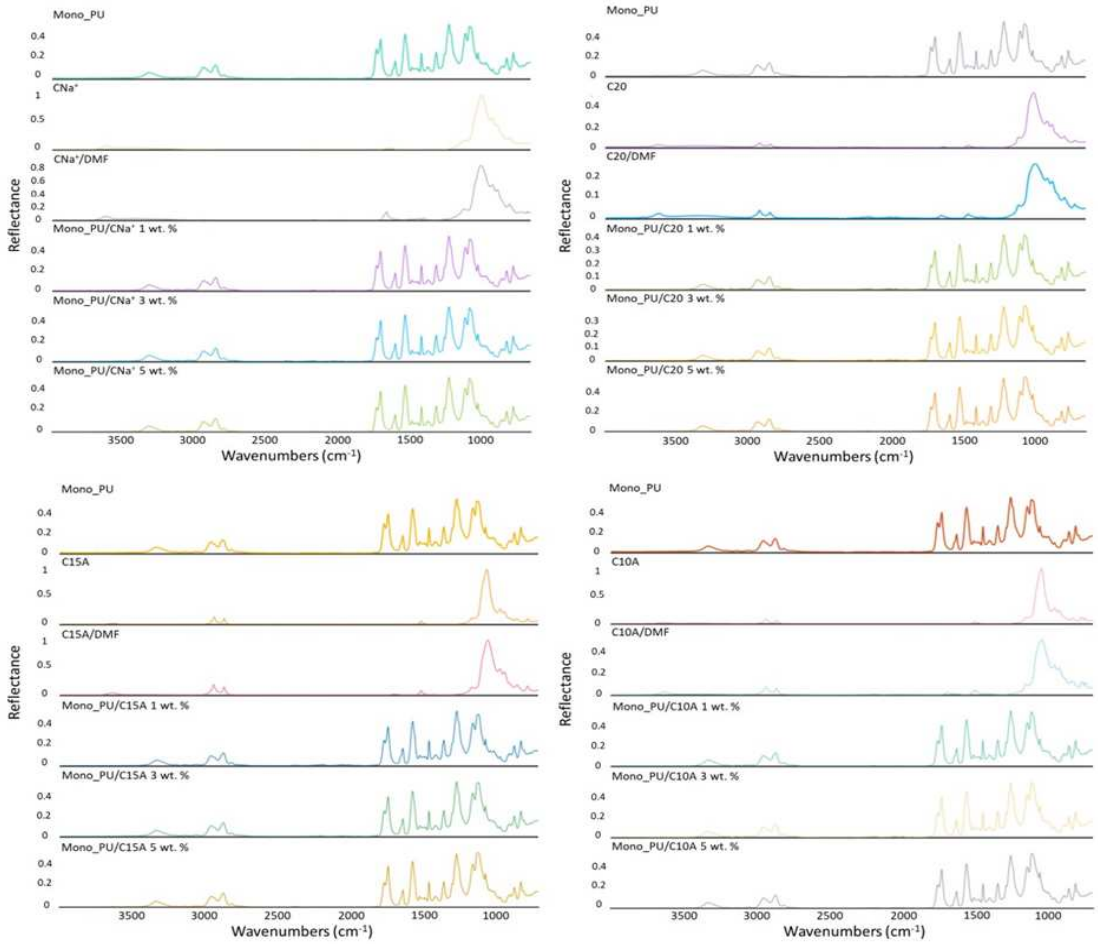

Figure 30. Top left to bottom right; ATR-FTIR spectra of Mono_PU/CNa^+, Mono_PU/C20, Mono_PU/C15A and Mono_PU/C10A nanocomposites compared against Mono_PU.

4.2.1.3 Scanning Electron Microscopy with Energy Dispersive X-ray Analysis

Clay is composed of oxygen, silicon, and aluminium atoms; through elemental analysis using EDX the presence of clay within the membrane can be observed. The elemental composition and concentrations of these atoms has been used to assess clay dispersion of samples containing 5 wt. % clay compared against Mono_PU.

EDX images collected from the cross-section of freeze fractured Mono_PU membranes show a high density of carbon due to both the polymer and the carbon coating. There is an even distribution of oxygen due to the urethane links and ether bonds within Mono_PU (Fig. 31).

SEM of the freeze fractured cross section of Mono_PU/CNa^+ 5 wt. % shows white artefacts (due to charging effects), which were suspected as clay aggregates. EDX was applied, the white artefacts had a high density of oxygen, silicon, and aluminium with a reduction in carbon density confirming they are aggregates rich in clay. These aggregates

of clay were seen along the whole length of the fractured surface, but their frequency did not account for the 5 wt. % of CNa^+ added. Therefore, it is believed there is also CNa^+ dispersed (either intercalated or non-intercalated) homogeneously throughout the rest of the membrane.

SEM shows the addition of C20 5 wt.% changed the cross-sectional morphology of Mono_PU from smooth to a stacked interconnected layered topography (wafer like structure). SEM/EDX was used to confirm good dispersion of C20 at 5 wt.% within Mono_PU; an even distribution of oxygen, aluminium and silicon was observed across the fractured structure. Between XRD and SEM/EDX it appears C20 was at the very least partially exfoliated within Mono_PU.

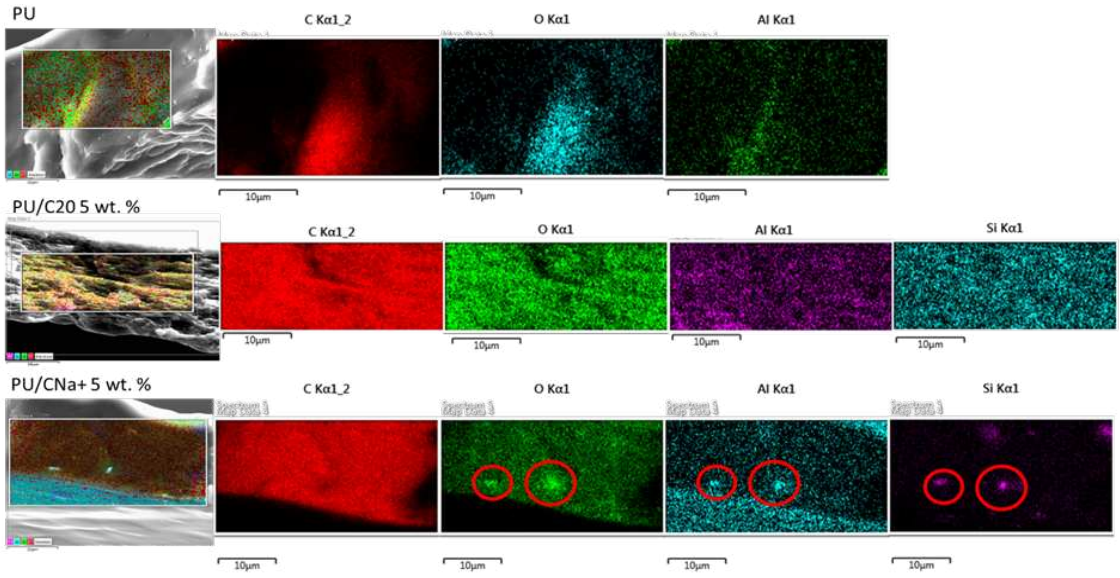

Figure 31. SEM/EDX Images of fracture cross section of Mono_PU/Clay nanocomposite monolithic membranes showing the distribution of carbon, oxygen, aluminium, and silicon.

4.2.1.4 Scanning Electron Microscopy and Surface Topography

Scanning Electron Microscopy (SEM) was used to provide information on the surface topography of Mono_PU/clay membranes. Figure 32 shows back scattered electron images of the upper surface topography of Mono_PU, Mono_PU_Con and Mono_PU/clay membranes. The upper surface has not been in contact with the release paper and thus has been in contact with the air during preparation. The SEM images in Figure 32 were analysed using ImageJ to determine the diameter of 20 randomly chosen dimples/pimples from each sample, the data are presented in Figure 33.

Mono_PU has a smooth topology with shallow dimples of uneven sizes and distribution with an average size of 1.4 +/- 0.7 μm on the surface described as the "orange peel effect" which could be caused by the quick drying process of the cast membranes. This 'orange peel effect' is increased for Mono_PU_Con with more numerous and larger dimples, on average 1.9 +/- 0.9 μm and is presumably due to the presence and evaporation of more DMF during the drying process.

The inclusion of CNa^+ has had a significant impact upon the topography of Mono_PU's upper surface compared to the other clay nanofillers. There is little change in surface morphology at 1 wt. %, but at 3 wt. % large dimples which resemble shallow craters begin to form. Despite the formation of larger dimples there remains much smaller dimples evidenced by a larger spread in standard deviation, average dimple size of 5.1 μm +/- 3.1. At 5 wt. % the structure is vastly different to all the other samples; the structure resembles 'bubble wrap'. The topology appears bumpy, and the shadowing makes the bumps appear pronounced like pimples. A possible contribution to this unusual structure at 5 wt. % CNa^+, is the aggregation of the poorly dispersed clay that has altered the order and arrangement of polymer chains thus creating a vastly different surface structure.

The addition of C20 had minimal impact on the surface topography. At 1 wt. % the dimples became slightly larger in size and less numerous whereas at 3 wt. % the shape of the dimples become more irregular. At 5 wt. % dimples become more irregular in shape and similar in size.

C15A also had minimal impact on the surface topography at low clay loading. At 1 and 3 wt. % C15A the surface is similar to C20 at the same concentration. At 5 wt. % the surface is significantly different to Mono_PU_Con, and Mono_PU/C15A at 1 and 3 wt. %. Mono_PU/C15A 5 wt. % has larger dimples of irregular shape and appear darker possibly indicating they are deeper than other samples.

C10A at 1wt. % has large areas that appear 'sunken' however at 3 wt. % these disappear. At 3 wt. % the sample is very similar to C20 and C15A at 3 wt. %. Again, the greatest change is observed at 5 wt. %, however this is less severe than C15A and CNa^+ at 5 wt. %. Mono_PU/C10A 5 wt. % dimples have maintained a regular shape of similar size. The darkening of the dimples indicates they may be deeper than those observed at lower

C10A loading. If the "orange peel effect" is caused by the fast drying of the membranes, the clay may be increasing the rate of drying inducing the production of larger dimples.

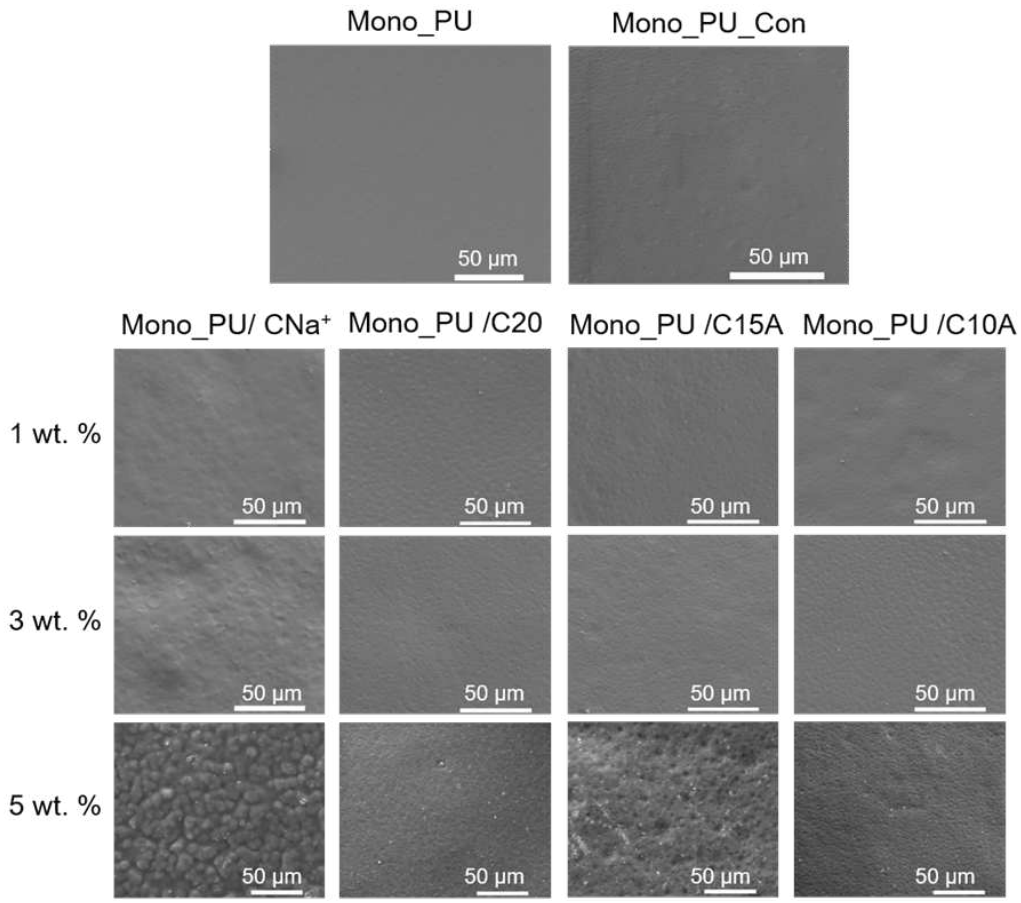

Figure 32. SEM images of upper surface topography of Mono_PU/Clay nanocomposite membranes compared to Mono_PU and Mono_PU_Con.

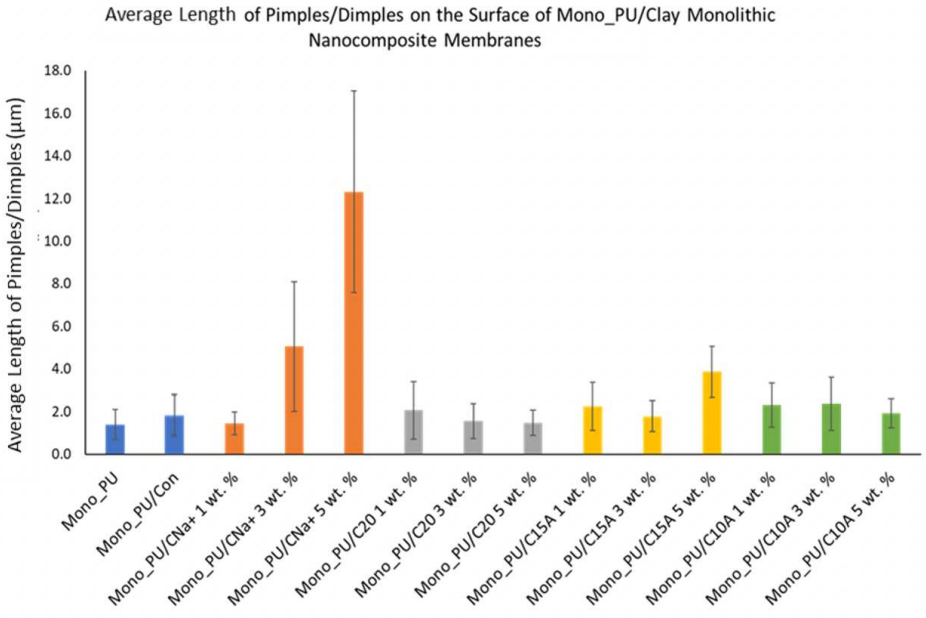

Figure 33. Average length (µm) of the pimples and dimples of Mono_PU/clay nanocomposites obtained using SEM images from Figure 32 using ImageJ (measured in triplicate).

4.2.1.5 Variant Focus Microscopy

Variant focus microscopy (VFM) is a novel technique used for imaging and analysing the surface topography of relatively flat polymer membranes. To date VFM has been predominantly used for larger samples, often 3D metal objects such as drill bits or fractured welds. Due to limited studies into using VFM to image flat polymer membranes the methodology required significant time to develop, and in the case of very flat samples, such as C10A 1 wt. % there is a hole in the sample image (Fig. 34a). This sample pushed the machine to its limits, the only way to achieve a complete image would have required over smoothing of the sample thus reducing reliability of data collected as well as reproducibility. The development of new methodology and individualised image collection per sample along with limited laboratory access during Covid-19 meant sample were only imaged once. However, images are representative of the samples surface and support the images collected via SEM, thus providing evidence that the images and data collected using VFM are reproducible and representative of the samples whole surface.

To analyse the 3D images collected, they are transformed into 2D images, this process removes 'waviness' of the sample, for example air bubbles trapped under the membrane's surface which could occur during preparation when attached to the substrate as well as edge effects. The processing from 3D to 2D also provides a range of information on the sample topography including the surface roughness value referred to as *Sq*. In cases of holes being present in 3D images such as C10A 1 wt. %, only part of the 3D image was selected to avoid edge effects present due to the hole (missing data). Thus, ensuring the 2D images and surface roughness measurements are not skewed by the hole(s).

If attempts were made to 'remove' the hole, it would require over smoothing of the sample and thus affecting the repeatability, reproducibility as well as the *Sq* measurement. As such it was decided that an imperfect image was more desirable than a false image.

VFM was used to characterise, image, and quantify the macro-surface morphology and roughness of Mono_PU/clay nanocomposite membranes. Figure 34 presents the 3D

surface maps of Mono_PU/clay membranes imaged using VFM, and Figure 35 presents the pseudo-coloured version on these images. Although it should be noted that sample preparation can cause microscopic air bubbles which can affect the pseudo-coloured 3D images. For this reason, the 3D images are processed to remove sample 'waviness' which may be linked to sample preparation (e.g., microscopic air bubbles) or sample thickness. This processing is necessary for quantitative analysis of the sample. Figure 36 and Figure 37 show the processed 2D images and pseudo-coloured 2D images, respectively. The 2D pseudo-coloured image is far more indicative of the true troughs and peaks of each pimple and dimple than the 3D pseudo images. However, it should be noted that both the 3D and 2D pseudo-coloured images have individual scales, unfortunately the scales could not be synchronised and thus they cannot be compared on colour alone. This must be considered when directly comparing the pseudo colours between samples. Due to this, the surface roughness was calculated to give a more comparable measurement of surface texture (Fig. 38).

VFM has allowed for better clarity to distinguish whether surface textures are pimples or dimples compared to SEM. 2D VFM images have a dimension of 268 x 200 µm, with a total area of 53,600 μm^2 while SEM images are 141 x 122 µm, with an area of 17,202 μm^2. Thus, VFM image area is roughly 3.1 times larger than SEM images.

The VFM images have a similar topography to those obtained via SEM. Mono_PU shows some 'orange peel effect', with dimples on average ~0.2 µm deep and pimples on average ~0.4 µm high, with some pimples reaching heights of 0.8 µm (Fig. 37). Mono_PU_Con has pimples of similar height to Mono_PU but the dimples have deepened, it appears the average depth is ~0.4 µm with several dimples reaching ~0.8 µm in depth. The increased depth and quantity of deeper dimples results in an increased 'orange peel effect' being observed.

The addition of CNa^+ 1 wt. % causes the number of pimples/dimples to decrease but the depth and height increases compared to Mono_PU_Con. Many dimples are ~0.6-0.8 µm in depth with the deepest ones reaching ~1.2-1.4 µm deep. While the pimples are ~0.8-1.2 µm in height. At 3 wt. % the peaks and valleys deepen and widen slightly, with max heights of 1.5 – 2 µm and maximum depths of ~1-1.5 µm. There are more dimples and

pimples forming both large and small in size. At 5 wt. % the number of dimples and pimples has increased compared to lower clay loading, however the 2D VFM images do not reflect the SEM images while the 3D VFM images hold more similarities to the 'bubble wrap' topography seen in SEM. In Pseudo 2D images there appear numerous pimples of ~0.8-1.2 μm in height and dimples of ~1- 1.6 μm. There is a larger spread in the peaks and valleys between the dimples and pimples within this sample.

The addition of C20 at 5 wt. % produces an increase in 'orange peel effect' with more numerous smaller sized pimples and dimples than at lower C20 loading. Using the pseudo 2D images shows the height and valleys of all three C20 samples were similar. The typical depth of the dimples was ~0.4-0.6 μm with a few dimples reaching 0.8 μm in depth. While the pimples on average ranged between ~0.4 and 0.6 μm with heights of up to 1 μm.

The 3D image and 2D pseudo images of the C15A samples indicate C15A 3% has a smoother surface with fewer and wider pimples/dimples than the other two samples. Despite initial looks appearing significantly different to other samples however this is due to the individual scale bars for each image. In regard to dimples all three samples had a typical depth of ~0.4-0.6 μm with maximum depths of 0.8-1 μm. While the pimple heights varied slightly between samples, at 1 wt. % C15A pimples averaged ~0.6-0.8 μm with peaks of 1.2-1.4 μm and C15A 3 wt. % had much shallower peaks than the other C15A loading with peaks on average ~0.6 μm high with maximum peaks of 0.8 μm. C15A 5 wt. % was similar to C15A 1 wt. % with ~0.4-0.6 μm pimples with peaks of 1 μm. This was surprising considering visually the surface texture of C15A 5 wt. % using the 3D and 2D VFM images appears rougher, with more dimples and pimples of greater depth and height than samples at lower clay loading. However, the scale bar of the 2D pseudo suggests a smaller difference in surface texture compared to visual interpretation of the images.

Much like SEM images of C10A the VFM images show the sample does not vary much from the Mono_PU or Mono_PU_Con. It appears C10A samples at low clay loading may have a slightly smoother surface texture than Mono_PU samples. As concentration of C10A increases the 'orange peel effect' increases with C10A 5 wt. % having the roughest

looking surface. All four clays caused the largest changes at the highest clay loading. This smoother surface at low clay loading is reflected in the 2D pseudo coloured image, the scale indicated that both C10A 1 and 3 wt. % have a slightly concave surface of around ~0.1-0.2 µm with a few prominent dimples of ~0.3 µm for C10A 1 wt. % and ~0.6 µm for C10A 3 wt. %. The pimples on these samples are more prominent with averages of ~0.6 µm and peak maximums of ~0.8 µm. At 5 wt. % C10A has numerous dimples of ~0.4-0.6 µm depth and pimples of ~0.6-0.8 µm in height, this reflects the SEM and VFM images of this sample.

C20, C15A and C10A 5 wt. % have pimples and dimples approximately between 0.4 and 0.6 µm with maxima of 0.8 to 1 µm while CNa^+ samples produce much deeper and higher dimples and pimples of between approximately 0.8 - 1.2 µm and maxima of up to 1.4 - 2 µm. This reflects and confirms observations in both SEM and VFM images.

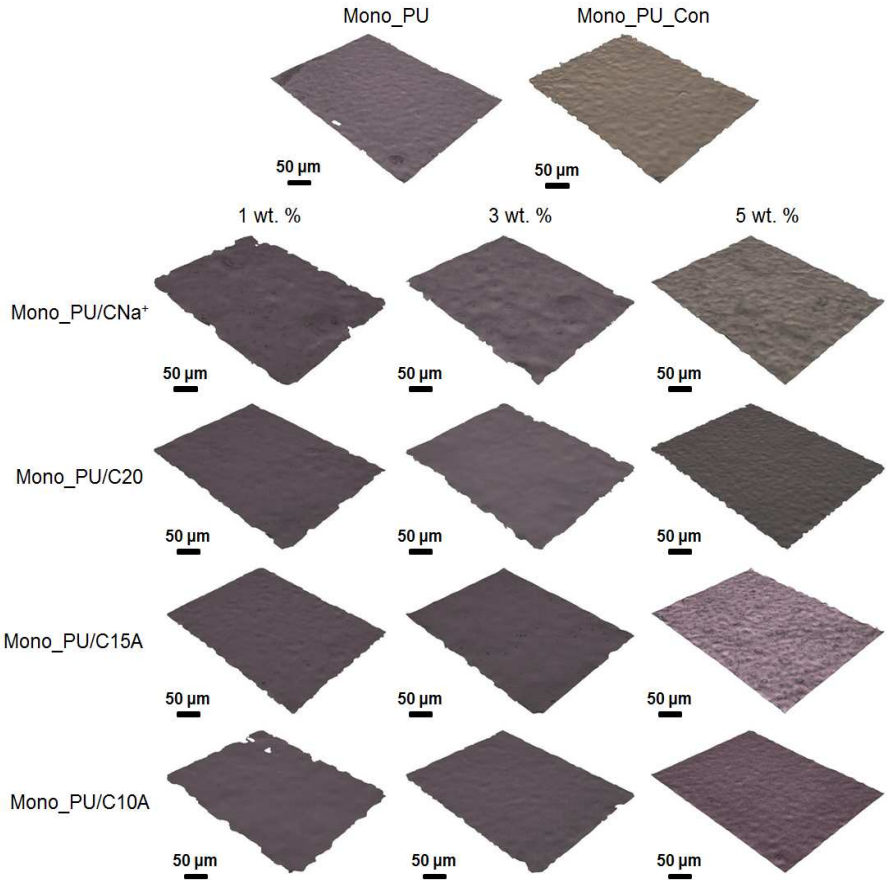

Figure 34. The 3D images of Mono_PU/clay nanocomposite membrane upper surface. Scale bar is 50 µm. Image dimensions are 268 x 200 µm. Z-axis varies depending on surface topography.

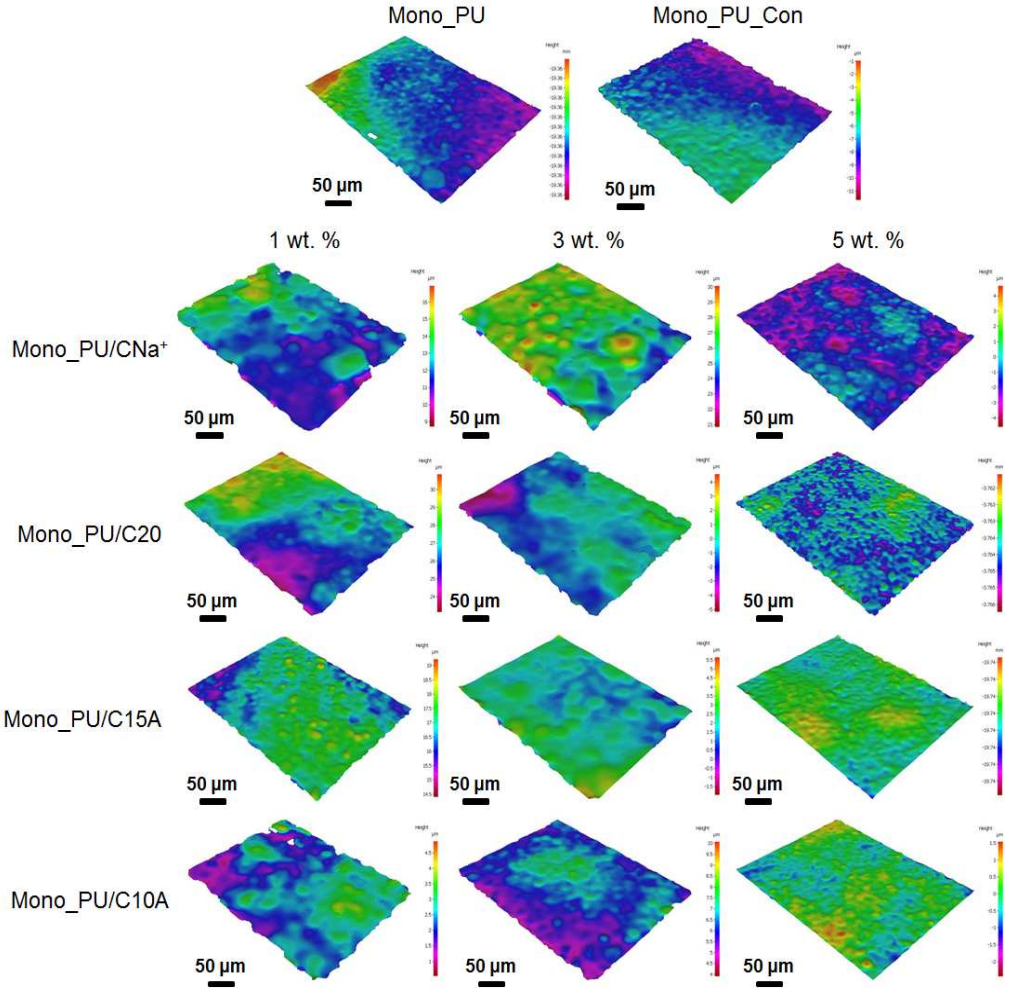

Figure 35. The pseudo-coloured 3D images of Figure 34. Scale bar is 50 µm. Image dimensions are 268 x 200 µm. Z-axis varies depending on surface topography. *N.B*. The scale for each image varies and should be noted before comparing samples based solely on the pseudo colouring.

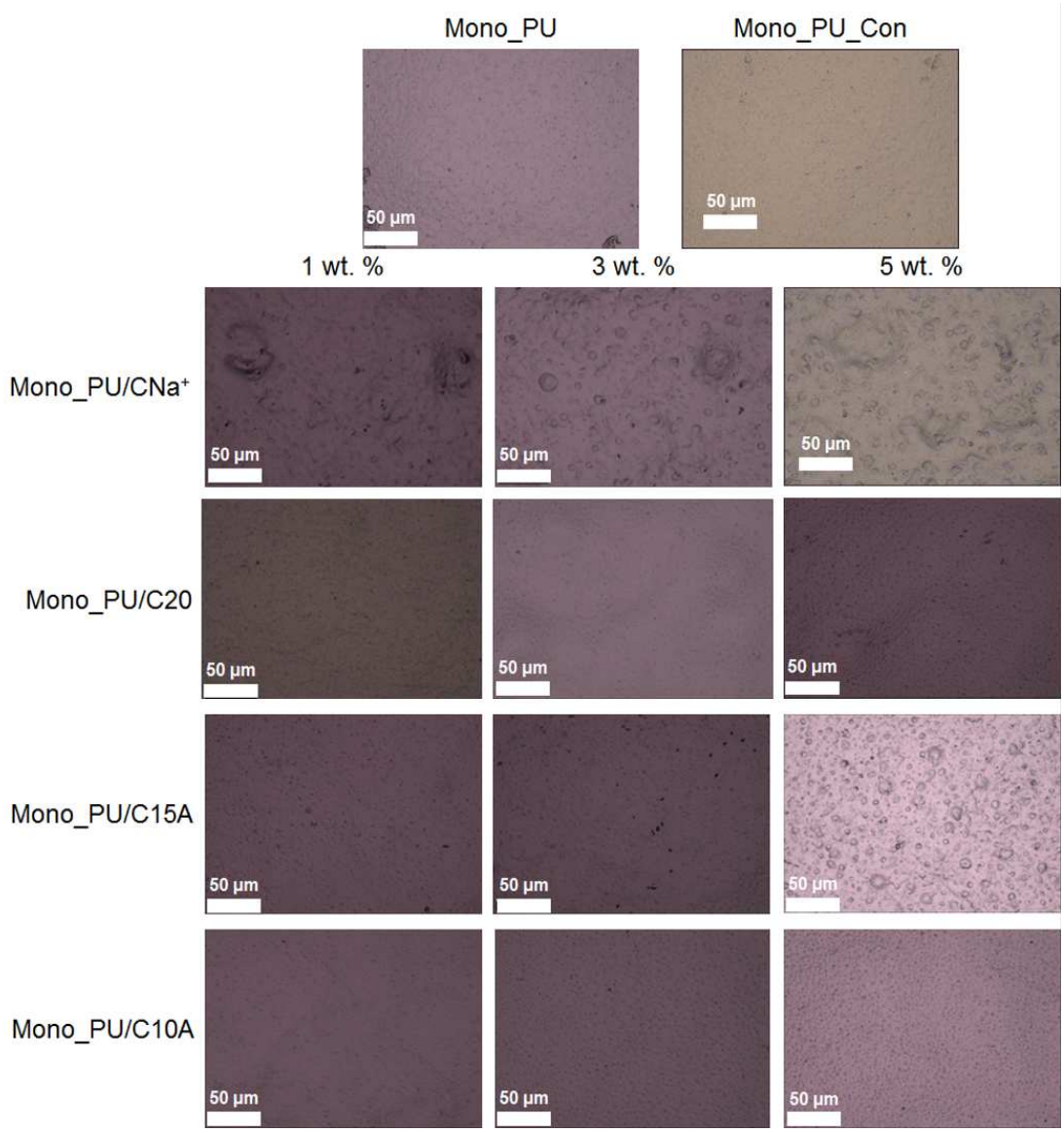

Figure 36. Shows the 2D images of all Mono_PU/clay nanocomposite membranes processed to remove edge effects and 'waviness' incurred during sample preparation prior to measuring the surface roughness. Scale bar is 50 µm.

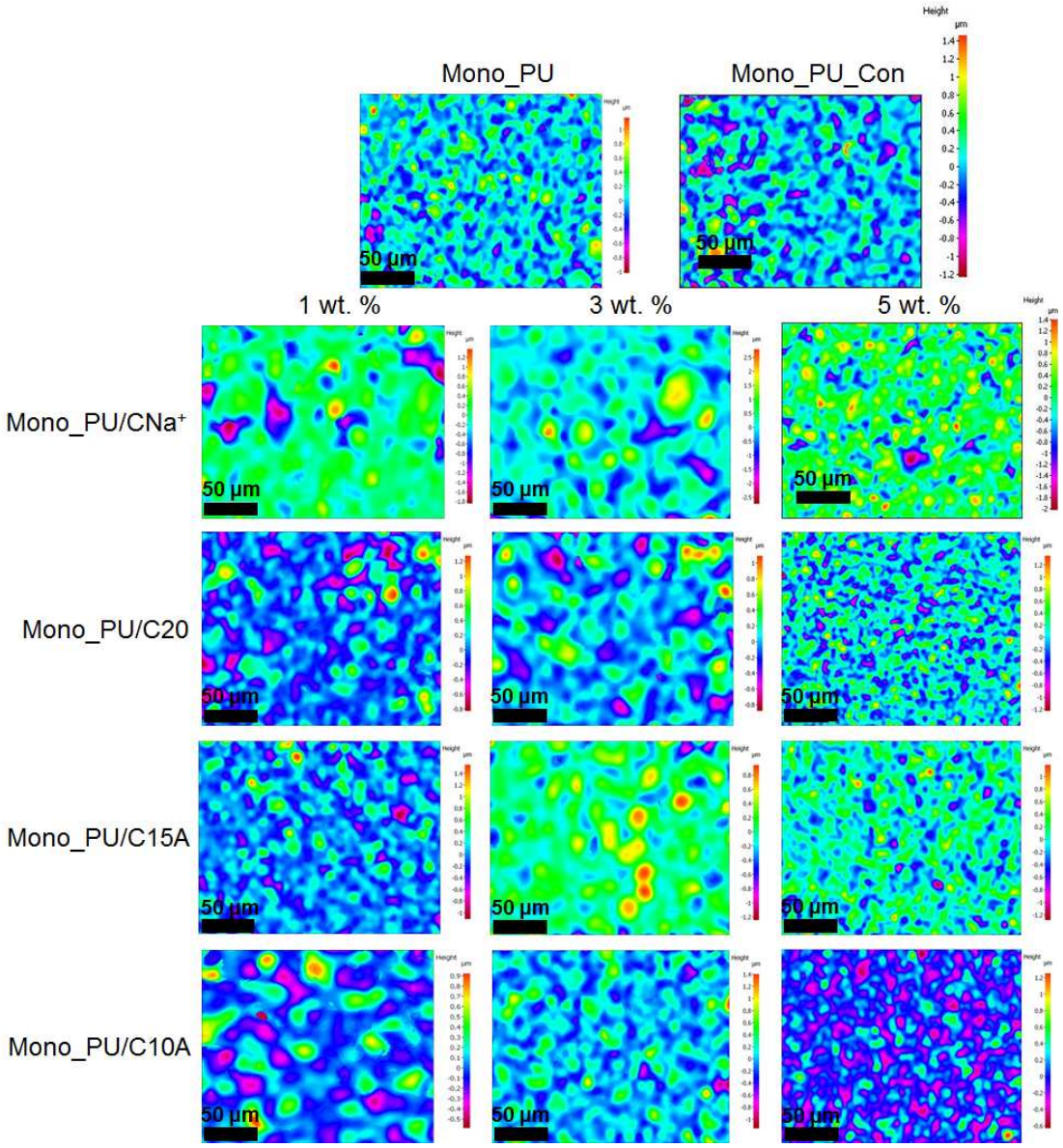

Figure 37. Shows the pseudo coloured 2D images of Figure 36. Scale bar is 50 µm. *N.B.* The scale for each image varies and should be noted before comparing samples based solely on the pseudo colouring.

The surface roughness (*Sq*) was calculated from the 2D image, Mono_PU had a *Sq* value of 0.23 µm, the addition of DMF to the control increased the *Sq* to 0.31 µm as expected due to the increased 'orange peel effect' observed in both the SEM and VFM images (Fig. 38).

All CNa^+ samples increased the *Sq* value compared to Mono_PU and Mono_PU_Con. CNa^+ 3wt. % increased the surface roughness the most to 0.53 µm, a 70% increase compared to Mono_PU_Con. However, C20, C15A and C10A did not increase the *Sq* value compared to Mono_PU_Con. Furthermore, there were no trends present between nanofiller type or concentration.

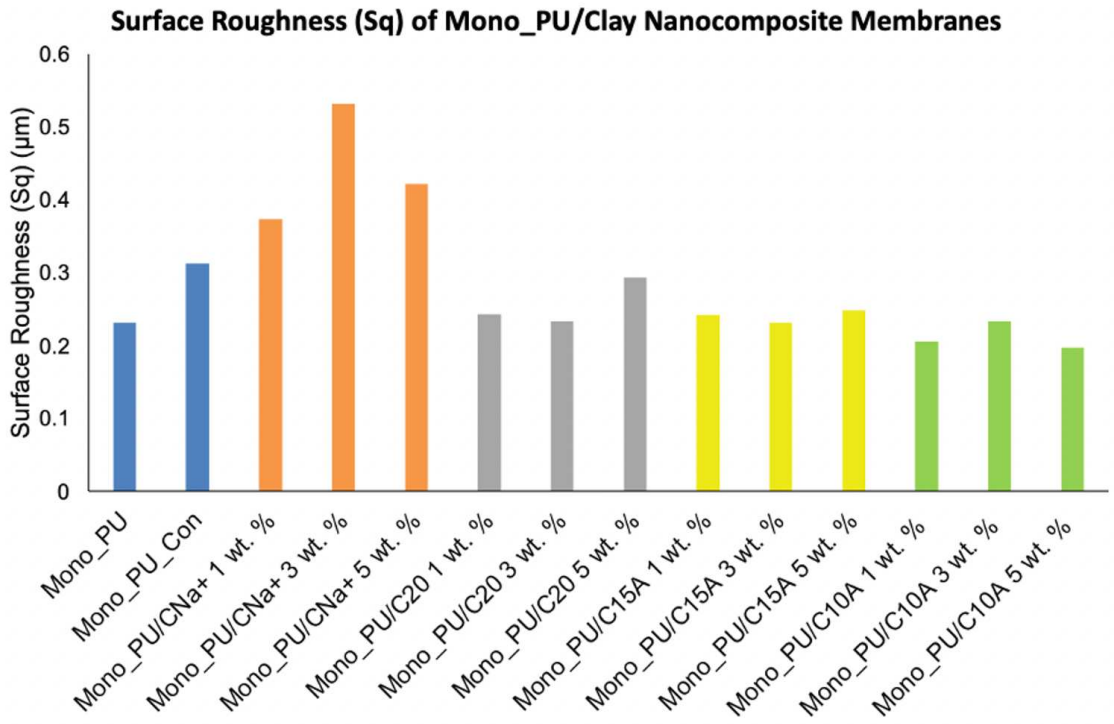

Figure 38. Surface roughness measurements (*Sq*) of Mono_PU/clay nanocomposite membranes obtained from VFM imaging.

4.2.2 Barrier Properties

Mono_PU is often utilised as a barrier membrane in outdoor apparel, as such the membrane must not be permeable to water but remain breathable to water vapour. It is therefore important to understand the effect of clay nanofillers on the barrier properties of Mono_PU. The wettability of the samples has been measured using contact angle, while a hydrostatic head test has been employed to understand the waterproofness of the membranes. The breathability of the membranes is also paramount for comfort and safety, the water vapour transmission rates have been calculated.

4.2.2.1. Contact Angle

Contact angle was used to measure the wettability of Mono_PU/clay membranes to understand how clay affects the wettability of the membrane's surface. Figure 39 presents the average contact angle and standard deviation for each sample.

Mono_PU is a hydrophilic polymer with a relatively smooth surface with a contact angle of 68°, indicating moderate wettability. Adding more DMF to the polymer suspension (Mono_PU_Con) caused an increase in contact angle of 9° to 77°. Due to this increase

with the addition of DMF, the changes in contact angle when clay is added are subtle compared to Mono_PU_Con.

As CNa^+ loading increases, the contact angle increases. The addition of CNa^+ 5 wt. % produced the largest increase for all samples of 81°, a 4° increase compared to Mono_PU_Con. There was no change in contact angle relating to concentration of C20, which produced a contact angle between 75° and 76° depending on concentration. The largest decrease of 5° compared to Mono_PU_Con was seen for Mono_PU/C15A 3 wt. % with a contact angle of 72°. The addition of C10A increased the contact angle, with values between 79° and 80° depending on concentration.

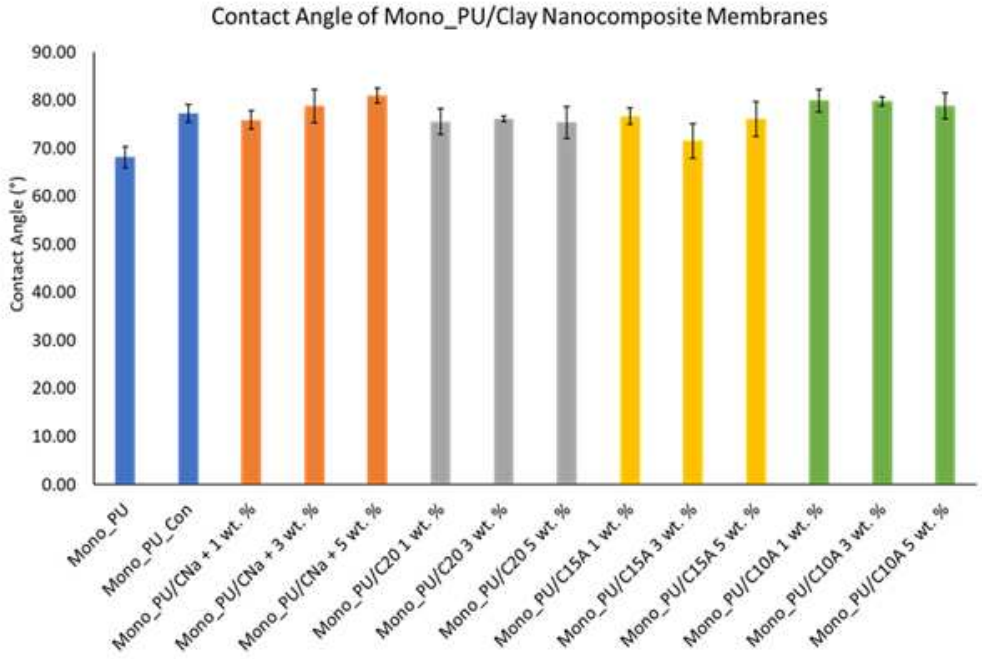

Figure 39. Average contact angles for Mono_PU/clay nanocomposite membranes with standard deviation (measured in triplicate).

4.2.2.2. Hydrostatic Head

Hydrostatic head tests were performed on selected samples (CNa^+ and C20) due to time constraints. It is important to note samples could not be repeated due to a limited sample size. The test was performed to assess how the clay affected the waterproofness of Mono_PU (Fig. 40).

A hydrostatic head value of 5000 mm is considered rainproof, and 10,000 – 15,000 mm is classed as waterproof. At 15,000 to 30,000 mm, the material is considered a high-

quality waterproof membrane suitable for aggressive conditions.[100] Mono_PU_Con has a hydrostatic head value of 10,020 mm and is considered waterproof.

The addition of CNa+ at 1 and 3 wt. % increased the waterproofness of the membrane significantly by 101% and 52%, respectively. Indicating these samples are suitable for aggressive conditions. However, at 5 wt. % a huge decrease is observed.

The addition of C20 at 1 wt. % caused no significant change compared to Mono_PU_Con. At 3 and 5 wt. % the samples experienced a large decrease, similar to Mono_PU/ CNa^{+} 5 wt. %.

The large decreases observed for these samples are possibly due to the presence of higher nanofiller concentration, but it should also be noted that air bubbles can be commonly present within these membranes leading to low values. Hydrostatic head tests are not known for good repeatability for this reason and unfortunately this experiment could not be repeated due to limited sample size. Despite these issues, the results are promising and show that low clay loading can have a positive significant impact on increasing the waterproofness of Mono_PU.

Table 7 shows the membrane thickness of Mono_PU/clay membranes are all very similar, this is important to consider since hydrostatic head values are very dependent on membrane thickness. Thus, improvements observed are not influenced by thicker membranes.

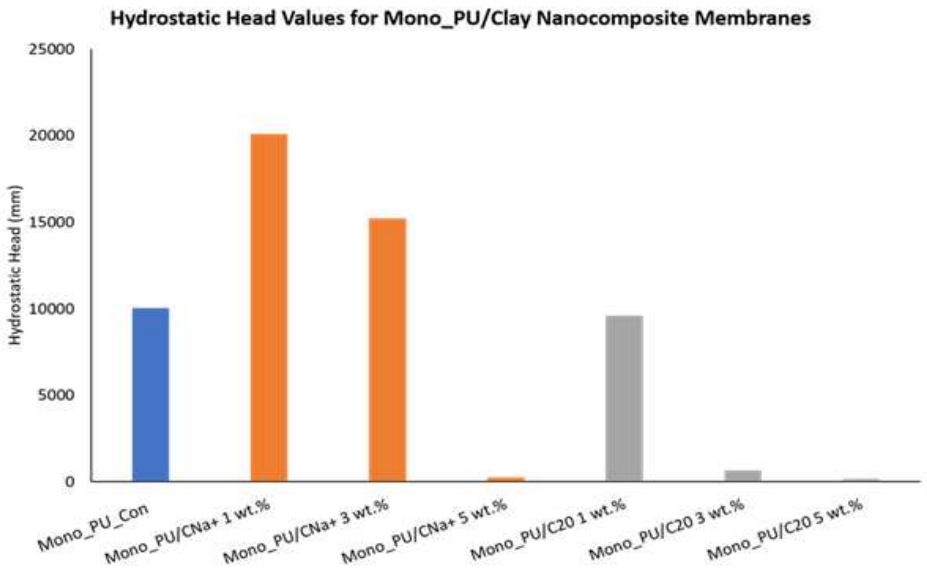

Figure 40. Hydrostatic head values for Mono_PU/clay nanocomposite membranes.

Table 7. The average membrane thickness of Mono_PU/clay membranes (measured in triplicate).

Mono_PU	Mono_PU_Con
0.05	0.03

	CNa+	C20	C15A	C10A
1 wt. %	0.03	0.02	0.03	0.02
3 wt. %	0.02	0.02	0.02	0.02
5 wt. %	0.02	0.03	0.03	0.02

4.2.2.3. Water Vapour Transmission Rates

Water Vapour Transmission Rates (WVTR) was investigated to understand the effect of clay on the breathability of Mono_PU (Fig. 41). The WVTR value for Mono_PU is 1027 g/m²/24h, adding more DMF to the polymer suspension did not significantly affect the WVTR, Mono_PU_Con has a WVTR value of 1013 g/m²/24h.

The addition of clay reduced WVTR for all samples. As the concentration of CNa^+ increased, the WVTR values decreased. At 1 wt. % CNa^+, WVTR decreased to 860 g/m²/24h, a 15% decrease compared to Mono_PU_Con. At 5 wt. % CNa^+ this dropped to 672 g/m²/24h, a 34% decrease.

No successive decrease in WVTR was observed with increasing concentration of C20 or C15A. At 1 wt. % C20 WVTR decreased by 20% compared to Mono_PU_Con, this decreased further to 35% at 3 wt. %, and at 5 wt. % C20 had a 26% decrease in WVTR though the larger standard deviation gives less significance to this change.

C15A at 1 wt. % had no effect on WVTR; it remained the same as Mono_PU_Con. However, at 3 wt. % a decrease of 30% was observed. This reduced to only a 6% decrease at C15A 5 wt. % compared to Mono_PU_Con.

The addition of C10A saw the overall largest decrease, but only a small decreasing change in WVTR values as concentration increased. At 1 wt. % C10A the WVTR was 683 g/m²/24h which decreased to 613 g/m²/24h at 5 wt. %. C10A produced the largest decrease in WVTR of 39% compared to Mono_PU_Con.

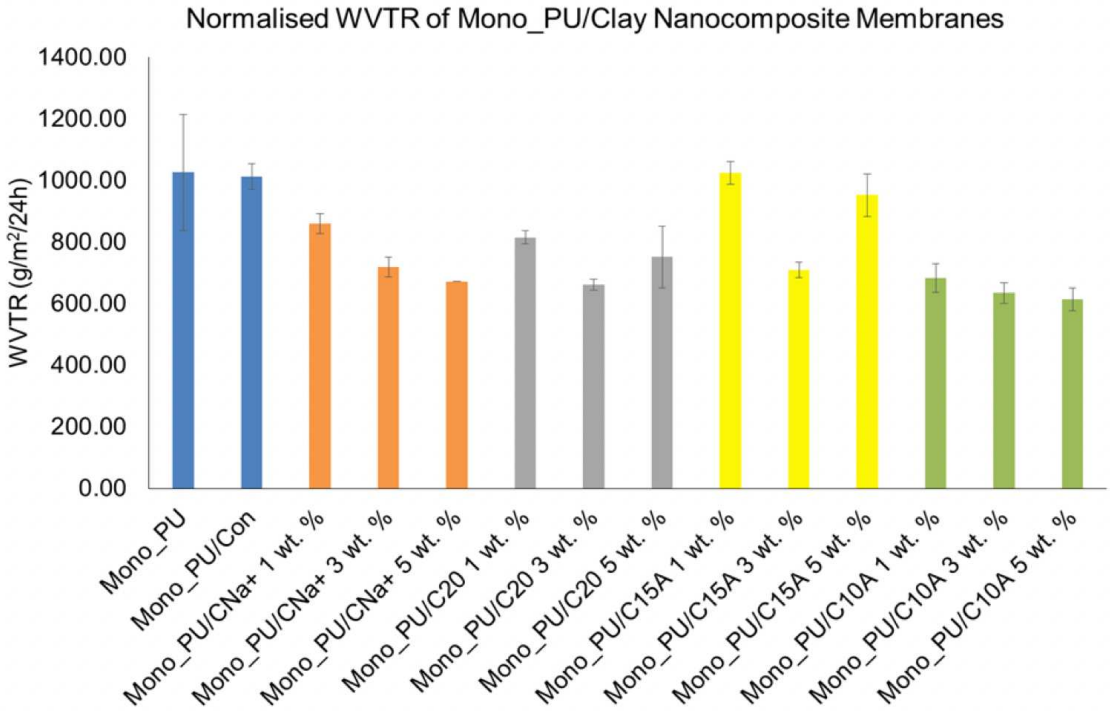

Figure 41. Average WVTR measurements of Mono_PU/clay nanocomposite membranes with standard deviation (measured in triplicate). WVTR values were normalised to average membrane thickness.

4.2.3 Mechanical, Thermal and Antistatic Properties

Mechanical and thermal properties of Mono_PU/clay membranes were explored through three different mechanical and thermal techniques, differential scanning calorimetry (DSC), dynamic mechanical analysis (DMA) and tensile strength. These three techniques provided information on how clay nanofillers affected the membrane's glass transition temperature, crystallinity, storage modulus, Young's modulus, elongation at break, and yield point. It is important that barrier membranes for apparel are strong and flexible. Improvements in strength and flexibility may require less material thus making garments lighter. Furthermore, the current optimised strength and flexibility of the membrane should not be negatively impacted by the addition of nanofillers. In addition to this, antistatic testing was conducted to assess if membranes had antistatic properties.

4.2.3.1 Differential Scanning Calorimeter

Figure 42 shows the DSC thermograms of Mono_PU and Mono_PU_Con when cooled to -80°C, then heated to 230°C and cooled again to -80°C. When heated there are three endothermic melting events (T_{mI} - T_{mIII}) between 165 and 220°C for both samples; there

is no significant difference between the onset T_m temperatures for Mono_PU and Mono_PU_Con. For Mono_PU_Con T_{m}I occurred at 170°C, T_{m}II at 195°C and T_{m}III at 201°C. Replicates were performed on both Mono_PU_Con and on Mono_PU/CNa^+ 5 wt. %, repeats have similar values and provides confidence that DSC testing and analysis was repeatable.

Three T_m (T_{m}I - T_{m}III) were also present for all Mono_PU/clay membranes (Fig. 43). Only small changes in onset temperatures (difference of 1-3°C) were observed compared to Mono_PU_Con. T_{m}I occurred around ~170°C, T_{m}II at ~193°C and T_{m}III at ~200°C for all samples.

Although DSC can be used to identify the T_g, unfortunately it could not be distinguished within these samples. This is because not all polymers possess a strong enough signal to be detected by DSC. Due to this, DMA was utilised as it is a more sensitive technique for measuring T_g events.

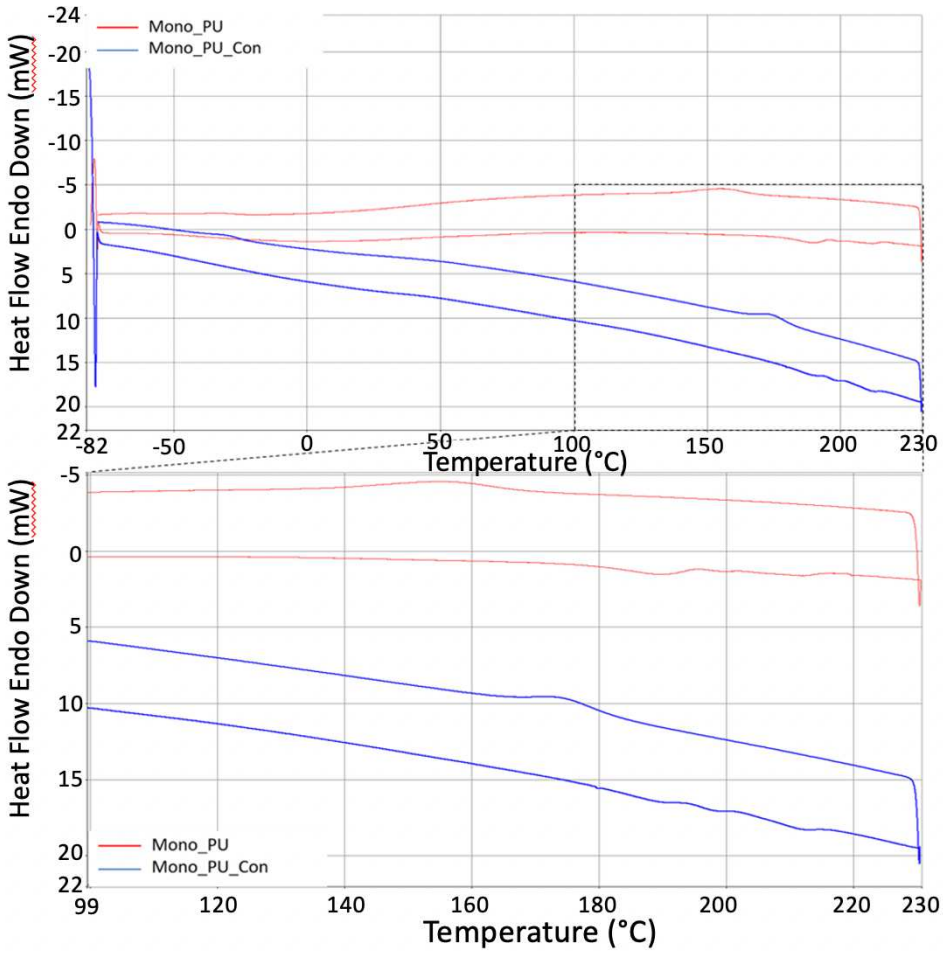

Figure 42. DSC curves for Mono_PU (red) and Mono_PU_Con (blue) cooled to -80°C, heated to 230°C and cooled again to -80°C and close-up of 100 to 230 showing the 3 T_m's and T_c.

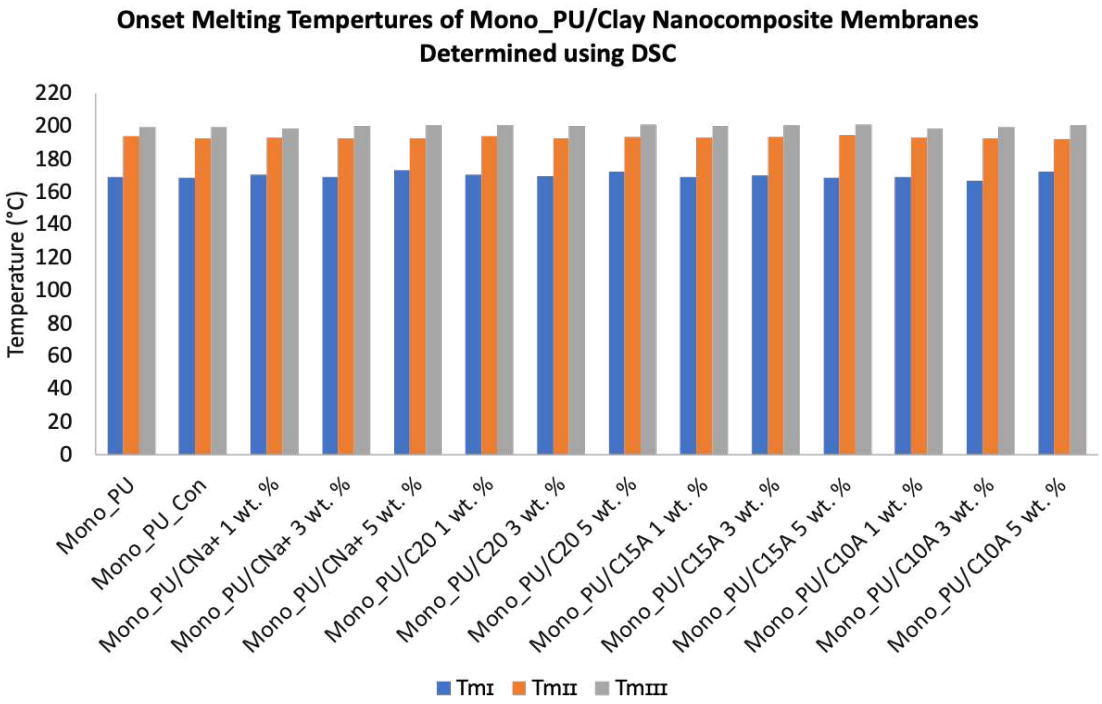

Figure 43. Melting temperatures of Mono_PU/clay monolithic nanocomposite membranes.

4.2.3.2 Dynamic Mechanical Analysis

Figure 44 shows a characteristic DMA thermogram of Mono_PU; storage modulus and tan δ are plotted as a function of temperature. DMA was performed from -100°C to 120°C to observe how Mono_PU/clay membranes performed at extreme temperatures. The temperature initially takes a while to stabilise and then increases at a steady rate hence the false initial dip in storage modulus at -100°C, stabilising occurs around -90°C. The tan δ data after 100°C is sporadic due to the softening and melting of the polymer membrane, the lower modulus values, and the sensitivity of the instrument.

Mono_PU membranes are used within the apparel industry at end range temperatures of -5°C and 40°C, thus the data points were analysed for the storage modulus at these two temperatures. No significant trends were observed regarding addition of clay type or concentration.

Literature indicates the tan δ peak at a lower temperature (-87°C to -50°C) corresponds to the T_g soft segment (T_g (S)) and the tan δ peak at higher temperatures (-45°C to 23°C) corresponds to the T_g hard segment (T_g (H)).[128] DMA was employed in this study to identify the T_g (S) and T_g (H) values of Mono_PU/clay nanocomposites and assess the impact of clay nanofillers on these values and provide insights concerning the

morphology of the hard and soft segments of Mono_PU. While DMA curves did present a T_g (S) and T_g (H) there were no trends or significant changes observed with the addition of clay nanofillers at any concentration.

It has been well established that numerous parameters significantly impact the reliability and repeatability of DMA experiments.[129] These short comings are furthermore exacerbated when analysing malleable samples with low structural rigidity. The identification of the storage modulus, T_g (S) and T_g (H) values of samples using DMA is prone to error, therefore such data cannot accurately be interpretated quantitatively unless supported by other characterisation techniques.

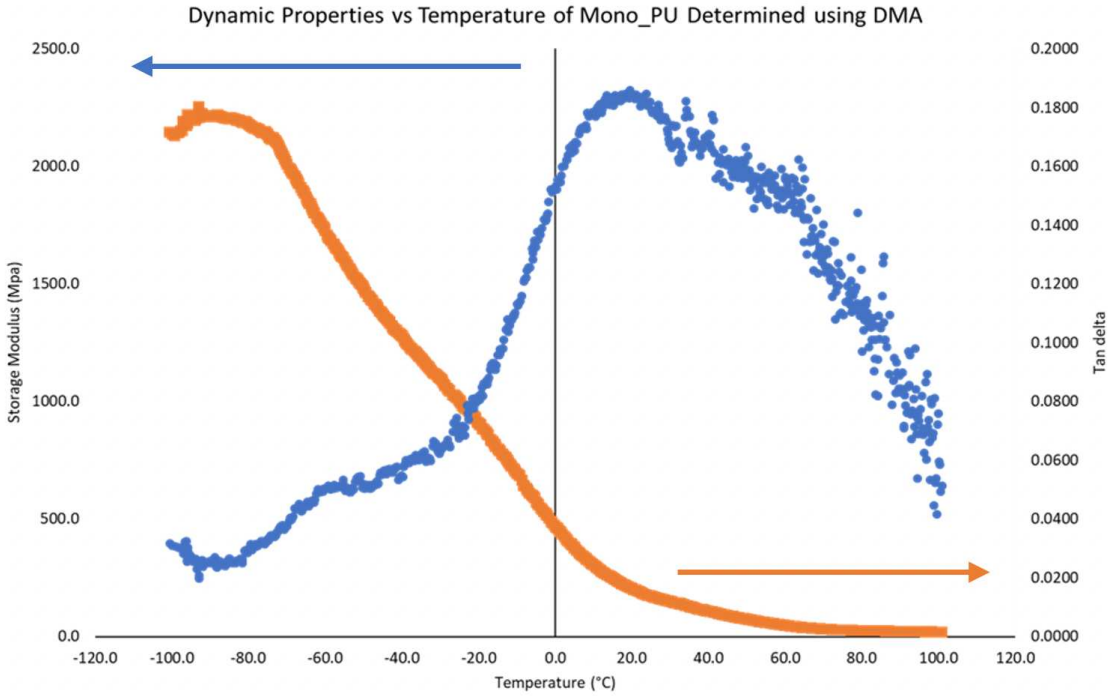

Figure 44. Storage modulus and tan δ of Mono_PU from -100°C to +100°C. Orange line represents storage modulus and blue line tan δ.

4.2.3.3 Tensile Testing

Tensile tests were performed to assess the Young's modulus, elongation at break and yield stress of Mono_PU/clay membranes. Only selected samples were tested due to limited sample size and time. The samples were tested in triplicate and a stress-strain curve produced for each. These curves provided the elongation at break, the yield stress and Young's modulus. Young's modulus was calculated using the equation of the line of the linear section of the curve, an example is shown in Figure 45. Values for each sample

were averaged and standard deviation was calculated. The Young's modulus, elongation at break and yield stress of Mono_PU/clay membranes are presented in Figure 46. Mono_PU_Con has a Young's modulus of 1.42 MPa.

The addition of CNa^+ did not cause a significant change in Young's modulus compared to Mono_PU_Con. However, the addition of C20 at 3 and 5 wt. % did cause an increase in Young's modulus compared to Mono_PU_Con. Young's modulus increases by 26% for C20 at 3 wt. % and 20% for C20 at 5 wt. %. The decrease in Young's modulus between 3 and 5 wt. % is possibly caused by poorer dispersion at higher C20 loading, this would create weak points due to clay agglomerates thus lowering the physical properties.

The addition of nanofillers causes minor changes to the elongation at break, however none are significant changes when compared to the Mono_PU_Con. Thus, the addition of CNa+ and C20 at 1, 3 and 5 wt. % does not affect the elongation at break of Mono_PU.

Minor changes are observed for most of the yield stress values of Mono_PU/clay membranes however these are not significantly different from Mono_PU_Con. Mono_PU/C20 5 wt. % is the only sample that is and incurs a decrease of 26% compared to Mono_PU_Con.

In summary, the Young's modulus incurred a significant increase of 26% for C20 3 wt. % compared to Mono_PU_Con, which slightly decreased to 20% with 5 wt. %. At 5 wt.% there was a corresponding decrease of 26% in yield stress at 5 wt. % compared to Mono_PU_Con.

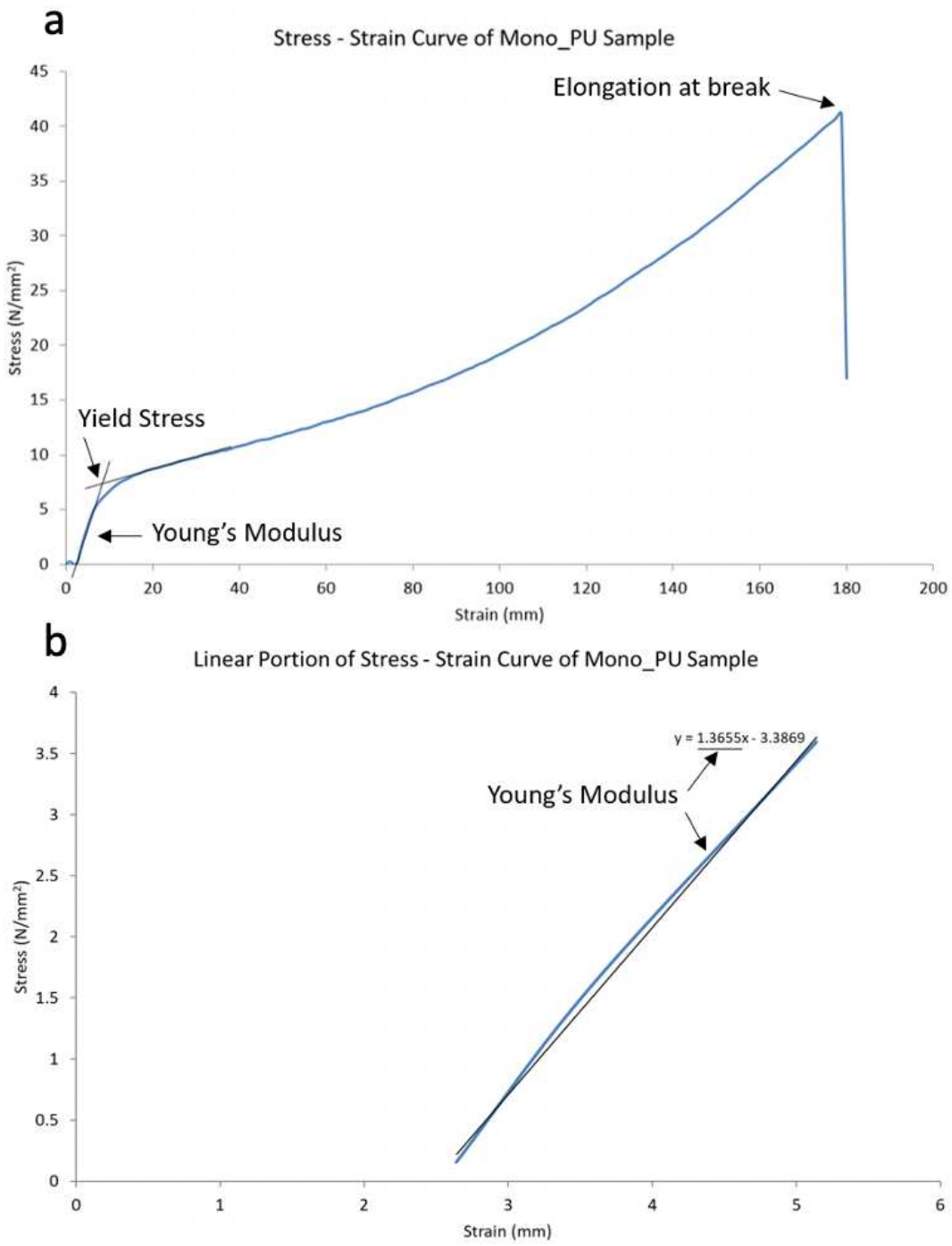

Figure 45. a) Stress-strain curve of one of the triplicate Mono_PU samples, showing the elongation at break, yield stress and linear portion of the curve. b) Linear portion of the stress strain curve for Mono_PU with the equation of the line and thus the Young's modulus.

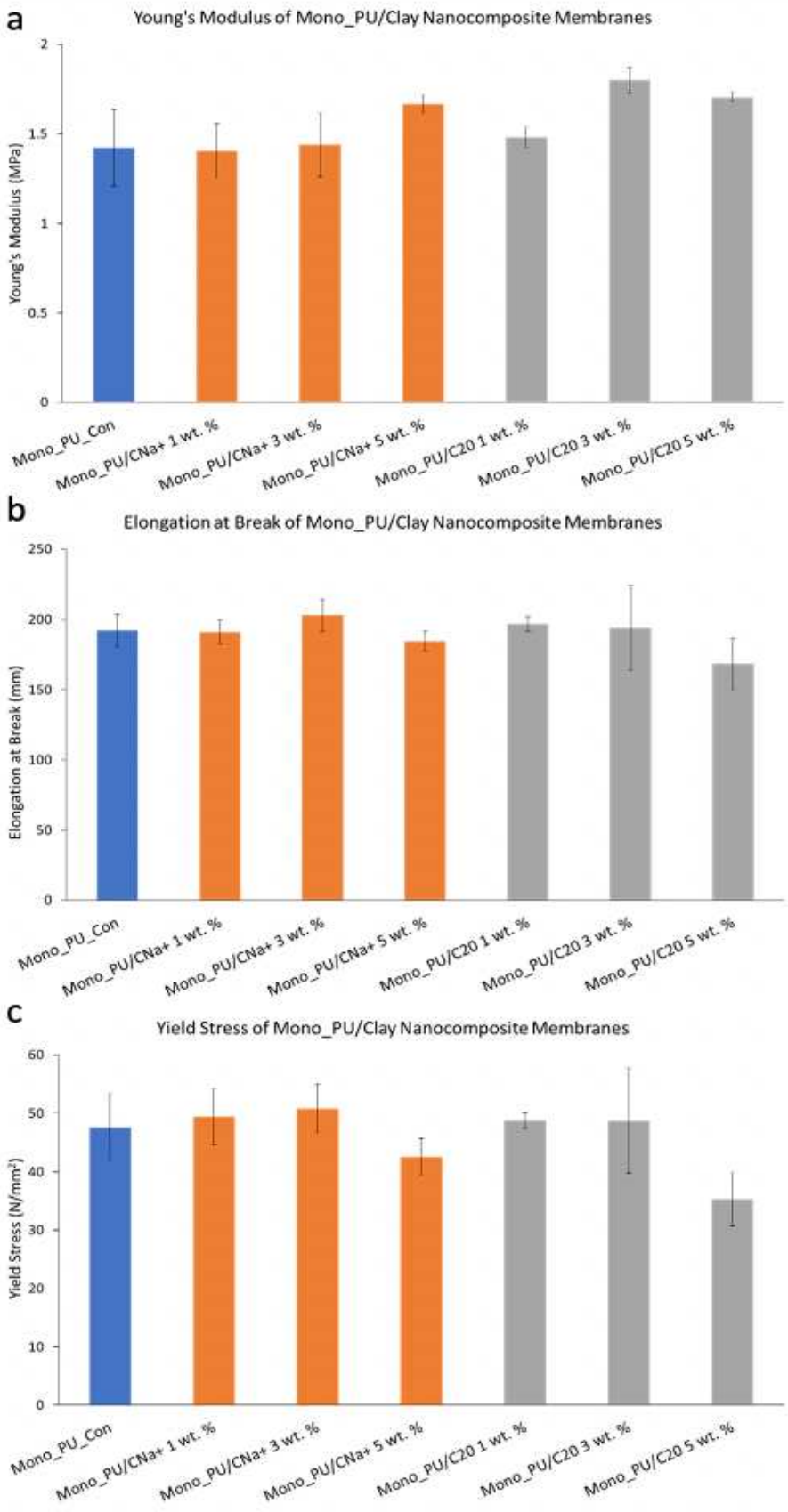

Figure 46. Tensile graphs of Mono_PU/ clay nanocomposite membranes, presenting the average value with standard deviation (measured in triplicate) for the following, a) Young's modulus, b) elongation at break, c) Yield stress.

4.2.3.4 Antistatic Properties

The antistatic properties of Mono_PU CNa^+ and C20 at 1, 3 and 5 wt. % nanocomposite membranes were measured in Ohms per centimetre (Ω^{-cm}) using Antistat™ surface resistance metre, Section 3.5.3.4 Figure 27.

All Mono_PU/CNa^+ nanocomposite membranes and Mono_PU/C20 1 wt. % registered as insulative. Mono_PU/C20 3 wt. % produced a reading of 10^{12} Ω^{-cm}, and Mono_PU/C20 5 wt. % registered as static dissipative with a reading of 10^{11} Ω^{-cm} (Fig. 47).

Figure 47. Testing for antistatic properties of Mono_PU/C20 5 wt. %, light indicates this material is static dissipative with a reading of 10^{11} Ω^{-cm}.

4.3 Discussion

XRD, SEM/EDX and FTIR were used to assess the dispersion of clay nanofillers within Mono_PU. FTIR analysis confirmed the purity and structure of Mono_PU and indicated no difference between upper and lower surfaces of membranes. Regarding

Mono_PU/clay nanocomposites only very minor changes for two samples were observed. FTIR was able to indicate clay was present in the sampled areas but did not indicate any intermolecular interactions between Mono_PU and the nanofillers.

C15A produced an unusual XRD pattern, indicating a highly ordered intercalated system possibly due to intercalation of the polymer chains within the interlayer spacing. This was likely initiated by the addition of DMF evidenced by C15A/DMF which created a highly ordered intercalated system with strong order of reflections. C15A becomes more ordered either by reordering the organomodifier or by removing it from the interlayer spacing during mixing with DMF. Mono_PU/C10A produced an ordered intercalated system with a strong order of reflection, similar to but weaker than Mono_PU/C15A traces. As with C15A/DMF the same occurred for C10A/DMF, the addition of DMF increased the order of C10A prior to mixing with Mono_PU likely leading to the highly ordered intercalated systems of C10A and C15A. SEM/EDX was not conducted on C10A and C15A.

XRD findings showed CNa^+ did not disperse as well as other nanofillers, this was expected due to the lack of organomodifier.[130] Mono_PU/CNa^+ produced an intercalated structure at all three concentrations. SEM/EDX of Mono_PU/CNa^+ 5 wt. % showed white artefacts, confirmed to be clay aggregates using EDX, across the whole length of the fractured surface but their frequency did not account for the 5 wt. % of CNa^+ added. Therefore, it is believed there is also CNa^+ dispersed (either intercalated or non-intercalated) homogeneously throughout the rest of the membrane; this is supported by XRD trace.

Whereas C20, in part due to the presence of an organomodifier, was the best dispersed clay.[130] Producing a partially exfoliated system, as concentration increased the system became slightly less exfoliated and slightly more intercalated. SEM/EDX of Mono_PU/C20 5 wt. % indicated a well dispersed at least partially exfoliated system with even elemental distribution (no clay aggregates) and stacked interconnected layered cross-sectional topography. This supports XRD traces for the same sample. However, it should be noted SEM/EDX cannot be used to confirm a fully exfoliation system as it is limited to the micro-scale, transmission electron microscope (TEM) would be required for true confirmation.

Interestingly SEM of Mono_PU/C20 5 wt. % cross-section saw a different morphology from Mono_PU. The cross-section changed from smooth to a stacked interconnected layered topography (wafer-like structure). A similar structure was observed by Ho *et al*., when 50 wt. % of montmorillonite was added to trimethylammonium-modified nanofibrillated cellulose.[131] The change shown in Figure 31 was achieved using 90% less clay than that reported by Ho *et al*. It should be noted the difference in topography between Mono_PU and Mono_PU/C20 5 wt. % results from the very well disordered and dispersed clay layers having an effect on the fracture mechanics.

It is thought the 'orange peel effect' topography observed in SEM images is formed when DMF evaporates during drying it pools on the surface thus creating dimples. The increase in 'orange peel effect' for Mono_PU_Con supports this idea as more DMF is present in the system compared to Mono_PU. CNa^+ at 3 wt. % presents a surface topography with broader and deeper dimples than other samples. It is thought the clay polarity may affect the pooling and evaporation of DMF. SEM images indicate an extreme effect with CNa^+, particularly at 5 wt. % to the surface morphology likely due to poor dispersion and the highly polar nature of the clay. Furthermore, the surface is also impacted by C15A at 5 wt. %, again due to the highly ordered dispersion and relatively non-polar clay. C20 and C10A have a relatively less severe effect on Mono_PU topography, even at high concentration likely due to better dispersion, polarity in between the two extremes of CNa^+ and C15A which results in an increased compatibility of C20 and C10A with the polymer and DMF. It is thought the poor compatibility of CNa^+ and C15A with the polymer could change the wettability with DMF thus causing changes to the surface morphology.

While SEM provides a relatively quick way to image a membrane's surface to a high level of resolution it is limited to 2D images and lacking the ability to provide quantitative information on surface roughness. VFM total image area is approximately 3.1 times that of SEM images. VFM was utilised as a novel way to image and analyse flat polymer membranes. VFM uses a small depth of focus of an optical system combined with vertical scanning, analysing the sample through the variation of focus along the vertical axis, to produce a 3D topographical image. This 3D image can give better indications of surface topography, in particular the peaks and troughs of a sample's pimples and dimples compared to 2D SEM images. Furthermore, this 3D image can be processed and

analysed using surface texture measurements which removes waviness and edge effects. This process converts the 3D image into a 2D image and provides a variety of information on the samples surface topography, including an areal surface roughness measurement known as *Sq*.

It should however be stressed that this technique is primarily used on relatively large 3D metal samples such as drill bits, fractured metal or engineering parts used in the aerospace industry.[71] To the best of the author's knowledge imaging of relatively flat polymer membranes by VFM is novel. Due to the novel nature and the design limitations of the VFM the development of the methodology was time consuming. This process due to its novelty required extensive protocol optimisation to ascertain the best imaging methodology. After method was established, imaging samples was relatively fast, reliable, and comparable to the imaging of SEM samples. However, VFM provided far more quantitative and qualitative information on surface topography than SEM. It should be noted the shading of the VFM 3D and 2D images are due to slight changes in the individual optimisation of imaging parameters and does not have any bearing on surface roughness, texture, or colour.[94]

VFM 3D and 2D images (Fig. 34, 35, 36 & 37) are similar to the SEM images (Fig. 32), for example C15A 5 wt. % has good correlation between SEM and VFM images, with both presenting a textured surface morphology with relatively numerous pronounced dimples and pimples. One of the benefits of VFM imaging is that 3D maps allow for clearer analysis of surface texture. VFM 3D images clearly show if surface texture consists mainly of pimples or dimples. The peaks and valleys are much easier to distinguish as opposed to trying to analyse the shadow effect present in flat SEM images.

However, VFM 3D images with pseudo-colour (Fig. 35) highlight the instrumental limitations when imaging relatively flat transparent membranes. Due to the subtle nature of dimples and pimples on Mono_PU's surface, often less than 1 μm in height or depth, the pseudo-colouring of the machine struggles to highlight these subtle differences on 3D images. Instead, the instrument picks up on the broader surface texture (low frequency signals), known as waviness. Waviness is always present when imaging using VFM unless filtered out, but it is proposed that waviness can be affected

by two factors within this study: sample preparation or sample thickness.[90,93] The challenge of preparing these samples involved attaching the sample flat and parallel to the substrate. It is possible air bubbles may be present, and these could not be forcibly removed without damaging the membrane surface. In regard to surface thickness, a 1 mm difference in thickness from one side of the sample to the other would provide a far greater surface change compared to 1 µm of dimple depth or pimple height. An example of this limitation is the pseudo-coloured image of CNa^+ 1 wt. % which shows a sample with one side raised and one side concave as opposed to the individual dimples and pimples. It is proposed that the relatively smooth surface roughness (high frequency signals) is being overshadowed by waviness (low frequency signals) from either sample preparation or variation in thickness across a sample.[93] When waviness is filtered out the 2D surface texture image (including the pseudo-coloured version) of CNa^+ 1 wt. % is similar to that of the SEM image. This however is not an issue for every sample, C20 5 wt. % presents a good pseudo coloured 3D image with clear dimples and pimples that are reflective of both the SEM images and the VFM 2D images (Fig. 32 and Fig. 35). It should be noted that 3D pseudo imaging of Micro_PU membranes in chapter 6 are less likely to incur issues from waviness dominating the image due to increased surface roughness and presence of pores and craters (i.e., increase in high frequency signals).[78] This evidence shows that imaging Mono_PU samples, due to their relatively flat nature and required sample preparation steps, pushed the VFM instrument to its limits and as such the information obtained from VFM came mostly from the surface texture 2D images which had filtered the waviness out (Fig. 36 & 37). As well as the surface roughness, *Sq* (Fig. 38).

Due to the removal of sample waviness, the pseudo-coloured 2D images (Fig. 37) are more accurate, they pick up on the fine surface texture of subtle dimples and pimples rather than broader surface texture (waviness). For example, the 2D image of CNa^+ 3 wt. % (Fig. 36) makes it challenging to distinguish if the large blemish on the right-hand side is a pimple or dimple. This issue is also present in SEM image (Fig. 32). With pseudo-coloured 2D VFM images it is clear to see the blemish is a pimple with a peak height of ~ 2 µm. The scale bar of the pseudo-coloured image allows for quantitative analysis of the dimples and pimples depths and peaks which is otherwise missing from SEM images and even 3D VFM images which present only qualitative information.

It was theorised that the inclusion of nanofillers would change the surface topography and in turn increase the surface roughness of the membrane thus decreasing wettability with regards to water droplets. However, the addition of C20, C15A and C10A did not increase the surface roughness above Mono_PU_Con and in some cases the *Sq* for these polymer nanocomposites was lower than Mono_PU. Only the addition of CNa^+ caused an increase in surface roughness with CNa^+ 3 wt. % producing the largest increase of 70%. It was theorised that CNa^+ 5 wt. % with its more unique surface morphology would produce the greatest increase in surface roughness however it appears the *Sq* values do not directly correlate with what is visually observed with the VFM and SEM images. One possible explanation is the resolution of VFM is not great enough to adequality identify the membranes subtle possibly nano-scale surface roughness. VFM's ability to identify nano-scale details is debated and appears to be dependent on the type of sample studied. One study validated VFM against AFM and confirmed VFM was able to accurately assess wear and tear at the nanoscale on metal alloys used in hip replacements.[76] While another study found VFM did not accurately access the nanoscale surface roughness of polymer surfaces compared to AFM.[78] It is likely this technique, despite showing progress in providing alternative quantitative and qualitative imaging and analysis of relatively flat polymer surfaces, is currently unable to adequately image samples with limited texture. In Chapter 6, VFM was more successful in imaging and analysing Micro_PU nanocomposites due to their porosity and increased surface texture (6.2.1.6).

There is limited research on barrier properties of monolithic polyurethane membranes used in apparel, herein lies one of the novelties of this research. With regards to contact angle it should be noted there is little rationalisation as to why a surface change from hydrophilic to hydrophobic at 90° and in fact the increase in contact angle is more closely related to a material surface roughness and surface tension as opposed to its chemistry.[97] The wettability of the surface by a liquid is an indication of adhesion. A study suggested a contact angle below 85° can improve a materials adhesive property.[132] Mono_PU has a contact angle of 68° and Mono_PU_Con has a contact angle of 77°. The addition of CNa^+ 5 wt. % produced the largest increase for all samples of 81°, a 4° increase compared to Mono_PU_Con. It appears the addition of DMF to Mono_PU had a greater impact than the further addition of clay nanofillers. A study investigating

the adhesion of steel with PU found monolithic PU had a contact angle of 76°, this is similar to the contact angle of Mono_PU_Con investigated in this thesis.[132] A study on waterborne polyurethane and various nanocomposites found the addition of montmorillonite clay increased the contact angle from 62° to 82°, a similar increase is observed for Mono_PU/clay nanocomposite membranes thus validating this work.[133]

As discussed above, it was thought from the SEM and VFM images that the changes in surface texture would cause a decrease in wettability. Contact angle was used to assess wettability of the membrane surface against water droplets. While the contact angle did increase for all samples compared to Mono_PU, they did not all increase compared to Mono_PU_Con. CNa+ at 5 wt. % produced the greatest increase in contact angle which was initially assumed to be due to the unusual surface topography seen in SEM images. However, when investigated further using VFM to assess surface roughness no correlation or trends were found between clay type and concentration when comparing contact angle to surface roughness. This ruled out the effect of surface roughness on the membrane wettability thus leaving the possibility that hydrophobicity and surface polarity were more crucial to determining wettability of these membranes.[132] Unfortunately, these could not be measured within the scope of this project. Furthermore, there is no relationship between clay polarity and wettability which may indicate the clay is not near or on the surface and that the polymer has enveloped the clay. This is supported by SEM/EDX images which show the clay within the membrane rather than on the surface.

To assess other barrier properties of these membranes, hydrostatic head testing was performed. The results appear promising, the addition of CNa 1 wt. % doubling the hydrostatic head value from 10,020 mm for Mono_PU to 20,140 mm. This is significantly greater than a patent which found a microporous PU organomodified clay nanocomposite membrane had a hydrostatic head value of 5000 mm.[59] The results from this study show further promise, when compared to a study on PTFE microporous membranes laminated to a variety of textiles, including PU, the hydrostatic head values ranges between 10,870 mm (PTFE-PU membrane) to 15,780 mm (other PTFE membranes).[134] Samples within this thesis either met or far exceeded this range. However, it must be noted that this test was outsourced, and samples could not be repeated due to limited sample quantity. This test is regarded as having issues with

reliable repeatability and as such the data, although promising for some samples, must take this into account. Membrane thickness was maintained across samples and is unlikely to have impacted the test.

As anticipated the WVTR decreased with the addition of nanofillers and increasing nanofiller concentration due to the tortuosity effect.[135] C15A at 1 and 5 wt. % did not follow the trend, it is thought the highly ordered dispersion caused changes to the orientation of the clay, along with 'pin holes' on the surface which caused a shorter pathway for water vapour thus producing a greater WVTR.[136]

To assess the mechanical properties of these membranes DSC, DMA, tensile testing, and static testing was performed on the samples. DSC showed all samples had three T_m events with a very minor difference of 1-3°C between samples. DSC was repeated on Mono_PU and T_m events were repeatable with similar values across all three repeats. Unfortunately, T_g events were unable to be observed in DSC data. DMA was utilised to assess the T_g and storage modulus of samples. It was anticipated storage modulus would increase with increasing clay concentration, but this would depend on the extent of clay dispersion and its compatibility with the polymer chains. However, no trends nor significant changes in storage modulus or T_g were observed.

Tensile testing showed C20 3 and 5 wt. % and CNa^+ 5 wt. % increased the Young's Modulus slightly. A slight reduction in elongation in break and yield stress was observed as expected with increases in Young's Modulus. Indicating the addition of clay has slightly reinforced the membrane.

Surprisingly the addition of C20 at 3 and 5 wt. % produced antistatic properties within the membrane. The literature indicates that it is unusual for clay alone to act as an antistatic agent, clay nanofillers are normally utilised in conjunction with a typical antistatic agent (3-9 wt. %).[137,138] However, a patent found a laponite (40-70 wt. %) was coated continuously on a laminate surface provided antistatic properties.[139] Due to the rareness of clays alone producing antistatic properties it is possible the unusual wafer-like cross sectional structure of C20 5 wt. % played a part in this result. The industrial scale production of these Mono_PU membranes can generate large amounts of static, having static dissipating membranes could help reduce the static produced during

production. Furthermore, it could provide static dissipating properties to protective garments for various workers in numerous industries.

4.4 Conclusions

To conclude chapter 4, the nanofiller C20 dispersed the best within the Mono_PU membrane. The surface topography changed with the addition of clay, particularly at the highest clay loading of 5 wt. %. However increased surface texture did not directly correlate with increased surface roughness which in turn did not directly affect the wettability of the membranes. WVTR decreased as expected and hydrostatic head testing provided promising results regarding waterproofness however repeats are required for more confidence. The addition of clay nanofillers had minor impacts on mechanical properties of Mono_PU. Interestingly, C20 3 and 5 wt. % provided static discharge to Mono_PU.

The addition of C10A had very little impact on Mono_PU, the surface remained relatively smooth, and there were no significant changes in barrier or mechanical properties. C15A, produced a highly ordered intercalated system which may in turn have maintained a greater WVTR than other clays. However, it did not produce any other interesting results compared to other samples. CNa^+, despite being the most poorly dispersed clay, caused unusual topography at 5 wt. % and was the least wettable sample however no correlation between wettability, surface roughness and clay polarity was observed. Waterproofness appears promising with CNa^+ 1 wt. % doubling the hydrostatic head compared to Mono_PU_Con, however repeats are necessary. CNa^+ produced some interesting results despite relatively poor dispersion. C20 dispersed the best of all four clays and produced an unusual cross-sectional structure at 5 wt. % which could be linked to the antistatic properties of C20.

Chapter 5

Mono_PU/GO and GNP Nanocomposites

5.1 Introduction

This chapter studies the addition of graphene oxide (GO) and graphene nanoplatelets (GNP) to Mono_PU and the subsequent effects these nanofillers have on Mono_PU membranes. The Mono_PU (batch 2) used in this study differs from Mono_PU (batch 1) used in Chapter 4. Batch 1 was extracted directly from PIL Membranes LTD production line whereas batch 2 used in this chapter was produced in a more controlled manner in the PIL Membranes LTD lab. Therefore, there are slight differences in the properties of Mono_PU batch 1 and batch 2. Differences are minor but do occur and are discussed throughout this chapter to make comparison between clay, GO and GNP nanofillers.

GO and GNPs were chosen due to their novelty, Graphene was first isolated via mechanical exfoliation in 2004 at the University of Manchester by Professors Andre Geim and Kostya Novoselov.[24] Their Nobel winning discovery has led to a variety of studies using graphene for a range of applications such as electronics, biomedical, membranes, composites, and coatings. Making it a natural nanofiller to investigate for improving polymer membranes for protective apparel. Single layer graphene is extremely difficult to produce, even at a lab scale, due to this graphene is defined as having fewer than 10 layers, anything greater than this is deemed graphite.

GO and GNPs are of great interest due to their light weight, good mechanical, and thermal properties, as well as electrical conductivity. Graphene is lightweight at 0.77 mg per square metre and highly elastic making it very promising for applications in protective apparel.[28,29] Furthermore, GO has been found to increase mechanical properties of PU.[52] Despite the vast interest in graphene, there have been several issues in the development of affordable large-scale graphene production, this is due to the presence of inter-tubular interactions, lack of functional sites and restacking of graphene sheets. This also accounts for graphene's poor dispersion in many polymer matrices.[140] Due to the difficulties producing large scale amounts of graphene and GO, the cost is extremely high. Table 8 displays the price of GO from three different

manufacturers used within the study, Graphitene, Abalonyx (now known as LayerOne), and Sigma Aldirch (now known as Merck). Costs of GO samples described below, it should be noted that the GO from Graphitene came in a specialised project specific formula, the cost of which will be greater than that described within Table 8.

Table 8. Price of GO from the three different suppliers used within this study as of May 2023.[141–143]

Brand & Type of GO	Amount GO	Cost
Graphitene	50g powder	£900
Abalonyx	50g GO within a 250G AW-GO paste	$160 (~£126)
Sigma Aldirch (Merck)	250g powder (GNP-A500)	£183 (50g = ~£45)

GO supplied by Graphitene came pre-dispersed in DMF and water, custom made for this particular project as opposed to the typical powder formation. Three other GOs were investigated from Abalonyx, these were water wet GO (WW-GO), acid wet GO (AW-GO), basic wet BW-GO. These three GOs were produced by a proprietary modified Hummers method, AW-GO was stored directly as a paste and underwent no additional treatments while BW-GO is hydrochloric acid (HCl) free, and ammonia is added. WW-GO was washed with HCl-solution, stored as aqueous acidic paste then extensively washed with deionized water. This study looked at three different types to assess whether a more acidic, basic, or neutral processing affected the dispersion of GO and the subsequent properties.

Graphene and GO are complex to synthesise/isolate, costly to produce and have difficulties being mass produced. To overcome these issues, GNPs are a low-cost alternative due to being easier to manufacture as they have a few graphite layers, which can vary in thickness from 0.7 to 100 nm, as opposed to Graphene or GO, which are less than 10 graphene layers thick (1 graphene layer is 0.3 nm).[144] As a more cost-effective solution, two different types of GNPs were also investigated in this study. GNP-A120 and GNP-A500, they are almost identical however A500 has a larger surface area (~ 3x larger than A120).

Due to these reasons a range of GOs and GNPs from three different manufacturers, Graphitene, Abalonyx and Sigma-Aldrich were chosen for this study. GO was chosen, despite a potential reduction in properties due to the processing, in the hopes the oxidised surface would aid in dispersing the nanofiller into the Mono_PU matrix. The oxidation of graphene helps prevent re-stacking of the graphene layers. Furthermore, it was hoped the oxidised surface may be more compatible with Mono_PU due to matching the polarity of the polymer.

GO and GNP were used at a lower wt. % compared to clay nanofillers for several reasons; the cost of graphene is significantly higher than layered silicates, the GO and GNP may create a more viscous suspension due to their thinner layers increasing surface area thus making practical processing challenging and the literature often presents GO used at low wt. % of 0.1-0.5 wt. %.[27,33,44,145,146]

5.2 Characterisation of Mono_PU/GO and GNP Nanocomposite Membranes

Mono_PU/GO and GNP membranes have been characterised using various techniques which have subsequently been divided into three overarching categories: morphology and structure, barrier properties and mechanical properties. The characterisation techniques within each section will be discussed separately but also in combination with one another were necessary. The first section of this chapter focuses on the dispersion of GO and GNP within Mono_PU matrix and the effect these nanofillers have upon the polymer's morphology and structure. The latter sections will explore the effects of GO and GNP on the wettability, breathability, and mechanical properties of Mono_PU.

5.2.1 Morphology and Structure

Two techniques were utilised to assess the dispersion of GO and GNP within the Mono_PU matrix; these were X-ray powder diffraction (XRD) and attenuated total reflection - Fourier-transform infrared spectroscopy (ATR-FTIR). It is useful to know and understand how well GO or GNP at a specific concentration are dispersed within Mono_PU when assessing their effects on mechanical and barrier properties. The effect of the nanofillers on surface topology and roughness were investigated using scanning

electron microscopy (SEM) and focus-variation microscopy (FVM) on the upper membrane surface.

5.2.1.1 X-ray Powder Diffraction

X-ray powder diffraction (XRD) was used to assess how dispersed GO and GNP were within the Mono_PU matrix. Figures 48 and 49 show the XRD traces of Mono_PU/GO and GNP nanocomposite membranes at 0.1, 0.3 and 0.5 wt. % compared against Mono_PU, Mono_PU_Con, GO/GNP powders and GO/GNP powders dispersed in DMF and dried. All samples which contain Mono_PU produce a broad reflection at 19.9 °2θ which corresponds to the amorphousness and the 110 crystalline planes for PU.[147]

XRD investigations on GO samples within the literature and this thesis, suggests the d_{001} of GO, GNPs and rGO varies depending on the type of GO, the production method and supplier. One paper found GO had a d_{001} at 9.98 °2θ and a d_{002} at 42.26 °2θ.[148] Another paper only saw one reflection at 11.0 °2θ for GO.[149] Within this study two major reflections are exhibited in XRD analysis of graphene related materials. A reflection at ~26/27°2θ is indicative of graphite while a reflection at ~10/11°2θ is indicative of GO, both of which correspond to the d_{001} reflection. The diffraction shift from 27°2θ to 10°2θ occurs due to the interlayer space increasing through the oxidation of graphite to form GO.[150] While d-spacing and Bragg's Equation (Eq. 2 Section 3.5.1.1) are related to the exfoliation of nanofillers within a polymer matrix; the Scherrer equation relates to the XRD peak position (Eq. 6). The peak width at half maximum relates to the number of crystallite layers, as the peak width increases the crystallite size decreases.[151] Dr. Ronak Janani analysed several kinds of the GOs and GNPs within this study and found GO had ~ 5 crystallite layers while the GNPs averaged 40-50 crystallite layers, with GNP-120 having slightly fewer crystallite layers compared to GNP-500. Due to this, GO can be defined as few layer graphene (3-10 layers) while GNPs are closer to graphite.[145] This is reflected in the price of GO which is 20 times the prices of GNP's for 50 g powder.

GO displays a reflection at 11.4 °2θ, when incorporated into Mono_PU this reflection is no longer present which may indicate good dispersion into Mono_PU at all three concentrations.

WW-GO presents a strong reflection at 11.1 °2θ when DMF is added the reflection shifts left slightly to 10.8 °2θ, when mixed with Mono_PU this reflection is no longer present, indicating good dispersion.

AW-GO has a strong reflection at 10.5°2θ and has a shoulder at 10.9°2θ when mixed with DMF the reflection shifts slightly left to 10.2°2θ. When AW-GO is incorporated into Mono_PU a small reflection is present at 10.7°2θ for AW-GO at 0.1 and 0.3 wt. % and at 10.9°2θ for AW-GO at 0.5 wt. %. As concentration increases the reflections increase in intensity and broadness. This indicates the AW-GO is not as well dispersed as WW-GO or GO.

GNP-A120 has a strong reflection at 30.8°2θ, when mixed with DMF and dried the reflection shifts to a lower angle of 26.8°2θ and reduces in intensity; both reflections indicate graphite-like structures.[150,152] Combined with Mono_PU the GNP-A120 causes reflections at all three concentrations at 26.8°2θ. As concentration increases the reflection increases in intensity. Since graphite has a reflection at 26.8°2θ this shows a phase separated system.

GNP-A500 produces a broader less intense reflection compared to GNP-A120 due to it having a larger surface area and poorer order of platelets. As a powder GNP-A500 produced a strong reflection at 30.8°2θ, this also shifted to 26.8°2θ when incorporated with DMF. It is unusual for graphene to display a reflection at ~30°2θ but has been reported.[153] When dispersed into Mono_PU, a small reflection is present at 26.8°2θ for all three concentrations, indicating a phase separated/microcomposite dispersion in Mono_PU.

Under a light microscope, small black spots were visible for both GNP samples, the number of black spots increased as concentration increased. It was confirmed these specs were poorly dispersed GNP agglomerates which are supported by the XRD traces.

It should be noted that another GO sample, BW-GO from Abalonyx was explored; however, after casting Mono_PU/BW-GO 0.1 wt. % there were numerous visible aggregates of GO present in the sample. These visible aggregates were far more numerous and larger in size than those observed for GNP samples at 0.5 wt. %. Due to

this the sample was not analysed and studies on BW-GO at higher concentrations were abandoned.

Although it appears that GO, WW-GO, and AW-GO dispersed well within Mono_PU it is possible that XRD is not sensitive enough to detect such low amounts thus appearing dispersed when samples might be a microcomposite. However, GNP samples have similar intensities as a powder to GO samples, but when dispersed in Mono_PU at the same concentrations, the d-spacing reflection can still be observed. Although GNP varies slightly to GO this does offer some confidence that GO, WW-GO and AW-GO are better dispersed than GNP.

Equation 6. Scherrer Equation.[154]

$$\boldsymbol{FWHM} = (\boldsymbol{k}\,\boldsymbol{X}\,\boldsymbol{\lambda})/(\boldsymbol{D}\,\boldsymbol{X}\,\boldsymbol{cos\theta})$$

- FWHM is the full width at half-maximum of the diffraction peak.
- k is a shape constant
- D is the crystallite size
- Cos$\boldsymbol{\theta}$ is the Bragg angle.

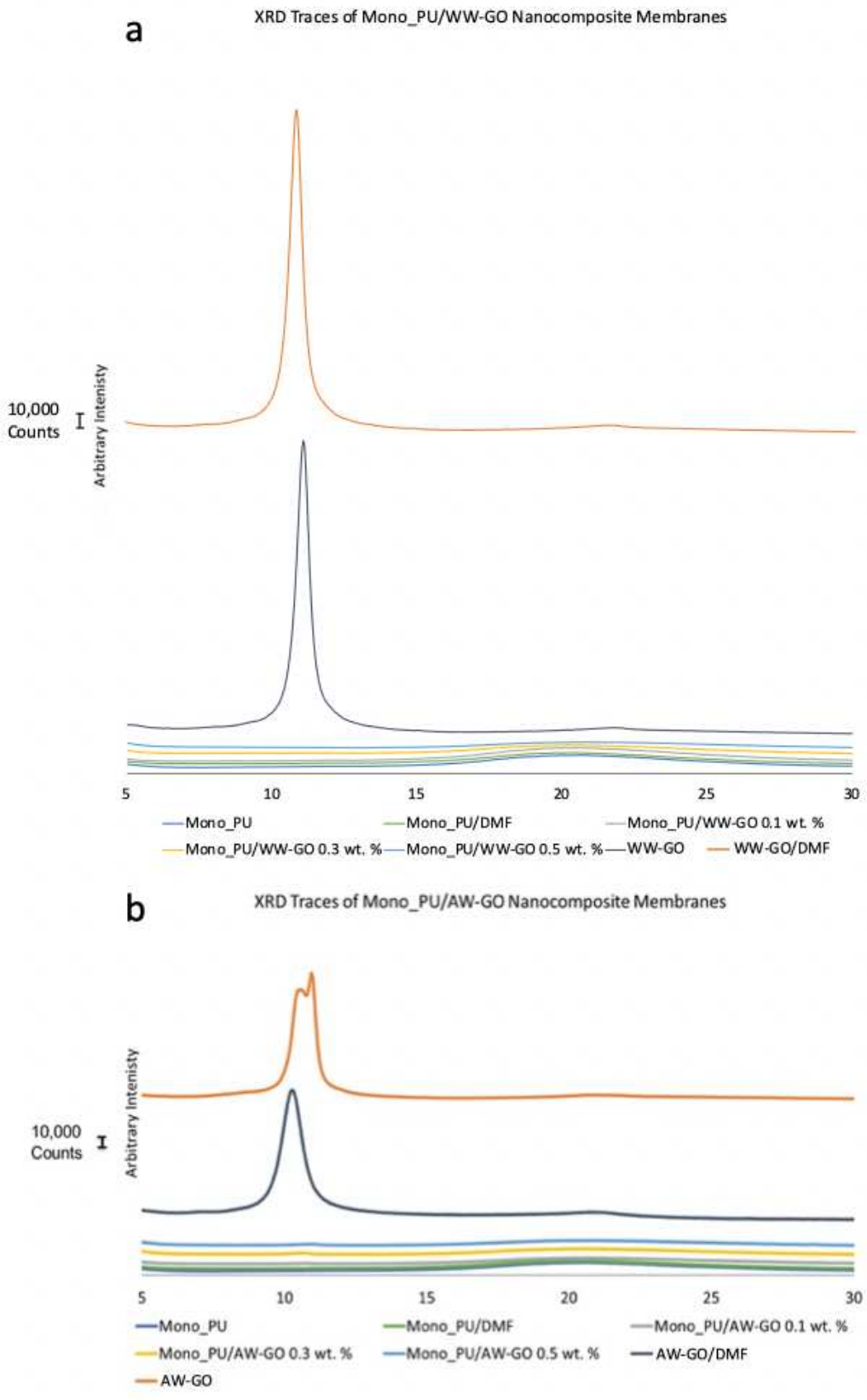

Figure 48. XRD traces of Mono_PU/GO and GNP nanocomposite membranes a) Mono_PU/WW_GO b) Mono_PU/AW_GO. The X-axis for both graphs is $2\theta(^{\circ})$.

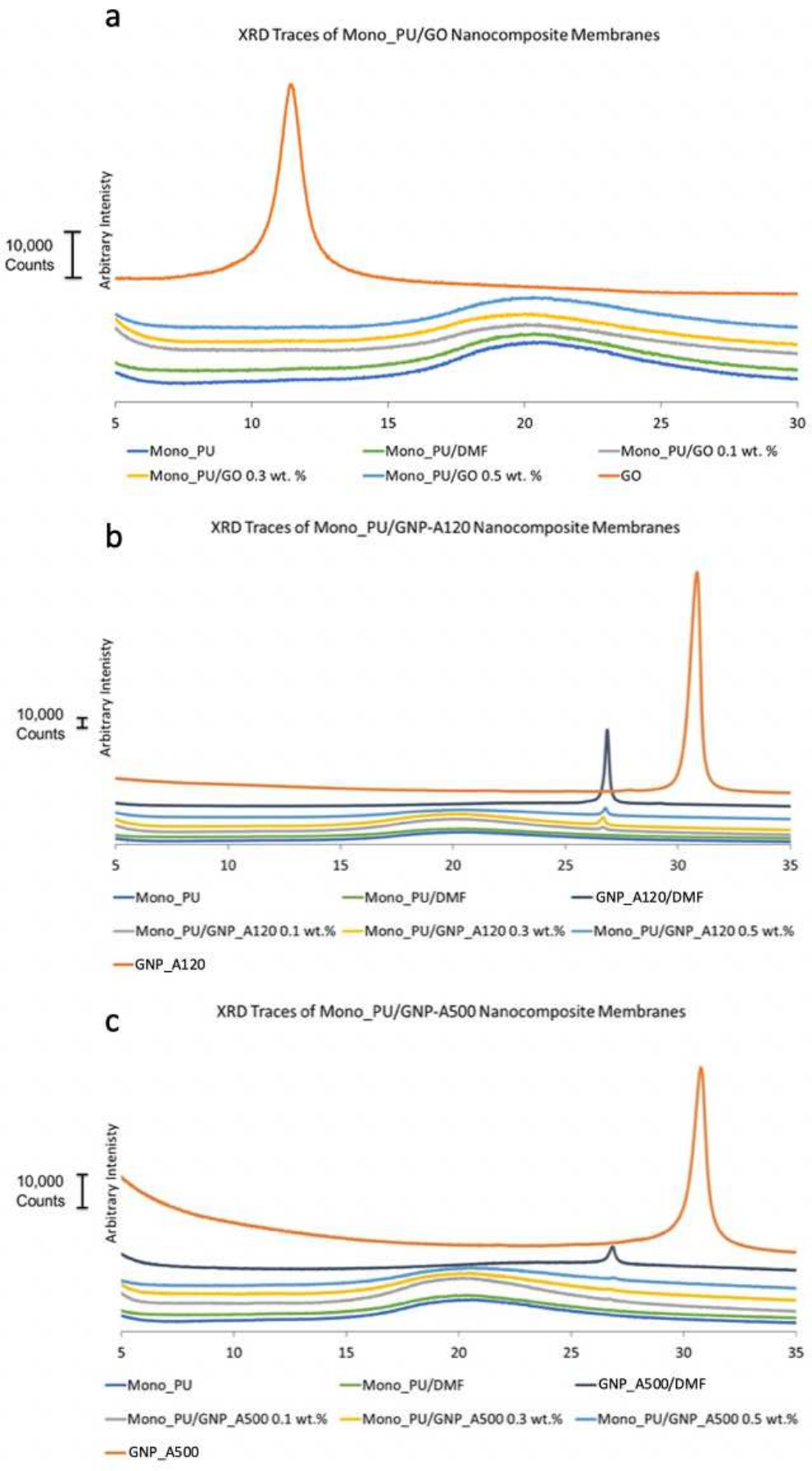

Figure 49. XRD traces of Mono_PU/GO and GNP nanocomposite membranes a) Mono_PU/GO b) Mono_PU/GNP-A120 c) Mono_PU/GNP-A500. The X-axis for these three graphs is $2\theta(^{\circ})$.

5.2.1.2 Attenuated Total Reflection - Fourier-Transform Infrared Spectroscopy

Attenuated Total Reflection - Fourier-Transform Infrared Spectroscopy (ATR-FTIR) was used in triplicate on all Mono_PU/GO and GNP membranes on both the upper and lower surfaces. However, no differences were observed, there were no spectral contributions from the nanofillers, and as such the data has not been included in this chapter.

5.2.1.3 Scanning Electron Microscopy

Scanning electron microscopy (SEM) was used to collect high resolution surface topography 2D images. Figure 50 presents backscattered SEM images of the upper surface of Mono_PU/GO and GNP membranes. The upper surface faced the atmosphere during preparation and was not in contact with the release paper. Mono_PU has a smooth topography and has no 'orange peel' effect, as seen in batch 1 of Mono_PU (Chapter 4 Fig. 32). The addition of DMF appears to have induced a very slight 'orange peel' effect for Mono_PU_Con which is likely due to the evaporation of more DMF during the drying process. This also occurred in Mono_PU batch 1 when additional DMF was added.

At 0.1 wt. % of GO the surface topography appears similar to Mono_PU_Con, however as concentration increases to 0.3 and 0.5 wt. %, a 'flake' like surface develops. The surface appears rougher with what looks like sharp protrusions between ~ 5-15 µm in diameter.

The addition of WW-GO at 0.1 wt. % caused broad 'waviness' of the surface compared to Mono_PU and Mono_PU_Con. As the concentration of WW-GO increased to 0.3 wt. % the 'waviness' and 'orange peel' effect increased. At 0.5 wt. % the 'waviness' increased again this time producing a rolling hill type topography (like a bird's eye view of a mountain range), of between ~ 20 and 30 µm in diameter.

Addition of AW-GO produces a similar surface to WW-GO however it is significantly smoother, with minimal 'waviness' compared to WW-GO nanocomposites. The 'waviness' at 0.5 wt. % AW-GO reflects the same observed for 0.1 wt. % WW-GO.

The inclusion of A120 and A500 GNP do not affect the surface topography as much as the other nanofillers minus the appearance of a few bumps at higher concentrations.

However, A500 GNP at 0.1 wt.% appears to significantly increase the surface roughness forming many tiny bumps of ~1-2 µm in diameter upon the surface. The white specs and tiny bumps within GNP membranes may be poorly dispersed GNP agglomerates as noted that for both A120 and A500 samples as black spots present under a light microscope.

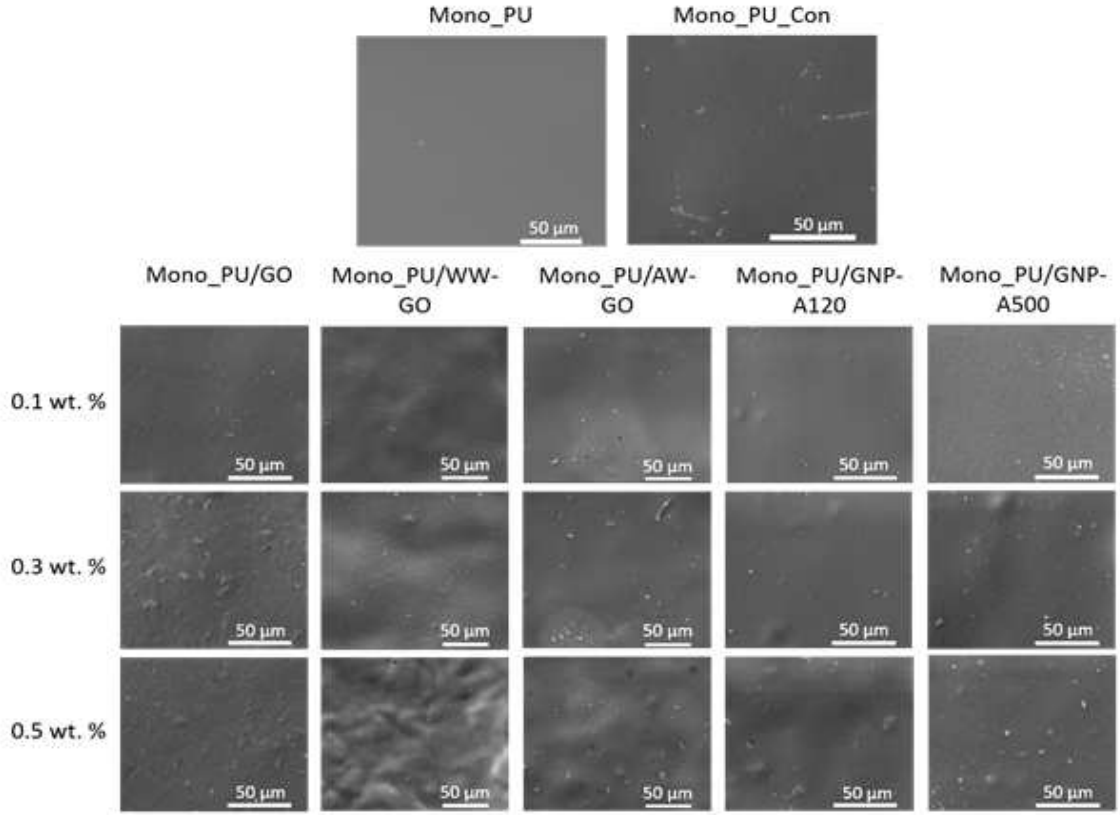

Figure 50. SEM images of upper surface topography of Mono_PU/GO and GNP nanocomposite membranes compared to Mono_PU and Mono_PU_Con.

5.2.1.4 Variant Focus Microscopy

Variant focus microscopy (VFM) was used to characterise, image, and quantify the macrosurface morphology and roughness of Mono_PU/GO and GNP nanocomposite membranes. Due to the sensitivity limitations of the equipment, areas of the sample were unable to be imaged due to their smoothness. Measuring samples as flat as Mono_PU/GO and GNP nanocomposite membranes pushed the equipment to its limits. For reference 2D VFM image area is roughly 3.1 times larger than SEM images.

As mentioned above the Mono_PU/GO and GNP membranes are easily identifiable as smoother than Mono_PU/clay membranes (Section 4.2.1.5) as the samples shown in

Figures 51 and 52 are missing a far greater portion of the image than the Mono_PU/clay samples.

Figures 53 and 54 presents the 3D surface maps and 3D pseudo coloured surface maps, respectively, of Mono_PU/GO and GNP nanocomposite samples imaged using VFM. To help analyse the 3D images shown below, each sample is converted into a 2D image and then processed using the VFM software. This removes edge effects and 'waviness' from the image which has been potentially added during sample preparation, i.e., the membrane not lying flat on its glass slide substrate. This processing allows for more accurate quantification of sample surface roughness. These 2D images and 2D pseudo-coloured images of Mono_PU/GO and GNP nanocomposites are shown in Figures 53 and 54, respectively.

Mono_PU and Mono_PU_Con both have a very smooth upper surface. The addition of the nanofillers causes some changes to the surface morphology. With the addition of GO, VFM analysis demonstrated a similar morphology as seen using SEM however the protrusions observed in 0.3 and 0.5 wt. % GO shown in the SEM images are not observed with the VFM images. This may be due to the reduced magnification of the VFM which presents a larger surface area than SEM images. 3D and 2D VFM images are 268 x 200 µm, making the total area 53,600 μm^2 while SEM images are 141 x 122 µm, an area of 17,202 μm^2. The image area of VFM is ~ 3.1 times larger than SEM images. The resolution of VFM is not great enough to distinguish these protrusions.

The VFM images appeared similar to those obtained from SEM with the addition of WW-GO. 'Waviness' is present for all concentrations using both techniques. However, there is a greater appearance of 'waviness' in the VFM image compared to SEM again due to the difference in scale. The addition of WW-GO has had a significant difference upon the surface morphology of Mono_PU, creating a more textured surface with rolling 'hills'.

VFM images of Mono_PU/AW-GO at 0.1 and 0.5 wt. % both present a textured 'wavy' surface but to a lesser degree than the Mono_PU/WW-GO samples. AW-GO 0.1 wt. % appears 'wavy' under VFM but not SEM, it is likely the waviness is present on a larger scale which is only identified under VFM. However, the VFM image for Mono_PU/AW-

GO 0.3 wt. % does not show a 'wavy' topography but instead has a textured 'bumpy' surface which was not observed under SEM.

Similarities were present between the VFM and SEM images of A120 samples, large 'bumps' were present at 0.3 and 0.5 wt. % using both imaging techniques.

The inclusion of A500 produced a similar texture at 0.1 wt. % for both imaging techniques. It appears the 'bumps' present in SEM images of 0.3 and 0.5 wt. % SEM may also be present within VFM however significant portions of the sample could not be imaged using VFM making interpretation difficult.

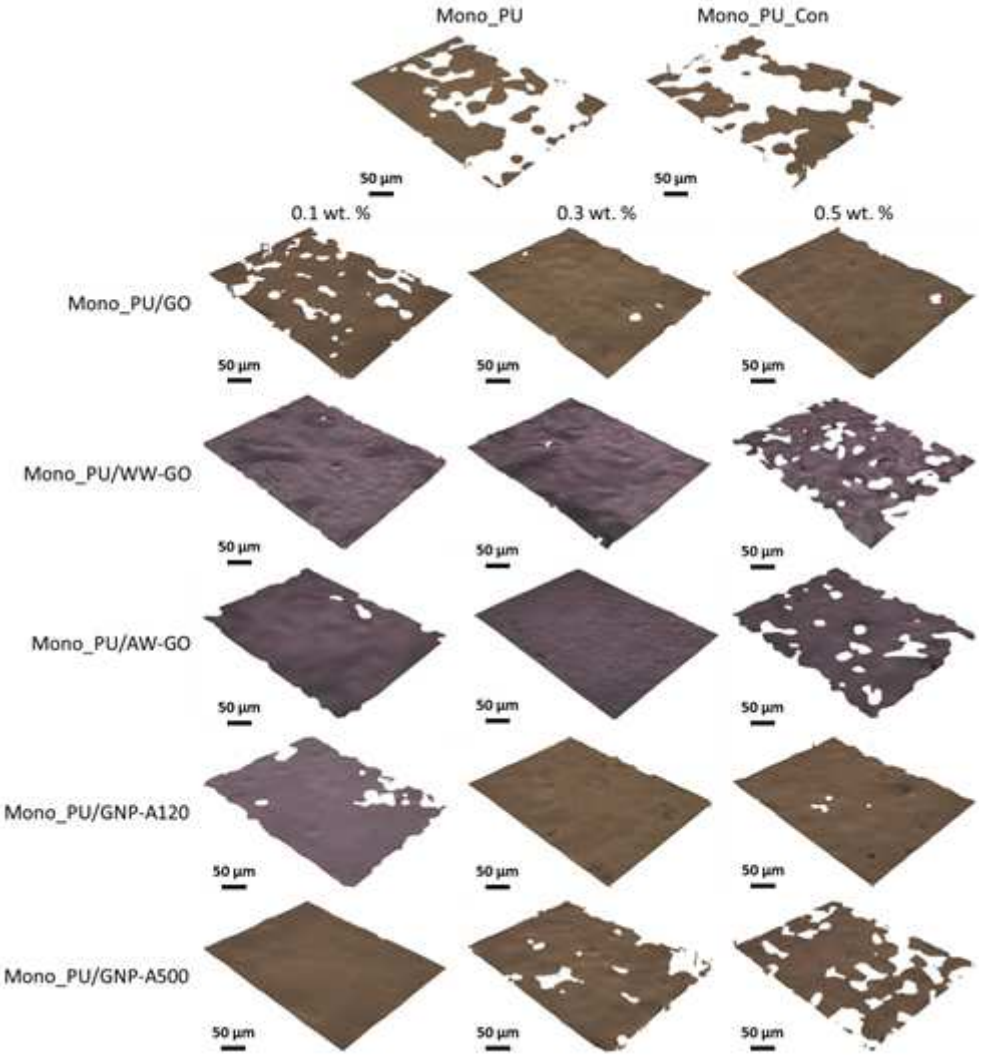

Figure 51. 3D images of Mono_PU/GO and GNP nanocomposite membrane upper surface. Scale bar is 50 µm. Image dimensions are 268 x 200 µm. Z-axis varies depending on surface topography.

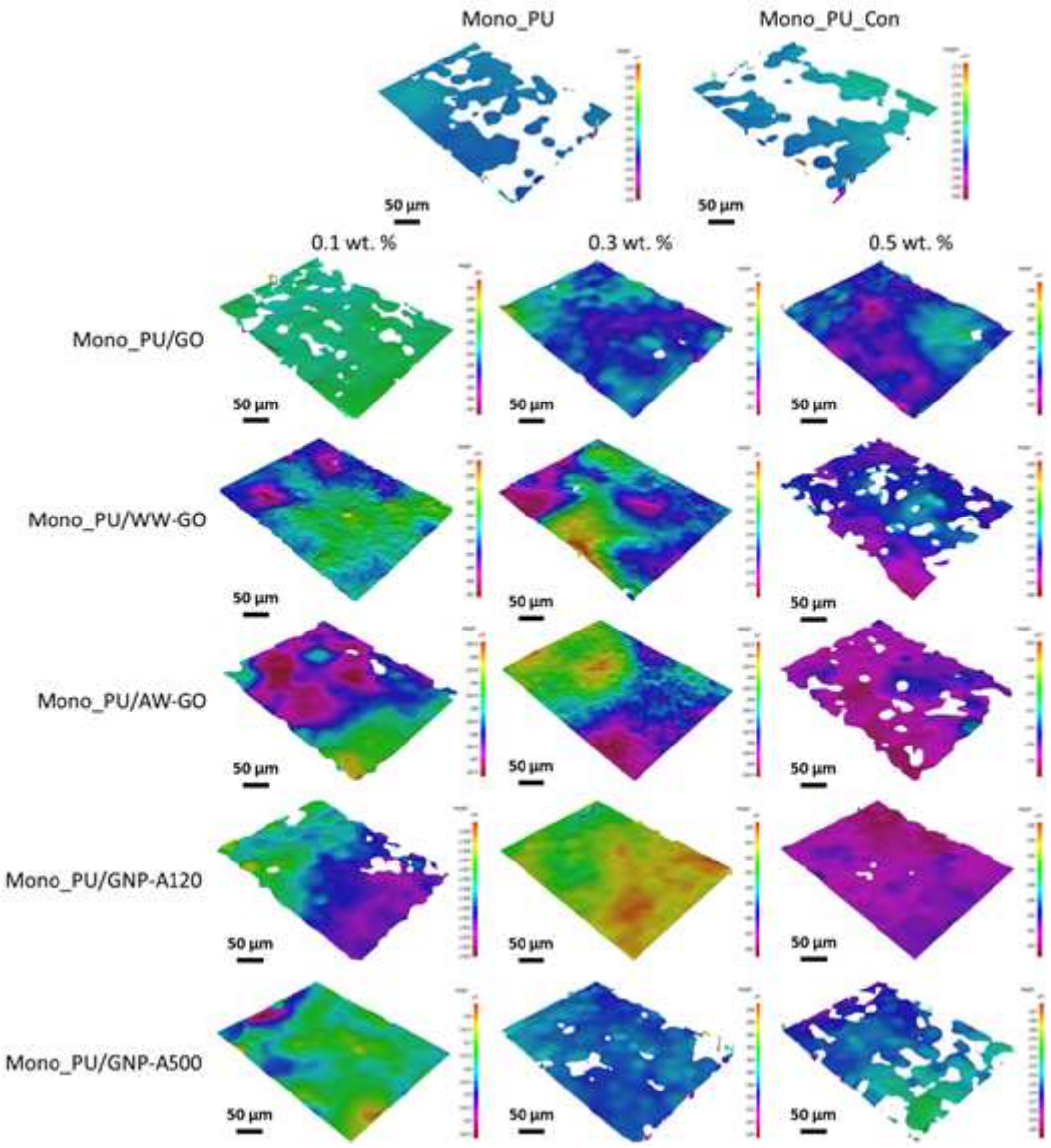

Figure 52. Pseudo coloured 3D images of Figure 51. Scale bar is 50 µm. Image dimensions are 268 x 200 µm. Z-axis varies depending on surface topography. *N.B.* The scale for each image varies and should be noted before comparing samples based solely on the pseudo colouring.

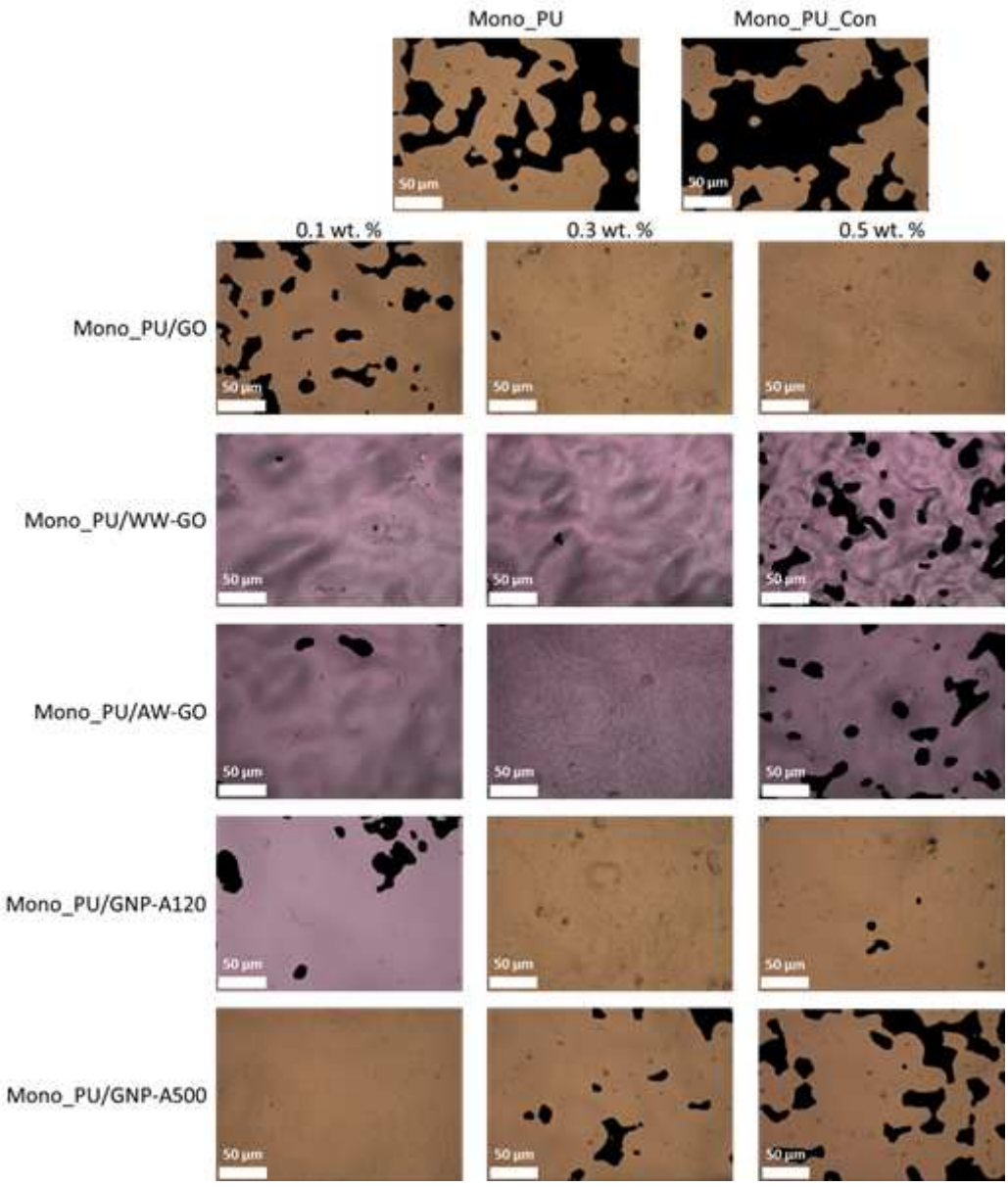

Figure 53. 2D images of all Mono_PU/GO and GNP nanocomposite membranes processed to remove edge effects and 'waviness' incurred during sample preparation prior to measuring the surface roughness. Scale bar is 50 µm.

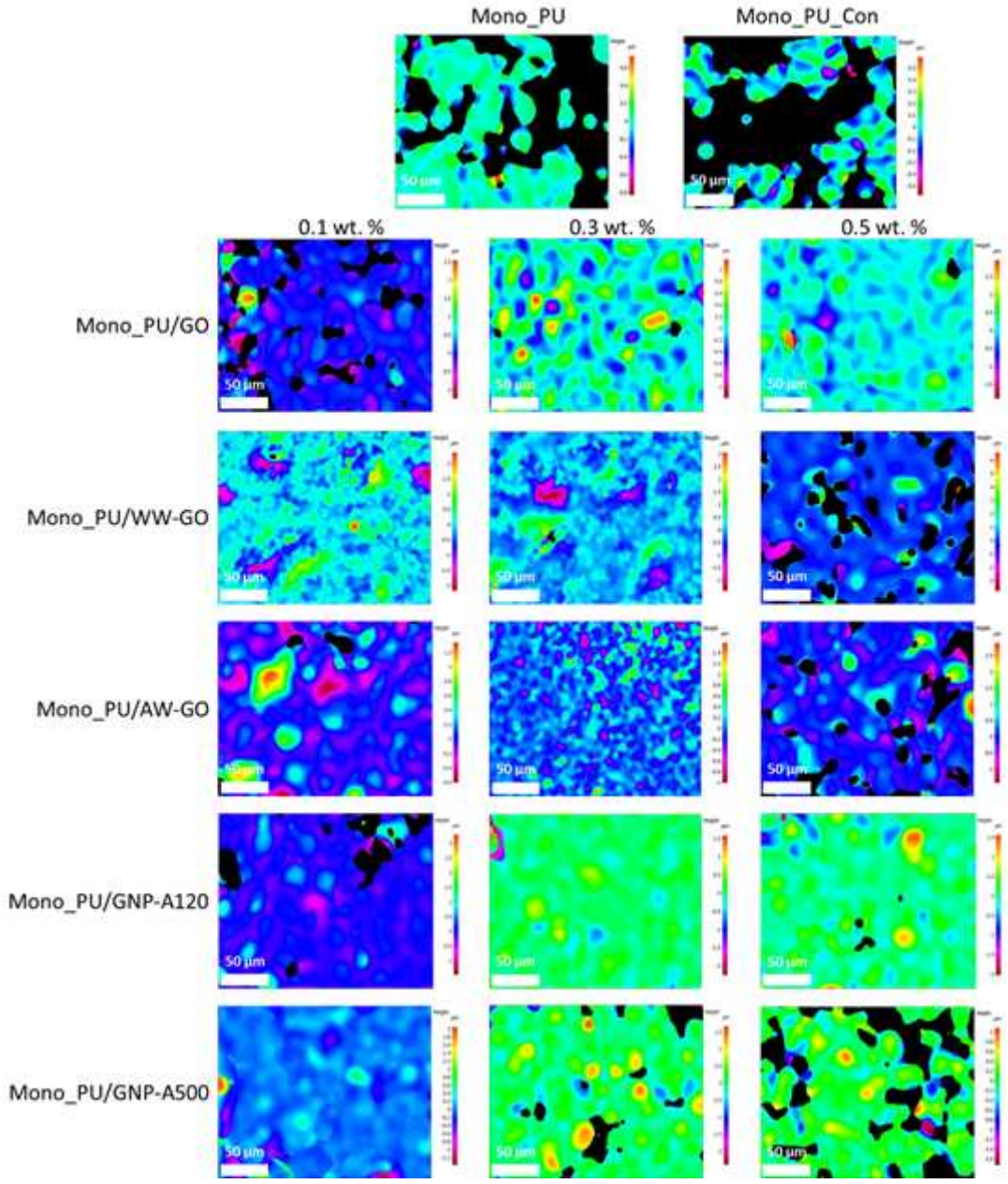

Figure 54. Pseudo coloured 2D images of Figure 53. Scale bar is 50 µm. *N.B.* The scale for each image varies and should be noted before comparing samples based solely on the pseudo colouring.

Figure 55 shows the surface roughness values obtained from VFM imaging of Mono_PU/GO and GNP nanocomposite membranes. Mono_PU has an *Sq* value of 0.10 µm and Mono_PU_Con has an *Sq* value of 0.12 µm. It should be noted that when holes are present within a VFM image, edge effects can occur around the outer edge of the holes which may affect surface roughness measurements.

The addition of GO caused the surface roughness to increase to 0.29 µm at 0.1 wt. % GO. At higher concentrations of GO the *Sq* value decreased slightly. WW-GO produced the largest increase in surface roughness out of all the nanofillers. At 0.1 and 0.3 wt. %

WW-GO the *Sq* value was 0.44 μm. An *Sq* value of 0.64 μm, a 420% increase compared to Mono_PU_Con was observed for 0.5 wt. % WW-GO, the largest difference of all samples. This is likely related to the 'wavy' topography seen in both SEM and VFM images.

AW-GO also increased the surface roughness, with 0.5 wt. % causing an increase of 0.27 μm compared to Mono_PU_Con. The inclusion of GNP-A120 caused a similar increase in surface roughness as GO of between 0.23 and 0.26 μm depending on concentration. GNP-A500 at 0.1 wt. % produced the same *Sq* value (0.20 μm) as AW-GO 0.3 wt. %, the smallest change compared to Mono_PU_Con.

The *Sq* values appear to reflect the VFM and SEM images, with GO, GNP-A120 and GNP-A500 causing slight changes to the surface topography and thus increasing the surface roughness slightly. While WW-GO produced visually rougher topography as well as increasing the *Sq* values the most. However, AW-GO despite producing a surface topography similar to WW-GO the *Sq* values were similar to the other nanofillers.

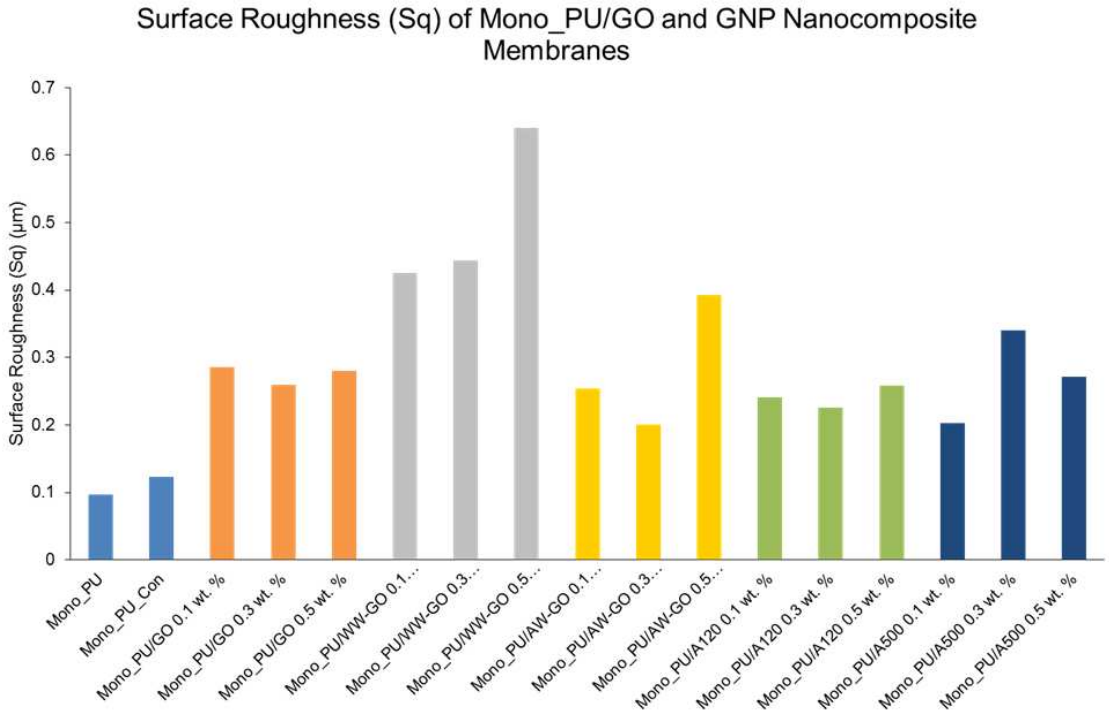

Figure 55. Surface roughness measurements (*Sq*) of Mono_PU/GO and GNP nanocomposite membranes obtained from VFM imaging.

5.2.2 Barrier Properties

Mono_PU is a barrier membrane often used in protective outdoor apparel; it must not be permeable to water but remain breathable and comfortable. To understand how the GO and GNP nanofillers have affected the barrier properties of Mono_PU, three tests have been carried out, these are contact angle, hydrostatic head, and water vapour transmission rates (WVTR).

5.2.2.1 Contact Angle

Contact angle measurements were used to assess the wettability of the Mono_PU/GO and GNP membranes. Samples were measured in triplicate and the average and standard deviation calculated (Fig. 56). As previously stated, the differences between batch 1 and 2 of Mono_PU has resulted in Mono_PU batch 2 having a contact angle of 75° this is 7° greater than Mono_PU batch 1 at 68°. Mono_PU_Con has a contact angle of 73°. The addition of GO and GNP nanofillers did not significantly increase or decrease the contact angle compared to Mono_PU_Con. Largest increase was by 4° by WW-GO 0.1 wt. % compared to Mono_PU_Con. While both AW-GO 0.1 wt. % and GNP-A120 0.1 wt. % caused a decrease of 1° compared to Mono_PU_Con.

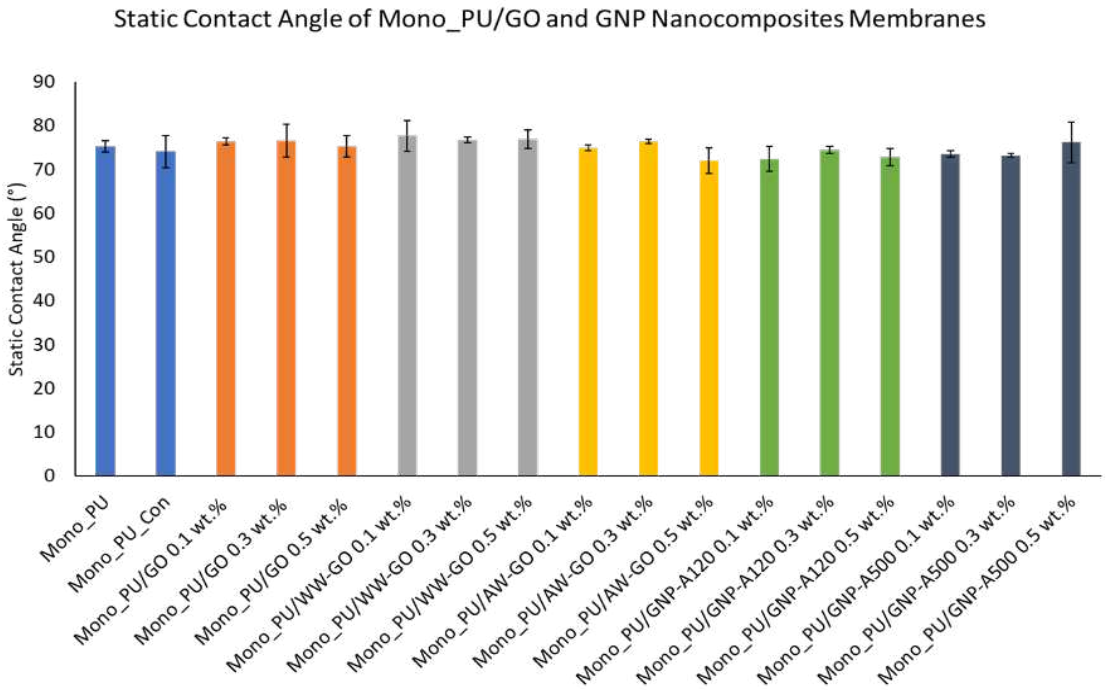

Figure 56. Average contact angle measurements with standard deviation for Mono_PU/GO and GNP nanocomposite membranes (measured in triplicate).

5.2.2.2 Hydrostatic Head

Selected samples were chosen to undergo a hydrostatic head test in order to understand the nanofillers effect on Mono_PU's waterproofness. Mono_PU/GO and WW-GO samples at 0.1, 0.3 and 0.5 wt. % were chosen for hydrostatic head testing due to relatively good dispersion observed in XRD analysis and unusual surface topography observed for WW-GO in SEM and VFM analysis. It should be noted that due to the limited quantity of sample this test was only performed once (Fig. 57). As previously mentioned, (Section 4.2.2.2) hydrostatic head tests are not known for good repeatability.

Mono_PU_Con had a hydrostatic head value of 10,020 mm; the addition of GO caused a decrease in hydrostatic head at all three concentrations. GO at 0.1 and 0.3 wt. % reduced the hydrostatic head value by half compared to Mono_PU_Con, however at 0.5 wt. % GO the decreased waterproofness was smaller at 22%.

The addition of WW-GO at 0.1 and 0.5 wt. % again decreased the hydrostatic head value of Mono_PU. With a drastic decrease of 99% occurring at 0.5 wt. %, which is possible due to an air bubble or pin hole in the film. WW-GO at 0.3 wt. % is the only sample to cause an increase in hydrostatic head of 89%, increasing the waterproofness from 10,020mm to 18,920mm. As per the categorisation of hydrostatic head values and degree of waterproofness detailed in (Section 4.2.2.2) Mono_PU_Con would be considered waterproof and Mono_PU/WW-GO 0.3 wt. % a high-quality waterproof membrane suitable for aggressive conditions.

However, as previously stated due to the small-scale casting method to produce these samples air bubbles may be present which limits the reproducibility of hydrostatic head tests. As such the values discussed here are merely a suggestion of the potential effects of the nanofillers on Mono_PU.

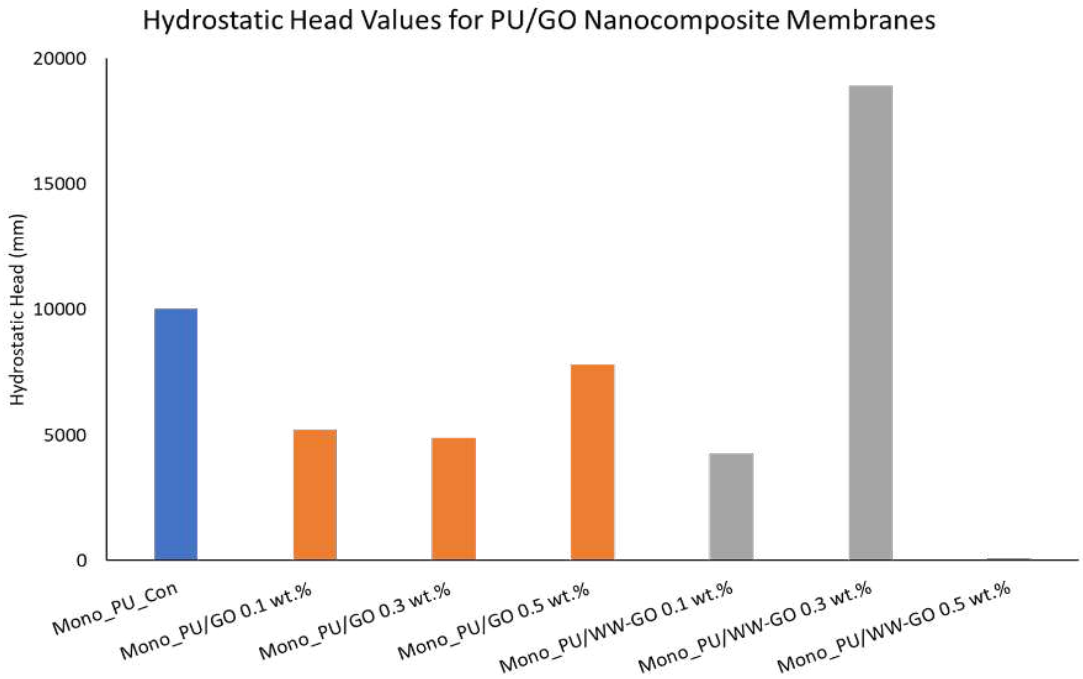

Figure 57. Hydrostatic head values for Mono_PU/GO and GNP nanocomposite membranes.

5.2.2.3 Water Vapour Transmission Rates

Water vapour transmission rate measurements were taken for Mono_PU/GO and GNP membranes to assess the nanofiller effect on Mono_PU breathability (Fig. 58). The WVTR of Mono_PU was 967 g/m^2/24hrs, this increased slightly to 1048 g/m^2/24hrs for Mono_PU_Con, however this increase is not significant. The inclusion of GO and GNP nanofillers caused a decrease in breathability for all samples, this was expected due to the tortuosity effect where the nanofillers act as physical blockade to the pathway of water vapour diffusion through the membrane as discussed in Section 4.2.2.3.

The addition of GO at 0.1 wt. % caused a decrease of 23% in WVTR compared to Mono_PU_Con. As concentration of GO increased the WVTR decreased, this can be expected due to the tortuosity effect. At 0.5 wt. % GO a 56 % decrease in WVTR was observed.

As the concentration of WW-GO increased the WVTR decreased, however not in relation to nanofiller concentration. 0.3 wt. % WW-GO caused a 16% decrease, the 3rd lowest out of all samples, although the standard deviation shows there was significant variation in WVTR values.

At the lower wt. % of AW-GO only relatively small decreases in WVTR were seen, 18% and 11% for 0.1 and 0.3 wt. % AW-GO. Again, a large standard deviation at 0.3 wt. % was seen. At 0.5 wt. % however a significant decrease of 42% was observed.

The addition of GNP-A120 resulted in the most similar WVTR measurements compared to other GO and GNP nanofillers in this study. WVTR measurements ranging from 21% to 34% decrease compared to Mono_PU_Con. As concentration increases, WVTR decreases, as expected.

Similar to the majority of other samples as concentration of GNP-A500 increased the WVTR decreased. At 0.1 wt. % GNP-A500 the smallest decrease of 8% in WVTR was observed compared to Mono_PU_Con, this decreased further to 32% at 0.5 wt. % GNP-A500.

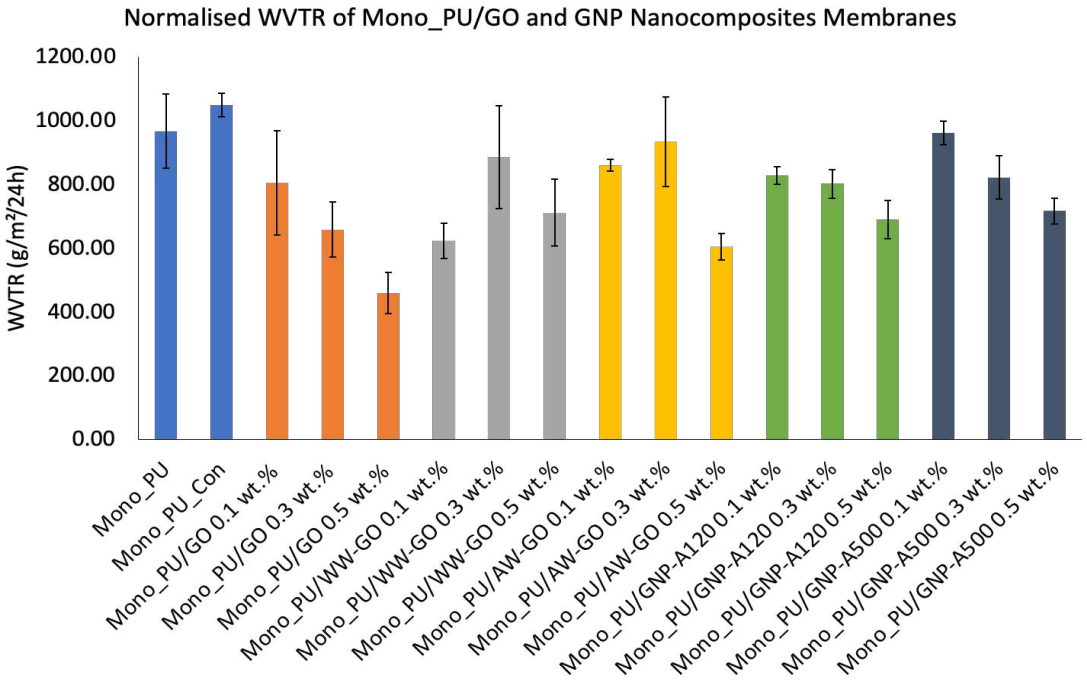

Figure 58. Average WVTR measurements of Mono_PU/GO and GNP nanocomposite membranes with standard deviation (measured in triplicate). WVTR values were normalised to average membrane thickness.

5.2.3 Mechanical, Thermal and Antistatic Properties

Four different techniques, differential scanning calorimetry (DSC), dynamic mechanical analysis (DMA), tensile strength and antistatic testing were used to analyse the mechanical, thermal, and antistatic properties of Mono_PU/GO and GNP nanocomposite membranes. These techniques provided information on how the

nanofillers affected the membrane's glass transition temperature, crystallinity, storage modulus, Young's modulus, elongation at break, stress at peak and antistatic properties.

5.2.3.1 Differential Scanning Calorimetry

Differential scanning calorimetry (DSC) was used to assess the melting events of Mono_PU/GO and GNP membranes. Similar to the Mono_PU/Clay nanocomposite membranes, three melting events were observed for Mono_PU/GO and GNP nanocomposite membranes; the onset temperatures for these three melting events are displayed in Figure 59. For Mono_PU_Con T_{mI} occurred at 173°C, T_{mII} at 194°C and T_{mIII} at 201°C. Melting events of PU are dependent on several factors which are detailed in (Section 4.2.3.1). All three melting events (T_{mI} - T_{mIII}) were observed for all Mono_PU/GO and GNP nanocomposites and only small changes in the onset temperature were observed. There were very few temperature changes for T_{mII} and T_{mIII} events, and the majority of temperature fluctuations occurred in T_{mI}.

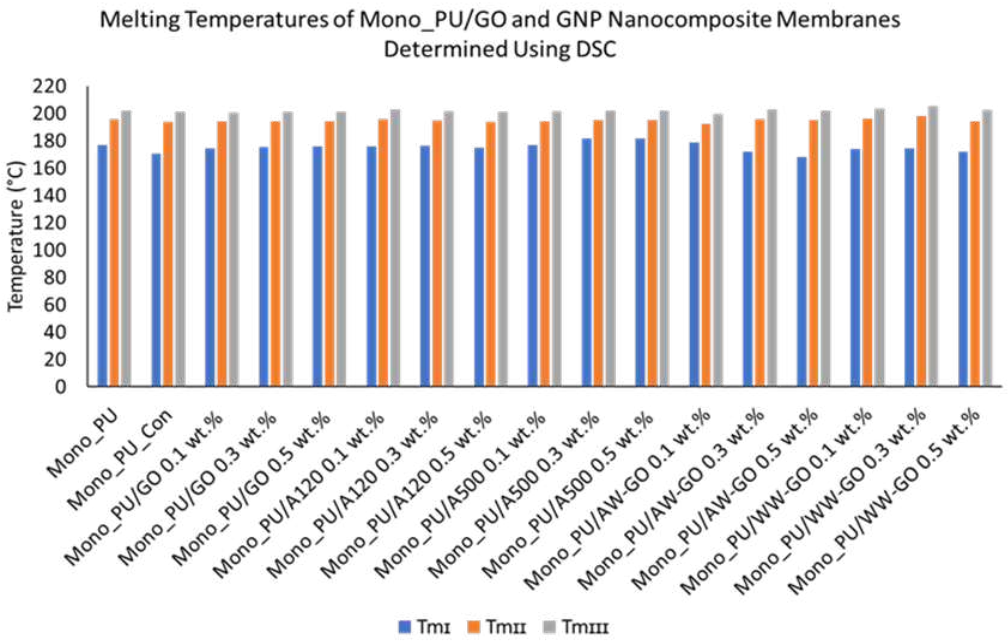

Figure 59. DSC melting temperatures of Mono_PU/GO and GNP nanocomposite membranes.

5.2.3.2 Dynamic Mechanical Analysis

DMA was performed from -100°C to 120°C to observe the storage modulus values at -5°C and 40°C and assess the T_g (S) and T_g (H) values. Additional explanation is within Section 4.2.3.1.

Similarly, to Section 4.2.3.1 the addition of GO or GNP nanofillers did not produce any significant trends or changes with regards to nanofiller type or concentration for storage modulus or T_g (S) and T_g (H) values.

5.2.3.3 Tensile Testing

Young's modulus, elongation at break and yield stress was obtained via tensile testing of the Mono_PU/GO and GNP nanocomposites (Fig. 60). Due to limited sample quantity and time, tensile testing was only conducted on GO and WW-GO samples.

Mono_PU_Con has Young's modulus of 1.4 MPa, an elongation at break of 192.1 mm and a yield strength of 47.6 N/mm^2. The addition of nanofillers caused no significant difference in the Young's modulus, elongation at break or yield stress of Mono_PU_Con.

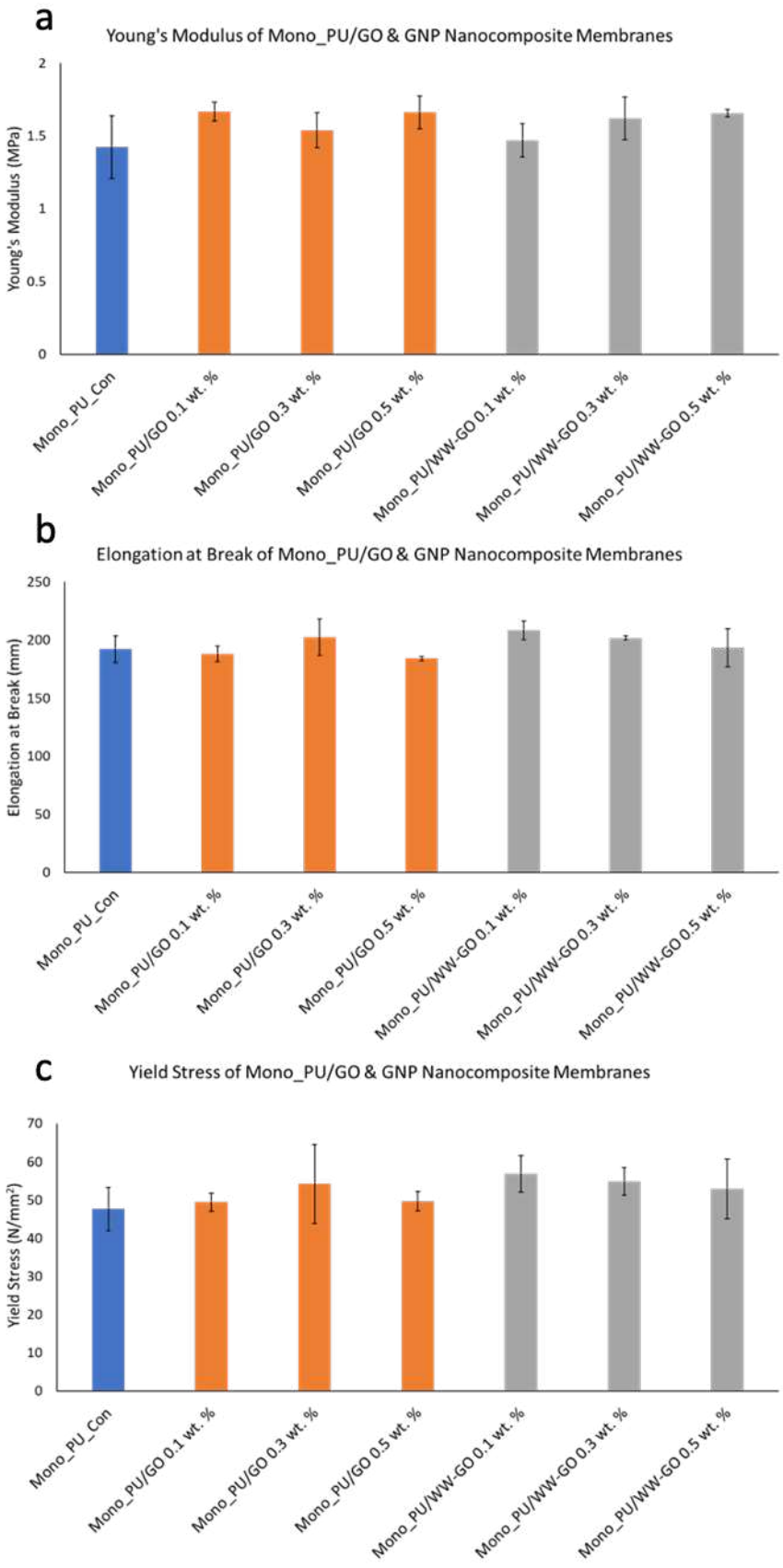

Figure 60. Average tensile measurements with standard deviation (measured in triplicate) of Mono_PU/GO and GNP nanocomposite membranes. a) Young's modulus, (b) elongation at break, (c) Yield stress

5.2.3.4 Antistatic Properties

Mono_PU membranes with antistatic properties are useful for several reasons outlined in Section 4.2.3.4. The antistatic properties of Mono_PU/GO and WW-GO nanocomposite membranes at 0.1, 0.3 and 0.5 wt. % were measured in Ohms per centimetre (Ω^{-cm}) using an Antistat^{TM} surface resistance metre (Fig. 61). All Mono_PU/GO and WW-GO membranes registered as insulative.

Figure 61. Antistat^{TM} surface resistance metre for measuring antistatic properties of Mono_PU/GO and WW-GO nanocomposite membranes.

5.3 Discussion

XRD analysis of Mono_PU/GO and GNP membranes found two major reflections, one at ~26/27 °2θ, is indicative of graphite and another at ~10/11 °2θ, which is indicative of GO, both correspond to the d_{001} reflection. The diffraction shift from 27°2θ to 10°2θ occurs due to the interlayer space increasing through the oxidation of graphite to form GO.[150] This d_{001} reflection in all samples confirms that GO, WW_GO and AW-GO are graphene oxides while GNP-A120 and GNP-A500 are mostly graphite.

Out of all five samples, GO dispersed the best with a fully exfoliated system likely due to being pre-dispersed by the company, Graphitene, in a mixture of DMF and a small amount of water. WW-GO was the next best dispersed nanofiller, again XRD indicated a fully exfoliated system. AW-GO showed evidence of non-dispersed GO likely an intercalated system. While GNP-500 and GNP-120 produced a micro-composite/phase separated system likely due to the difficulty of separating the layers within graphite. Further analysis of XRD data by a colleague found GO to have ~5 layers of graphene while GNP's have ~50+ layers of graphene thus explaining the difference in dispersion between nanofillers.

SEM imaging of Mono_PU batch 2 shows the membrane appears smoother than Mono_PU batch 1 and has no 'orange peel effect' compared to its batch 1 counterpart. Similar to Mono_PU_Con batch 1, the addition of DMF to Mono_PU batch 2 caused a slight increase in the 'orange peel effect'. The addition of GO at higher concentrations presents 'flake' like structures, and sharp protrusions. WW-GO and AW- GO presented samples that have a broad 'waviness' that increases in intensity with increasing concentration. The broad 'waviness' might have been caused by the dispersion of the nanofillers within the polymer causing stresses and strains as the film dried and shrinks. The GNPs had minimal effect on the broader surface topography. However, with higher concentrations of nanofillers small protrusions were observed and are believed to be resulting from small clumps of GNPs.

VFM imaging and the relevant data analysis was pushed to its limits when imaging Mono_PU/GO and GNP nanocomposites. For reference 2D VFM image area is roughly 3.1 times larger than SEM images. It is clear to see from the 3D VFM images that many samples resulted in 'holes' during imaging; this is likely due to the smoothness of these samples compared to other samples within this thesis Section 4.2.1.5 & Section 6.2.1.6. An investigation into VFM on polymer surfaces stated VFM resolution was not robust enough to identify nano-scale roughness of smooth polymer surfaces, this resulted in 'holes' within collected images.[78] Attempts to adjust parameters to collect the missing data results in heavy software manipulation of the images thus skewing the surface roughness results.[78,93] Due to this 'holes' within Mono_PU/GO and GNP VFM images were kept thus evidencing the limitations of VFM. Although this will have affected the surface roughness measurements Mono_PU/GO and GNP membranes. Edge effects can

occur around the outer edge of the 'holes' which has been shown to affect surface roughness measurements.[78] This explains why *Sq* values for Mono_PU and Mono_PU_Con batch 2 more than doubled compared to Mono_PU and Mono_PU_Con batch 1. Due to these edge effects detailed comparison between Mono_PU/GO and GNP membranes and Mono_PU or Micro_PU nanocomposite membranes should be avoided.[93]

This thesis demonstrates how VFM imaging of similar samples with slight variations in surface topography has led to different outputs. Imaging in Chapter 4 was mostly successful; however, analysis of the surface roughness did not directly correlate with what is visually observed with the VFM and SEM images. In this chapter imaging proved difficult, and as such the analysis may have been affected by edge effects of the 'missing image data'. In Chapter 6, VFM was more successful in imaging and analysing Micro_PU nanocomposites due to their porosity and increased surface texture.

The difficulty of imaging Mono_PU/GO and GNP membranes shows that despite progress in providing alternative quantitative and qualitative imaging and analysis of relatively flat polymer surfaces, this technique does have limitations which cannot currently be overcome.

Two different batches of Mono_PU were used Mono_PU batch 1 is explored in Chapter 4 and Mono_PU batch 2 in Chapter 5. A more detailed description of the minor difference between these batches caused by slightly different production routes can be found in Section 3.2.1. This difference in production has resulted in characterisation variations between Mono_PU in chapter 4 and Mono_PU in Chapter 5. With regards to contact angle Mono_PU batch 2 has a contact angle, of 75°, this is 7° greater than Mono_PU batch 1 at 68°. Despite a study by Ye *et al*., which found the addition of rGO to PU increased the contact angle, the addition of GO and GNP nanofillers to Mono_PU batch 2 did not affect the contact angle.[155]

The WVTR for batch 2 Mono_PU was 967 g/m^2/24hrs, this increased slightly to 1048 g/m^2/24hrs for Mono_PU_Con. Unlike the contact angle data, WVTR measurements between Mono_PU batches 1 and 2 remained similar averaging around 1000 g/m^2/24hrs. The inclusion of GO and GNP nanofillers caused a decrease in breathability for all samples, this was expected due to the tortuosity effect where the nanofillers act

as a physical blockade to the pathway of water vapour diffusion through the membrane as discussed in, Section 4.2.2.3.[135,146] The nanofillers GO, GNP-120 and GNP-500 all showed a trend of WVTR decreasing as nanofiller concentration increases, this is to be expected. However, the WW-GO and AW-GO showed WVTR initially decreased at 0.1 wt. %, before increasing at 0.3 wt. % and decreasing again at 0.5 wt. % this could be due to variations in how the nanofillers are dispersed and orient themselves within the membrane.[146]

Selected samples, Mono_PU/GO and WW-GO samples at 0.1, 0.3 and 0.5 wt. %, were chosen to undergo a hydrostatic head test in order to understand the nanofillers effect on Mono_PU's waterproofness. All but one sample showed a decrease in hydrostatic head value compared to Mono_PU_Con. The only sample that indicates an improvement in waterproofness is Mono_PU/WW-GO 0.3 wt. % with a hydrostatic head value of 18,920 mm this an 89% increase compared to Mono_PU_Con. A study by Bramhecha and Sheikh found cotton was permeable to water could be made impermeable by coating with 0.1 wt. % graphene paste, this produced a hydrostatic head value of more than 10,000 mm.[156] It should be noted that due to the limited quantity of sample this test was only performed once (Fig. 57). As previously mentioned in Section 4.2.2.2 hydrostatic head tests are not known for good repeatability and as such the results show promise, but it must be investigated further before drawing strong conclusions.

DSC data showed three melting events (T_{mI} - T_{mIII}) were observed for Mono_PU/GO and GNP nanocomposite membranes. Only small changes in the onset temperature were observed for all three events within the composites. The three melting events of Mono_PU/GO and GNP membranes consistently occurred at slightly higher temperatures when compared to Mono_PU/clay nanocomposite samples. GO and GNP nanofillers had no effect on temperature changes for T_{mII} and T_{mIII} events, with the majority of temperature fluctuations occurring in T_{mI} which is linked to the hard segments of PU which are relatively disordered, increased T_{mI} temperature suggests better ordering of the hard segments.[157] These slight differences in temperature in each melting event is similar to what was observed with clay nanofillers in Section 4.2.3.1.

No trends nor significant changes were identified for storage modulus or T_g. DMA analysis of both Mono_PU/clay nanocomposites and Mono_PU/GO and GNP nanocomposites has proved to be unfruitful.

Tensile testing of Mono_PU/GO and WW-GO membranes found the addition of GO and WW-GO had no significant difference on the Young's modulus, elongation at break or yield stress of Mono_PU_Con.

Unlike the surprising antistatic properties of Mono_PU/C20 at 3 and 5 wt. % in Chapter 4, the Mono_PU/GO and WW-GO membranes were found to be insulative. It shows there were no interconnecting, conducting networks of nanofillers present in the films.

5.4 Conclusions

GO and WW-GO dispersed the best within Mono_PU batch 2. SEM and VFM imaging and analysis of Mono_PU batch 2 indicated it is relatively smoother compared to Mono_PU batch 1 with a reduction in 'orange peel effect'. The addition of GO and GNP nanofillers did cause slight changes to the membrane surface topography however these were minimal compared to the addition of clay. VFM imaging proved particularly difficult, likely due to the smooth surface of the Mono_PU/GO and GNP membranes. As such the resulting edge effects of the 'holes' means analysis using VFM surface roughness is unreliable in this particular instance. However, understanding regarding the novel technique for relatively smooth transparent membranes has been improved.

Despite initial theories, an increase in surface roughness did not directly affect the wettability of the membranes, similar results were observed in Chapter 4. WVTR decreases as expected with the addition of nanofillers due to the tortuosity effect. The Hydrostatic head test increased for Mono_PU/WW-GO 0.3 % compared to control, indicating an increase in waterproofness. However, all other samples decreased, and no trends were observed.

No trends were observed for Mono_PU/GO and GNP nanocomposite membranes regarding melting events obtained by DSC or storage modulus and T_g obtained by DMA. Results were similar to those of Mono_PU/clay membranes (Sections 4.2.3.1 and 4.2.3.2). Unlike tensile and anti-static testing in Chapter 4, where some minor changes were observed due to the inclusion of clay, the tensile testing and anti-static testing indicated no changes with the addition of GO and WW-GO compared to Mono_PU.

Despite worldwide excitement regarding the novel use of GO and GNP nanofillers within PU matrices, this study found graphene nanofillers did not live up to the hype of the past decade. One major issue is due to the current popularity of graphene, many suppliers overestimate their product capabilities. It is a matter of finding the right matrix, processing, and application to realise the benefits they can offer. Often manufacturers market and sell their product as graphene however analysis often shows the nanofillers are closer to graphite than graphene.[158] This is in part due to the challenges facing large scale production of pure graphene. Within this study, GO, the closest nanofiller to pure graphene in terms of number of layers, dispersed the best. However, the addition of GO and GNPs did not impart any significant properties or improvements to the Mono_PU.

Chapter 6

Micro_PU/clay and GO Nanocomposites

6.1 Introduction

Microporous polyurethane (Micro_PU) is a specifically formulated PU, designed to produce a microporous membrane after submersion in a coagulation bath. Two types of Cloisite® clays (C20 and CNa^+) and two types of graphene oxides (GO) (water-wet GO (WW-GO) and GO) were selected from previous studies on monolithic PU (Mono_PU) membranes and were dispersed within the Micro_PU using a Dispermat® mixer. C20 was chosen due to good dispersion and all-around improvements to properties within Mono_PU. Although CNa^+ did not disperse well in Mono_PU, it was chosen due to providing an unusual surface topography (4.2.1.4) and has positive effects on Mono_PU properties such as providing the greatest decrease in wettability of Mono_PU (4.2.2.1). CNa^+ also serves as a comparator to C20 as a relatively poor disperser in PU. WW-GO and GO were selected due to their good dispersion in Mono_PU, both provided the best improvements in properties compared to other GO and graphene nanoplatelets' (GNP) studied (Chapter 5). The Micro_PU nanocomposite membranes were formed at PIL Membranes and characterised at SHU. This chapter explores how the addition of these various nanofillers affected the porosity, surface topography and roughness, as well as the membranes' barrier and mechanical properties. Specific interest was taken in assessing if changes to the porous structure and membrane surface directly impacted the breathability and wettability of the membrane.

6.2 Characterisation of Polyurethane Nanofiller Nanocomposites Membranes

Several techniques have been used to characterise the Micro_PU nanocomposite membranes, which have been divided into three main sections: morphology and structure, barrier properties and mechanical properties. Within each section the characterisation techniques are discussed separately but also in combination with one another where necessary. The first section of this chapter, 'Morphology and Structure' focuses on how successfully the nanofillers were dispersed into the Micro_PU matrix

and the effect they have upon the polymer's morphology and structure, in particular their porous composition and surface morphology. The effects of the nanofillers on the porous membrane are explored later on in regard to their wettability, breathability, mechanical and thermal properties.

6.2.1 Morphology and Structure

Understanding how well the nanofillers at a specific concentration dispersed within Micro_PU is important when assessing their effects on the barrier and mechanical properties. The characterisation techniques used to assess the dispersion of the nanofillers within the Micro_PU matrix were X-ray diffraction (XRD), attenuated total reflection - Fourier-transform infrared spectroscopy (ATR-FTIR), scanning electron microscopy (SEM) and energy dispersive X-ray (EDX). Focus-variation microscopy (FVM) was used to understand the surface morphology and roughness which can later be compared to the barrier properties of the nanocomposites.

6.2.1.1 Membrane Images

Microporous membranes were photographed to illustrate the successfulness of producing a homogenous microporous membrane with the addition of nanofillers. The images give an indication to the colour, homogeneity, and surface texture of the membranes (Fig. 62). All membranes were produced using the same standard method (not disclosed), devised by PIL Membranes and so any changes observed are due to the effect of the nanofillers on pore formation and surface morphology.

Opaque areas of the membrane indicate a microporous structure whereas transparent areas indicate the porous structure has collapsed and failed to adequately form. The scattering of light causes the formation of the opaque membrane. Membranes with low concentrations of clay have a similar texture and colour to Micro_PU, however at higher clay concentrations membranes formed changed in appearance compared to Micro_PU. The addition of CNa^{+} and C20 at 5 wt. % caused the membrane to become more transparent and increased the macrosurface roughness. It is likely the increase in transparent areas was caused by a loss of porous structure and/or larger pores.

GO membranes were less homogenous in appearance than clay membranes. More transparent areas were observed and as concentration increased the amount of transparent area increased. As expected, the GO caused slight darkening in colour of the membranes, this is not problematic, but may not be ideal for aesthetic applications or where colour chemistry is required. Both the opaque and transparent areas of the membrane became darker due to GO, indicating an even dispersion of GO throughout the membrane.

Despite some slight issues in homogeneity of the membrane's opacity, the formation of microporous membranes containing nanofillers worked very well with the utilised production method for Micro_PU membranes. With some further work and optimisation of the coagulation process, it should be possible to form large scale homogenous Micro_PU nanocomposite membranes containing clay or GO. It should be noted that Micro_PU/clay and GO membrane samples taken for characterisation within this chapter, were obtained from the opaquest areas to ensure good porous structure.

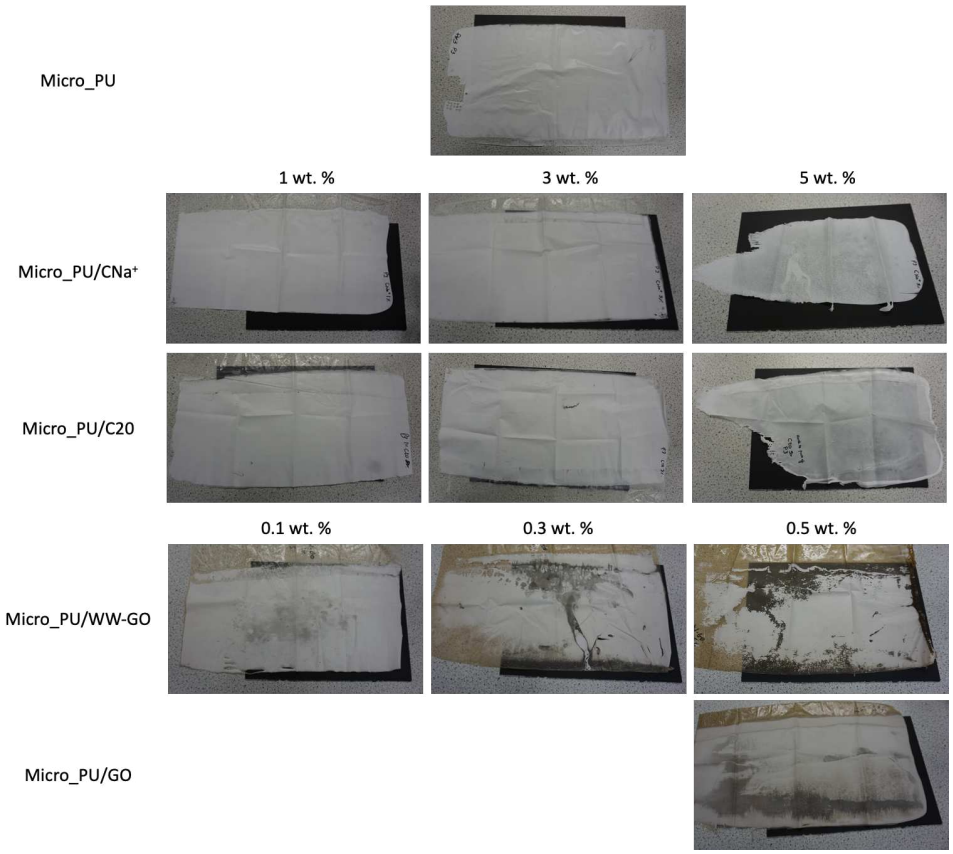

Figure 62. Images of formed Micro_PU/nanocomposite membranes showing membrane opacity, colour, and hence successful formation of microporous membrane.

6.2.1.2 X-ray Powder Diffraction

X-ray powder diffraction (XRD) traces collected from Micro_PU/clay and GO nanocomposite membranes at 1, 3, 5 wt. % and 0.1, 0.3 0.5 wt. %, respectively are shown in Figure 63. Diffraction reflections collected from Micro_PU containing each nanofiller are plotted against those of the Micro_PU, and respective clay powders or dried GO pastes. The relatively low crystallinity and small particle size of Cloisite® clay powder samples cause broad XRD reflections (Fig. 63 a and b). The broad d_{001} reflections of Cloisite® C20 and CNa^+ are consistent with those found in XRD traces characterised in the literature.[118,119]

CNa^+ powder has a broad d_{001} reflection at 7.3 °2θ (12.1 Å) which remains when dispersed in the Micro_PU matrix. However, the reflection does shift to a slightly lower angle (6.9°2θ, 12.8 Å) indicating an intercalated structure. This trend also occurs within Mono_PU/clay nanocomposite membranes. The amorphous region, represented by the broad hump between 17 to 28°2θ which also considers the crystallinity of the polymer, does not significantly change for any nanofiller which reflects the DSC data.

Within this study a strong d_{001} reflection at 12.7 °2θ is observed for WW-GO. Similar to the inclusion of WW-GO within Mono_PU, the addition of WW-GO to Micro_PU presented no reflections. There is no increase in baseline at low angles. This indicates it is likely WW-GO is exfoliated or at least very well dispersed within Micro_PU at all concentrations.

A strong d_{001} reflection is observed for GO at 10.6 °2θ. When GO is incorporated into Micro_PU at 0.5 wt. % a broad hump is present between 7 °2θ and 12 °2θ however when plotted on the same axis as WW-GO samples the 'broad hump' is present for both types of GO. This broad hump is relative to those observed in the clay samples. XRD traces suggest GO is very well dispersed and possibly exfoliated in Micro_PU.

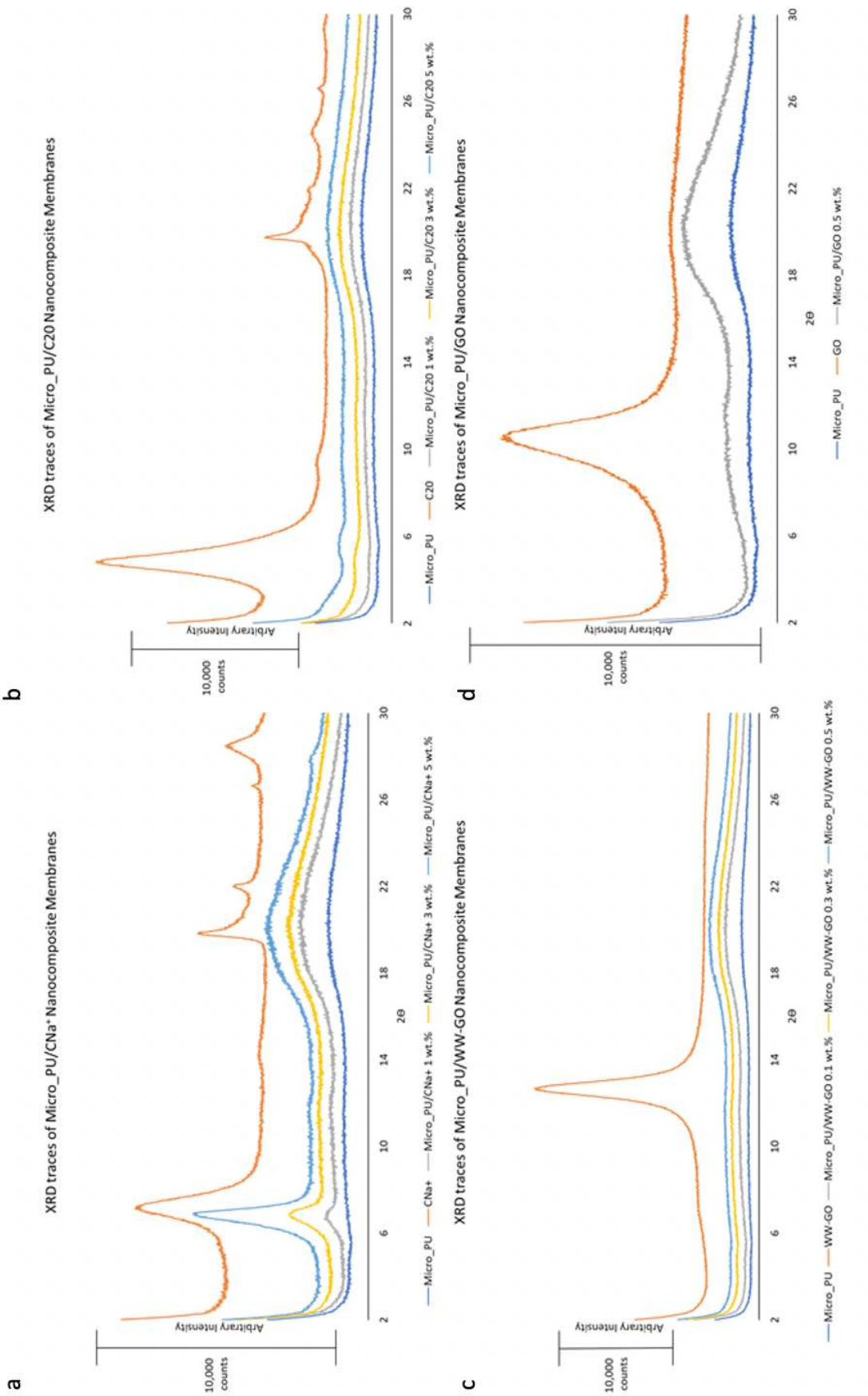

Figure 63. Stacked XRD traces collected from Micro_PU/clay and GO nanocomposite membranes, each image has a spectrum of Micro_PU, clay or GO nanofiller and the Micro_PU/clay or GO nanocomposite at different concentrations. a) C20 b) CNa^+ c) WW-GO d) GO.

C20 powder has a strong d_{001} reflection at 4.9°2θ, despite having a stronger intensity reflection than CNa^+ powder, when C20 is dispersed in Micro_PU the d_{001} reflection becomes significantly less intense. Furthermore, an increasing baseline towards lower angles indicates a partially exfoliated system. As concentration increases, the system becomes slightly less exfoliated and slightly more intercalated.[48] Micro_PU/C20 5 wt. % has an unusual but repeatable XRD reflection that shows a small reflection at 5.3 °2θ, and indicates either the d_{001} reflection has moved to a lower d-spacing due to the removal of extra surfactant (i.e. not in cation exchange sites), or it is a d^{002} reflection resulting from a d_{001} reflection that is hidden under the increasing baseline towards lower angles, however both scenarios are uncertain. It should be noted this feature was not present in Mono_PU/C20 5 wt. %, where a small d_{001} reflection was observed at the same d-spacing as the C20 clay in conjunction with an increased baseline similar to the lower clay loaded membranes. This small feature for Micro_PU/C20 5 wt. % may be due to the surface roughness and microporous nature of the membrane but is of little concern as the majority of C20 has shown good dispersion in both Mono_PU and Micro_PU.

6.2.1.3 Scanning Electron Microscopy

Scanning electron microscopy (SEM) images of the Micro_PU nanocomposite membranes were taken to study the effects of the nanofillers on the surface topography, membrane composition, and porosity. The number of pores, craters and area of these pores and craters were calculated using ImageJ (Table 9). Craters were defined as disproportionately larger than the rest of the porous structure of each sample and larger than the pores present in Micro_PU which have pores as large as 3 to 4 µm in diameter. As such, craters were only defined as being equal to or larger than 4 µm. Pore/crater size was collected from all samples, but pore/crater area was only collected from 3 wt. % clays and 0.5 wt. % GO samples. The area of the pores and craters were calculated to understand and compare relationships between the upper surface topography and both the membrane breathability (WVTR) and the surface roughness. For example, does a larger porous area have a correlation with increased WVTR? Furthermore, the area was calculated for both pores only and for pores and craters combined to help distinguish the impact upper surface craters may have on the

membrane's surface roughness and breathability. For example, a crater may provide a shorter distance for water vapour molecules to travel through the membrane and/or may have thinner walls than the upper surface which may increase WVTR.

6.2.1.3.1 SEM of Micro_PU Membrane

Figure 64 shows the SEM images of the top, bottom, and cross-sectional surface of Micro_PU at three different magnifications. The top surface of Micro_PU consists of many small uniformed-sized pores that puncture the membrane surface and are equally distributed across the surface. It should be noted that the SEM images show darker shaded circles on the upper and lower surfaces. These are pores of the interconnected porous network of the cross section covered with a thin layer of membrane, they have not punctured the surface and are larger than the pores that puncture the membrane surface.

Micro_PU upper surface (analysed from the middle magnification) has 449 pores and a total porous area of 40.32 μm^2. When the 2 craters that are present are included, the total area increases to 54.38 μm^2 (Table 9).

A box and whisker plot are used to show the range of pore sizes for all samples (Fig. 65), for example Micro_PU has an average pore diameter of 0.72 µm with a standard deviation (SD) of +/- of 0.85 µm. The bottom surface, due to being in contact with the casting paper, produces fewer but larger pores (average diameter 1.51 µm, SD. +/- 1.52 µm) across the surface. The shape of these pores is distorted by contact with the casting paper. The SEM images of the cross-sectional surface shows an interconnected porous structure of evenly sized and distributed pores across the membrane, with an average diameter of ~3 µm. Note the size of the cross-section pores are very similar to the darker shaded circles observed on the upper and lower surface.

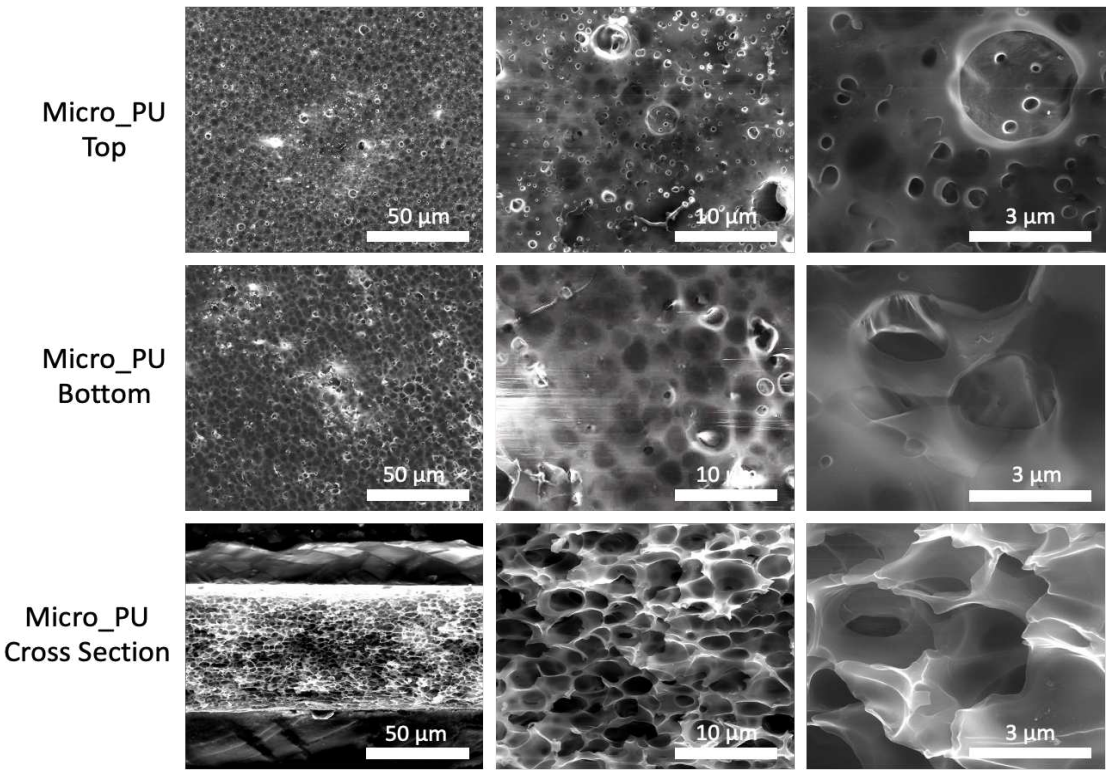

Figure 64. SEM images of Micro_PU top, bottom, and cross-sectional surfaces at three different magnifications.

6.2.1.3.2. SEM Upper Surface Images - Pore and Crater Size

Figure 65 presents the box and whisker plot and interpretation of SEM images for all Micro_PU nanocomposite membrane upper surfaces. The box represents the interquartile range, the whiskers are the upper and lower quartiles, the line is the median and the X the average. Outliers are shown by the dots, above 4 µm these dots represent craters. The box and whiskers plot gives a good visual indication of the range of pore lengths and how they vary for each sample. The median for Micro_PU indicates a higher density of smaller pores and two craters. At the lowest concentration of clay there was little change in average pore length and a decrease in the range of pore sizes indicating a higher density of pores of a similar size. At higher clay loading, pores become larger and have a greater range of pore sizes. As concentration of C20 increases average pore length increases. WW-GO at all 3 concentrations cause very little change to average pore length compared to Micro_PU, the range or pore size either decreases or remains similar. For Micro_PU/WW-GO at 5 wt. % the pore size range is skewed to a larger pore length. GO produced a similar plot to Micro_PU/C20 5 wt. % but the range of pore sizes is slightly reduced (GO measurements taken from non 'bridged' SEM image).

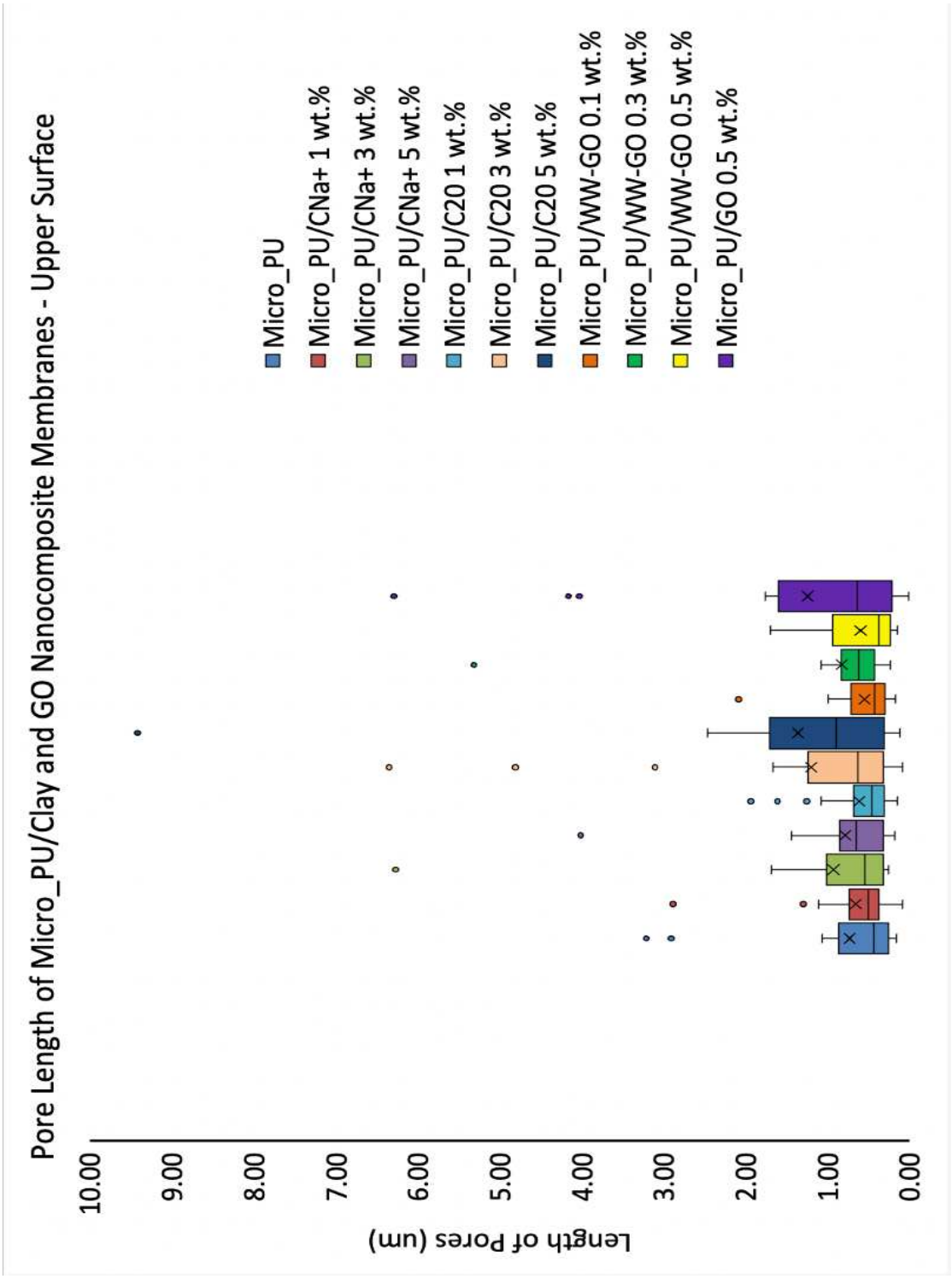

Figure 65. Box and whisker plot of pore lengths taken from analysis of SEM images of the upper surface of Micro_PU/Clay and GO membranes. The box represents the interquartile range, the whiskers are the upper and lower quartiles, the line is the median and X the average pore lengths. Outliers are shown by the dots, above 4 µm these dots represent craters instead of pores.

Table 9. Various measurements taken of Micro_PU/Clay and GO membranes average pore size with standard deviation, number of craters, including total number of pores, craters, and their respective areas for selected samples. Measurements were taken from upper surface SEM images (specifically the middle SEM images).

	Average Pore Size	Number of Craters & Respective Diameters	Number of Pores	Area of Pores (μm^2)	Area of Craters (μm^2)	Area of Pores & Craters (μm^2)
Micro_PU	0.72 (± 0.85)	**0**	449	40.32	14.06	54.38
Micro_PU/CNa+ 1 wt. %	0.65 (± 0.62)	**0**	-	-	-	-
Micro_PU/CNa^+ 3 wt. %	0.91 (± 1.32)	**1** 6.27 µm	101	13.94	30.77	44.71
Micro_PU/CNa^+ 5 wt. %	0.78 (± 0.84)	**1** 4.01 µm	-	-	-	-
Micro_PU/C20 1 wt. %	0.61 (± 0.49)	**0**	-	-	-	-
Micro_PU/C20 3 wt. %	1.18 (± 1.66)	**2** 4.81 µm 6.35 µm	148	62.70	52.76	115.46
Micro_PU/C20 5 wt. %	1.32 (± 2.06)	**1** 9.41 µm	-	-	-	-
Micro_PU/WW-GO 0.1 wt. %	0.55 (± 0.42)	**0**	-	-	-	-
Micro_PU/WW-GO 0.3 wt. %	0.81 (± 1.08)	**1** 5.31 µm	-	-	-	-
Micro_PU/WW-GO 0.5 wt. %	0.60 (± 0.52)	**0**	151	4.38	0	4.38
Micro_PU/GO 0.5 wt. %	1.22 (± 1.67)	**2** 4.03 µm 4.16 µm	60	18.12	42.14	60.26

6.2.1.3.3 SEM of Micro_PU/CNa^+ Membranes - Upper Surface

Figure 66 shows the effect CNa^+ has on the upper surface morphology of Micro_PU. Average pore size decreases with addition of CNa^+ 1 wt. % to 0.65 µm, SD. +/- 0.62 and then increases with higher clay loading to 0.91, SD. +/- 1.32 and 0.78, SD. +/- 0.84 for CNa^+ 3 wt. % and 5 wt. %, respectively. The images show that the addition of clay causes an increase in the quantity of craters while decreasing the number of smaller pores. The total area covered by the pores decreases from 40.32 μm^2 with Micro_PU to 13.94 μm^2 for Micro_PU/CNa^+ 3 wt. %. The number of pores also decreased from 449 to 101. When the area of craters is also included the total area of pores and craters for Micro_PU/CNa^+

3 wt. % is 44.71 μm^2, which shows the significance craters have on the total area of the punctured membrane surface.

The macrosurface of Micro_PU/CNa^+ 5 wt. % has been affected the most by the addition of the nanofiller. Some of the largest craters have 'bridged', where strands of polymer create bridges from one side of the pore to the other. It can be seen on the bottom left image of Micro_PU/CNa^+ 5 wt. %, at both the upper left corner and lower right corner (circled in red). A couple of other craters have also begun to 'bridge' nearby (green arrows). It is suggested that the 'bridged' pores form when bubbles are formed on the membrane surface, which pop causing a crater and/or 'bridged' pore.

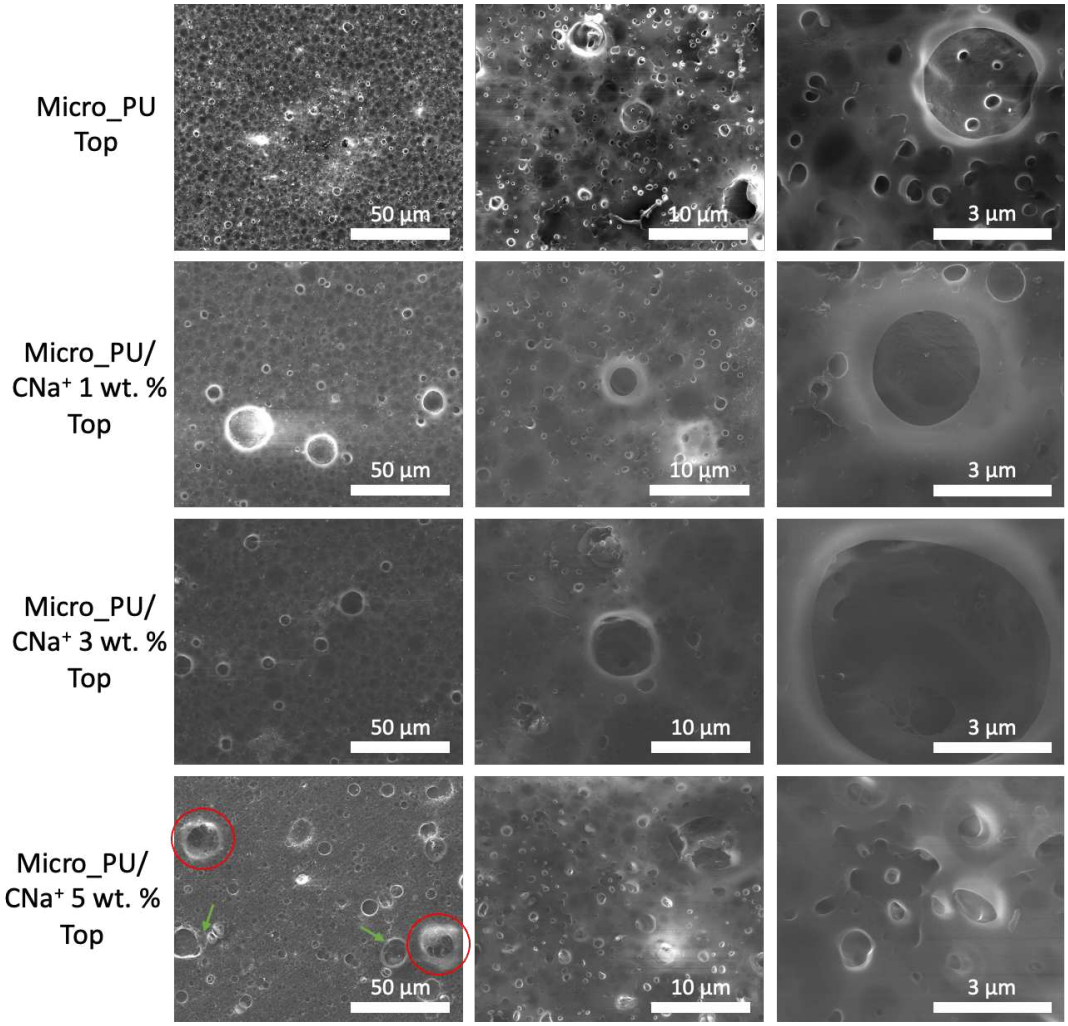

Figure 66. Comparison of SEM images of top surface of Micro_PU against Micro_PU/CNa^+ 1, 3 and 5 wt. %.

6.2.1.3.4 SEM of Micro_PU/C20 Membranes - Upper Surface

Figure 67 shows the effect C20, at various concentrations, has on the Micro_PU upper surface morphology. At 1 wt. % of C20 pores appear similar to Micro_PU except the average pore length decreases to 0.61 μm SD. +/- 0.49 (a decrease is also observed with CNa^+ at this same amount). At 3 wt. % the average pore length increases to 1.18 μm SD. +/- 1.66, pores have become less uniform in shape losing their circular nature. The average pore length of Micro_PU/C20 5 wt. % is 1.32 μm SD. +/- 2.06, the quantity of larger pores has increased. The pores are no longer evenly distributed over the surface. The total number or pores for Micro_PU/C20 3 wt. % was 148 with a total area of 62.70 μm^2. This increased to 151 pores with a total area of 115.46 μm^2 when craters are included.

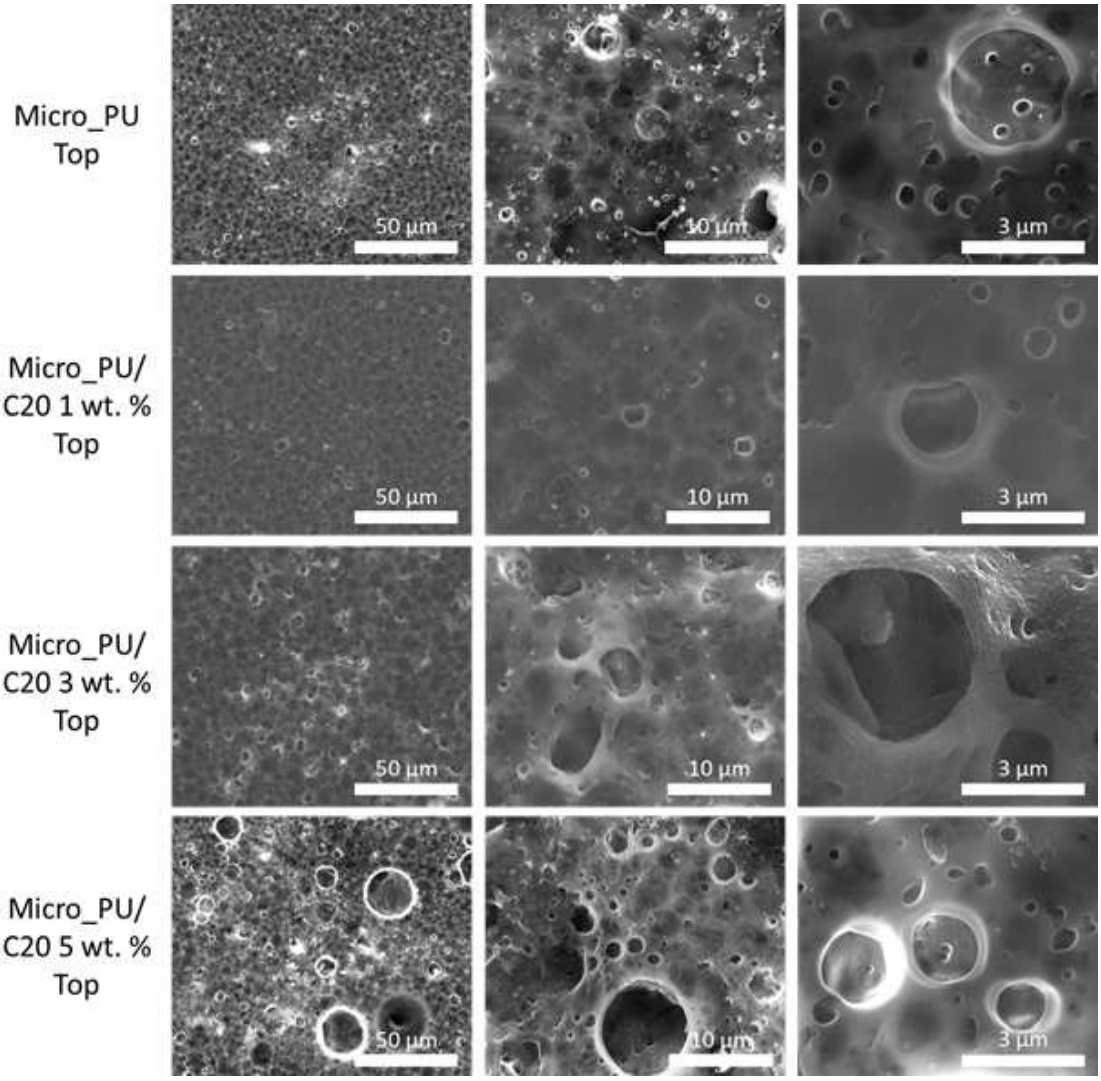

Figure 67. Comparison of SEM images of top surface of Micro_PU against Micro_PU/C20 1, 3 and 5 wt. %.

6.2.1.3.5 SEM of Micro_PU/WW-GO Membranes - Upper Surface

Figure 68 shows the effect of WW-GO at three different concentrations on Micro_PU. The effect of WW-GO in some respects mirrors that of CNa^+ on the surface morphology of Micro_PU. Similar to the clay nanofillers at small amount, WW-GO (0.1 wt.%) leads to a decrease in average pore length to 0.55 µm, SD. +/- 0.42 µm. The addition of more WW-GO increased pore size, however, this increase is fairly uniform across all pores and the distribution of pores remains even across the whole surface. There are no standalone large pores or 'bridge' pores present. Average pore length increases to 0.81 µm, SD. +/- 1.08 µm for Micro_PU/WW-GO 0.3 wt. %. However, pore length decreases for Micro_PU/WW-GO 0.5 wt. % at a value of 0.60 µm, SD. +/- 0.52 µm.

Despite pore distribution and length remaining similar to Micro_PU, it does appear that the number of pores that pierce the surface have decreased. It appears that as concentration of WW-GO increases the numbers of pores piercing the surface decrease. For Micro_PU/WW-GO 0.5 wt. % the number of pores has decreased to 151, similar to the nanocomposite membranes, however total pore area has significantly decreased to 4.38 μm^2. There are no craters present within that sample image, so no change occurred.

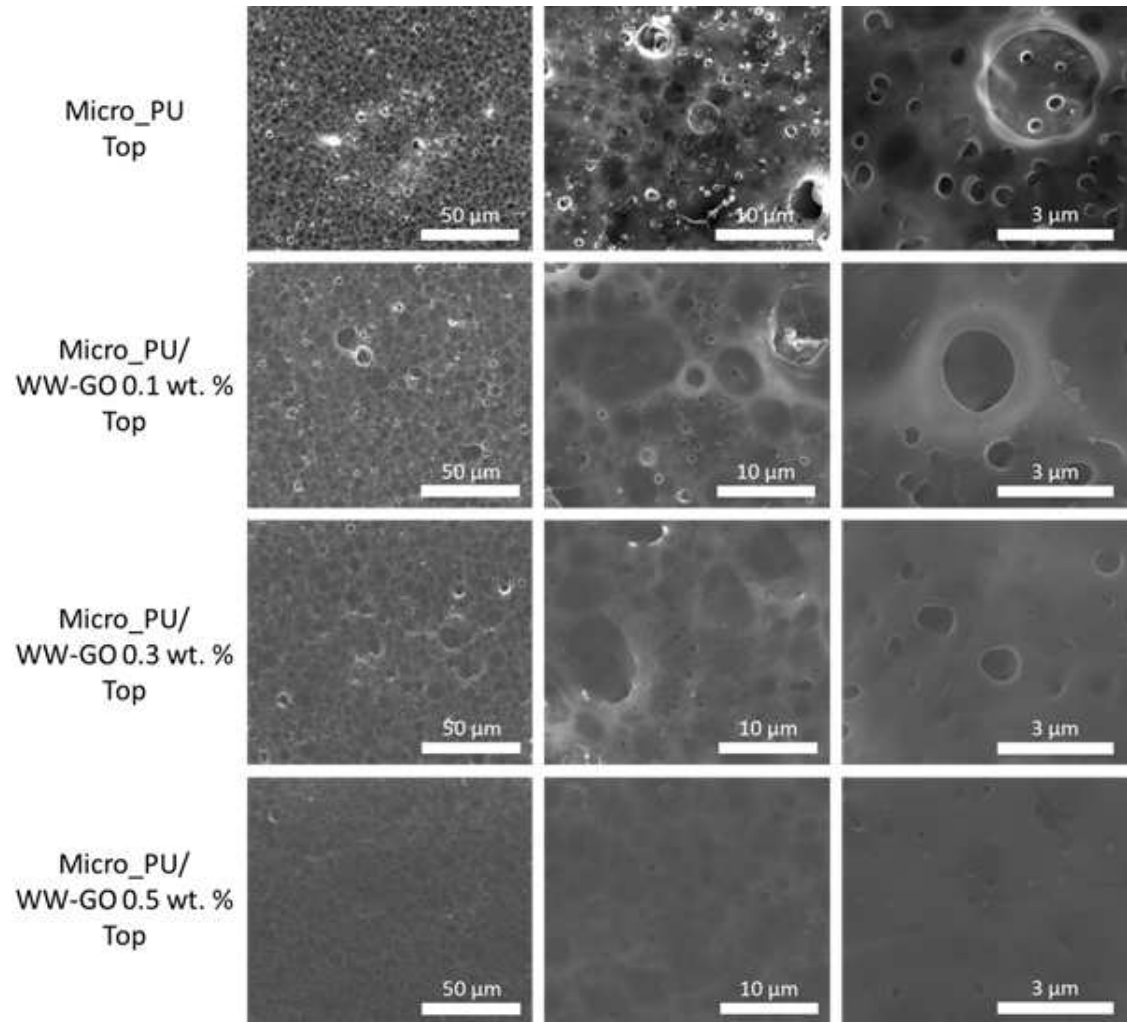

Figure 68. Comparison of SEM images of top surface of Micro_PU against Micro_PU/WW-GO 0.1, 0.3 and 0.5 wt. %.

6.2.1.3.6 SEM of Micro_PU/GO Membrane - Upper Surface

The effect of GO at 5 wt. % on Micro_PU is shown in Figure 69. GO caused a very different surface morphology compared to the other nanofillers. Large 'bridged' pores were observed and were typical across the whole surface; this may indicate the sample contains contaminants in a similar manner to that observed with CNa^+, i.e., CNa^+ is an impure form of bentonite and is less clean than C20, which did not display any 'bridged' pores. Where 'bridged' pores are not present, pores are nonuniform, have an average pore size of 1.22 µm, SD. +/- 1.67 µm and are unevenly distributed. The number of pores decreased significantly from 449 to 60 for Micro_PU/GO 0.5 wt. % with a total area of 18.12 μm^2. Increasing to 60.26 μm^2 with 4 additional craters.

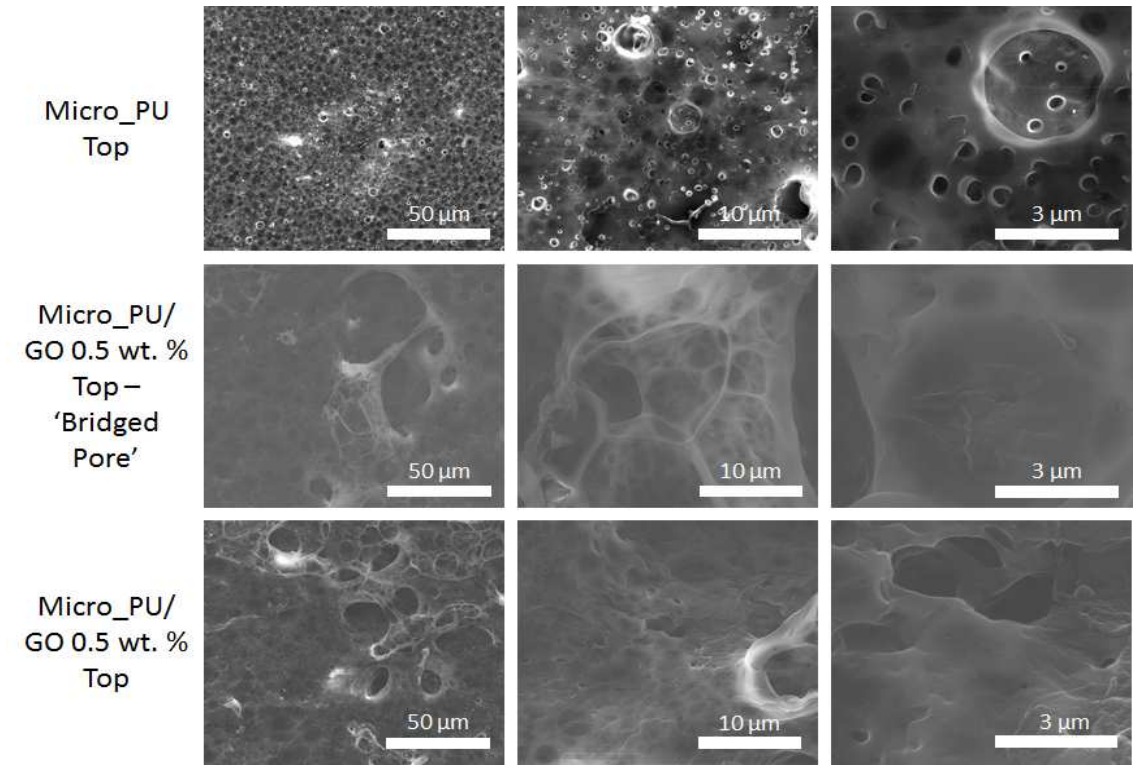

Figure 69. Comparison of SEM images of top surface of Micro_PU against Micro_PU/GO 0.5 wt. %.

6.2.1.3.7 SEM of Membrane Lower Surface

Figure 70 shows SEM images of the lower surface of Micro_PU and selected Micro_PU nanocomposite membranes. Generally, the bottom pores tend to be less uniform in shape, size and distribution compared to the upper surface due to being in contact with the casting paper. The addition of clay nanofillers did not significantly change the porosity of the bottom layers of the membranes. WW-GO did cause a reduction in the number of pores and the pore size appears to have increased, this is likely due to the gradual collapse of the interconnected porous network as observed in the cross-sectional SEM images.

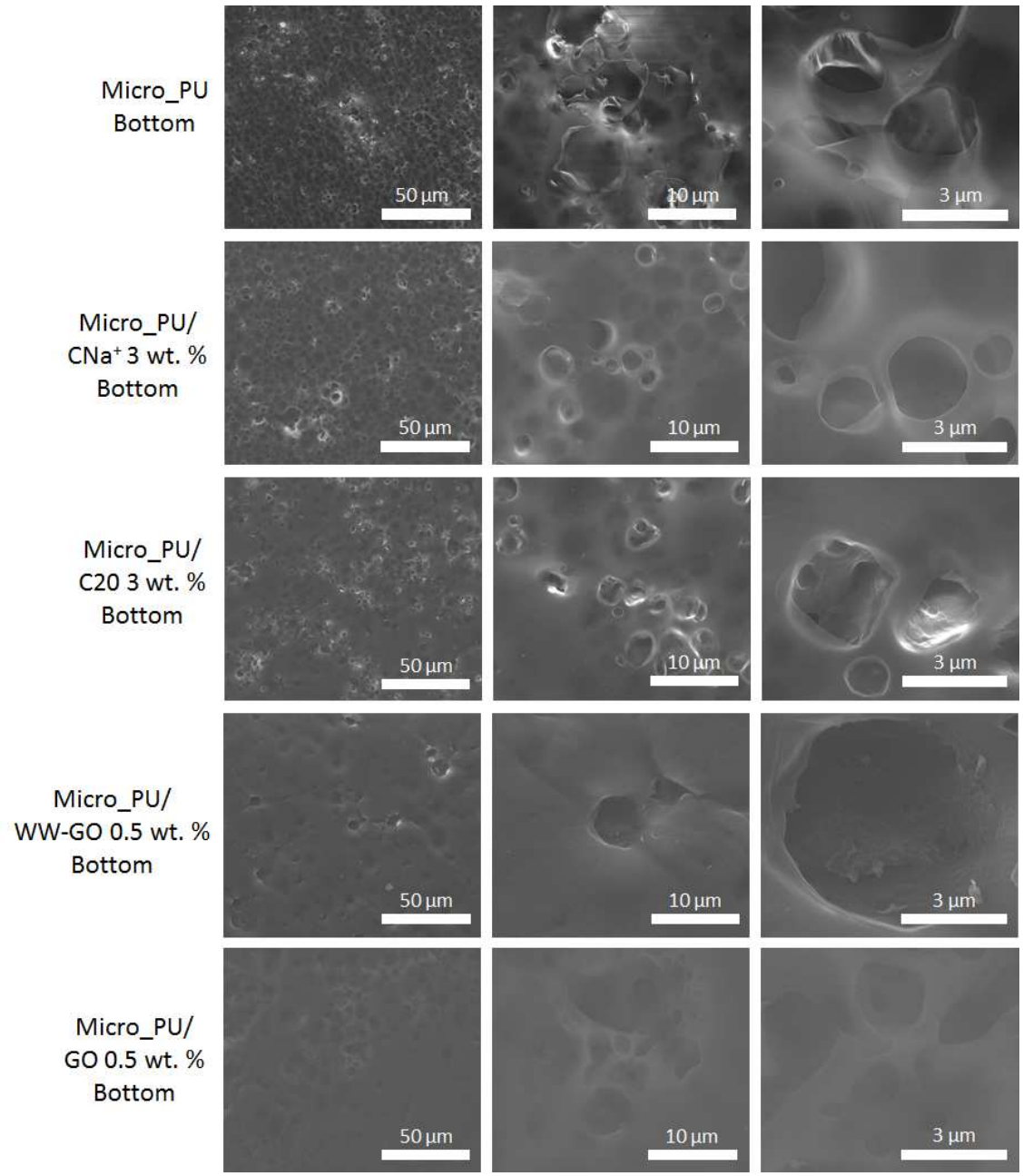

Figure 70. SEM images of the bottom of Micro_PU, Micro_PU/CNa^+ 3 wt. %, Micro_PU/C20 3 wt. %, Micro_PU/WW-GO 0.5 wt. % and Micro_PU/GO 0.5 wt. %.

6.2.1.3.7 SEM of Membrane Cross-sections

A selection of samples was freeze fractured and the cross-sections along the depth of the membrane were imaged using SEM at three different magnifications. These images are presented in Figure 71. Micro_PU thickness measured from the SEM image is 60 µm thick, the cross-sectional pores have an average length of 1.94 µm, SD. +/- 1.08 µm (Fig. 72). The pores are equally shaped and evenly distributed across the whole membrane. The addition of CNa^+ 3 wt. % causes the average cross sectional pore length to increase to 2.25 µm, SD. +/- 1.81 µm and membrane thickness increases to 99 µm. The pores

have a more irregular shape and the walls of the pores become less defined. For example, pores begin to lose their circular shape. Craters that puncture the membrane surface are observed sporadically across the membrane cross-section, one such crater can be observed in the SEM images below for CNa^+ 3 wt. %. It is thought these craters are more closely related to the large defects shown in Figure 76 than the regular upper surface craters present in Figure 69. These craters are associated with large concave areas (approx. 150 µm in size, i.e., the shaded area). Concave areas were numerous along the entire cross section, but this did not appear to disrupt the porous structure. It remained the same across the concave and flat regions. The concave areas are the result of freeze fracturing the membrane and are not present before fracturing, for every concave area on one half there is an equal convex area on the other half.

When C20 at 3 wt. % is added, the average cross-sectional pore length increases to 2.50 µm, SD. +/- 2.08 and the membrane width increases to 84 µm. The cross sectional interconnected porous network of Micro_PU/C20 3 wt. % is the most similar to Micro_PU however some slight changes are observed such as the pores are larger and vary more in their length.

When freeze fracturing the Micro_PU/WW-GO 0.5 wt. % membrane it would only fracture diagonally, i.e., not perpendicular to the upper surface of the membrane. When imaged, a bilayer was observed (Fig. 74). The layer closest to the upper surface of the membrane, remained an interconnect porous structure. However, the pores have become distorted and more oval (sponge like) in shape compared to the Micro_PU membrane. Membrane thickness was 71 µm, the smallest increase in thickness observed across all membranes compared to Micro_PU.

Similar to the top surface morphology, the addition of GO at 0.5 wt. % caused the largest difference in the porous network of Micro_PU. The pores have lost their round shape and are no longer uniform in size or distribution. Large holes within the membrane are present. This has caused the membrane thickness to increase to 125 µm. The large increase in membrane thickness is likely due to the large pores, which on average have a length of 17.86, SD. +/- 17.47 µm.

Despite changes to the shape, size, and distribution there is very little difference in the average pore length of Micro_PU nanocomposites for all nanofillers except Micro_PU/GO 0.5 wt. % (Fig. 72).

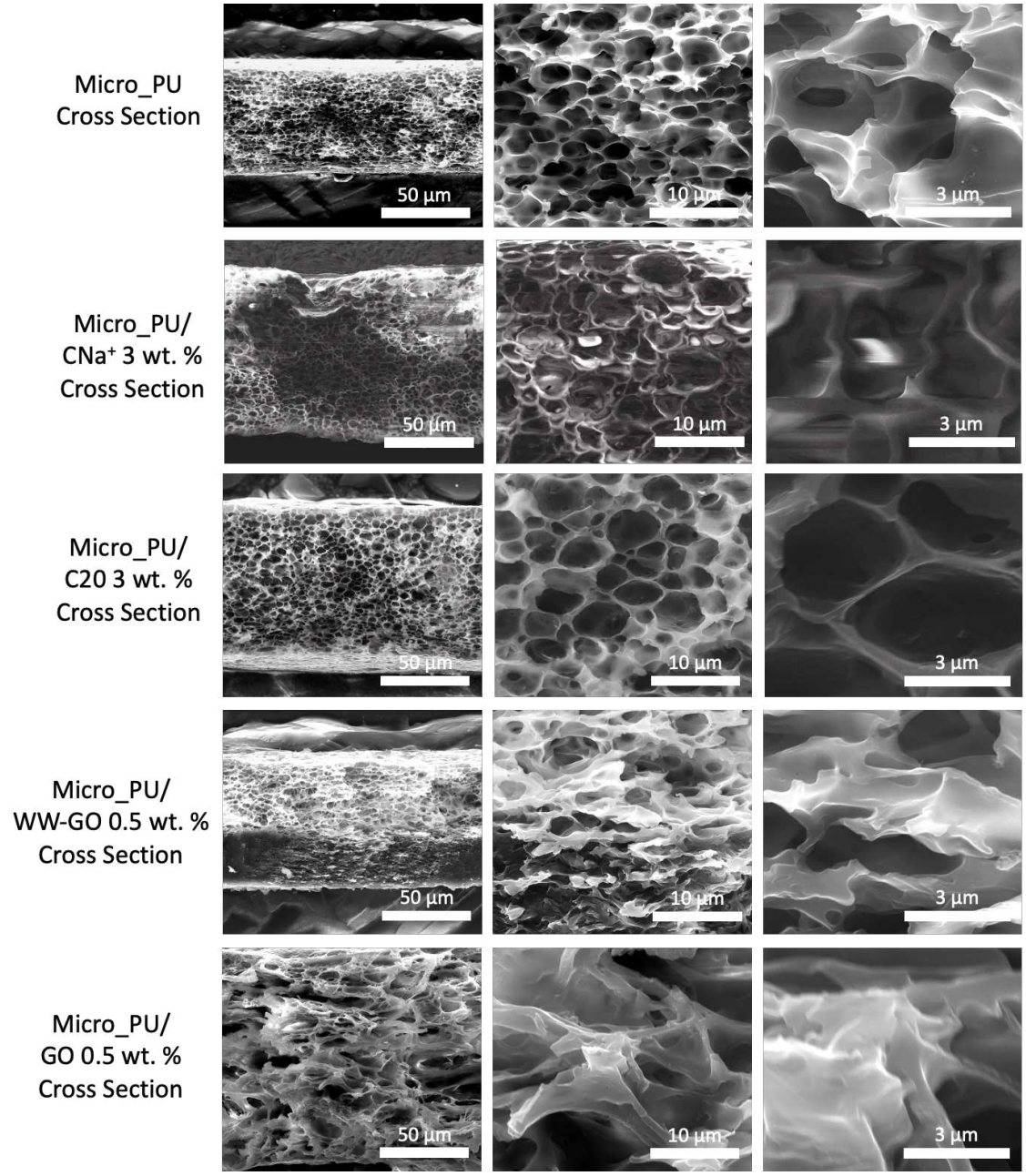

Figure 71. Comparison of SEM images of freeze fracture cross sections of Micro_PU, Micro_PU/CNa^+ 3 wt. %, Micro_PU/C20 3 wt. %, Micro_PU/WW-GO 0.5 wt. % and Micro_PU/GO 0.5 wt. % membranes.

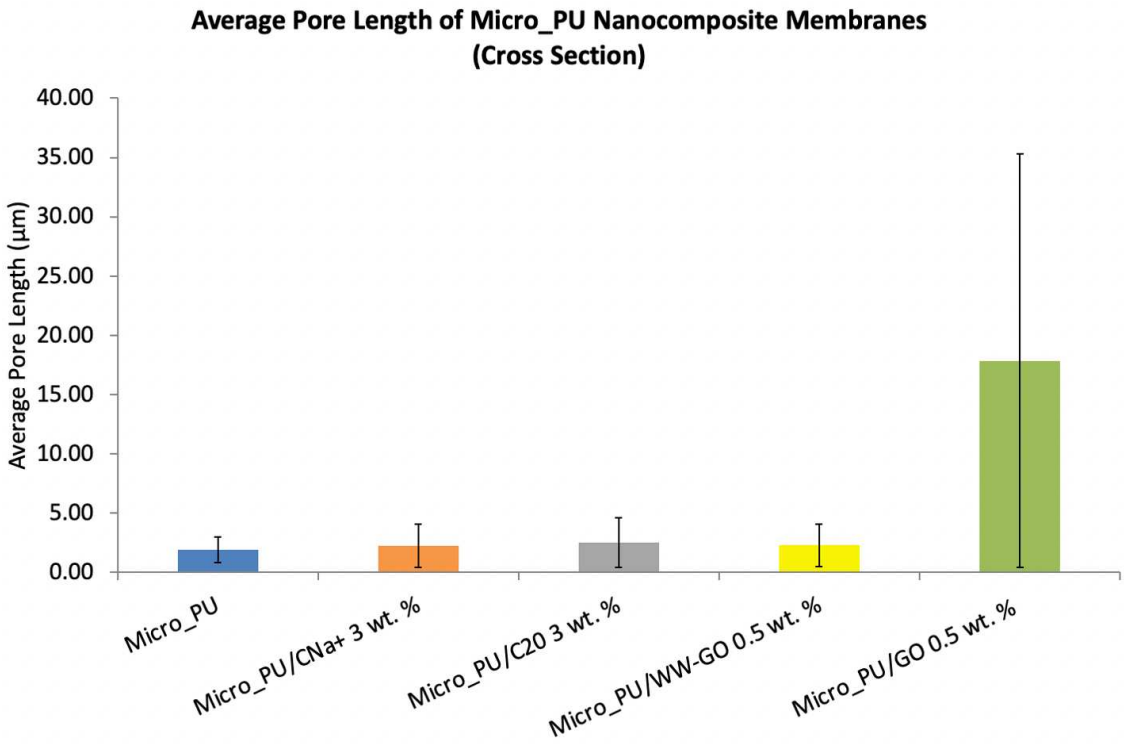

Figure 72. The average pore length with standard deviation of SEM images of freeze fracture cross sections of Micro_PU and Micro_PU/nanocomposite membranes. Measurements for GO 0.5 wt.% were taken from lower magnification images to allow for accurate representation of porous structure.

6.2.1.3.8 SEM of Top and Bottom Membrane Edges

The top and bottom edges of the cross sections (i.e., the skins of the membranes) of three samples were imaged in more detail using SEM in order to establish what the interconnected porous structure looks like at both the upper and lower surfaces (Figure 73). With Micro_PU the pores closest to the bottom edges appear more squashed than those at the top edges. A similar effect occurs for Micro_PU/C20 3 wt. % however it is less extreme. Images of the upper surface also support the idea that dark circles on surface images are due to pores lying just beneath the surface. This can be observed on all images but is particularly clear on Micro_PU/WW-GO 0.5 wt. % upper images. A large pore, measuring 8.32 µm wide, is present underneath a thin membrane layer. The 'skins' (upper and lower surfaces of the membrane) are very thin compared to the thicknesses of the membranes and all look similar between samples, however, it is difficult to quantify. This is also applicable to the thickness of the pore walls.

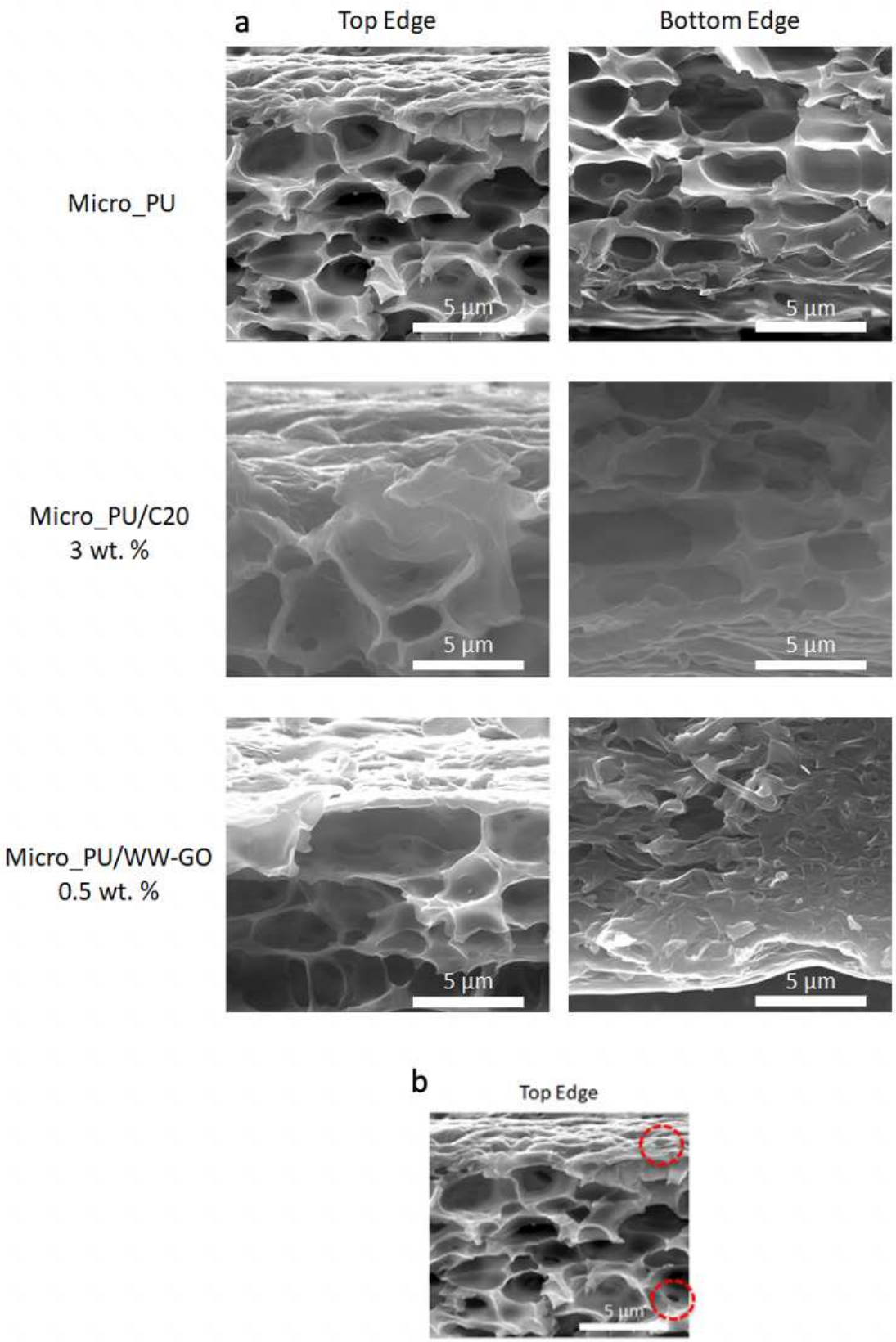

Figure 73. a) SEM images of top and bottom edges of the cross section of Micro_PU, and Micro_PU/C20 3 wt. % and Micro_PU/WW-GO 0.5 wt. %. b) Micro_PU small, interconnected pores circled in red.

Micro_PU presents a clear example of how smaller and larger pores interact to form the interconnected porous network. Larger pores range from ~1-3 μm in diameter while smaller pores that pierce the larger pores are often less than 1 μm. The image in Figure 74b collected from Micro_PU circle red, clearly shows these smaller pores circled in red, one on the membrane surface and one acting as an interconnected pore between two larger pores. These smaller interconnected pores are present within both the Micro_PU/C20 3 wt. % and Micro_PU/WW-GO 0.5 wt. %. It is likely these smaller interconnected pores are present in all Micro_PU nanocomposite samples, however the frequency of these pores is unknown.

The two different types of porous structure for the Micro_PU/WW-GO 0.5 wt. % bi-layer structure was imaged using SEM (Figure 74). The lower half of the bilayer has two distinct porous states (Fig. 74 b & c), it is microporous in nature or in the process of becoming monolithic as the pore walls become less defined and the pores are less separated. This monolithic vs semi-porous nature alternates along the lower half of the membrane, with sections that intertwine as the two types of membranes meet (Fig. 74 d & e).

SEM images of Micro_PU/WW-GO 0.5 wt. % in Figure 74 d & e highlight the point where the upper and lower parts of the bi-layer meet including the convergence of the three distinct types of porous structure (upper porous layer, lower semi-porous section, and lower monolithic section). It is clear to see how the upper porous layer maintains an expected porosity which diminishes as pores collapse and compress in the lower semi-porous section and eventually fully collapse forming a monolithic type of lower section. These three different porous structures repeatedly converge, intertwine and merge into one another across the whole membrane cross section, much like an ombre effect.

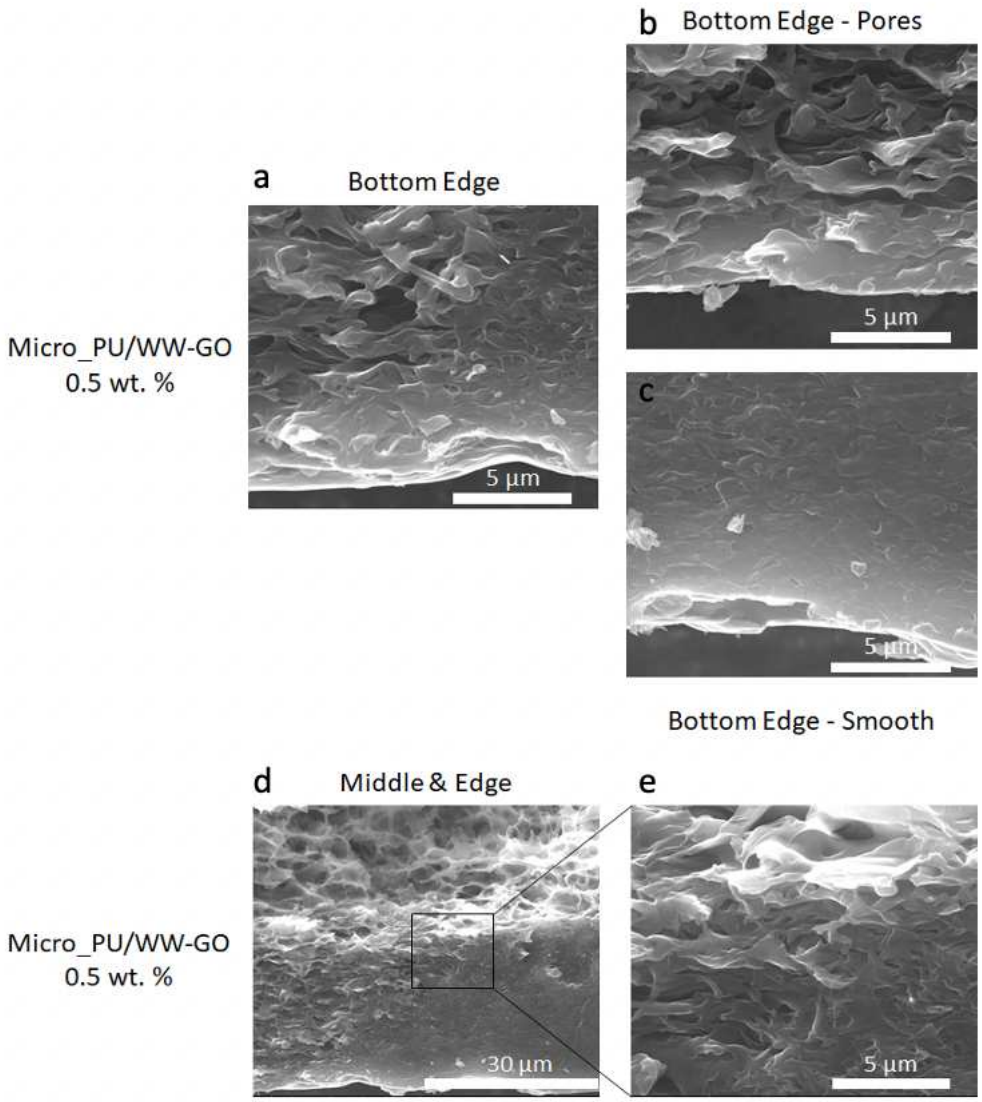

Figure 74. SEM images of Micro_PU/WW-GO 0.5 wt. % bottom edge of the cross section. a) the overlap between the smooth (monolithic) and porous areas. b) the porous section of Micro_PU/WW-GO 0.5 wt. %. c) the smooth (monolithic) section of Micro_PU/WW-GO 0.5 wt. %. d) the overlap between the 3 different types of porosity e) magnification of image d.

6.2.1.4 Scanning Electron Microscopy with Energy Dispersive X-ray Analysis

Scanning Electron Microscopy/Energy Dispersive X-ray Analysis (SEM/EDX) of the top surfaces and cross sections of Micro_PU nanocomposite membranes was used to assess nanofiller dispersion on the macroscale, as well as understand if and how the nanofiller affected the porosity of the membranes. Figure 75 compares SEM/EDX images obtained from the upper surfaces of Micro_PU and nanocomposite membranes containing 3 wt. % of clay nanofiller. Each sample has a map of the elements carbon, oxygen, silicon, and aluminium, as well as a combined map of all elements overlapped.

Micro_PU has an even distribution of all elements at expected intensity relevant to composition. With the addition of CNa^+ at 3 wt. % some aggregation of nanofiller at larger pores is suggested, including large pores just underneath the membrane surface (skin) (Fig. 66, circled in red). This aggregation is displayed as a higher intensity of silicon and aluminium.

C20 at 3 wt. % has better dispersion compared to CNa^+ at 3 wt. %, as evidenced by XRD and now SEM/EDX. There is no indication of aggregates of silicon and oxygen elements across the surface of the Micro_PU/C20 3 wt. % membrane. The distribution of C20 appears to be even across the surface of the membrane.

Interestingly, the carbon images provide insight into the porous nature under the uppermost surface (skin) of the membrane since the dark circles are not directly due to craters or pores within a skeletal polymer framework (i.e., the dense red areas), but rather a representation of the pores under the skin of the membrane. The areas are simply darker due to less polymer being present within the area from which the signal is collected. This supports the interpretation made in the SEM section that the darker shaded areas are pores underneath a thin membrane surface.

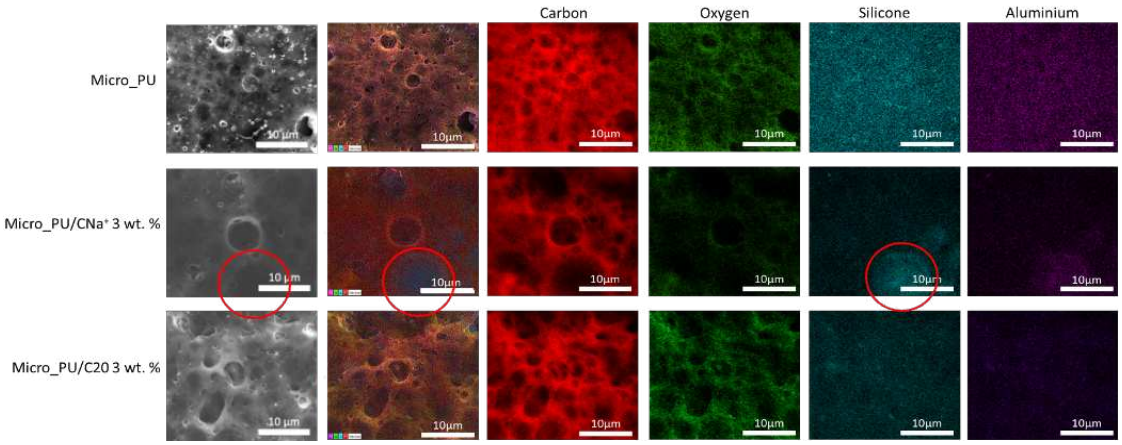

Figure 75. Comparison of the upper surface SEM/EDX maps of Micro_PU, Micro_PU/CNa^+ 3 wt. % and Micro_PU/C20 3 wt. % membranes.

It should be noted that despite having a good dispersion of nanofiller, one-off defects and aggregation can still occur. Figure 76 presents the SEM/EDX maps of observed defects in the upper surface of Micro_PU/CNa^+ 3 wt. % and Micro_PU/WW-GO 0.3 wt. %. The large defects as presented below were rare but did occur on these samples. Large

aggregates of CNa^+ caused the large defect observed (~ 100 µm by 153 µm in size), clearly disrupting the microporous membrane formation. High intensities of oxygen, silicon and aluminium confirm the presence of the clay, particularly at the lower part of this defect where the pores are largest.

GO, being composed of only carbon and oxygen, does not normally show up well in carbon-rich samples using SEM/EDX maps. However, with a similar-sized large defect for Micro_PU/WW-GO 0.3 wt. % as Micro_PU/CNa^+ 3 wt. % it strongly indicates an aggregate of WW-GO (~ 35 µm by 7 µm in size) as evidenced with the large concentration of oxygen across the 'bridged' pore. There is also a small aggregate containing mostly silicon; however, this does not seem to have disrupted the porosity and so appears as though it is a contaminant on the surface which was deposited after the membrane was prepared. This aggregation of WW-GO appears to be a one-off. A large defect like this was not present in the sample of any other WW-GO sample. The XRD data also suggests good dispersion of WW-GO. It should be noted that despite having a good dispersion of nanofiller, one-off defects and aggregation can still occur.

Micro_PU/GO 0.5 wt. % was imaged using SEM/EDX to observe if the 'bubbled'/'bridged' pores were the result of aggregation of GO. There is an increased intensity of oxygen surrounding the pore walls which may indicate that GO, although not aggregated, is dispersed in higher concentrations within the 'bridged'/'bubbled' porous walls. However, the increased intensity may be a surface phenomenon during data collection, if the 'bridged'/'bubbled' pores are protruding from the surface they would be closer to the detector, could cause shadowing and thus produce higher elemental intensity contrasts. This is observed in the concave region of the Micro_PU cross section SEM/EDX shown in Figure 71. There may also be a higher polymer density resulting from the overlapping collapsed wall structure of the 'bubbled'/'bridged' pores.

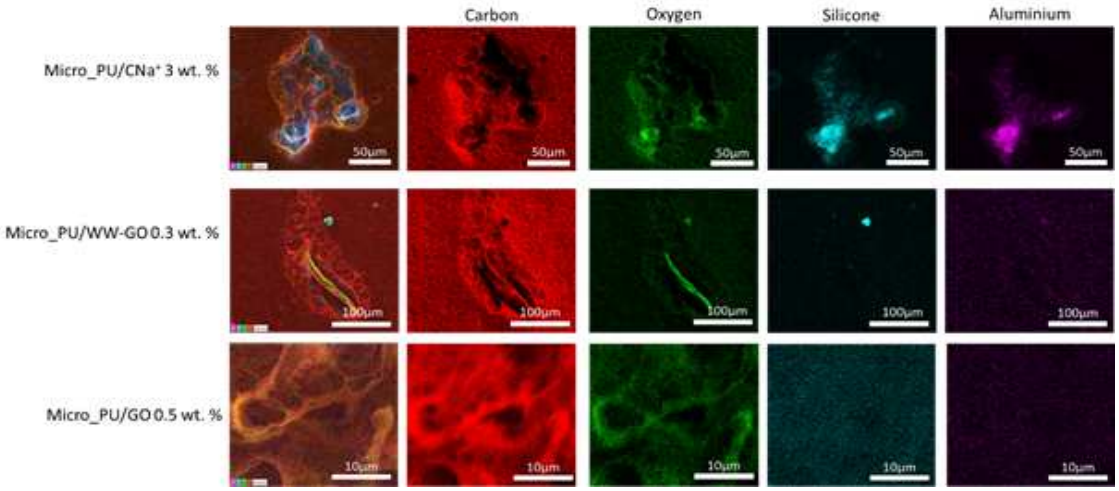

Figure 76. SEM/EDX maps of example defects observed in Micro_PU/CNa^+ 3 wt. % and Micro_PU/WW-GO 0.3 wt. %. As well as the unusual surface morphology of Micro_PU/GO 0.5 wt.%.

Figure 77 shows SEM/EDX maps of freeze-fractured cross-sections of Micro_PU nanocomposite membranes. The aluminium maps have not been included due to large interference from the aluminium stub, which could not be avoided due to the sample preparation and mounting methodology required to achieve a good image and map. It should be noted that no aluminium at any significant level was noted in any other areas of SEM/EDX maps apart from the aggregate seen in the Micro_PU/CNa^+ 3 wt. % sample shown above in Figure 76.

Micro_PU has an even distribution of carbon and oxygen, with background scattering of silicon. The addition of CNa^+ as discussed above caused craters to form when the clay aggregated. The image below provides a cross-section of one of these craters and it is clear to see it was caused by a large aggregate of CNa^+ clay as evidenced by the high density of oxygen and silicon. Despite not being shown there was also a high intensity of aluminium for this clay aggregate. There is strong intensity of all three elements around the bottom of the large pore.

SEM/EDX maps of Micro_PU/C20 3 wt. % show a good dispersion evidenced by an even distribution of intensity for both oxygen and silicon maps. No large defects were observed with the addition of C20, which is likely due to C20 having fewer contaminants than CNa^+. These contaminants are removed during the organomodification process. There are some very small intense spots that are clear to see in the silicon map, however

these do not correlate to any changes in porous structure and are likely due to external contamination after membrane preparation.

SEM/EDX of Micro_PU/WW-GO 0.5 wt. % shows no aggregates of GO, the maps appear similar to that of Micro_PU with very little intensity for the silicon map compared to other samples. Furthermore, there is no elemental difference between the two bilayers of the membrane's cross section. Micro_PU/GO 0.5 wt. % presents an even intensity of elements showing no signs of GO aggregation.

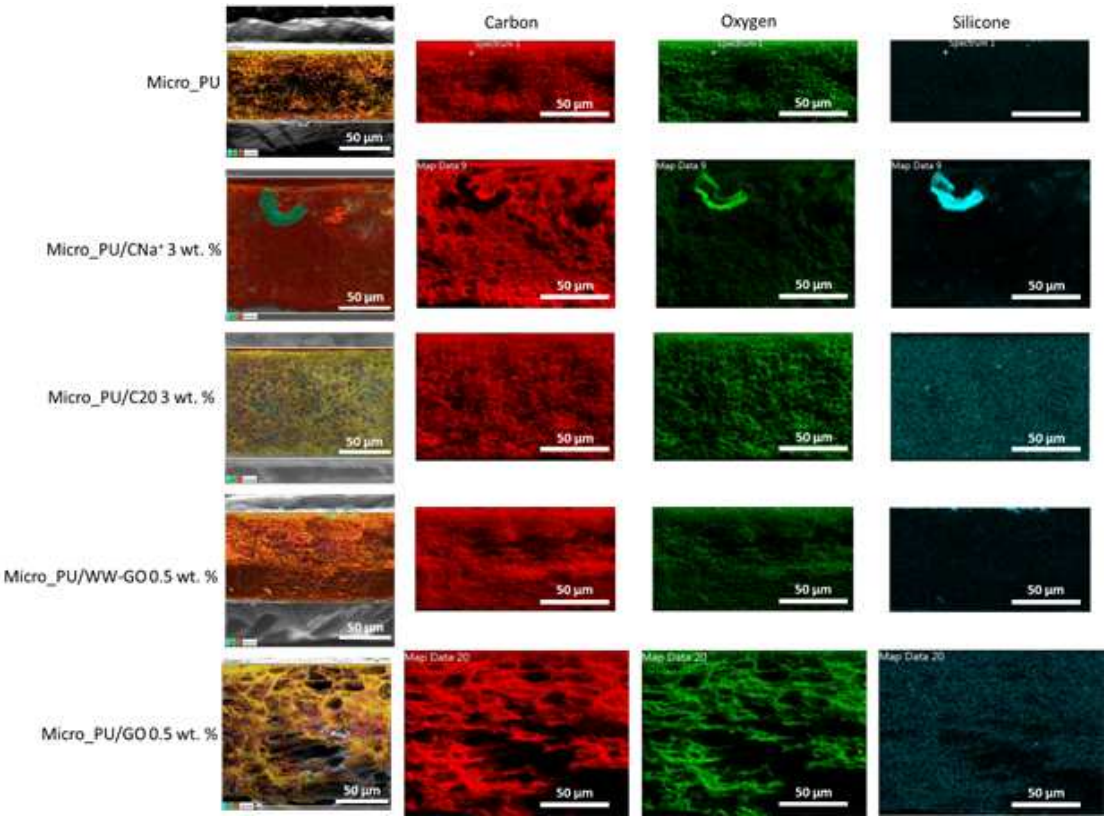

Figure 77. SEM/EDX maps of the freeze fractured cross sections on Micro_PU, Micro_PU/CNa+ 3 wt. %, Micro_PU/C20 3 wt. %, Micro_PU/WW-GO 0.5 wt. % and Micro_PU/GO 0.5 wt. % membranes.

6.2.1.5 Attenuated Total Reflection - Fourier-Transform Infrared Spectroscopy

Attenuated total reflection - fourier-transform infrared spectroscopy (ATR-FTIR) was performed in triplicate on both the upper and lower surfaces of the Micro_PU nanocomposite membranes. The samples were found to be homogenous with no spectral change between the repeats of either surface or between surfaces, this supports a homogeneous nanofiller distribution on a macroscale.

Figure 78 shows representative spectra from each nanocomposite membrane's upper surface at each concentration compared against Micro_PU and nanofiller. It was not possible to collect spectra from the dried GO or WW-GO nanofiller due to their dark colouring. The spectra were collected from the wet samples of GO and WW-GO, hence the spectra represent DMF and water, respectively. As the concentration of CNa^{+} increased, the intensity of the band at ~1100 – 1050 cm^{-1} also increased. There is a slight change in the shoulder at ~1050 cm^{-1} for all Micro_PU/CNa^{+} nanocomposite membranes in that they become less sharp and less pronounced. The same occurs for C20, a slight broadening of the reflection at ~1050 cm^{-1} with increases in intensity of reflections between ~1100 – 1050 cm^{-1}, at ~3300 cm^{-1} and between ~2950 – 2800 cm^{-1} as clay concentration increases. There are no relevant shifts in the bands of Micro_PU graphene oxide composites providing no indication of how Micro_PU is interacting with the nanofillers.

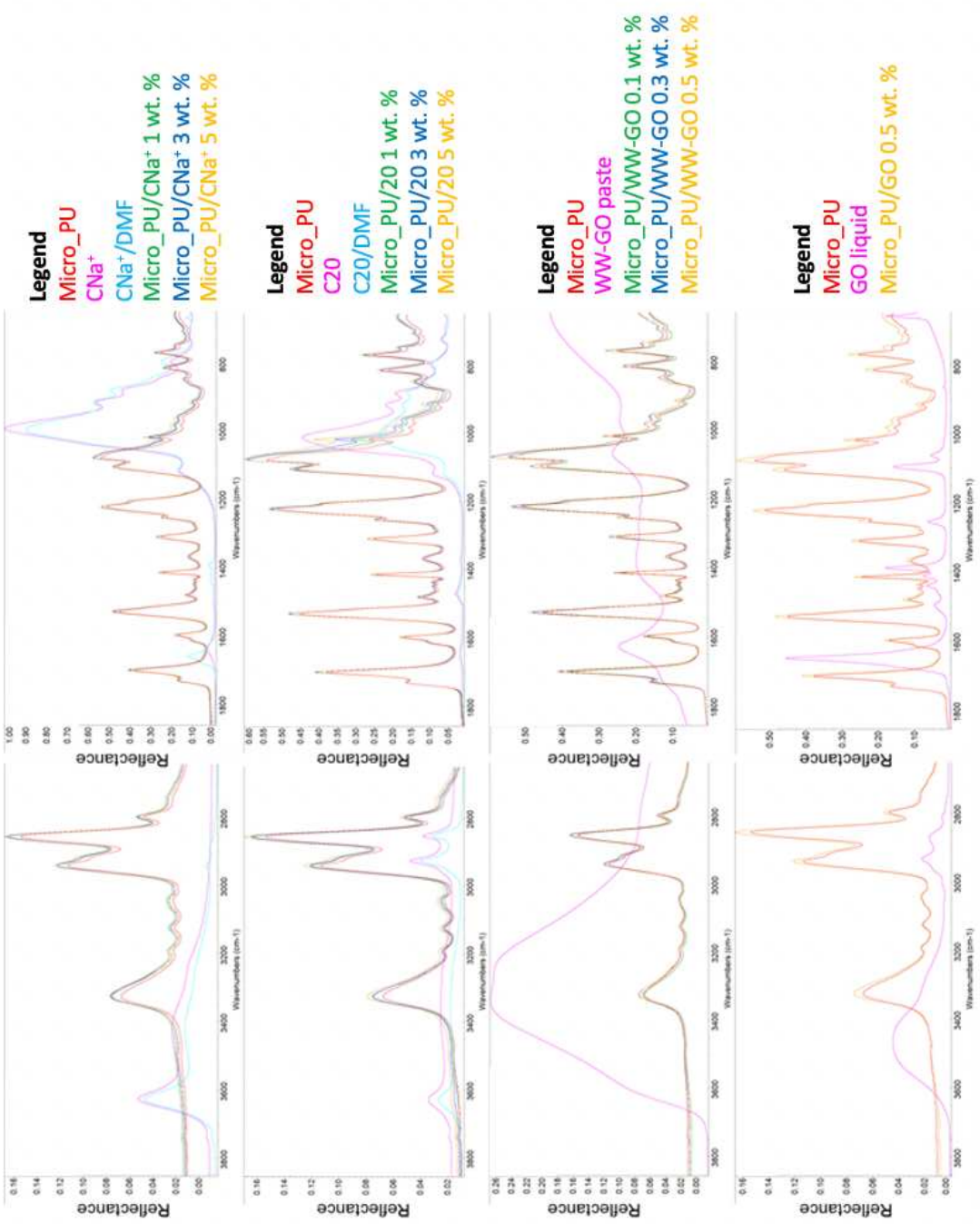

Figure 78. ATR-FTIR overlaid spectra (common scale) of Micro_PU and CNa+, C20, WW-GO and GO nanofillers, dried clay nanofiller with DMF and Micro_PU/CNa+, Micro_PU/C20, Micro_PU/WW-GO and Micro_PU/GO nanocomposite membranes at different concentrations in the region of 3800-2800 cm^{-1} and 1800-800 cm^{-1}.

6.2.1.6 Variation Focus Microscopy

Variation focus microscopy (VFM) was used to characterise, image, and quantify the macro-surface morphology and roughness of Micro_PU nanocomposite membranes. Although SEM shows the surface morphology at a high-resolution, SEM cannot quantify the surface roughness like VFM. Chapter 4 delves deeper into the understanding of VFM

and the current limitations and advantages of VFM vs SEM regarding imaging PU membranes. Comparative to imaging Mono_PU membranes in Chapters 4 and 5, Micro_PU samples within this chapter have a more textured surface due to the porous nature of the samples. This resulted in clearer images of Micro_PU samples compared to Mono_PU (e.g., no holes/missing parts of an image). Figures 79 and 80 present the 3D surface images and pseudo-coloured images while Figures 81 and 82 present the 2D surface images and respective pseudo-coloured images of Micro_PU nanocomposite samples imaged using VFM. The VFM images display a similar topography to those obtained via SEM, but it should be noted that due to the lower resolution of VFM compared to SEM, membrane pores, which were defined in this study as less than 4 µm in diameter are harder to identify. The scale of 2D VFM images is 268 x 200 µm, with a total area of 53,600 μm^2 while SEM images (for the least magnified) are 141 x 122 µm, a total area of 17,202 μm^2. Meaning VFM image area is roughly 3.1 times larger than SEM images with a 50 µm scale bar. As such, the smallest pores identified with VFM range between 1-2 µm and can be seen more clearly in the Micro_PU, 2D images and pseudo-coloured images (Fig. 81 and 82). However, the majority of the visible microporosity are pores between 3-4 µm in diameter and craters larger than 4 µm. VFM of Micro_PU shows the largest craters are 10 µm in diameter. During SEM imaging some craters measuring 6 µm were found in Micro_PU. Table 10 provides the total number of craters observed as well as crater/pore diameters and depths taken from pseudo coloured 2D VFM images.

Micro_PU has a relatively flat surface compared to the corresponding Micro_PU/nanofiller membranes. Micro_PU has many pores and craters ranging from 1 to 10 µm in diameter. Most pores have an average depth ~0.8 µm with maximum depths of up to 1.2 µm (Fig. 82). There is a correlation between pores having shallower depths compared to craters, where typically the larger the crater the deeper it is. The majority of the surface is either flat or has slight protrusions, ranging between 0 to 0.3 µm. There are a few noticeable protrusions of 0.4 - 0.6 µm in height, it should be noted these are far fewer than the pores and craters present. With the addition of nanofillers the number of pores decrease.

VFM images of samples containing CNa^+ are similar to SEM images. Craters are present in all samples with the quantity of craters increasing as clay loading increases. The following description is taken from the 2D pseudo-coloured images in Figure 82. For all three samples the surface remains relatively flat at 0 µm with some slight broad protrusions ranging up to 1 µm in height. Micro_PU/CNa^+ 1 wt. % has 4 craters ranging from 6 to 10 µm with depths ranging from 8-10 µm. CNa^+ 3 wt. % displays several pores and small craters of 6 µm diameter and ~4 µm deep and 4 larger craters, one of which appears to have a more concave nature with shallow side and a much larger diameter than the other craters, the blue region measures 40 µm at its widest points. These craters range from 14 µm to 40 µm and have a depth of 10-14 µm with 1 of them reaching a depth of 16 µm. At 5 wt. % CNa^+ there are several smaller craters from 4 to 8 µm with depths of 2- 4 µm (light blue craters). There are also 10 larger craters ranging from 12 to 45 µm in diameter with depths ranging from 6 to 14 µm.

C20 at 1 and 3 wt. % has a similar topography to Micro_PU than CNa^+ samples, with a surface that has protrusions, pores, and craters. At 1 wt. % C20 there are several pores shaded in light blue and three shaded in dark blue with diameters of 2-3 µm and depths of 1-2 µm, there are also surface protrusions ranging from 0 to 0.5 µm and 5 craters ranging from 4 to 16 µm in diameter and 2-3 µm in depth. C20 3 wt. % has more craters than C20 1 wt. %, with 17 craters ranging between 5 and 27.5 µm in diameter with depths of 2.5 - 4.5 µm. Despite C20 3 wt. % having larger and more numerous craters than C20 1 wt. % the depth of these craters is similar. Surface protrusions range from 0 - 1 µm and several pores are present with diameters of 2.5 - 4 µm and depths of 2-2.5 µm. At 5 wt. % C20 the surface resembles CNa^+ samples as opposed to Micro_PU with a relatively flat surface (no noticeable protrusions) and a range of crater sizes. Again, the number of craters increases as C20 concentration increases, resulting in 25 craters at C20 5 wt. % with a diameter range of >4 to 57.5 µm, they have a range of depths between 3 and 16 µm. Pores are still present and range between 1-4 µm with depths of 1-3 µm.

Micro_PU/WW-GO nanocomposite membranes present a very textured surface, with peaks and valleys which are more pronounced at the lower WW-GO concentrations. WW-GO at 0.1 wt. % has several large protrusions measuring between 12 and 30 µm in

diameter with peaks of 2 to 3 µm. There are numerous pores and craters across the surface, with 37 craters in total measuring >4 to 20 µm wide and 0.5 - 4 µm deep. The pores are between 1- 4 µm wide and 0.5 to 1 µm deep. At 3 wt. % WW-GO there are even more protrusions with a maximum diameter of 17.5 µm and between 2 and 3 µm in height. The number of craters has significantly increased to 57 compared to the lower concentration of WW-GO. Craters are >4 to 35 µm in diameter, despite being larger than 0.1 wt. % WW-GO the craters have the same depth range of 0.5 - 4µm. The pores of 0.3 wt. % WW-GO have the same diameter and depth range as 0.1 wt. % WW-GO. At 0.5 wt. % WW-GO the number of craters reduced to 41, with diameter ranges of >4 - 37.5 µm and depths of 1 - 2.5 µm, and thus shallower craters compared to 0.3 wt. % WW-GO. Again, pores have the same diameter and depth as 0.1 and 0.3 wt. % WW-GO membranes. At 0.5 wt. % WW-GO the number of protrusions has increased compared to 0.3 wt. % WW-GO, there is a similar number of protrusions as there are craters and pores. Protrusions are smaller in height at only 0.5 - 1 µm compared to both 0.1 and 0.3 wt. % WW-GO. Diameter of protrusions for 0.5 wt. % WW-GO ranges from 1-27.5 µm which is larger than the lower WW-GO concentration membranes.

Micro_PU/GO 0.5 wt. % presents a textured surface where the 'bubbled'/'bridged' pores on the surface of the membrane are raised, these were observed under both SEM and VFM. It should be noted that the sharp peaks in Figure 81 (pseudo-coloured 3D) are not a true representation of the surface and likely a limitation of the imaging and processing software of VFM. However, when processed into 2D images (Fig. 82) these sharp peaks are no longer present, indicating they behaved like an edge effect in the 3D images. Due to the very different surface of GO 0.5 wt. % no discernible pores could be identified in VFM (2d images & pseudo colour). Pseudo coloured 2D images show large protrusions of the 'bubbled'/'bridged' pores which average a peak height of 3-6 µm with one protrusion maxing out at 8 µm in height. The largest continuous protrusion measures 100 µm from end to end. Craters are still present within the sample, 24 were identified with a diameter range of 4.5 - 22.5 µm and depth range of 2-6 µm.

Table 10. Number of craters and crater/pore size and depths range taken from pseudo-coloured 2D VFM images (Fig. 82).

	Number of Craters	Size Range of Craters (µm)	Depth Range of Craters (µm)	Size Range of Pores (µm)	Depth Range of Pores (µm)
Micro_PU	17	> 4 -10	0.5 – 1.2	1- 4	0.8 – 1.2
Micro_PU/CNa+ 1 wt. %	4	6 – 10	8 - 10	-	-
Micro_PU/CNa$^+$ 3 wt. %	6	5 – 40	4 – 16	1 - 4	1-2
Micro_PU/CNa$^+$ 5 wt. %	14	> 4 – 45	5 – 14	1- 4	2- 4
Micro_PU/C20 1 wt. %	5	>4 – 16	2-3	2- 3	1-2
Micro_PU/C20 3 wt. %	17	>5 – 27.5	2.5 – 4.5	2.5-4	2-2.5
Micro_PU/C20 5 wt. %	25	>4 - 57.5	3 – 16	1 – 4	1- 3
Micro_PU/WW-GO 0.1 wt. %	37	>4 – 20	0.5 – 4	1 - 4	0.5 – 1
Micro_PU/WW-GO 0.3 wt. %	57	>4 – 35	0.5 – 4	1 – 4	0.5 – 1
Micro_PU/WW-GO 0.5 wt. %	41	>4 – 37.5	1 – 2.5	1 – 4	0.5 – 1
Micro_PU/GO 0.5 wt. %	24	4.5 – 22.5	2- 6	-	-

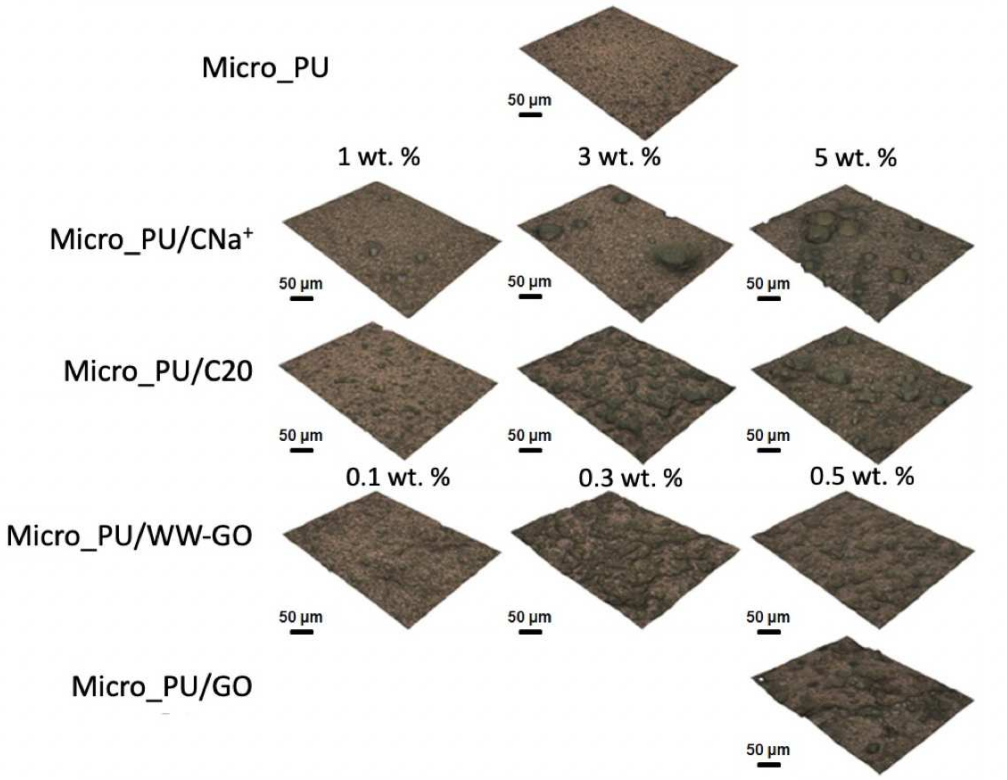

Figure 79. VFM 3D images of top surface of Micro_PU nanocomposite membranes. Scale bar is 50 µm and image dimensions are 268 x 200 µm.

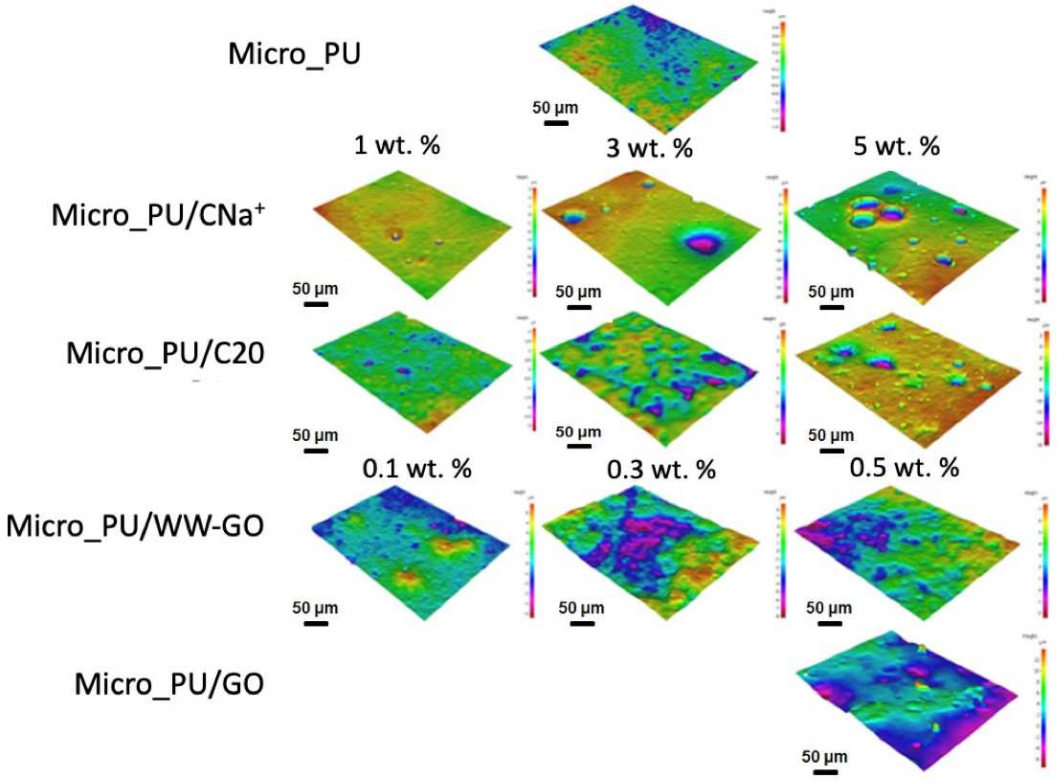

Figure 80. Pseudo-coloured image of Figure 79. Scale bar is 50 µm and image dimensions are 268 x 200 µm. *N.B.* Z-axis varies depending on surface topography. The scale for each image varies and should be noted before comparing samples based solely on the pseudo colouring.

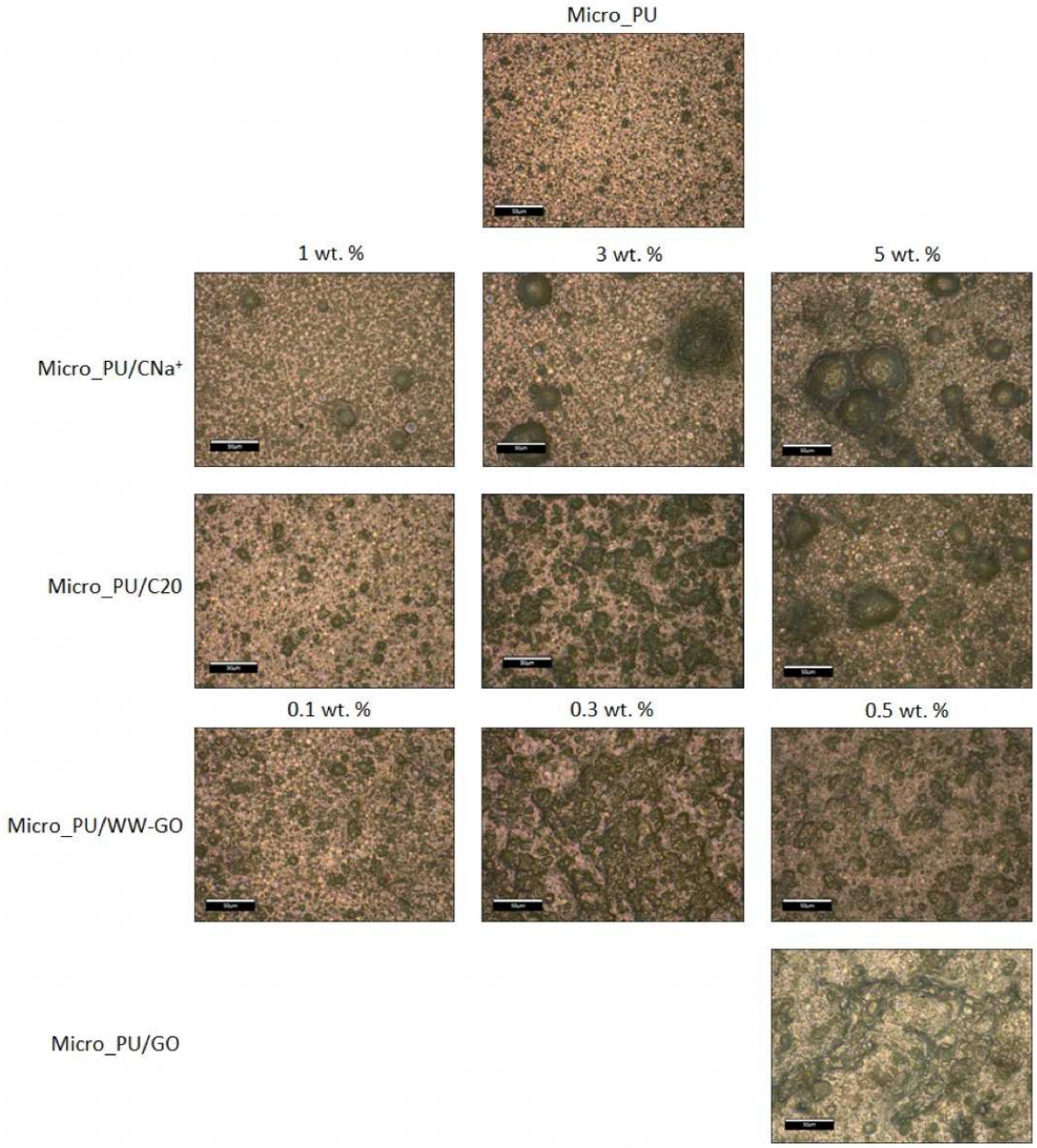

Figure 81. VFM images of top surface of Micro_PU/nanocomposite membranes after processing for S-parameter calculations. Scale bar is 50 μm.

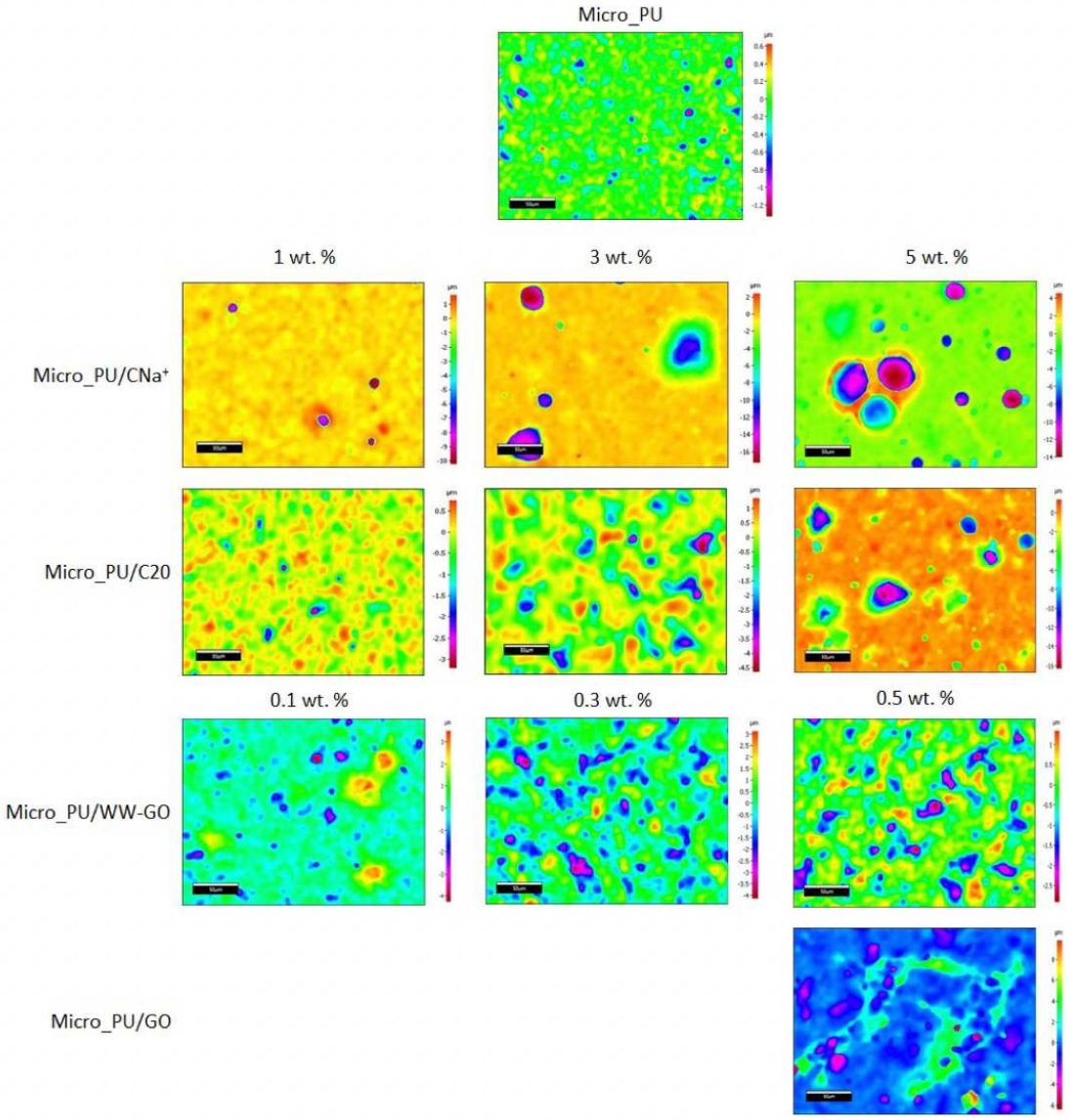

Figure 82. Pseudo-coloured images of Figure 81. Scale bar is 50 μm. *N.B.* The scale for each image varies and should be noted before comparing samples based solely on the pseudo colouring.

Before surface roughness measurements obtained using surface texture measurement analysis are described, it should be noted that typically VFM surface roughness analysis is assessed using the Ra method, this technique is often applied in the very typical uses of VFM, such as analysing the surface roughness of machine parts i.e., drill bits. For this project S-value analysis was utilised as it analyses a set rectangular area vs the Ra method which the user must manually draw a zig-zag line. Due to the nature of manually drawing a zig-zag differences in the length of line and distribution of the measured area changes with every sample, consistent measurements are not possible with this technique. Furthermore, at the time this work was being conducted internal communications with other groups using VFM to analyse and characterise packing

materials, much similar to these membranes than drill bits, S-value analysis was being used.[81] In addition, *Sq* was chosen over Sa due to improved statistical accuracy, *Sq* is the square root of Sa this removes outliers from the data hence the improved accuracy.[92]

Figure 83 presents the surface roughness of the Micro_PU nanocomposite membrane obtained from the root-mean-square height (*Sq*) of the surface area analysis of the 2D images. Micro_PU has a surface roughness of 0.18 µm. The addition of clay and GO nanofillers increases the surface roughness. The addition of CNa^+ at 3 and 5 wt. % produced the greatest increase in surface roughness of 2.97 µm, (1150% increase compared to Micro_PU) and 2.84 µm (1478%), respectively.

The addition of C20 caused a gradual increase in surface roughness as the clay loading increased. C20 at 1 wt. % causes a relatively small increase in surface roughness of 0.29 µm, (61%). This increases to 0.83 µm (361%) for C20 3 wt. %. At the highest clay loading of 5 wt. % the surface roughness is 2.45 µm (1261%).

Micro_PU/WW-GO membranes produced a textured surface in the 3D images, specifically Micro_PU/WW-GO 0.3 wt. % exhibited the most visible texture of the three membranes and in turn the greatest increase in surface roughness of WW-GO samples with an increase of 0.72 µm (400%). WW-GO produced membranes with lower surface roughness than C20 or CNa^+ at higher loading.

Despite Micro_PU/GO 0.5 wt. % having sharp peaks and the 'bubbled'/'bridged' pores the surface roughness was less than samples with high clay loading but greater than WW-GO samples. Micro_PU/GO 0.5 wt. % has a surface roughness of 1.15 µm (539%).

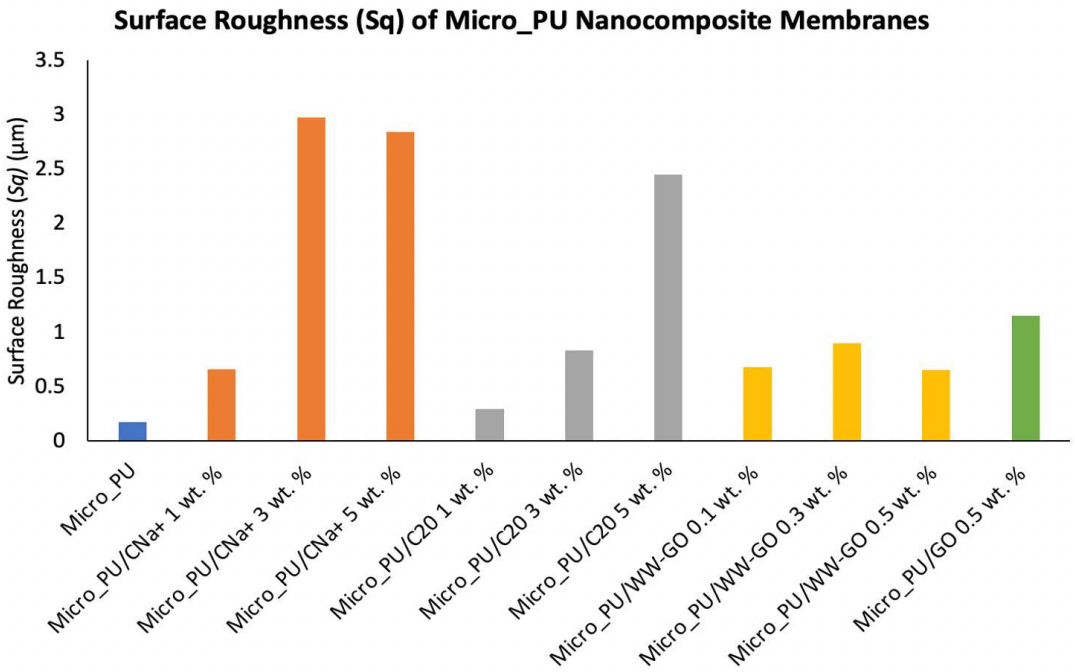

Figure 83. shows the surface roughness values (*Sq*) of Micro_PU nanocomposite membrane obtained from VFM 2D images.

Despite some samples appearing more textured than others when imaged using VFM there appeared to be no correlation between surface roughness and how visually textured the sample surface was. Further analysis to determine what factors contribute to the surface roughness measurements was conducted. Surface roughness measurements for each sample were plotted against five different factors: number of craters, median diameter of craters, median of crater depths, median diameter of pores and median depth of pores. Figures 84 and 85 present all five of these graphs. When the blue and orange dots are closer together the better the correlation.

The strongest correlation of data points is present for median depth of craters vs surface roughness, closely followed by diameter of craters vs surface roughness. Pore depth has a mild correlation. Pore diameter and number of craters have little to no correlation with surface roughness.

It is proposed that the depth of craters and pores as well as diameter of craters is factored into the VFM software analysis while pore diameter and number of craters do not hold weight when VFM software is determining surface roughness.

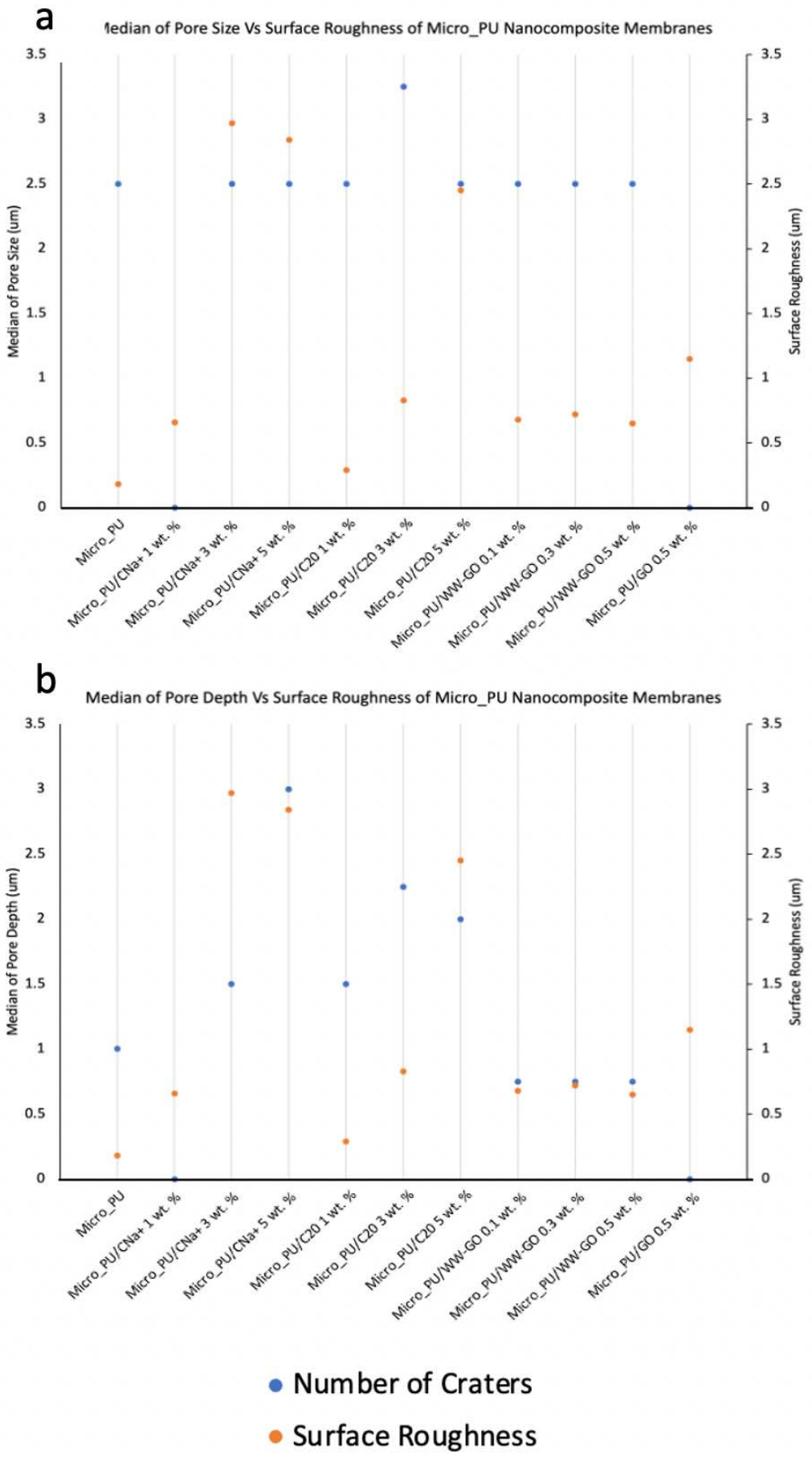

Figure 84. a) Surface roughness measurements plotted against median of crater depths, b) Surface roughness measurements plotted against median diameter of craters

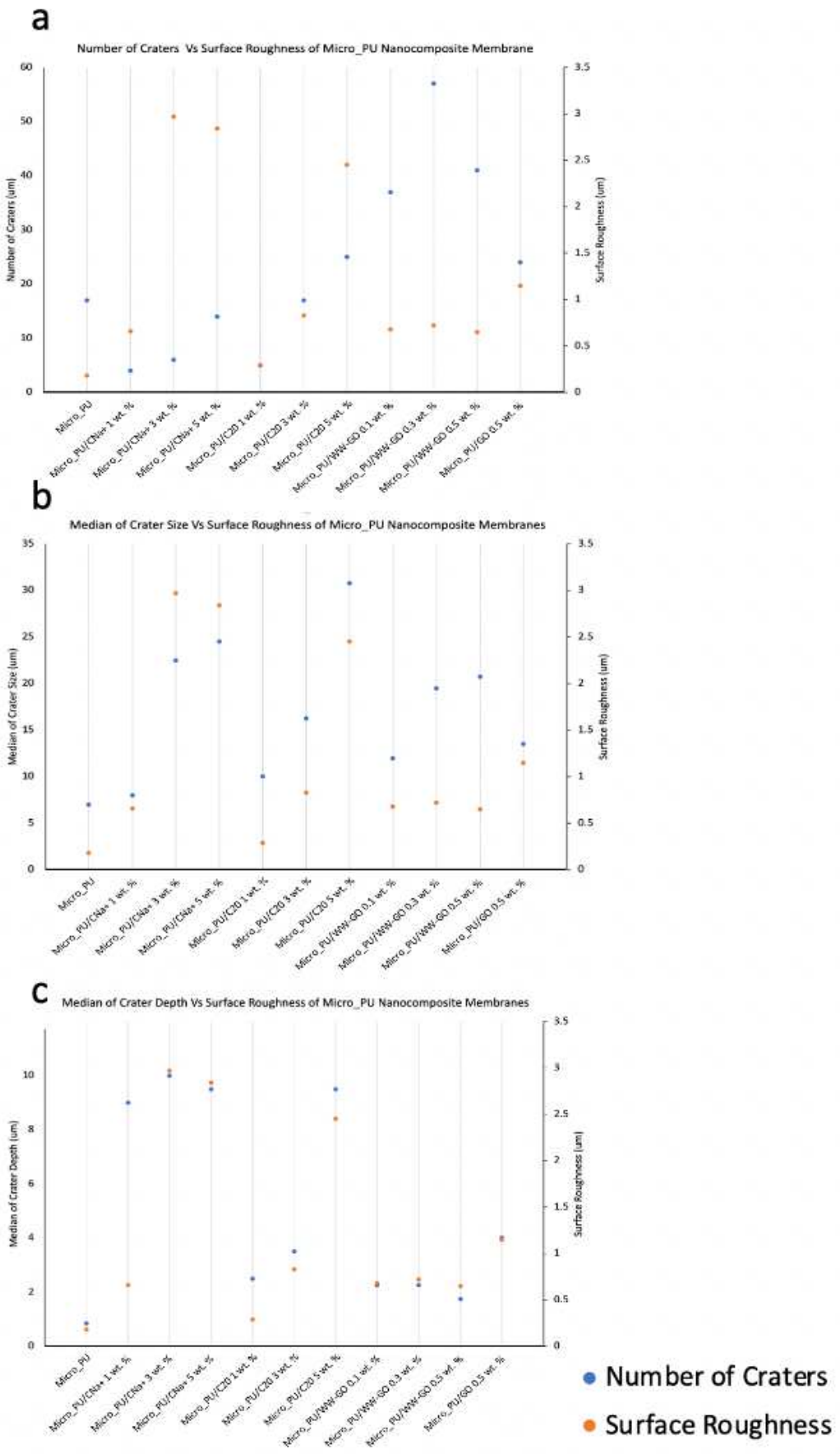

Figure 85. a) Surface roughness measurements plotted against median depth of pores, b) Surface roughness measurements plotted against median diameter of pores, c) Surface roughness measurements plotted against number of craters.

6.2.2 Barrier Properties

Micro_PU is an excellent barrier membrane, it is not permeable to water but due to the interconnected porous structure is breathable to water vapour, in fact it is 41% more breathable than Mono_PU. To assess the effects the nanofillers have on Micro_PU two characterisation techniques were used to understand the barrier properties of Micro_PU nanocomposite membranes. The wettability of the membranes was investigated using contact angle measurements and the breathability assessed using water vapour transmission rates.

6.2.2.1 Contact Angle

The wettability of the Micro_PU nanocomposite membranes was investigated using contact angle measurements, which were taken in triplicate and the average contact angle and standard deviation were calculated (Fig. 86). Micro_PU has a contact angle of 84°, compared to Mono_PU batch 1 and 2 with contact angles of 68° and 75° respectively. The increased contact angle for Micro_PU maybe due to the porous structure creating a rougher surface reducing the wettability of the membrane and/or due to the difference in chemical components within Micro_PU compared to Mono_PU.

The inclusion of clay and GO nanofillers at different concentrations caused an increase in contact angle for most samples. The largest increase of 14% was caused by CNa^+ at 1 and 5 wt. % loading which produced a contact angle of 96°. CNa^+ also provided the largest increase in contact angle within Mono_PU membranes. Another significant increase was caused by C20 3 wt. % of 11%. The addition of WW-GO caused little change to the contact angle of Micro_PU although at 0.5 wt. % WW-GO a 6% increase was observed. Micro_PU/GO 0.5 wt. % reflected the same increase of 6%. Despite GO at 0.5 wt. % loading causing a very different surface morphology to the rest of the samples the contact angle was not significantly affected.

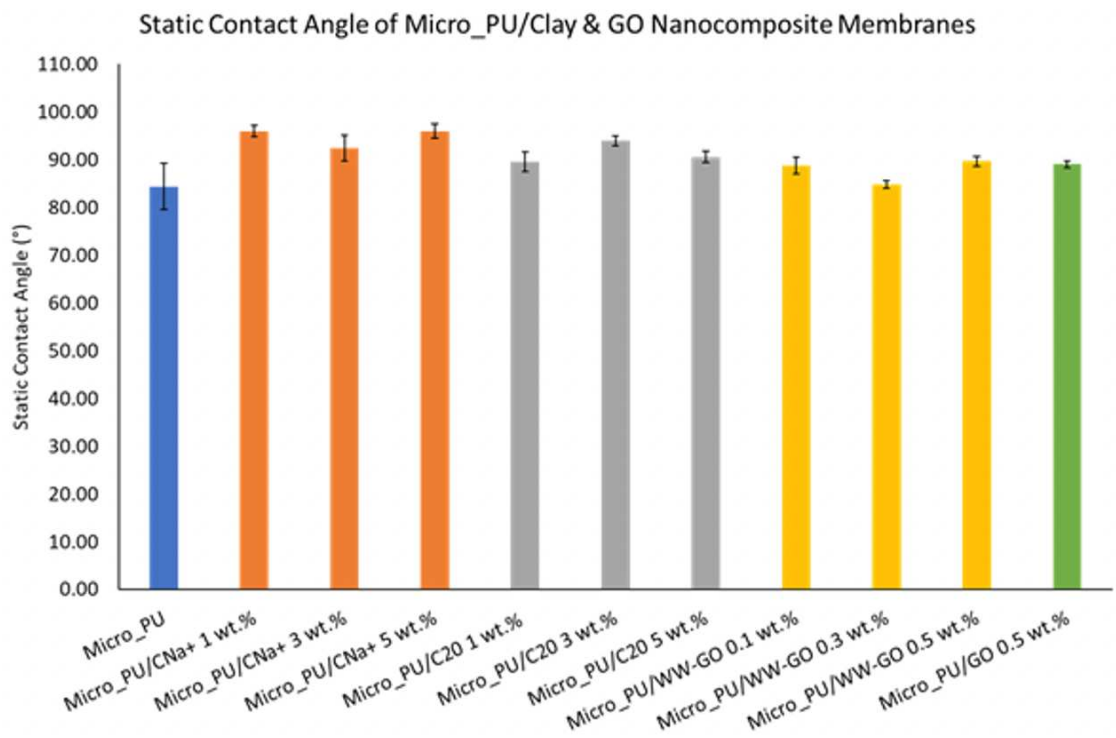

Figure 86. Average contact angle with standard deviation (measured in triplicate) of Micro_PU/clay or GO nanocomposite membranes.

6.2.3.2 Surface Roughness Compared to Contact Angle

VFM was used to assess the macro surface roughness; it was anticipated that an increase in surface roughness would directly relate to an increase in contact angle and thus a decrease in wettability. However, when surface roughness (*Sq*) is plotted against contact angle the trends are weaker than expected (Fig. 87). A general observation is the addition of a nanofiller causes an increase in surface roughness and an increase in contact angle. As the concentration of C20 and CNa^+ increases the surface roughness increases, however this trend is not observed in regard to contact angle. Despite Micro_PU/WW-GO 0.3 wt. % increasing surface roughness more than Micro_PU/WW-GO 0.1 and 0.5 wt. % and Micro_PU/C20 1 wt. % it has a lower contact angle measurement.

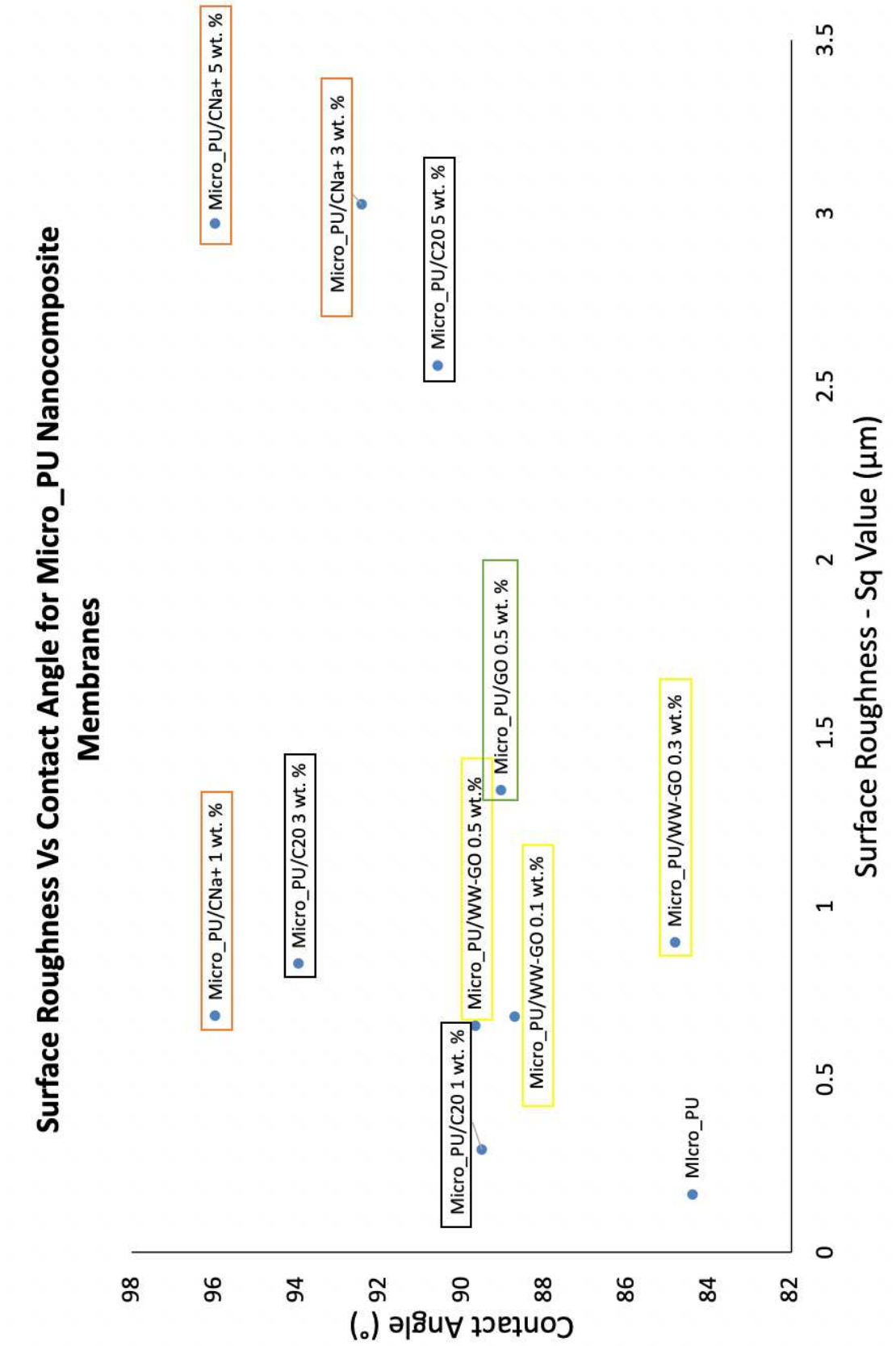

Figure 87. Surface roughness measurements from VFM plotted against average contact angle measurements for Micro_PU nanocomposite membranes.

6.2.3.3 Water Vapour Transmission Rates

For a barrier membrane to remain comfortable when worn the membrane must be permeable to water vapour, the higher the permeability the better. Water vapour transmission rates (WVTR) was used to assess the permeability of Micro_PU nanocomposite membranes, they were measured in triplicate, normalised to membrane thickness, averaged and the standard deviation calculated (Fig. 88). Micro_PU has a WVTR value of 1736 g/m²/24h. The inclusion of clay and GO nanofillers to Micro_PU caused an increase in the WVTR for all samples. The addition of the same nanofillers caused a decrease in the Mono_PU/clay and Mono_PU/GO membranes due to the tortuosity effect (Sections 4.2.2.3 and 5.2.2.3).

Micro_PU/CNa^+ 1 wt. % caused a 109% increase, causing WVTR to increase to 3627 g/m²/24h compared to Micro_PU. WVTR decreased by 95% and 45% for CNa^+ 3 and 5 wt. %, respectively compared to control.

Micro_PU/C20 1 wt. % produced an increase of 71% and has a WVTR value of 2970 g/m²/24h. At 3 wt. % C20 this decreased to a 56% increase in WVTR compared to Micro_PU and at 5 wt. % C20 a 27% increase. Despite having the smallest increase when compared to the other nanofillers, C20 still had a significant improvement on Micro_PU's breathability.

Micro_PU/WW-GO at 0.1 wt. % caused the largest increase of 182% compared to Micro_PU with a WVTR value of 6187 g/m²/24h. Despite producing the largest increase in breathability, as the concentration of WW-GO increased to 0.3 and 0.5 wt. % the WVTR dropped drastically producing only a 17% and 14% increase, respectively when compared to Micro_PU. This is likely due to a bilayer forming and the collapse of the porous membrane as observed in cross-sectional as seen in Figures 71 and 74.

Micro_PU/GO 0.5 wt. % increased WVTR by 159% with a WVTR value of 4500 g/m²/24h. It would be interesting to investigate the WVTR of GO at lower weight percentages as the trend of the other Micro_PU/nanocomposite membranes indicate lower weight percentages produce a greater WVTR.

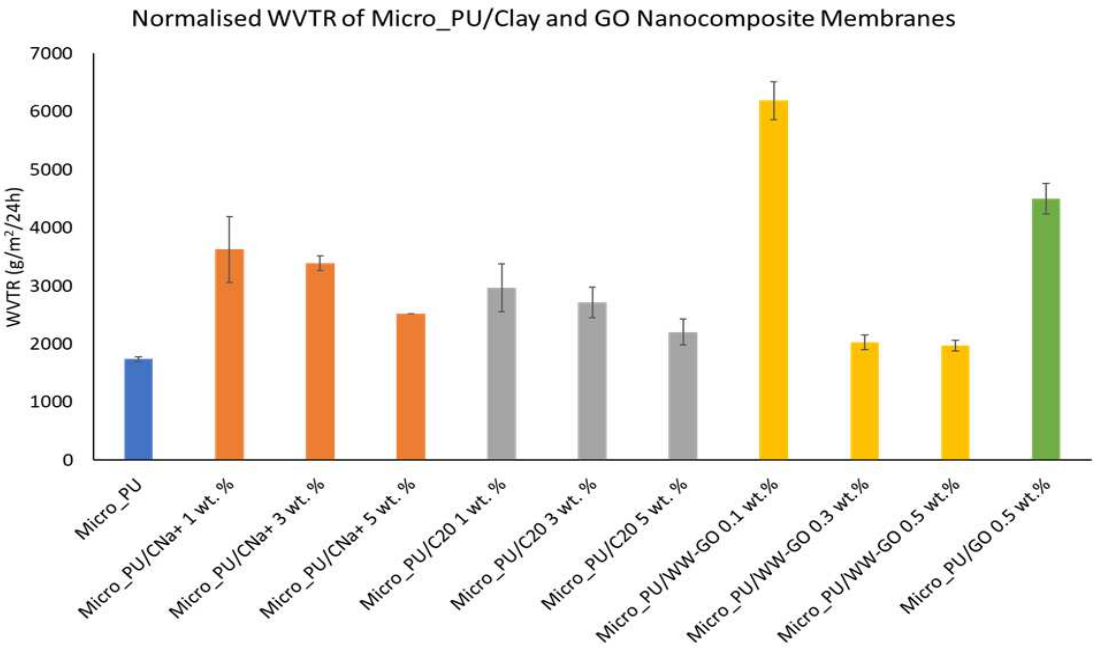

Figure 88. Average WVTR with standard deviation (measured in triplicate) of Micro_PU/nanocomposite membranes. Average WVTR vales normalised against average membrane thickness for each sample.

6.2.3.4 WVTR Compared to Porosity

Various factors involving pore and crater area as well as pore length were obtained from SEM upper surface and cross-sectional images using ImageJ (Table 10), these values were plotted against their respective WVTR measurements for each sample to assess if changes to membrane porosity had any correlation to breathability of membranes. The study found that porous area either with or without the inclusion of crater area has no correlation with WVTR measurements. There are also no correlations between average pore diameter of the upper surface and the WVTR (Fig. 89). However, there is a trend for C20 where increasing clay concentration leads to a decrease in WVTR as average pore length increases. Although this trend is the opposite of what would be expected. When the average pore length of the cross-sectional pores is plotted against WVTR a minor correlation emerges, as average cross-sectional pore length increases WVTR increases (Fig. 90).

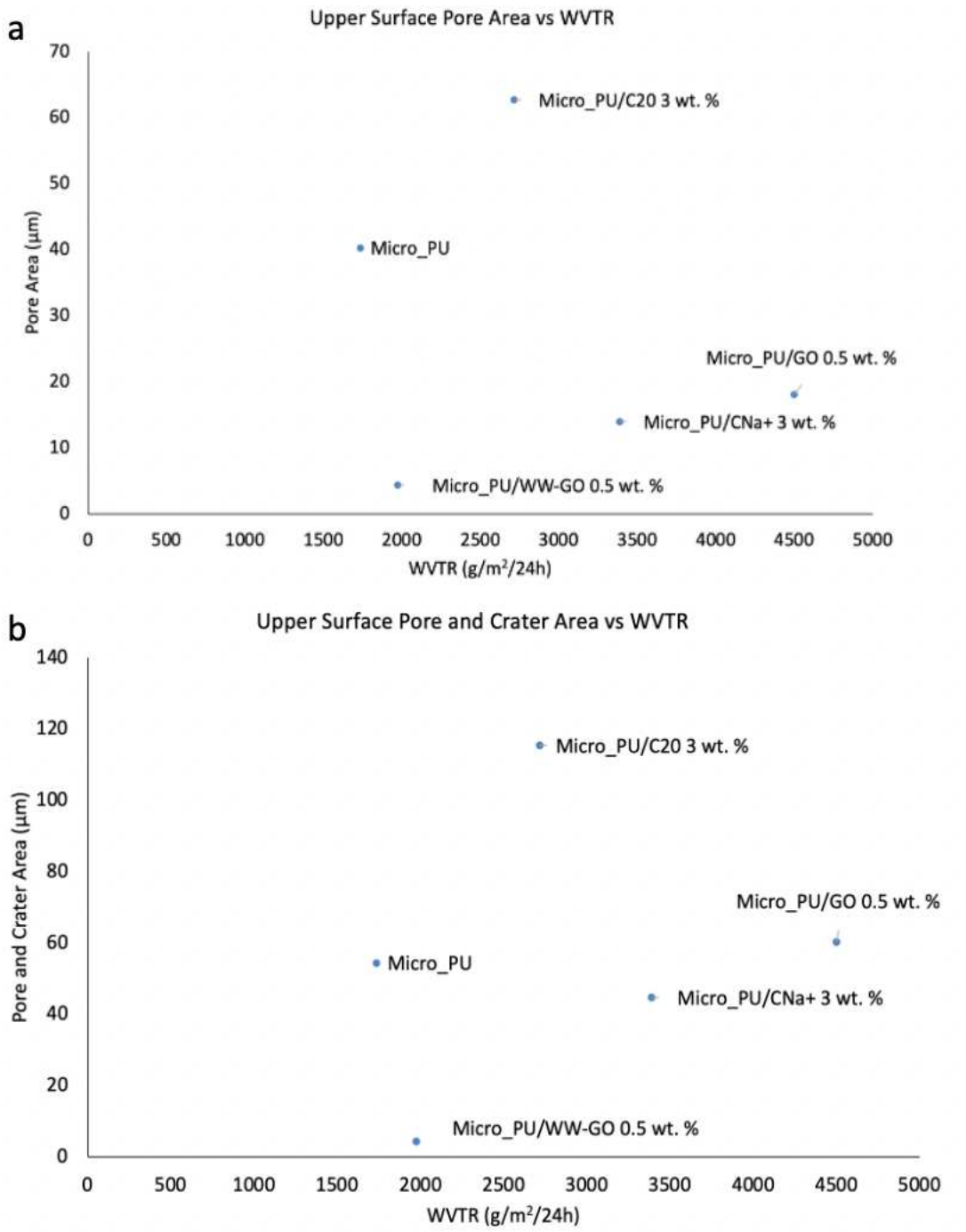

Figure 89. Comparison between average WVTR values and measured porosity obtained from SEM images for Micro_PU and chosen nanocomposite membranes. a) WVTR vs pore area b) WVTR vs pore and crater area

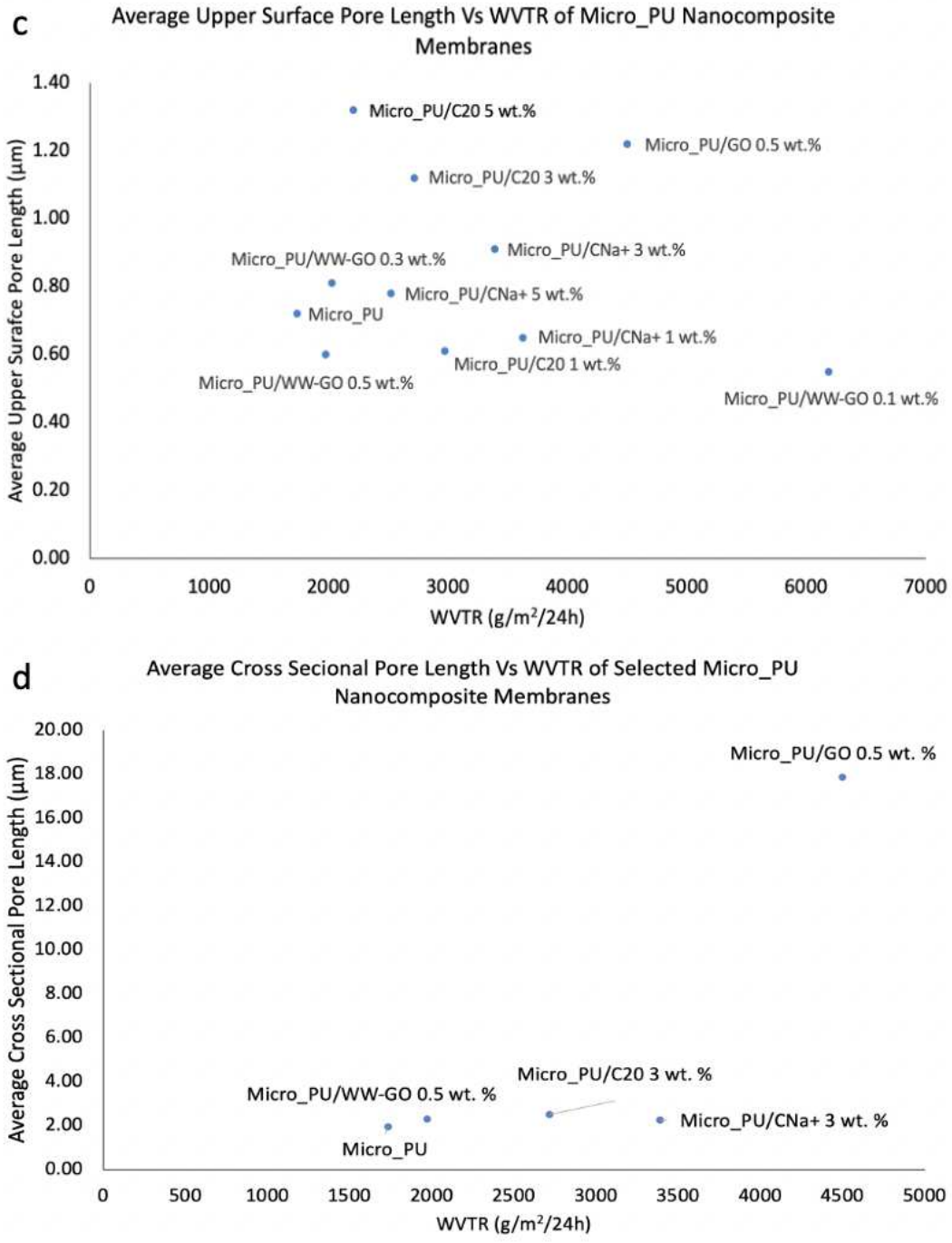

Figure 90. Comparison between average WVTR values and measured porosity obtained from SEM images for Micro_PU and chosen nanocomposite membranes. a) WVTR vs upper surface pore length b) WVTR vs cross-sectional pore length.

6.2.3.5 Contact Angle Compared to WVTR

Contact angle and WVTR were plotted to determine if there were any trends (Fig. 91). Although there was a general trend of addition of nanofillers increased contact angle and WVTR compared to Micro_PU no specific trends regarding nanofiller types or concentrations were found. Both CNa^+ 1 wt. % and WW-GO 0.5 wt. % were determined to be slightly better at improving both breathability and wettability rather than just one property.

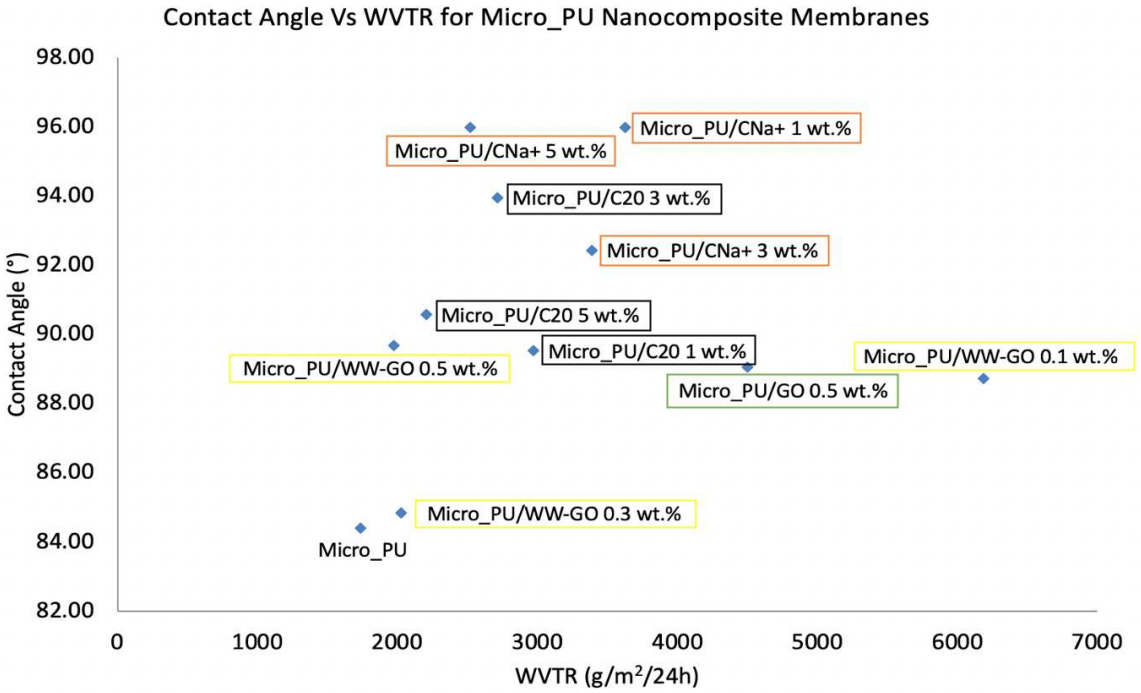

Figure 91. Comparison between average contact angle and average WVTR values for Micro_PU and nanocomposite membranes.

6.2.3 Mechanical and Thermal Properties

Differential scanning calorimetry (DSC) and dynamic mechanical analysis (DMA) was used to analyse the mechanical and thermal properties of Micro_PU nanocomposite membranes. These techniques were used to assess the nanofillers effects on the glass transition temperature, crystallinity, and storage modulus of Micro_PU membranes. Unfortunately, tensile strength could not be performed due to the limited quantity of sample material.

6.2.3.1 Differential Scanning Calorimetry

Differential scanning calorimetry (DSC) was used to assess the melting events of Micro_PU nanocomposite membranes (Fig. 92). Section 4.2.3.1 provides details on the three melting events of PU. With regards to Micro_PU T_{mI} occurred at 179°C, T_{mII} at 198°C and T_{mIII} at 205°C, these three melting events are all at higher temperatures compared to Mono_PU batch 1 and 2 (Table 11). The slight differences in temperatures are likely to be due to the minor difference in polymer batches, and the different chemical structure of Micro_PU. All three melting events (T_{mI} - T_{mIII}) were observed for all Micro_PU nanocomposite membranes, the addition of nanofillers only caused minor variations in temperature of ~0-4°C for all three melting events. T_{mI}, has the greatest temperature fluctuations, a similar trend occurs in Mono_PU/clay and Mono_PU/GO and GNP nanocomposite membranes (Sections 4.2.3.1 and 5.2.3.1).

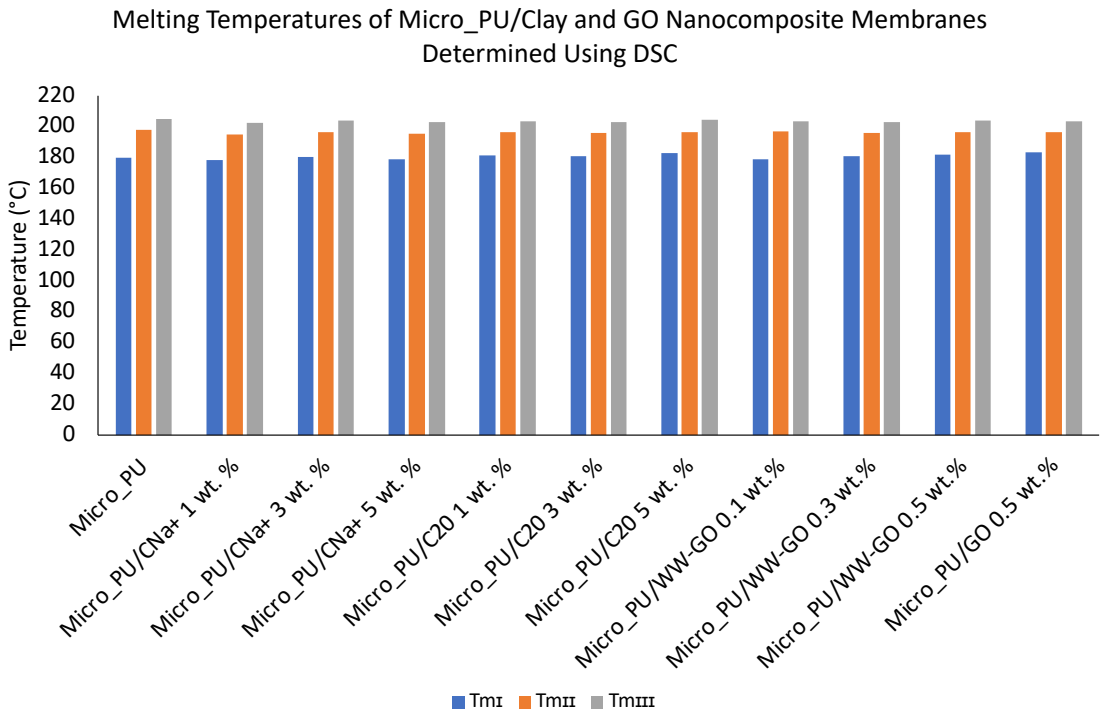

Figure 92. Melting onset temperature of three melting events for Micro_PU/clay and GO nanocomposite membranes determined using DSC.

Table 11. The three different melting temperatures of Micro_PU, Mono_PU_Con batch 1 and Mono_PU_Con batch 2 (Sections 4.2.3.1 and 5.2.3.1).

	T_{mI}	T_{mII}	T_{mIII}
Micro_PU	179°C	198°C	205°C
Mono_PU_Con batch 1 (Chapter 4)	170°C	195°C	201°C
Mono_PU_Con batch 2 (Chapter 5)	173°C	194°C	201°C

6.2.3.2 Dynamic Mechanical Analysis

The viscoelastic properties and thermal transitions of Micro_PU nanocomposite membranes were investigated using DMA, which was performed from -100°C to 120°C. DMA provides information on the membranes' storage modulus (elastic modulus, G') and tan δ (damping coefficient, tan δ). The storage modulus values at both -5°C and 40°C and T_g value were determined.

As with both the Mono_PU/clay, GO and GNP nanocomposites detailed in Sections 4.2.3.2 and 5.2.3.2, no significant changes or trends were observed for the storage modulus of Micro_PU/clay and GO nanocomposites compared to Micro_PU.

However, with regards to the T_g discussed within chapter 4 section 4.2.3.2, Micro_PU samples only displayed a single well defined T_g event in comparison to Mono_PU nanocomposite samples that displayed two well defined T_g events referred to as T_g (S) and T_g (H). Figure 93 presents DMA data of Micro_PU evidencing only one well defined T_g compared to the two T_g events observed in Section 4.2.3.2, Figure 44. It is proposed this is due to the difference in polymer chemistry between Mono_PU and Micro_PU. As with the Mono_PU nanocomposites in both Chapter 4 and Chapter 5 the addition of clay and GO nanofillers to Micro_PU induced no trends nor significant changes.

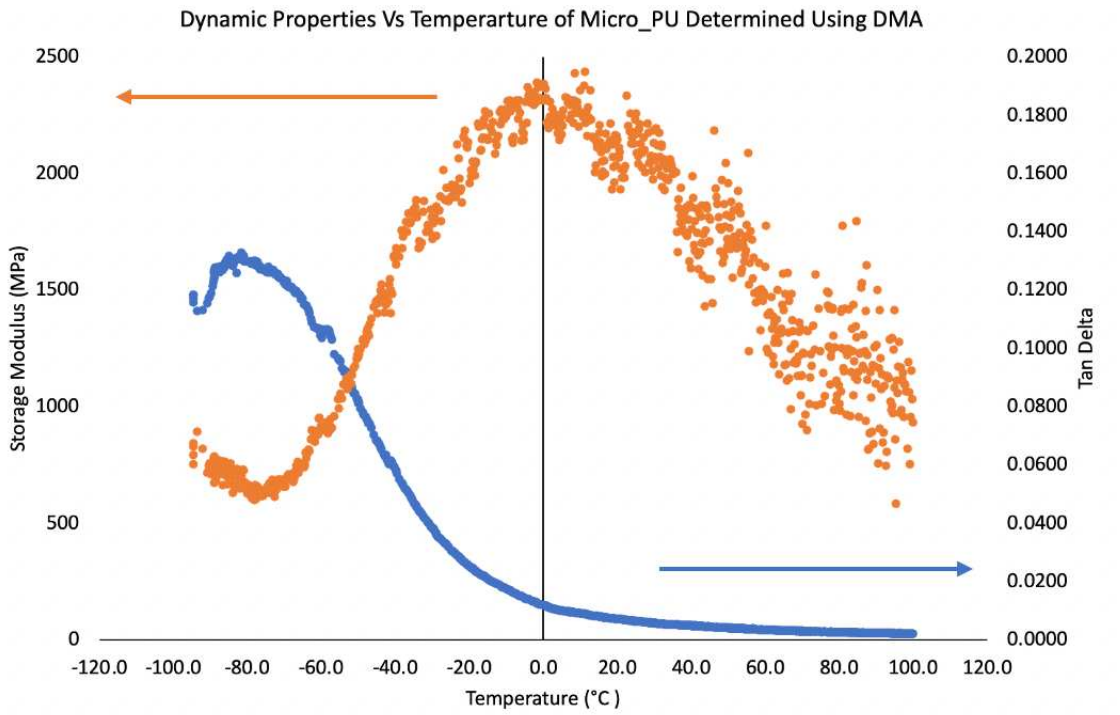

Figure 93. Storage modulus and tan δ of Micro_PU from -100°C to +100°C. Orange line represents storage modulus and blue line tan δ.

6.3 Discussion

XRD and SEM/EDX showed CNa^+ had a mixed dispersion, partly intercalated and partly a micro-composite with some clay aggregation. CNa^+ did not disperse as well as C20 in Micro_PU. SEM/EDX showed no signs of aggregation and XRD data suggested an exfoliated system for Micro_PU/C20. Further analysis with TEM would be required to confidently state if an exfoliated system was present. Analysis of SEM images shows the addition of clay nanofillers reduced the quantity of pores present. SEM of Micro_PU/clay membranes show pores remain evenly distributed across the membrane. The average pore size decreased compared to Micro_PU samples at low clay loading (0.1 wt. %), at higher clay loading (3 and 5 wt. %) the average pore size increased.

XRD indicated WW-GO and GO were very well dispersed and possibly exfoliated into Micro_PU, a similar result was found in Mono_PU/GO and WW-GO membranes. However, SEM and SEM/EDX indicated the possibility that WW-GO and GO were not exfoliated due to observed craters, collapsing porous structure, and 'bridged' pores. SEM/EDX images indicated that GO, although not aggregated, is possibly dispersed in higher concentrations within the 'bridged'/'bubbled' porous walls. SEM and SEM/EDX

of surface porosity displayed several instances of large defects, craters and 'bridged' pore, this was most prevalent in the Micro_PU/GO 0.5 wt.% membrane. SEM/EDX of Micro_PU/GO 0.5 wt. % indicated that GO may be dispersed in higher concentrations within the 'bubble'/'bridged' porous walls (Fig. 76). Furthermore, SEM/EDX indicated that surface defects in Micro_PU had been caused by agglomerates of CNa^+ 3 wt. % and WW-GO 0.3 wt. % nanofiller (Fig. 76). A possible explanation for these large defects is poor dispersion, internal communication regarding the formation of microporous membranes indicated that poorly dispersed additives have previously caused the formation of large surface defects in Micro_PU, such as those observed in Micro_PU/WW-GO 0.3 wt. % and Micro_PU/GO 0.5 wt.% membranes. This is likely due to the more complex structure of Micro_PU and the increased chemical sensitivity of the polymer batch to changes in chemical composition as indicted by other internal communications. This raised concerns that GO and WW-GO nanofillers are not as well dispersed as XRD initially indicated. It was considered that the concentration of GO nanofillers were too low to be identified using XRD. However, XRD of Mono_PU/GO and GNP membranes reduced this concern as GNP was poorly dispersed in Mono_PU and presented with clear reflections in XRD. This offered reassurance that XRD can distinguish between dispersed and intercalated GO or GNP samples at low concentrations. Another explanation is that the 'bridged' pores form when polymer bubbles are formed on the membrane surface during the coagulation process and escaping DMF, these polymer bubbles pop causing a crater and/or 'bridged' pore.

SEM images of the membranes cross-section indicate that the addition of nanofillers disrupts the formation of the porous network. SEM and EDX images clearly display that poorly dispersed nanofillers such as CNa^+ directly cause issues with pore formation due to the aggregation of the nanofiller (Fig. 77). In addition, it is possible that the formation of craters and 'bridged' pores are the result of nanofillers disrupting the coagulation process, with higher density of nanofiller found in the region of craters and 'bridged' pores via SEM/EDX. Additional experimentation and optimisation of the sample preparation and membrane casting process would be required to reduce the unwanted disturbance of the nanofiller on membrane porosity.

It was initially thought that craters were directly caused by agglomerates of nanofillers in the same way the large defects in Figure 76 were. However, SEM/EDX of the membrane surface did not show increased nanofiller concentration around craters (Fig. 75). Images of Micro_PU/CNa^+ 3 wt. % indicates some aggregation around a large pore underneath the surface (circled in red, Fig. 75). Which relates to cross sectional SEM/EDX of CNa^+ 3 wt. % of a large surface crater which expanded downwards creating a hole in the interconnected porous structure which was likely caused by an agglomeration of CNa^+ (Fig. 77). This was not observed for other nanofillers subjected to EDX analysis of the cross-sectional SEM images (Fig 77). C20, unlike CNa^+, was well dispersed, causing the smallest change in porosity compared to other nanocomposites. The cross-section of Micro_PU/C20 3 wt. % was very similar to that of Micro_PU, except pores were less numerous, slightly larger with more variation in length. Whereas pores of Micro_PU/CNa^+ 3 wt. % were less defined and had begun to lose their circular shape.

One reason proposed for the poorly dispersed GO and WW-GO is the platelets have dried out and stacked together during the mixing process, possibly at the side/edge of the solution which would prove difficult to re-disperse in the polymer again. This indicated the current mixing method is not optimum. Attempts were made to improve dispersion by using a triple roll mill after initial mixing with a Dispermat®. Samples were collected after every pass through the triple roll mill up to seven passes. In each pass DMF was lost, samples become thicker and opaquer which indicates enhance dispersion. Despite initial assessments indicating promise, a detailed investigation of this method was not possible due to Covid. When laboratories reopened samples were no longer suitable for testing. It should be noted that with regards to industrial scale up the Dispermat® method was the most functional, transferable, and cost effective compared to introducing an additional step and equipment such as triple roll mill.

Poor dispersion of CNa^+ was partly credited to the use of a Dispermat® not being the optimal mixing method as stated above. In addition, CNa^+ is a bentonite clay, which are inherently impure with containments present. It should be noted that CNa^+ is a relatively pure bentonite and is cheaper than organo-modified clays investigated within this thesis, hence the reason it was chosen. Much like CNa^+ it is also possible that WW-GO

and GO nanofillers contained contaminates which may have resulted in large defects observed.

Figure 62 indicated the addition of WW-GO and GO affected the formation of a homogenous microporous membrane compared to the addition of C20 and CNa^{+}. Membranes with GO had more transparent areas (pores collapse/failed to form) than clay samples. As concentration of WW-GO increased more transparent areas appeared (Fig. 62). SEM of Micro_PU/WW-GO 0.5 wt. % cross section found the bottom layer of the membrane had begun to collapse with some areas fully collapsed (Fig. 74). It is proposed that as the concentration of WW-GO increased from 0.1 wt. % to 0.5 wt. % the membrane becomes a bilayer, within the bottom layer pores begin collapsing. This is likely why WVTR decreased by 68% between Micro_PU/WW-GO 0.1 wt. % and 0.5 wt. %. This could be due to the tortuosity effect from the nanofillers however the decrease in WVTR for WW-GO samples is drastic, unlike other samples were WVTR decline gradually as nanofiller concentration increased. However further cross-sectional SEM analysis of WW-GO 0.1 wt. % and 0.3 wt. % would be required to evidence this. When relating the cross-sectional SEM of WW-GO 0.5 wt. % to the upper membrane surface SEM images and analysis it is speculated that the decrease in pores piercing the surface and the pore area decreasing is related to the collapsing of the cross-sectional porous structure. When the membrane forms it is likely DMF escapes through the pores that pierce the surface. If the porous surface area is low, as is the case for WW-GO 0.5 wt. %, DMF may become trapped in the membrane which may have led to the formation of the bilayer and the collapse of the porous network. It should be noted that although a bilayer microporous membrane for the application of protective apparel is likely undesirable there are some applications where a bilayer is advantages. For example, adopting a biodegradable bilayer membrane has proven to overcome challenges with subpar mechanical performance of biodegradable single layer membranes.[159,160]

The more open sponge-like porous structure of Micro_PU/GO 0.5 wt. % observed in cross-sectional SEM (Fig. 71) may have been integral to the 159% increase in WVTR compared to Micro_PU. Despite the unusual cross-sectional structure there were positive changes to the storage modules with an increase of 44% at -5°C and 69% at 40°C compared to Micro_PU.

VFM imaging supports SEM images, surface texture is similar between the two techniques, indicating both provide reliable images of membrane surfaces at two different resolutions. 2D VFM images are 268 x 200 µm, thus the total area is 53,600 μm^2 while SEM images (for the least magnified) are 141 x 122 µm, an area of 17,202 μm^2. VFM image area is roughly 3.1 times larger than SEM images with a 50 µm scale bar. SEM provides almost nano-scale imaging, excellent for identifying and analysing sample porosity (pores ≥0.2 µm have been observed) while VFM provides macro-scale imaging of large pores (1-4 µm) and a greater focus on surface craters (>4 µm) with the additional benefit of craters and pore depth analysis. When comparing Table 9 summarising analysed SEM images for craters and pores to the equivalent VFM data in Table 10 the difference in resolution is clear to see, VFM identifies a far greater number of craters compared to SEM, 17 craters for Micro_PU using VFM compared to 0 craters observed using SEM. The quantity of pores identified using VFM was determined to be unreliable given the low resolution. VFM indicated that increasing clay loading had a positive correlation to increasing quantity of craters. WW-GO at all concentrations had the most craters of any other nanofiller. WW-GO 0.3 wt. % has 57 observed craters while SEM images for the same sample only identified 1 crater. Individually each technique, VFM and SEM, could skew the perception of a surface topography however when used synergistically they can provide a clearer understanding of surface topography.

Due to the increased surface texture of Micro_PU samples imaging via VFM was far more reliable with no missing areas, optimisation was easier and more efficient compared to Mono_PU samples. VFM is no longer being pushed to it limitations however, the addition of nanofillers sees a decrease in pores with craters becoming more prominent, this potentially limits VFM capabilities to image pores.[76,78]

Unlike SEM, VFM analysis allowed for the depth of large pores and craters to be assessed, a correlation was observed between pores having shallower depths compared to craters, typically the larger the crater the deeper it is, however there are some exceptions. 16 µm was the observed maximum depth of a crater found for both CNa^+ 3 wt. % and C20 5 wt. % samples. Meanwhile maximum pore depth was 4 µm for craters in a sample containing CNa^+ at 5 wt. %.

Micro_PU has a relatively flat surface compared to the nanocomposite membranes, with many pores and craters ranging from 1 to 10 µm, pores have an average depth of ~0.8 µm with maximum depths of up to 1.2 µm (Fig. 82). VFM vertical resolution can range from several um down to 10 nm the range is dependant om the chosen objective and sample type.[161,162] As concentration of CNa^+ increases the number of craters and their respective diameters increases. The same occurs of C20 samples, with increasing crater depth too. For clay samples pore diameter and depths are similar across all six samples except for C20 at 1 and 3 wt. % where no pores under 2 µm were identified using VFM. WW-GO and GO produce a high number of craters from 24 – 57 depending on the sample. Despite large crater diameters for GO samples reaching maximums of 37.5 µm for WW-GO at 0.5 wt. % the crater depth remains shallow at only 1 - 2.5 µm. Other GO samples do indicate crater depths of up to 6 µm but this is still relatively shallow compared to clay samples with a maximum crater depth of 16 µm. It appears that while GO and WW-GO samples visually indicate a heavily textured surface in both VFM and SEM images, the peaks and valleys of this surface are far shallower than they initially appear. This could infer why the surface roughness measurements for GO and WW-GO sample are in the middle compared to other Micro_PU membranes studied.

Micro_PU has a surface roughness of 0.18 µm. This is smoother than the *Sq* value for Mono_PU_Con batch 1 of 0.31 µm in Section 4.2.1.5 and Mono_PU_Con batch 2 of 0.12 µm in Section 5.2.1.4. As previously discussed, the *Sq* values for Mono_PU_Con batch 2 and Mono_PU/GO and GNP nanocomposites cannot be compared to other membrane samples due to edge effects of 'holes' skewing the surface roughness measurements. It is possible that Micro_PU has a lower surface roughness value than Mono_PU_Con batch 1 due to VFM's limits to assess the almost nano-scale roughness of polymer surfaces due to resolution limitations that focus on the macro-scale.[78]

In Section 4.2.1.5, CNa^+ 3 wt. % produced the largest increase in surface roughness compared to Mono_PU_Con batch 1 of 70%, with a value of 0.53 µm. Within this chapter, CNa^+ 3 wt. % was also responsible for the largest increase in *Sq* with a value of 2.97 µm a 1550% increase compared to Micro_PU. Surface roughness increased as C20 concentration increased with a maximum surface roughness of 2.45 µm (1261%) at 5

wt. % C20. Despite WW-GO producing the most visually textured surface topography the assessed surface roughness was low with only a 400% increase (0.72 μm) for WW-GO 0.3 wt. % compared to Micro_PU. Again, despite Micro_PU/GO 0.5 wt. % 'bubbled'/'bridged' pores the surface roughness was less than samples with high clay loading but greater than WW-GO samples. Micro_PU/GO 0.5 wt. % has a surface roughness of 1.15 μm, 539% increase compared to Micro_PU.

There is very little literature available regarding VFM surface roughness measurements on thin films, membranes, or polymers. Comparison of this study to those within the literature is further hindered by the range of parameters (e.g., R-parameters, S-parameters etc.) generated by VFM analysis. Only papers that supplied the *Sq* values of their samples are discussed and compared to the membranes tested within this thesis. A study investigating the surface roughness using VFM of abrasive tools i.e., microfinishing film type (IMMF) made from aluminium oxide, had a *Sq* value of 4.16 μm, results were considered robust and reliable.[69] The surface roughness of micro metal injection moulding (MIM) found *Sq* values ranged from 0.2 μm to 2 μm depending on the processing procedure of the different MIM's, results were considered robust and reliable.[74] Different VFM instruments compared to AFM measurements for unknown polymer surfaces found the *Sq* ranged from 0.084 μm to 0.18 μm, when validated there were significant deviations from the reference AFM standard thus questioning the reliability of surface roughness measurements in the nano-scale range.[78] These studies suggest VFM is capable of providing reliable *Sq* values within the macro-scale range from 0.2 μm upwards. While 0.18 μm and below falls into the sub macro-scale or nanoscale range and is deemed unreliable when validated against AFM. Within this thesis *Sq* values ranged from the sub-macro scale to macro-scale specifics are as follows; Mono_PU/clay nanocomposites *Sq* value ranged from 0.10 μm to 0.53 μm. Mono_PU/GO and GNP nanocomposites *Sq* value range from 0.31 μm to 0.64 μm and Micro_PU nanocomposite membranes *Sq* value ranged from 0.18 μm to 2.97 μm. Across all samples the lowest *Sq* values were for Mono_PU batch 2 and Micro_PU membranes these were in the sub macro-scale ($\leq$ 0.18 μm) thus the reliability of these values is called into question when compared to the literature. However, all other samples had an *Sq* value above 0.2 μm, the addition of nanofillers caused significant increases in *Sq* values, thus it can be inferred from the literature that these results are robust and reliable. This thesis

expands on the previous Tosello *et al.,* study by delving deeper into VFM analysis on different polymer surface topographies presenting a better understanding of VFM's limitations and possibilities.[78] This study infers VFM is a useful technique for quantifying the surface topography of polymer membranes, but the degree of smoothest of the membrane is an important consideration. The more textured the polymer surface the more reliable and robust VFM imaging and areal surface measurements (*Sq*). VFM should be used on polymer membranes with a surface roughness in the macro-scale for reliable results.

Despite some samples appearing more textured than others when imaged using VFM and even SEM there appeared to be no correlation between *Sq* values and how visually textured the sample surface appeared. With the novelty of VFM as a surface roughness analysis technique for relatively flat polymer samples it was key to understand which surface topographies factor into VFM calculations regarding *Sq* values. Surface roughness measurements for each sample were plotted against five different factors: number of craters, median diameter of craters, median of crater depths, median diameter of pores and median depth of pores (Fig. 84 and 85). This analysis indicated that the depth of craters and pores as well as diameter of craters is factored heavily into the VFM software analysis while pore diameter and number of craters do not hold weight when VFM software is determining surface roughness. This in collaboration with literature suggests due to VFM's lower resolution than AFM the surface roughness analysis is limited to the macro-scale thus alienating pores less than 1 µm which have been identified using SEM.[78] This further supports the previous statement regarding discrepancies in VFM's *Sq* values between Mono_PU_Con batch 1 and Micro_PU.

As discussed, VFM resolution is on the macro-scale while SEM is almost nanoscale, this limits VFM to large pores and craters while SEM has identified pores of 0.8 µm and larger. However, unlike SEM, VFM provides a 3D mapped image which provides an additional axis of information, indicating the depth of pores and craters imaged. This has proved particularly useful for samples like Mono_PU/CNa^{+} 5 wt. % where it is challenging to distinguish the peaks and troughs from flat SEM images alone. Additional imaging using VFM supports SEM images and indicates a homogenous membrane along with FTIR analysis.

With regards to these particular Micro_PU membranes initial optimisation required time; however, it was not as time consuming as optimising the imaging method for Mono_PU membranes which encountered issues with imaging due to their relatively flat surface texture. The established method was easily applied to Micro_PU samples and VFM analysis was fast and effective taking approximately 2 minutes per sample including accessing 3D and 2D images plus pseudo-coloured images and surface roughness measurements. Whereas SEM imaging incurred issues with charging for both flat and cross-sectional samples. To reduce the effects of charging allowing for a crisp SEM image and accurate SEM/EDX maps, a more time-consuming sample preparation step was used. Imaging via SEM could take between 10-20 minutes per sample, while running an EDX map takes an additional 30 minutes per sample. Furthermore, analysing SEM images using ImageJ is tedious and time consuming and required non-standard methods of data presentation e.g., pore diameters with large standard deviations as well as box and whisker plots. Attempts to automate analysis via Image J as per internal communications was not suitable for these samples leading to inaccurate analysis. Therefore, analysis of SEM image using ImageJ required not only time but was also at risk of human error and bias. These issues are not present using VFM surface roughness however identifying craters and pores, relevant diameters and depths is open to interpretation, though analysis time is shortened by pre-pseudo-coloured images produced via VFM. A step normally taken using ImageJ for analysing SEM images.

When comparing VFM and SEM it is important to remember each technique offers a specific analysis technique the other one does not. VFM informs on the surface roughness of the sample, quantifying the surface topography into a singular value. While SEM/EDX can be used in conjunction with XRD to analyse the dispersion of nanofillers within Micro_PU. Furthermore, it provides a visually on how aggerates of nanofillers can directly impact the surface and cross-sectional porosity of Micro_PU nanocomposite membranes. Individually each technique is adequate but together they provide a clear synergistic approach to qualitative and quantitative analysis of surface topography and the inter-connected porous structure.

While the addition of CNa^+ at both 1 and 5 wt. % to Micro_PU increased contact angle by 14% to 96° however the addition of nanofillers (clay, GO and GNP) to Mono_PU samples did not significantly change the contact angle. This may indicate that the chemistry/polarity of the different nanofillers does not affect the contact angle of the membranes but rather the surface tension or the porosity/surface roughness.[132] In addition, C20 is a more organophilic clay than CNa^+, but lower contact angles are observed for the former. One may expect higher contact angles with C20, therefore the organomodifier either has little influence or other factors are more dominant. Hence one of the reasons VFM was employed to explore the effect of other factors on contact angle such as surface roughness.

Micro_PU has a contact angle of 84°, this increased with the addition of clay and GO. The largest increase occurred with the inclusion of CNa^+ at 1 and 5 wt. % loading which produced a contact angle of 96°. CNa^+ also provided the largest increase in contact angle within Mono_PU membranes. Mono_PU/WW-GO 0.1 wt. % produced the largest increase of all GO and GNP nanofillers of 4° when compared to Mono_PU_Con. However, in Micro_PU/WW-GO 0.1 wt. % caused an increase of only 2° compared to Micro_PU, at higher WW-GO loading a 5° increase was observed. It appears the CNa+ provides a similar effect on wettability across both Mono_PU and Micro_PU membranes while WW-GO varies depending on the polymer matrix.

A theory throughout this work was an increase in surface roughness through the addition of nanofillers would directly relate to an increase in contact angle and thus a decrease in wettability. However, when *Sq* values were plotted against contact angles in Figure 87 there was a lack of correlation between the two measurements. It is possible that other factors have influence on the contact angle such as the nanometre surface roughness, the polarity of the nanofillers or the surface tension of the membranes potentially altered by the nanofillers. VFM assesses the macro surface roughness as previously discussed, while contact angle maybe more affected by the nano-scale surface roughness however this cannot be supported without further analysis using AFM to assess the nano-scale roughness. Another suggestion for lack of trends is clay polarity, there is a general trend that CNa^+ at high loading causes a greater increase in both contact angle and surface roughness than C20 at the same loading. Despite being

the most polar of the four clays studied in this project CNa^+ at 5 wt. % caused the largest increase in contact angle in both Micro_PU and Mono_PU by 14% and 18%, respectively. This suggests that the CNa^+ clay may have a direct effect on contact angle, independent of porosity, craters, or macro surface roughness. Finally surface tension maybe the main factor in determining wettability of the membranes, analysis of surface tension and energy using a Brighton Science Surface Analyst would be required.[132]

To the best of the author's knowledge there is only one published document detailing the effects of clay nanofillers on microporous PU films for applications in protective clothing. A patent for Toray Industries Inc. from 1996 claims microporous PU organomodified clay nanocomposite membraned had a breathability of 8000 $g/m^2/24hr$.[59] Unfortunatly this patent does not disclose the inital WVTR of the microporous PU thus it is hard to grasp the full extent the organomodified clay nanofiller had on the membrane's breathability. However, results from this thesis can be compared to that of the patent. Within this thesis Micro_PU had a breathability of 1736 $g/m^2/24h$, the addition of 0.1 wt. % of CNa+ (a non organomodified clay) increased WVTR to 3627 $g/m^2/24h$, this is 54% lower than that achieved by the patent. Despite C20 being an organomodified clay the resulting WVTR was less than CNa+ and 63% lower than that of the patent at 2970 $g/m^2/24h$ for 0.1 wt. % C20. The largest increase in breathability in this thesis came from WW-GO at 0.1 wt. % with a WVTR value of 6187 $g/m^2/24h$ this is only 23% lower than the WVTR value quoted in the patent. Although membranes in this study did not meet or exceed the WVTR of the patent membrane the results were still promising, the addition of nanofillers to Micro_PU significantly increase the breathability of the membrane. This is explored in more detail below. Modern high-tech polyurethane films for wound dressings applications have a WVTR of 3000 $g/m^2/24$ h or greater.[163] The addition of all four nanofiller types to Micro_PU produced a WVTR of close to or greater than 3000 $g/m^2/24$ h, opening up potential applications in the medical industry to use Micro_PU/nanocomposite membranes as a secondary wound dressing in conjunction with hydrogels, hydrocolloids, and alginates.[163]

Micro_PU nanocomposites see an overall increase in WVTR compared to Micro_PU whereas in Mono_PU membranes clay and GO nanofillers decreased the WVTR

compared to Mono_PU_Con which was attributed to the tortuosity effect. This observation supports previous SEM images which show the addition of clay and GO nanofillers affect the porosity of Micro_PU membranes which has direct impact on its breathability property. The link between porosity and breathability is evidenced by a study on microporous PTFE membranes which concluded blocked pores due to contamination and/or a reduction in total porous area resulted in a reduction in WVTR.[164] As concentration of clay and possibly WW-GO increased WVTR decreases which could either be attributed to the tortuosity effect within the pore walls, linked directly to a change within membrane porosity or increased stiffness of polymer chains.[1,165] In this thesis the melting temperatures and glass transition temperature of Micro_PU did not change with the addition of nanofillers this infers that breathability of Micro_PU nanocomposite membranes is not directly related to the soft and hard segments. The polar nature of the clays may have encouraged the passage of water vapour through the membrane. CNa^+ is more polar than C20 and as such produced a greater increase in WVTR across all concentrations. It is possible that an increased amount of nanofiller causes an increase in membrane density thus decreasing WVTR.

The addition of WW-GO and GO caused a greater difference in surface and cross-sectional porosity than the clay nanofillers. SEM of WW-GO shows little change in pore size compared to Micro_PU but number of pores decreased significantly which reduced the surface porous area. This may have been caused by DMF becoming trapped resulting in the collapse of porous membranes and a bilayer to form at 0.5 wt. %. The collapse of the porous membrane of WW-GO 0.5 wt. % in conjunction with a sharp decrease in WVTR at higher WW-GO loading could indicate that as WW-GO concentration increases the porous network begins to collapse resulting a reduction in WVTR. However, to support either of these claims further investigation using SEM to image the cross-section of each sample at each concentration would be required to fully understand the interconnected porous structures impact on WVTR.

Micro_PU/GO 0.5 wt. % produced the second largest increase in WVTR compared to Micro_PU and following trends of decreasing WVTR as concentration increases it could be argued that GO at lower loading may produce an even greater increase in WVTR. Although this initially appears promising it should be noted that GO 0.5 wt. % produced

a thick membrane at 125 µm compared to Micro_PU at 60 µm thickness. Although WVTR values were normalised to membrane thickness a thicker membrane may cause issues during industrial production of Micro_PU/GO 0.5 wt. %, its likely attempts to spread a thinner cast may change the membrane porosity and thus it's properties. Further production optimisation and investigation would be required to mitigate these issues.

When WVTR was compared against pore and crater area as well as pore length of upper surface and cross-section. There was no correlation between WVTR and pore and/or crater area however average pore length of the cross-sectional pores had a minor trend. As average cross-sectional pore length increases WVTR increases. Suggesting that internal porous structure is important for breathability, the larger the cross-sectional pores the greater the membrane's breathability, visually this can be seen using SEM cross-section images of Micro_PU/GO 0.5 wt. % which has large open pores that appear to be well connected. The correlation between increasing cross-sectional pore length and increasing WVTR could indicate that the upper surface pores and craters play no crucial role in the membrane's breathability while the cross-sectional porosity is pivotal. However, there is more at play here, the complexity of the interconnect porous structure followed by the variation in pore shape, size, and distribution as well as the difficulties incurred when trying to quantify the cross-sectional porosity indicate further investigation is required to confidently claim the interconnected porous structure is critical to breathability as opposed to surface porosity. As previously stated, further investigation using SEM to image all samples at all concentrations would be required. Pin holes (continuous holes throughout the membrane) are common occurrences within cast membranes however no pin holes were discovered using SEM analysis.[166]

The addition of nanofillers increased both the contact angle and WVTR compared to Micro_PU with CNa 1 wt. % and WW-GO 0.1 wt. % being slightly better at improving both breathability and wettability properties as opposed to just one. However, issues regarding adequate dispersion of CNa^{+} 1 wt. % and collapsing porosity structure of 0.5 wt. % limit the positive of improvements in barrier properties for these samples.

FTIR, DSC melting events and DMA storage modulus and T_g did not show any significant changes or trends for Micro_PU nanocomposites. The same occurred for

Mono_PU/clay, GO and GNP nanocomposite membranes in chapter 4 and 5. The one difference was T_g data obtained from DMA was different for Micro_PU compared to Mono_PU. Only one well defined T_g was observed for Micro_PU membranes compared to the two observed for Mono_PU membranes. A reduction in visible T_g curves could be attributed to the chemical differences of Micro_PU compared to Mono_PU. These differences can affect the hard and soft segment lengths however no evidence for this was observed on the macroscale however chemical differences could be causing changes at the molecular level potentially disturbing the soft and hard segments, in essence acting as a plasticiser reducing the number of T_g peaks observed.

6.4 Conclusions

XRD and SEM/EDX analysis indicated that CNa^+ was partly dispersed and partly intercalated while C20 appeared to be exfoliated, the same was observed for these two clays within Mono_PU in Chapter 4. Analysis of GO and WW-GO dispersion was contradictory, XRD indicated an exfoliated system similar to observations in Mono_PU in chapter 5 while SEM/EDX indicated the possibility that WW-GO and GO were mostly well dispersed with some agglomeration present. It is proposed that XRD may not be the best technique for assessing dispersion of GO nanofillers and further analysis with Raman maybe more suitable. It was concluded that further investigation using TEM would be required to confirm if a fully exfoliated system was present.

The addition of GO and WW-GO caused more disruption to the surface and interconnected porous structure than C20 and CNa^+ nanofillers. The surface and cross-sectional porosity was investigated using SEM, results suggested that the formation of craters and 'bridged' pores are the result of nanofillers disrupting the coagulation process. Analysis of SEM images show the addition of nanofillers reduced the number of pores present and increasing nanofiller concentration often increased the number of craters. Some anomalies with regards to large defects in poorly dispersed samples (CNa^+ at 3 wt. %) was discovered using SEM/EDX, while GO at 0.5 wt. % produced unusual 'bridged' pores high in oxygen. Defects were not identified in Mono_PU samples in either Chapters 4 or 5, this could be due to the more complex structure of Micro_PU

and the increased chemical sensitivity of the polymer batch to changes in chemical composition as indicted by internal communications.

There was little change in the porosity of C20 samples likely due to the good dispersion of C20 within the Micro_PU matrix. When comparing cross sectional porosity of C20 3 wt. % to other samples, C20 was most similar to Micro_PU expect for a reduction in the quantity of pores, they were slightly larger with more variation in length.

VFM imaging supported SEM images, VFM produced 3D maps of samples which allowed for analysis of pore and craters depth. Typically, the larger the crater the deeper it is, however there were some exceptions, particularly with WW-GO samples. VFM has a lower resolution compared to SEM and as such provides information on the macro-scale surface roughness, and as such identifying the quantity of pores using VFM was deemed unreliable. However, VFM gave a clearer picture of the macro surface identifying a far greater number of craters compared to SEM, 17 craters for Micro_PU using VFM compared to 0 craters observed using SEM. VFM analysis of Micro_PU was far more reliable, and optimisation was easier compared to Mono_PU due to the increased surface texture, VFM was no longer being operated at its limits as was found in Section 5.2.1.4.

Micro_PU has a relatively flat surface compared to the nanocomposite membranes, the addition of nanofillers increased the surface roughness (*Sq*) compared to Micro_PU and VFM indicated that increasing clay loading had a positive correlation to increasing the number of surface craters. CNa^+ 3 wt. % was also responsible for the largest increase in *Sq* with a value of 2.97 µm, a 1550% increase compared to Micro_PU. As C20 concentration increased the *Sq* value increased, C20 at 5 wt. % had a *Sq* value of 2.45 µm a 1261% increase compared to Micro_PU. While GO and WW-GO samples visually indicate a heavily textured surface in both VFM and SEM images, depth of pores and craters are far shallower than they initially appear which leads to a comparably smoother surface than clay nanofillers. Analysis of VFM software indicated that the depth of craters and pores as well as diameter of craters is factored heavily into the VFM software analysis.

The addition of CNa^+ at both 1 and 5 wt. % to Micro_PU increased contact angle by 14% to 96°, this was the largest increase of all nanofillers. The hypothesis was that an increase in surface roughness through the addition of nanofillers would correlate to an increase in contact angle and hence a decrease in wettability however, no correlation was found.

Micro_PU nanocomposites see an overall increase in WVTR compared to Micro_PU whereas in Mono_PU membranes clay and GO nanofillers decreased the WVTR due to the tortuosity effect. Several suggestions for why this is observed in Micro_PU samples has been put forward; tortuosity effect within the pore walls, changes in membrane porosity, polar nature of the clays or increased membrane density which decreases WVTR. Although the GO and WW-GO samples produced the largest increase in WVTR compared to clay nanofillers there are issues. WW-GO porosity had collapsed at 0.5 wt. % and is thought to begin to collapse at lower concentrations while GO produced a thick membrane, double the thickness of Micro_PU, making industrial production of this membrane a challenge.

WVTR was compared against pore and crater area as well as pore length of upper surface and cross-section, no correlation was found between WVTR and pore and/or crater area. However, a minor trend indicated that as the average cross-sectional pore length increases WVTR increases, this suggests that internal porous structure is important for breathability although there are issues when attempting to quantify the complexity of the interconnect porous structure.

It is important that these barrier membranes are both breathable and waterproof and while the addition of nanofillers increased both the contact angle and WVTR compared to Micro_PU, two specific nanofillers at a specific concentration produced a comparatively large increase in one of these properties while also providing a moderate improvement in the other. These are CNa 1 wt. % and WW-GO 0.1 wt. %. However, CNa^+ 1 wt. % encounters minor issue with poor dispersion while WW-GO may have issues with maintaining an interconnected porous structure as at higher concentration of 0.5 wt. % the porous structure partially collapsed.

Melting events obtained from DSC and the storage modulus and T_g obtained from DMA show no significant changes nor trends. T_g data was unusual for Micro_PU compared to Mono_PU. Only one well defined T_g event was observed for Micro_PU membranes compared to the two observed for Mono_PU membranes. A reduction in visible T_g curve could be attributed to slight changes in chemistry between Mono_PU and Micro_PU which has an effect on the hard and soft segment lengths.

Chapter 7

Conclusion and Future Work

7.1 Conclusion

This study focused on two different types of PU membranes, Mono_PU and Micro_PU and the inclusion of two different nanofillers, layered silicates: MMT/OMMT and GO/GNP into both PU membranes. Numerous characterisation techniques were used to assess a range of properties including understanding the dispersion of the nanofillers within Mono_PU and Micro_PU, and their effect on the barrier, mechanical, and chemical properties. Additionally, VFM was studied, a novel technique for assessing surface topography and roughness. The results were compared to other characterisation techniques such as SEM, contact angle and WVTR.

XRD and SEM/EDX were used to assess the dispersion of nanofillers within Mono_PU and Micro_PU. The addition of clay to Mono_PU found C20 clay dispersed best in comparison to the other clays, producing a partially exfoliated system in part due to the presence of an organomodifier. While CNa+ was the worst dispersed clay, producing an intercalated structure at all three concentrations with clay aggregates confirmed using SEM/EDX, this is partially due to the lack of organomodifier, its high polarity and poor compatibility. C15A and C10A both produced a highly ordered intercalated system possibly due to intercalation of the polymer chains within the interlayer spacing potentially enhanced due to the addition of DMF increasing the order of C15A and C10A prior to mixing with Mono_PU.

XRD analysis confirmed GO, WW-GO and AW-GO are graphene oxides while GNP-A120 and GNP-A500 are mostly graphite. GO dispersed the best with a fully exfoliated system likely due to being pre-dispersed suspension in a mixture of DMF and a small amount of water (as supplied by Graphitene). WW-GO produced a fully exfoliated system, while AW-GO indicated a partially exfoliated/partially intercalated system. The GNP-500 and GNP-120 samples, due to being mostly graphite produced a micro-composite/phase separated system.

Nanofillers chosen to be dispersed within Micro_PU were, C20, CNa+, GO and WW-GO. As expected CNa+ within Micro_PU had a mixed dispersion, partly intercalated and partly a microcomposite with some clay aggregation. C20 in both SEM/EDX and XRD suggested an exfoliated system for all concentrations within Micro_PU. XRD indicated WW-GO and GO were very well dispersed and possibly exfoliated within Micro_PU. However, further investigation with SEM and SEM/EDX indicated the possibility that WW-GO and GO were not fully exfoliated due to observed craters, collapsing porous structure, and 'bridged' pores.

SEM analysis of Mono_PU samples found the addition of DMF increased the 'orange peel' effect in both batches of Mono_PU_Con. SEM images also indicated that Mono_PU batch 2 (Chapter 5) was far smoother in topography compared to Mono_PU batch 1 (Chapter 4) likely due to difference in processing. It is thought the 'orange peel' effect is caused by DMF-rich areas pooling on the membrane surface during drying. The addition of nanofillers often increased the 'orange peel' effect and influenced different surface topographies such as the 'bubble wrap' topography of Mono_PU/CNa+ 5 wt. %, the 'flake' like topography of Mono_PU/GO 0.5 wt. % and the "waviness' topography of WW-GO and AW-GO samples. Different topographies have the potential to influence the adhesive properties of these membranes, this is important when applied to multi-layered membranes which can be used in protective appeal. Mono_PU/C20 at 5wt. % produced an unusual cross sectional 'wafer' like structure.

SEM of Micro_PU samples allowed for quantifying the porosity of membranes, Micro_PU/C20 3 wt. % had the most similar upper surface and cross-sectional porosity to Micro_PU. Micro_PU/C20 3 wt. % provided modest improvements to breathability, wettability, and surface roughness. Within Mono_PU C20 at 5 wt. % was found to be static dissipative a similar effect maybe present in Micro_PU/C20 membranes. While the other nanofillers provided some improvements in properties they were often hindered by one of more issues for example Micro_PU/WW_GO 0.5 wt. % had a semi-collapsed porous cross section network. Micro_PU/GO 0.5 wt. %, had an unusual 'sponge' like surface topography with large craters and 'bridged' pores. Due to CNa+ being poorly dispersed, Micro_PU/CNa+ 3 wt. % had partial aggregates which formed large craters in the membranes surface.

VFM imaging and analysis of relatively flat barrier membranes is in its infancy. Due to its novel analysis application, the initial methodology was time consuming but successful. VFM images support those taken by SEM across all three chapters. VFM provided a vital take on the surface topography allowing for analysis in the Z-axis providing information on the depth and height of dimples and pimples in Mono_PU nanocomposite samples as well as pore and crater depths in Micro_PU nanocomposite membranes. However, issues were present as VFM 3D pseudo-coloured images were limited in their ability to accurately describe the surface topography, and likely due to 'waviness' caused by air bubbles formed during sample preparation. 2D pseudo-coloured images which removes this 'waviness' are far more accurate. This thesis displays the limitations and potential application of VFM in imaging barrier membranes, Mono_PU/GO and GNP nanocomposites were far too flat to be imaged flawlessly, and falsely presented 'holes' were present in the images which potentially affected the surface roughness measurements due to the edge effects of these false 'holes'. As Mono_PU batch 1 and clay nanocomposites had comparably more textured surfaces than Mono_PU batch 2/GO nanocomposites, these were easier to image with no 'holes' present. Micro_PU membranes due to their porosity and heavily textured surface in comparison were very easy to image. VFM provides detailed information regarding the depths of dimples, pimples, pores, and craters which SEM cannot.

There are distinct positives and negatives for both SEM and VFM these are as follows.

Resolution: SEM has greater resolution providing almost nano-scale imaging identifying pores >0.2 μm while VFM provides macro-scale imaging of large pores (1-4 μm) and a greater focus on surface craters (>4 μm).

2D vs 3D map: SEM provides only 2D images which can provide inaccurate ideas of surface topography, WW-GO samples appear heavily textured when imaged by SEM but VFM analysis using 3D maps indicates they are relatively flat samples. VFM produces a 3D map which allows for visual qualitative analysis of a surface's texture as well as quantitative analysis of depths of pore/craters, moreover, this is a mostly automated process.

Sampling Time: for these particular samples collecting SEM/EDX was challenging due to charging effects which required a more labour intensive and time-consuming sample preparation technique to mitigate charging (3.5.1.2). This is compared to gold coating samples for SEM or VFM imaging. SEM images took 10-20 minutes to image and a further 30 minutes to take an EDX map. Analysing sample porosity of SEM images using ImageJ was time-consuming and at risk of human error and bias. Attempts to automate image analysis of SEM images produced unreliable results, manual analysis using ImageJ was preferential. VFM imaging was initially time consuming to optimise (~60 minutes) thereafter imaging each sample took less than 5 minutes to image and analyse and provided far more detailed information than SEM such as 3D maps, 2D maps, relative pseudo-coloured maps, surface roughness measurements plus many more surface measurements not discussed within the scope of this work. However, analysis of pore/crater diameter, quantity and depth was manual, which took additional time and was at risk of human error/bias.

Dispersion: SEM/EDX maps were used to assess dispersion of both clay and GO nanofillers however GO nanofillers were less responsive using this technique. VFM cannot assess dispersion.

VFM and SEM may initially both offer the ability to image a sample's surface however each technique provides unique information about the surface topography which the other technique cannot. Individually each technique is adequate but together they provide a clear synergistic approach to qualitative and quantitative analysis of surface topography, surface roughness, the inter-connected porous structure and sample dispersion.

It's critical that barrier membranes are both breathable and resistant to harsh climates. With Mono_PU/clay, GO and GNP nanocomposite membranes no large changes in contact angle were observed when compared to the Mono_PU controls. Within Micro_PU more significant difference was observed from some samples, CNa+ at both 1 and 5 wt. % to Micro_PU increased contact angle by 14% to 96°. The addition of CNa+ also produced the largest increase in contact angle in Mono_PU.

A theory proposed was that increased surface roughness would directly correlate with an increased contact angle, however when these values were plotted against one another no correlation or trends were found in any of the samples analysed in this thesis. It is likely other factors are more dominate in determining the wettability of a barrier membrane other than surface roughness in this case. Such as nano-scale roughness or surface tension.

WVTR was used to ascertain the breathability of samples, within Mono_PU samples and as anticipated, the addition of clay, GO and GNP all decreased the WVTR due to the tortuosity effect. While in Micro_PU nanocomposite membranes the WVTR increased, and likely due to changes in the surface and interconnected porous structure of these membranes. It was noted that too much nanofiller was detrimental since as nanofiller concentration increased the WVTR decreased.

Hydrostatic head tests produced promising results, Mono_PU/CNa+ 1 wt. % and Mono_PU/WW-GO 0.3 wt. % both doubled or almost doubled the hydrostatic head compared to controls. However, samples repeats would be required for certainty. FTIR and DSC did not show any strong effects on molecular bonding interactions between or nature of morphology (crystallinity/amorphousness).

Given that data obtained from FTIR, DSC and DMA showed no significant changes for Mono_PU or Micro_PU nanocomposite membranes it is likely that the nanofillers have little impact on either the hard or soft segments. Data did not show any strong effects on molecular bonding interactions between the nanofillers and Mono_PU or Micro_PU or the nature of morphology (crystallinity/amorphousness). It could be inferred that the mechanical method of incorporating the nanofillers into the pre-polymerised PU did not encourage strong chemical interactions between the nanofillers and the PU. Despite weak chemical attraction the nanofillers still had a significant effect on the porosity, WVTR and surface roughness with slight changes observed for contact angle, Young's modulus, and anti-static properties dependant on specific samples.

Tensile tests were carried out on only the Mono_PU/clay and GO samples. Only slight changes were observed for clay samples, C20 3 and 5 wt. % and CNa+ 5 wt. % increased the Young's Modulus slightly, indicating the addition of clay has slightly reinforced the membrane. The addition of GO and WW-GO had no significant difference on the Young's modulus, elongation at break or yield stress of Mono_PU_Con.

Antistatic properties of selected Mono_PU/clay and GO samples were assessed, the addition of C20 at 3 and 5 wt. % produced antistatic properties within the membrane. It is unusual for clay alone to act as an antistatic agent. It is proposed to assess if the static dissipative property is the result of the unusual wafer-like cross sectional structure of C20 5 wt. %. Mono_PU/GO and WW-GO membranes were found to be insulative.

7.2 Contribution to Knowledge

1) To explore and obtain optimum nanofiller dispersion as this often leads to the best performance while minimising changes to the current industrial processing methods for each membrane. It has been shown that nanofillers can be added to and subsequently effectively dispersed in pre-polymerised Mono_PU and Micro_PU thus leading to modest improvements in surface roughness, barrier, and mechanical properties. Both C20 and GO nanofillers dispersion effectively into pre-dispersed polymer (Mono_PU and Micro_PU) which is advantages as it minimises disruption to the already established chemical process, allowing for the potential of a quick and affordable industrial scale up. Mono_PU/C20 at 5wt. % produced an unusual cross sectional 'wafer' like structure possibly responsible for unexpected antistatic properties. Within Micro_PU, the addition of C20 did not significantly alter the porous structure or membrane thickness and provided modest improvements in surface roughness, breathability, and wettability of the membrane. However good dispersion does not directly relate to improvements in performance, GO despite being well dispersed produced small and often negligible improvements in properties. Within Micro_PU the addition of GO created an unusual 'sponge' like surface topography with large craters and 'bridged' pores resulting in a thicker membrane which could disrupt membrane formation at an industrial level.

2) Often when nanofillers are used to improve a polymers property it comes at the expense of another, hence this thesis considers the whole picture providing an in-depth study into a wide range of properties; surface and cross-sectional topography, surface roughness, barrier, and mechanical properties as opposed to cherry picking only the best results. Findings indicate that C20 is overall the best performing nanofiller, C20 provides good dispersion and improvement in properties including unexpected results at such low clay loading. Within Micro_PU C20 increases the breathability and surface roughness while not negatively affecting wettability. In addition, C20 within Mono_PU increased the Young's modulus but did not negatively impact the elongation at break. Mono_PU/C20 also provided surprising static dissipative properties.
3) This thesis explored the novel application of VFM to relatively flat polymer membranes providing a clear example of how VFM responds to slight changes in a membranes surface texture. Chapter 5 demonstrated how VFM was used at its limit, while chapter 4 demonstrates VFM can successfully image and analyse relatively flat monolithic polymer membranes as long as they have a moderate level of macro-scale surface texture. Finally, chapter 6 demonstrates VFM's ability to access the macro-scale and sub macro-scale porosity of microporous barrier membranes providing information on the depth of pores and craters which cannot be assessed via SEM. This includes determining which surface topographies factors into VFM calculations regarding surface roughness measurements. Results indicate the depth of craters and pores as well as diameter of craters is factored heavily into the VFM software analysis while pore diameter and number of craters do not hold weight when VFM software is determining surface roughness. Furthermore, a detail comparison of VFM to breathability and wettability has been conducted. As well as an in-depth comparison between VFM and SEM has been provided in this thesis contributing to the future use of VFM to image and analyse relatively flat polymer surfaces.

7.3 Future Work

- Regarding dispersion analysis, potential avenues for future work include using Raman spectroscopy and TEM. As XRD and SEM/EDX indicated a difference in dispersion regarding GO samples it is proposed that additional analysis using Raman spectroscopy for graphene/polymer nanocomposites is advisable. When assessing dispersion of GO within a polymer XRD is often used in conjunction with Raman spectroscopy. XRD and SEM/EDX indicated several clay and GO samples were possibly exfoliated, however the instrument is limited to the macro-scale, as such TEM would be required to confidently determine if a fully exfoliation system is present.

- One suggested way to improve dispersion of nanofillers involves using a triple roll mill. Initial steps and considerable time were taken during this project, passing samples through the triple roll mill up to seven times in order to assess effects on dispersion. Viscosity appeared to increase after each pass indicating good dispersion and samples became opaquer, however some DMF was lost, and it would need further characterisation to assess if better dispersion was achieved. Initial membranes casts looked promising. Triple roll mill would at the very least remove large aggregates of nanofillers, possibly preventing agglomerated nanofillers occurring at the edges of suspensions within the mixing vessel. However, Covid restrictions lead to seven months outside the lab and samples were no longer suitable for casting or testing. It is proposed that triple roll mill would improve dispersion and thus have a positive impact on properties however industrial scale up would be costly and time consuming.

- To better understand the cross section of particular membrane's and thus their impact on properties future work could include using SEM to image Mono_PU with different C20 amounts (i.e., 1 and 3 wt. %) and thus assess how and when the wafer structure forms with increasing clay concentration. This could then provide better understanding on how C20 provides static dissipative properties to Mono_PU at low clay loading. As well as SEM Micro_PU/WW_GO 0.1 and 0.3 wt. % cross section to determine when the porous structure begins to collapse.

Allowing for a clearer understanding how the interconnected porous structures of WW_GO impacts WVTR.

- In addition to the above, there are trends between WVTR and SEM porosity descriptions however these are tentative and missing the whole story. Further investigation into microporosity using a mercury porosimeter would allow for better understanding of the interconnected porosity and how this correlate to permeability, particularly in promising membranes such as Micro_PU/C20.

- A more in-depth study on VFM would involve investigating other parameters that describe a polymer membranes topography. A suggested parameter to explore is areal material ratio (Smr2), it is associated with the reduced valley depth (Svk and pit void volume (Vvv) parameters and represents the percentage of the measurement area that comprises of the deeper valley structures.[81] In addition, an in-depth study comparing and validating VFM against AFM, a commonly used technique to analyse polymer surfaces. This would build upon the work conducted in this thesis and provide a better understanding of how VFM can be applied to the analysis of polymer surfaces.

- Due to limited sample quantity, in future studies selected Micro_PU samples would require tensile testing, hydrostatic head, and antistatic testing. While selected Mono_PU samples would require repeats of hydrostatic head measurements.

8. References

1 S. Mondal and J. L. Hu, *J Memb Sci*, 2006, **274**, 219–226.

2 W. J. Choi, S. H. Kim, Y. Jin Kim and S. C. Kim, *Polymer (Guildf)*, 2004, **45**, 6045–6057.

3 C. N. Ha Thuc, H. T. Cao, D. M. Nguyen, M. A. Tran, L. Duclaux, A. C. Grillet and H. Ha Thuc, *J Nanomater*, 2014, **2008**, 1.

4 PIL Membranes LTD, Membrane and Polymer Specialists , https://www.porellemembranes.com, (accessed 31 January 2024).

5 A. Cornille, R. Auvergne, O. Figovsky, B. Boutevin and S. Caillol, *Eur Polym J*, 2017, **87**, 535–552.

6 Statista, Polyurethane demand worldwide from 2012 to 2024, https://www.statista.com/statistics/747004/polyurethane-demand-worldwide/, (accessed 17 September 2024).

7 S. Rost, *Macromol Mater Eng*, 2008, **293**, 373–386.

8 American Chemistry Council, Diisocyanates Explained, https://www.americanchemistry.com/industry-groups/diisocyanates-dii/diisocyanates-overview/diisocyanates-explained, (accessed 1 February 2024).

9 P. Król, *Prog Mater Sci*, 2007, **52**, 915–1015.

10 I. Yilgor, E. Yilgor, I. G. Guler, T. C. Ward and G. L. Wilkes, *Polymer (Guildf)*, 2006, **47**, 4105–4114.

11 John W Nicholson, *The Chemistry of Polymers*, RSC Publishing, London, 3rd edn., 2017.

12 J. M. Herrera-Alonso, E. Marand, J. C. Little and S. S. Cox, *J Memb Sci*, 2009, **337**, 208–214.

13 J. T. Haponiuk and K. Formela, in *Polyurethane Polymers: Composites and Nanocomposites*, Elsevier, Amsterdam, 1st edn., 2017, pp. 1–20.

14 S. S. Liow, V. T. Lipik, L. K. Widjaja, S. S. Venkatraman and M. J. M. Abadie, *Express Polym Lett*, 2011, **5**, 897–910.

15 T. K. Chen, Y. I. Tien and K. H. Wei, *Polymer (Guildf)*, 2000, **41**, 1345–1353.

16 A. R. Bunsell, S. Joannès and A. Marcellan, *Handbook of Properties of Textile and Technical Fibres | ScienceDirect*, Woodhead Publishing, Cambridge, 2nd edn., 2018.

17 T. Fukazawa, H. Kawamura, Y. Tochihara and T. Tamura, *Textile Research Journal*, 2003, **73**, 657–663.

18 P. W. Gibson, *Polym Test*, 2000, **19**, 673–691.

19 J. Fan and L. Hunter, *Engineering Apparel Fabrics and Garments*, Woodhead Publishing, Cambridge, 1st edn., 2009.

20 M. A. Minnath and E. Purushothaman, *Polyurethane Polymers: Blends and Interpenetrating Polymer Networks*, 2017, 17–44.

21 M. Alexandre and P. Dubois, *Materials Science and Engineering*, 2000, **28**, 1–63.

22 R. Larsson and A. Malek, *Applied Sciences*, 2021, **11**, 167–171.

23 K. Jlassi, I. Krupa and M. M. Chehimi, in *Clay-Polymer Nanocomposites*, Elsevier, Amsterdam, 1st edn., 2017, pp. 1–28.

24 B. Wang, J. Park, D. R. Dreyer, S. Park, W. Bielawski, R. S. Ruoff, Z. Liu, J. T. Robinson, X. Sun, H. Dai, B. Y. Zhu, S. Murali, W. Cai, X. Li, J. W. Suk, J. R. Potts, R. S. Ruoff, P. Avouris, C. Dimitrakopoulos, Y. Si, E. T. Samulski, C. Hill, N. Carolina, A. K. Geim, A. H. Macdonald, A. K. Geim, A. H. Macdonald, K. S. Novoselov, A. K. Geim, S. V Morozov, D. Jiang and P. Article, *Science (1979)*, 2004, **306**, 666–669.

25 Y. Hancock, *J Phys D Appl Phys*, 2024, **44**, 1–12.
26 E. P. Randviir, D. A. C. Brownson and C. E. Banks, *Materials Today*, 2014, **17**, 426–432.
27 M. Miculescu, V. K. Thakur, F. Miculescu and S. I. Voicu, *Polym Adv Technol*, 2016, **27**, 884–859.
28 C. Lee, X. Wei, J. W. Kysar and J. Hone, *Science (1979)*, 2008, **321**, 385–388.
29 K. F. Mak, L. Ju, F. Wang and T. F. Heinz, *Solid State Commun*, 2012, **152**, 1341–1349.
30 A. R. Urade, I. Lahiri and K. S. Suresh, *JOM*, 2023, **75**, 614–630.
31 N. Cao and Y. Zhang, *J Nanomater*, 2015, **2015**, 45–49.
32 S. Pei and H. M. Cheng, *Carbon N Y*, 2012, **50**, 3210–3228.
33 R. G. Bai, K. Muthoosamy, S. Manickam and A. Hilal-Alnaqbi, *Int J Nanomedicine*, 2019, **14**, 5753–5783.
34 V. Mittal, *Advances in Polymer Nanocomposite Technology*, 2011, **26**, 1–21.
35 I. V Khudyakov, D. R. Zopf and N. J. Turro, *Des Monomers Polym*, 2009, **12**, 279–290.
36 L. Nicole, C. Laberty-Robert, L. Rozes and C. Sanchez, *Nanoscale*, 2014, **6**, 6267–6292.
37 C. Hussain, *Handbook of Polymer Nanocomposites for Industrial Applications*, Elsevier, Amsterdam, 1st edn., 2021.
38 C. O. Blattmann and S. E. Pratsinis, *KONA Powder and Particle Journal*, 2019, **36**, 3–32.
39 J. M. Garcés, D. J. Moll, J. Bicerano, R. Fibiger and D. G. McLeod, *Advanced Materials*, 2000, **12**, 1835–1839.
40 G. Lalwani, A. M. Henslee, B. Farshid, L. Lin, F. K. Kasper, Y. X. Qin, A. G. Mikos and B. Sitharaman, *Biomacromolecules*, 2013, **14**, 900–909.
41 T. Gatti, N. Vicentini, M. Mba and E. Menna, *European J Org Chem*, 2016, **2016**, 1071–1090.
42 J. Y. Hong, B. M. Bak, J. J. Wie, J. Kong and H. S. Park, *Adv Funct Mater*, 2015, **25**, 1053–1062.
43 Y. S. Ye, H. Wang, S. G. Bi, Y. Xue, Z. G. Xue, X. P. Zhou, X. L. Xie and Y. W. Mai, *J Mater Chem A Mater*, 2015, **3**, 18064–18073.
44 A. Tarhini and A. R. Tehrani-Bagha, *Applied Composite Materials*, 2023, **30**, 74–79.
45 Q. Beuguel, J. Ville, J. Crepin-Leblond, P. Mederic and T. Aubry, *Appl Clay Sci*, 2017, **135**, 253–259.
46 F. Chavarria and D. R. Paul, *Polymer (Guildf)*, 2006, **47**, 7760–7773.
47 A. Tiwari and M. Syväjärvi, *Graphene Materials: Fundamentals and Emerging Applications*, John Wiley & Sons, Hoboken, New Jersey, 1st edn., 2015.
48 A. Witschnigg, S. Laske, M. Kracalik, M. Feuchter, G. Pinter, G. Maier, W. Marzinger, M. Haberkorn, G. R. Langecker and C. Holzer, *J Appl Polym Sci*, 2010, **117**, 3047–3053.
49 S. Fu, Z. Sun, P. Huang, Y. Li and N. Hu, *Nano Materials Science*, 2019, **1**, 2–30.
50 K. Müller, E. Bugnicourt, M. Latorre, M. Jorda, Y. E. Sanz, J. M. Lagaron, O. Miesbauer, A. Bianchin, S. Hankin, U. Bölz, G. Pérez, M. Jesdinszki, M. Lindner, Z. Scheuerer, S. Castelló and M. Schmid, *Nanomaterials*, 2017, **7**, 74–76.
51 Z. F. Li, S. J. Wang and J. Y. Li, *Macromol Mater Eng*, 2008, **2**, 251–258.
52 N. Yousefi, M. M. Gudarzi, Q. Zheng, X. Lin, X. Shen, J. Jia, F. Sharif and J. K. Kim, *Compos Part A Appl Sci Manuf*, 2013, **49**, 42–50.

53 K. Gao, Z. Shao, X. Wu, X. Wang, J. Li, Y. Zhang, W. Wang and F. Wang, *Carbohydr Polym*, 2013, **97**, 243–251.
54 H. T. Lee and L. H. Lin, *Macromolecules*, 2006, **39**, 6133–6141.
55 C. Esposito Corcione, P. Prinari, D. Cannoletta, G. Mensitieri and A. Maffezzoli, *Int J Adhes Adhes*, 2008, **28**, 91–100.
56 D. Cai, K. Yusoh and M. Song, *Nanotechnology*, 2009, **20**, 87–93.
57 H. W. Kim, J. H. Yoon, K. M. Diederichsen, J. E. Shin, B. M. Yoo, B. D. McCloskey and H. B. Park, *Macromol Mater Eng*, 2017, **302**, 45–52.
58 M. Strankowski, D. Włodarczyk, Ł. Piszczyk and J. Strankowska, *Int J Polym Sci*, 2016, **8**, 1–8.
59 US2012/0322328A1, *United States Patent Application Publication* , 2012.
60 A. Cuenat and R. Leach, in *Fundamental Principles of Engineering Nanometrology*, William Andrew Publishing, Norwich, NY, 2nd edn., 2014, pp. 205–239.
61 A. Ul-Hamid, *A Beginners' Guide to Scanning Electron Microscopy*, Springer Publishing, New York City, 1st edn., 2018.
62 M. Abd Mutalib, M. A. Rahman, M. H. D. Othman, A. F. Ismail and J. Jaafar, in *Membrane Characterization*, Elsevier, Amsterdam, 1st edn., 2017, pp. 161–179.
63 R. Leach, in *Optical Measurement of Surface Topography*, Springer Publishing, New York City, 1st edn., 2011, pp. 1–14.
64 R. E. W. Harrison, *J Fluids Eng*, 1931, **53**, 111–121.
65 R. Leach, in *Fundamental Principles of Engineering Nanometrology*, William Andrew Publishing, Norwich, NY, 2nd edn., 2014, pp. 133–204.
66 Taylor Hobson, Metrology 4.0, [https://www.taylor-hobson.pl/taylor-hobson-polska/niezawodnosc/], (accessed 17 September 2024).
67 L. A. Franco and A. Sinatora, *Precis Eng*, 2015, **40**, 106–111.
68 C. Pratt, *Journal of Applied Psychology*, 1925, **9**, 209–210.
69 W. Kapłonek, K. Nadolny and G. M. Królczyk, *Measurement Science Review*, 2016, **16**, 42–53.
70 International Organization for Standardization, *ISO 21920-2:2021 - Geometrical product specifications (GPS) — Surface texture: Profile — Part 2: Terms, definitions and surface texture parameters*, ISO, Geneva, 1st edn., 2021.
71 K. Walton, L. Fleming, M. Goodhand, R. Racasan and W. Zeng, *Surf Topogr*, 2016, **4**, 2501–2503.
72 L. Newton, N. Senin, C. Gomez, R. Danzl, F. Helmli, L. Blunt and R. Leach, *Addit Manuf*, 2019, **25**, 365–389.
73 X. Xu, T. Pahl, H. Serbes and P. Lehmann, in *60th Ilmenau Scientific Colloquium*, Universität Kassel, Kassel, Germany, 2023.
74 A. Islam, N. Giannekas, D. M. Marhöfer, G. Tosello and H. N. Hansen, in *International Conference of the Polymer Processing*, Cleveland, 2014, vol. 1664.
75 C. Halder and M. Bräker, *Powder Injection Moulding International*, 2015, 9, 5–11.
76 V. Martinez-Nogues, J. M. Nesbitt, R. J. K. Wood and R. B. Cook, *Tribol Int*, 2016, **93**, 563–572.
77 L. C. Sawyer, D. Grubb and G. Meyers, *Polymer microscopy*, Springer, New York City, 1st edn., 2008.
78 G. Tosello, H. Haitjema, R. K. Leach, D. Quagliotti, S. Gasparin and H. N. Hansen, *CIRP Ann Manuf Technol*, 2016, **65**, 529–532.
79 C. Al-Karawi, T. Kaiser and C. S. Leopold, *Int J Pharm*, 2017, **530**, 440–454.

80 A. Ward, K. Walton, K. Box, J. Østergaard, L. J. Gillie, B. R. Conway and K. Asare-Addo, *Int J Pharm*, 2017, **530**, 139–144.
81 A. Ward, B. Brown, K. Walton, P. Timmins, B. R. Conway and K. Asare-Addo, *Pharmaceutics*, 2020, **12**, 1–6.
82 J. Reitbauer, F. Harrer, R. Eckhart and W. Bauer, *Cellulose*, 2021, **28**, 6813–6827.
83 S. Calvert, H. Ryall, J. Power and P. Bills, in *Huddersfield University Conference: Transition- Re- thinking Textiles and Surfaces*, Huddersfield, 2014.
84 Y. Waseda, E. Matsubara and K. Shinoda, *X-Ray Diffraction Crystallography: Introduction, Examples and Solved Problems*, Springer Publishing, New York City, 2011.
85 H. Naeem, Loughborough University, 2019.
86 J. Abraham, B. Jose, A. Jose and S. Thomas, in *Phytonanotechnology: Challenges and Prospects*, Elsevier, Amsterdam, 1st edn., 2020, pp. 21–39.
87 B. (Barbara H.) Stuart, *Infrared spectroscopy : fundamentals and applications*, John Wiley & Sons, Ltd, Hoboken, New Jersey, 1st edn., 2004.
88 B. Jaleh and P. Fakhri, *Spectroscopy of Polymer Nanocomposites*, 2016, 112–129.
89 J. Smith, Fourier Transform Infrared Spectroscopy (FTIR) Principle, https://engineerscommunity.com/t/fourier-transform-infrared-spectroscopy-ftir-principle/4980, (accessed 1 February 2024).
90 C. Ullrich, Alicona Easy Way to Explain Roughness, https://www.alicona.com/en/blog-posts/the-easy-way-to-explain-roughness#:~:text=Roughness%20is%20the%20condition%20of,texture%20of%20the%20surface%20remains., (accessed 27 January 2024).
91 International Organization for Standardization, *ISO 25178-2:2021 - Geometrical product specifications (GPS) — Surface texture: Areal — Part 2: Terms, definitions and surface texture parameters*, ISO, Geneva, 1st edn., 2021.
92 D. Semnani, in *Electrospun Nanofibers*, Woodhead Publishing, Cambridge, 1st edn., 2017, pp. 151–180.
93 Alicona, *IF-Measure Suite Version 5.1 Manual*, Bruker Alicona, Raaba, Austria, 1st edn., 2013.
94 F. Helmli, in *Optical Measurement of Surface Topography*, Springer Publishing, New York City, 1st edn., 2011, pp. 1–23.
95 International Organization for Standardization, *ISO 21920-3:2021 - Geometrical product specifications (GPS) — Surface texture: Profile — Part 3: Specification operators*, ISO, Geneva, 1st edn., 2021.
96 A. Gugliuzza and E. Drioli, *J Memb Sci*, 2013, **446**, 350–375.
97 K. Y. Law, *J Phys Chem Lett*, 2014, **5**, 686–688.
98 P. S. Brown and B. Bhushan, *APL Mater*, , DOI:10.1063/1.4935126.
99 J. Zimmermann, S. Seeger and F. A. Reifler, *Textile Research Journal*, 2009, **79**, 1565–1570.
100 C. Loghin, L. Ciobanu, D. Ionesi, E. Loghin and I. Cristian, in *Waterproof and Water Repellent Textiles and Clothing*, Woodhead Publishing, Cambridge, 1st edn., 2018, pp. 3–24.
101 International Organization for Standardization, *BS EN 20811:1992 - Textiles. Determination of resistance to water penetration. Hydrostatic pressure test (British Standard)*, British Standards Institution, Milton Keynes, 1st edn., 1992.
102 International Organization for Standardization, *B.S. 2782:part 8:method 820a:1996.*, British Standards Institution, Milton Keynes, 1st edn., 1996.

103 nternational Organization for Standardization, *ISO 11357-1:2023 - Plastics — Differential scanning calorimetry (DSC) — Part 1: General principles*, British Standards Institution, Milton Keynes, 4th edn., 2023.
104 G. Jones, *DSC-8000 data sheet*, International Equipment LTD, St. Albans, 1st edn., 2016.
105 M. R. Vengatesan, A. M. Varghese and V. Mittal, in *Thermosets Structure, Properties, and Applications*, ed. Q. Guo, Elsevier, Amsterdam, 2nd edn., 2018, pp. 69–114.
106 A. Shrivastava, in *Introduction to Plastics Engineering*, William Andrew Publishing, Norwich, NY, 1st edn., 2018, pp. 49–110.
107 J. Bergström, in *Mechanics of Solid Polymers*, William Andrew Publishing, Norwich, NY, 1st edn., 2015, pp. 19–114.
108 Perkin Elmer, Application Note Thermal Analysis, https://resources.perkinelmer.com/lab-solutions/resources/docs/APP_007771B_05_Mechanical_Properties_of_Films_and_Coatings.pdf, (accessed 18 September 2024).
109 S. Spiegelberg, A. Kozak and G. Braithwaite, in *UHMWPE Biomaterials Handbook: Ultra High Molecular Weight Polyethylene in Total Joint Replacement and Medical Devices*, ed. S. Kurtz, William Andrew Publishing, Norwich, NY, 3rd edn., 2016, pp. 531–552.
110 H. Tan, Plasticity Lab, https://homepages.abdn.ac.uk/h.tan/pages/teaching/plasticity/lab.htm, (accessed 1 February 2024).
111 A. Vaidya and K. Pathak, in *Applications of Nanocomposite Materials in Dentistry*, eds. A. Asiri, A. Mohammad and I. Mohammad, Woodhead Publishing, Cambridge, 1st edn., 2018, pp. 285–305.
112 Y. Elmogahzy, in *Handbook of Properties of Textile and Technical Fibres*, ed. A. Bunsell, Woodhead Publishing, Cambridge, 2nd edn., 2018, pp. 21–55.
113 S. R. Djafari Petroudy, in *Advanced High Strength Natural Fibre Composites in Construction*, Woodhead Publishing, Cambridge, 1st edn., 2017, pp. 59–83.
114 H. He, Y. Yan, Z. Qiu and X. Tan, *Prog Org Coat*, 2017, **113**, 110–116.
115 C. J. Weng, Y. L. Chen, Y. S. Jhuo, L. Yi-Li and J. M. Yeh, *Polym Int*, 2013, **62**, 774–782.
116 W. Shen, L. Feng, X. Liu, H. Luo, Z. Liu, P. Tong and W. Zhang, *Prog Org Coat*, 2016, **90**, 139–146.
117 I. Zvonkina and M. Soucek, *Curr Opin Chem Eng*, 2016, **11**, 123–127.
118 M. Gholami, G. Mir and M. Sadeghi, *Journal of Particle Science and Technology*, 2015, **1**, 1–11.
119 O. C. Wokadala, S. S. Ray, J. Bandyopadhyay, J. Wesley-Smith and N. M. Emmambux, *Polymer (Guildf)*, 2015, **71**, 82–92.
120 K. E. Geckeler and H. Nishide, *Advanced Nanomaterials*, Wiley-VCH, New Jersey, 1st edn., 2009.
121 S. S. Mahapatra, S. K. Yadav, H. J. Yoo, M. S. Ramasamy and J. W. Cho, *Sens Actuators B Chem*, 2014, **193**, 384–390.
122 A. Reghunadhan and S. Thomas, in *Polyurethane Polymers: Blends and Interpenetrating Polymer Networks*, eds. S. Thomas, J. Datta, J. Haponiuk and Arunima. Reghunadhan, Elsevier, Amsterdam, 1st edn., 2017, pp. 1–16.
123 I. S. Ryu, X. Liu, Y. Jin, J. Sun and Y. J. Lee, *RSC Adv*, 2018, **8**, 23481–23488.
124 K. C. Cole, *Macromolecules*, 2008, **41**, 834–843.

125 L. Yan, C. B. Roth and P. F. Low, *Langmuir*, 1996, **12**, 4421–4429.
126 V. C. Farmer and J. D. Russell, *Spectrochimica Acta*, 1964, **20**, 625–627.
127 W. L. Ijdo, S. Kemnetz and D. Benderly, *Polym Eng Sci*, 2006, **46**, 1031–1039.
128 D. K. Lee and H. B. Tsai, *J Appl Polym Sci*, 1999, **75**, 167–174.
129 J. Schalnat, D. G. Gómez, L. Daelemans, I. De Baere, K. De Clerck and W. Van Paepegem, *Polym Test*, 2020, **91**, 67–75.
130 F. Clegg and C. Breen, *Appl Clay Sci*, , DOI:10.1016/j.clay.2013.08.048.
131 T. T. T. Ho, Y. S. Ko, T. Zimmermann, T. Geiger and W. Caseri, *J Mater Sci*, 2012, **47**, 4370–4382.
132 C. Ochoa-Putman and U. K. Vaidya, *Compos Part A Appl Sci Manuf*, 2011, **42**, 906–915.
133 L. Liao, X. Li, Y. Wang, H. Fu and Y. Li, *Ind Eng Chem Res*, 2016, **55**, 11689–11699.
134 A. Razzaque, P. Tesinova, L. Hes, J. Salacova and H. A. Abid, *Fibers and Polymers*, 2017, **18**, 1924–1930.
135 G. Choudalakis and A. D. Gotsis, *Eur Polym J*, 2009, **45**, 967–984.
136 B. Tan and N. L. Thomas, *Appl Clay Sci*, 2017, **141**, 46–54.
137 W. S. Chow and W. L. Tham, *Express Polym Lett*, 2009, **3**, 116–125.
138 W. S. Chow and W. L. Tham, *Polym Plast Technol Eng*, 2009, **48**, 342–350.
139 European Patent Officer, EP0924563A1, 1999.
140 B. Pradhan and S. K. Srivastava, *Polym Int*, 2014, **63**, 1219–1228.
141 LayerOne, LayerOne Advanced Materials, https://www.layeronematerials.com, (accessed 1 February 2024).
142 Graphitene, Graphene Oxide Powder, https://www.graphitene.com/shop/graphene-oxide-powder-1g/, (accessed 1 February 2024).
143 Merck, Graphene Nanoplatelets, https://www.sigmaaldrich.com/GB/en/search/graphene-nanoplatelets?focus=products&page=1&perpage=30&sort=relevance&term=graphene%20nanoplatelets&type=product, (accessed 1 February 2024).
144 A. Jiménez-Suárez and S. González Prolongo, *Graphene nanoplatelets*, Applied Sciences, Basel, 1st edn., 2020, vol. 10.
145 J. Schulte, Z. Jiang, O. Sevim and O. E. Ozbulut, in *The Rise of Smart Cities: Advanced Structural Sensing and Monitoring Systems*, Butterworth-Heinemann, Oxford, 2nd edn., 2022, pp. 79–114.
146 S. Peretz Damari, L. Cullari, R. Nadiv, Y. Nir, D. Laredo, J. Grunlan and O. Regev, *Compos B Eng*, 2018, **134**, 218–224.
147 C. Thiyagu, I. Manjubala and U. Narendrakumar, *Thermal and morphological study of graphene based polyurethane composites*, Elsevier, Amsterdam, 1st edn., 2021, vol. 45.
148 L. Stobinski, B. Lesiak, A. Malolepszy, M. Mazurkiewicz, B. Mierzwa, J. Zemek, P. Jiricek and I. Bieloshapka, *J Electron Spectros Relat Phenomena*, 2014, **195**, 145–154.
149 M. Strankowski, D. Włodarczyk, Ł. Piszczyk and J. Strankowska, *Journal of Spectroscopy*, 2016, **12**, 1–6.
150 C. Pierce, in *Graphene : An Introduction to the Fundamentals and Industrial Applications*, eds. M. Sharon, M. Sharon, H. Shinohara and A. Tiwari, John Wiley & Sons, Incorporated, New Jersey, 1st edn., 2015, vol. 1, pp. 73–106.
151 R. Sharma, N. Chadha and P. Saini, *Indian Journal of Pure and Applied Physics*, 2017, **55**, 625–629.

152 V. Srivastava and K. Jain, *Mater Lett*, 2016, **169**, 28–32.
153 R. F. De Farias, in *Interface Science and Technology*, Elsevier, Amsterdam, 1st edn., 2023, vol. 36, pp. 39–58.
154 F. T. L. Muniz, M. A. R. Miranda, C. Morilla Dos Santos and J. M. Sasaki, *Acta Crystallogr A Found Adv*, 2016, **72**, 385–390.
155 S. Ye, B. Wang, Z. Pu, T. Liu, Y. Feng, W. Han, C. Liu and C. Shen, *Sep Purif Technol*, , DOI:10.1016/j.seppur.2021.118553.
156 I. Bramhecha and J. Sheikh, *Carbon Trends*, , DOI:10.1016/j.cartre.2021.100067.
157 R. W. Seymour and S. L. Cooper, *Macromolecules*, , DOI:10.1021/ma60031a008.
158 R. Ikram, B. M. Jan and W. Ahmad, *Journal of Materials Research and Technology*, 2020, **9**, 11587–11610.
159 S. F. Hosseini, Z. Javidi and M. Rezaei, *Int J Biol Macromol*, 2016, **92**, 1205–1214.
160 Z. Qu, Y. Wang, N. Jin, G. Chen, Y. Chen and S. Li, *Food Biosci*, , DOI:10.1016/J.FBIO.2023.103512.
161 R. Danzl, F. Helmli and S. Scherer, *Journal of Mechanical Engineering*, 2011, **57**, 245–256.
162 Alicona, What is Focus-variation?, https://optimaxonline.com/newsdetails.php?newsId=117#:~:text=Measurement%20resolution%20can%20be%20changed,with%20full%20depth%20of%20field., (accessed 1 February 2024).
163 Y. Qin, in *Medical Textile Materials*, Woodhead Publishing, Cambridge, 1st edn., 2016, pp. 89–107.
164 A. Khakpour, M. Gibbons and S. Chandra, *Journal of Industrial Textiles*, , DOI:10.1177/15280837211014239.
165 G. C. Lainioti, G. Bounos, G. A. Voyiatzis and J. K. Kallitsis, *Polymers (Basel)*, , DOI:10.3390/polym8050190.
166 A. Phillips, M. Ulsh, J. Mackay, T. Harris, N. Shrivastava, A. Chatterjee, J. Porter and G. Bender, *Fuel Cells*, 2020, **20**, 60–69.